THE PRINCIPLE OF ADDITIVITY
and
THE PROEUTECTOID FERRITE TRANSFORMATION

By

Rajeev Gurunath Kamat

B.E., Visvesvaraya Regional College of Engineering, Nagpur, India, 1982
M.Tech., Indian Institute of Technology, Bombay, India, 1984

A THESIS SUBMITTED IN PARTIAL FULFILLMENT OF

THE REQUIREMENTS FOR THE DEGREE OF

DOCTOR OF PHILOSOPHY

in

THE FACULTY OF GRADUATE STUDIES

(Department of Metals and Materials Engineering)

We accept this thesis as conforming

to the required standard

THE UNIVERSITY OF BRITISH COLUMBIA

May 1990

In presenting this thesis in partial fulfilment of the requirements for an advanced degree at the University of British Columbia, I agree that the Library shall make it freely available for reference and study. I further agree that permission for extensive copying of this thesis for scholarly purposes may be granted by the head of my department or by his or her representatives. It is understood that copying or publication of this thesis for financial gain shall not be allowed without my written permission.

Department of METALS AND MATERIALS ENGINEERING

The University of British Columbia
Vancouver, Canada

Date 12th July, 1990

DE-6 (2/88)

Abstract

This study critically examines the additivity of the proeutectoid ferrite transformation. The study has been carried out in two parts with the first part involving experimental verification of the additivity of the proeutectoid ferrite transformation and the second part a theoretical assessment of the additive nature of the ferrite transformation with the aid of mathematical models.

Austenite-to-proeutectoid ferrite transformation kinetics were measured under a number of isothermal, stepped-isothermal and continuous-cooling conditions for three plain-carbon hypo-eutectoid steel grades (AISI 1010, 1020 and 1040) using a dilatometer and a Gleeble 1500 thermomechanical simulator. Isothermal transformation kinetics were characterized using the Avrami equation. The stepped-isothermal transformation tests were designed to experimentally assess the additive nature of the austenite to proeutectoid ferrite transformation by measuring transformation kinetics partially at one temperature and after a rapid temperature change to another temperature. Results on the 1010 and 1040 steels showed that the proeutectoid ferrite transformation with polygonal morphology is additive under changing temperature in that the ferrite transformation kinetics at the second temperature are quite similar to the isothermal kinetics at that temperature.

Stepped-isothermal transformation measurements were made on the 1020 steel with the resulting ferrite morphology either remaining Widmanstätten at both temperatures or changing from allotriomorph to predominantly Widmanstätten at the two temperatures. In both cases the results showed additive behavior. However, the stepped-isothermal test in which the proeutectoid ferrite was transformed to an equilibrium amount and equilibrated at the first temperature and then rapidly changed to the second temperature was not additive.

Characterizing the isothermal formation of proeutectoid ferrite in the three steels using the Avrami equation resulted in a reasonably constant value of n and the b parameter increasing with increasing transformation temperature. Early site saturation was evident in a number of test specimens.

In the second part of the study, two mathematical models with planar and spherical interface geometries were developed to theoretically assess the additivity of the proeutectoid ferrite transformation. A finite-difference numerical technique was employed to describe the austenite to ferrite diffusion controlled moving-interface problem for a system having finite boundaries. A test of additivity of the proeutectoid ferrite transformation was made by predicting the ferrite growth kinetics and the associated carbon gradients under stepped-isothermal conditions. The predictions were consistent with the observed experimental additivity of the proeutectoid ferrite transformation in the 1010 steel. The spherical model predicted isothermal ferrite growth kinetics compared more favorably with the experimentally measured kinetics of the 1010 steel than the planar model.

An unusual phase was detected in the 1020 steel. A number of tests were performed to measure the isothermal transformation kinetics of the new phase. Scanning electron microscopy (SEM) and scanning-transmission electron microscopy (STEM) were used to further investigate the structural details in this new phase. The results indicated that the new phase is a type of bainite but having some of the characteristics attributable to massive transformation products.

Table of Contents

List of Tables

List of Figures

List of Symbols

b	Kinetic parameter in Avrami equation
C_M	Carbon content in mole fraction
C_α	Concentration of carbon in ferrite
C_γ	Concentration of carbon in austenite
d	Prior austenite grain diameter (m)
D	Dilatometer response due to phase transformation (mV)
D_{MIN}	Minimum dilatometer reading prior to transformation (mV)
D_{MAX}	Maximum dilatometer reading after transformation (mV)
ΔD_F	Dilatometer change due to phase transformation (mV)
D_{TOT}	Total dilatometer change due to phase transformation (mV)
D_C^γ	Diffusion coefficient of carbon in austenite ($m^2\ s^{-1}$)
ΔF	Free energy change (kJ/mole)
J	Diffusion flux of carbon in austenite ($g\ cm^{-2}\ s^{-1}$)
n	Kinetic parameter in Avrami equation
N	Number of nuclei per unit volume
N_A	Number of particles per unit test area
N_L	Number of particles intercepting unit length of test line
P	Symbol denoting pearlite
Q	Activation energy (kJ/mole)
R	Gas constant (J/°C mole)
S	Thickness of planar ferrite precipitate (m)
t	Time (s)
Δt	Time increment (s)
T	Temperature (°C)

ΔT	Temperature change ($^{\circ}C$)
$T_{A_{c1}}$	Austenite-pearlite equilibrium transformation temperature during heating ($^{\circ}C$)
$T_{A_{c3}}$	Austenite-ferrite equilibrium transformation temperature during heating ($^{\circ}C$)
$t_{st_{TTT}}$	Experimental TTT start time for ferrite transformation (s)
$t_{st_{CCT}}$	Experimental CCT start time for ferrite transformation (s)
V	Interphase boundary migration rate (m/s)
x	Diffusion distance (m)
X	Fraction transformed
Δx	Node size (m)
α	Symbol denoting ferrite
β	Symbol denoting parabolic growth rate constant for ferrite
γ	Symbol denoting austenite

Acknowledgement

I would like to acknowledge with pleasure, my heartfelt gratitude toward my supervisors Prof. Bruce Hawbolt and Prof. Keith Brimacombe, for their valuable guidance and encouragement, throughout the course of this project. I am very grateful to Prof. Laurence Brown for all the help he provided by way of stimulating discussions on the subject of Phase Transformations in steels and for correcting the thesis.

I truly appreciate Mr. Binh Chau's expert assistance in the experimental part of the project. I would like to sincerely thank Ms. Laurie Fredrick for performing the STEM analysis and Ms. Mary Mager for helping in the SEM work.

I would like to thank past and present fellow graduate students and others who contributed to this project by way of interesting discussions, in particular Mr. B. Hernandez-Morales, Mr. K. Mukunthan, Ms. S. Gowri, Ms. V. Sahajwalla, Mr. V. Chaskar, Dr. R. Bommaraju, Dr. P. Campbell, Dr. E. Osinski and Dr. Kanthi Kalauarachchi during various stages of this project. I am very grateful to my friends Ms. Louise Panziera and Dr. R. B. Mahapatra for all the help they provided, especially in printing the photomicrographs.

I acknowledge with thanks the financial support provided by Natural Sciences and Research Council of Canada.

Chapter 1 - INTRODUCTION

The steel industry has adopted continuous processes to improve productivity through reduced production costs and better product quality. Hence, most of the industrial thermomechanical treatment of steel is performed under continuous cooling or heating conditions. However, isothermal transformation studies have a great advantage in that one of the variables, temperature, is kept constant and the study of transformation behaviour under isothermal conditions is relatively convenient from an experimental as well as a theoretical point of view. A critical examination of the literature available on transformation studies in steels, establishes that an enormous amount of effort has been expended in obtaining microstructural changes under predominantly isothermal conditions, for example, as indicated in Time-Temperature-Transformation(TTT) diagrams[1]. However, industrial thermomechanical treatments are usually performed under non-isothermal conditions, thereby creating a need to predict the microstructural evolution and associated mechanical properties of steels undergoing non-isothermal transformation. This need has resulted in the development of mathematical models which incorporate heat flow and physical metallurgy principles to characterize the continuous microstructural changes occurring during heating or cooling. The increasing use of continuous cooling transformation data (CCT)[2-5] for a range of plain-carbon and low-alloy steels has partially satisfied this need.

Over the last couple of decades there has been some success in predicting the continuous-cooling transformation behaviour using isothermal data by assuming that the non-isothermal austenite decomposition could be described in terms of a series of isothermal events. This linking of continuous cooling transformation kinetics to isothermal data is possible provided the transformation obeys the principle of additivity. Thus the application of the additivity principle in describing phase transformation kinetics under non-isothermal conditions is a powerful tool in the mathematical modelling of microstructural evolution

during non-isothermal treatment of steels. Although the additivity principle has been used quite successfully over the last two decades to predict non-isothermal transformation behaviour using isothermal data, there has been very little work to examine the reasons why it is applicable from a fundamental point of view. This study has been undertaken to gain further insight into the applicability of the additivity principle to the austenite-to-proeutectoid ferrite transformation in hypoeutectoid plain-carbon steels. An assessment of the applicability of the additivity principle has been carried out experimentally as well as by using mathematical models developed from theoretical considerations.

Chapter 2 - LITERATURE REVIEW

2.1 The Principle of Additivity

The principle of additivity is based on the theory advanced by Scheil[6], who proposed that the start of a transformation under non-isothermal conditions could be predicted by calculating the consumption of fractional incubation time at each isothermal temperature and adding these fractions to give a sum equal to unity. The Scheil theory has been extended to phase transformations to predict continuous-cooling transformation kinetics from isothermal data. In order to relate isothermal kinetic data to continuous cooling transformation behaviour it is necessary that the rate of transformation depend only on the state of the assembly and not on the thermal path by which it reached that state. If this is true, then the instantaneous transformation rate must be shown to be a function solely of the amount of prior transformation and the temperature[7] i.e.:

$$R_x = f(X,T) \tag{2.1}$$

where R_x is the rate of transformation, X is the amount of transformation product already present and T is the instantaneous temperature.

Figure 2.1 graphically illustrates the principle of additivity. Consider the simplest type of non-isothermal reaction obtained by combining two isothermal treatments as shown in Fig. 2.1. Suppose the assembly is partially transformed at temperature T_1 for a time t_1, where the kinetic law is fraction transformed $X = f_1(t_1)$. At time t_1 the assembly is cooled (or heated) rapidly to T_2 and the transformation continues at this temperature (T_2). If the transformation is additive, the course of the transformation at T_2 is exactly the same as if the transformed fraction ($f_1(t_1)$) had been formed at T_2. Thus if t_2 is the time taken at T_2 to produce the same amount of transformation as is produced at T_1 in a time t_1, we have,

$$X = f_1(t_1) = f_2(t_2) \tag{2.2}$$

and the course of the whole reaction is

$$X = f_1(t) \quad if \quad t < t_1 \tag{2.3a}$$

$$X = f_2(t + t_2 - t_1) \quad if \quad t > t_1 \tag{2.3b}$$

The Eq. (2.3a) refers to the time the assembly is at temperature T_1, such that the fraction transformed, X, is a function of the time at the temperature T_1. Equation (2.3b) gives the fraction transformed for $t > t_1$, such that the assembly has been cooled rapidly to T_2, with $X = f_1(t_1)$ already present. Since t_1 is the time spent by the assembly at T_1, the additional time that the assembly will spend at T_2 will be $(t - t_1)$. To this real time is added the virtual time, t_2, which is the time the assembly would have taken at T_2 to produce the same amount of transformation as is produced at T_1. It should be emphasized that the diagram (Fig. 2.1) does not imply that it takes time $(t_2 - t_1)$ for the assembly to change from temperature T_1 to T_2.

Referring to Fig. 2.1, if the reaction at temperature T_1 is allowed to continue until time t_{a_1}, a fixed amount of transformation, X_a, will be formed; t_{a_2} is the corresponding time to produce the same amount of transformation at T_2. In a composite process, the total time to form amount X_a over two stages will include the time spent at each temperature. Hence the total time, t, will be given by the time, t_1, spent at T_1 plus the time, $(t_{a_2} - t_2)$, spent at T_2. Thus,

$$t = t_1 + t_{a_2} - t_2 \tag{2.4}$$

if the reaction is additive. Rearranging Eq. (2.4)

$$\frac{t - t_1}{t_{a_2}} + \frac{t_2}{t_{a_2}} = 1 \tag{2.5}$$

During continuous cooling, the time the material spends at each temperature and the difference between the two successive temperatures can be assumed to approach zero. In other words, referring to Fig. 2.1, as the difference between T_1 and T_2 approaches zero, the two transformation curves approach one another, and the slopes become similar. For identical curves:

$$\frac{t_1}{t_{a1}} = \frac{t_2}{t_{a2}} \tag{2.6}$$

Substituting Eq. (2.6) into Eq. (2.5) we obtain,

$$\frac{t - t_1}{t_{a2}} + \frac{t_1}{t_{a1}} = 1 \tag{2.7}$$

In Eq. (2.7) t_{a1} and t_{a2} are isothermal transformation times. Thus, in the limit of very small temperature change, an additive reaction implies that the total time to reach a specified amount of transformation (X_a in this case) under continuous cooling conditions is obtained by adding the fractions of time to reach this stage isothermally until the sum reaches unity. This concept can be generalized into an equation which is equivalent to Eq. (2.7), that is:

$$\int_{t_s}^{t_{X_a}} \frac{dt}{t_a(T)} = 1 \tag{2.8}$$

where $t_a(T)$ is the isothermal time to reach stage X_a at temperature T and, t_s and t_{X_a} are the start time and the time to reach X_a respectively, under continuous cooling conditions.

Scheil[6] proposed an equation similar to Eq. (2.8). However, as mentioned earlier, Scheil was not considering the transformation stage of a reaction nor did he use the term "additivity" to define conditions under which such an equation could be applied to the transformation event. Instead, he proposed to use this approach to estimate the incubation period for the formation of ferrite, cementite and pearlite from austenite for continuous cooling conditions. He assumed that the time spent at a particular temperature, t_i, represented the fraction of the total incubation time required, $\frac{t_i}{\tau_i}$. When the sum of such fractions (called the "fractional incubation time") became equal to unity, the transformation started. Mathematically,

$$\sum_{i=1}^{n} \frac{t_i}{\tau_i} = 1 \tag{2.9}$$

defines the consumption of the incubation time prior to transformation. The sum of the fractional nucleation times will then be given by integration over the range of temperatures involved, that is:

$$\int_0^{t_t} \frac{dt}{\tau(T)} = 1 \tag{2.10}$$

The difference between Eq. (2.8) and Eq. (2.10) is that the former refers to the transformation event and the latter deals with the incubation period. Assuming a constant cooling rate, $\alpha = \frac{dT}{dt}$, the following expression can be given for the consumption of incubation period described in Eq. (2.10);

$$\int_0^{t_t} \frac{dt}{\tau(T)} \frac{dT}{dT} = 1$$

$$\int_0^{t_t} \frac{dT}{\tau(T)} \frac{1}{dT/dt} = 1$$

$$\int_{T_0}^{T_t} \frac{dT}{\tau(T)} = \alpha \tag{2.11}$$

Thus, although Scheil's equation (Eq. (2.9)) for additivity was meant exclusively for the incubation event, it has been extended to the transformation stage for a constant cooling rate as well.

2.2 Criteria for Use of the Principle of Additivity

Although the use of the additivity principle was seen as a requirement for describing non-isothermal reaction, in terms of isothermal kinetics, some reservations were held as to the type of transformations that could be described as being additive. Avrami[8] developed the following analytical expression to describe a sigmoidal-shaped, isothermal transformation-time event, such as that shown in Fig. 2.1:

$$X = 1 - \exp(-b\, t^n) \tag{2.12}$$

where X is the normalized fraction transformed, b and n are constants and t is the duration of transformation. The sigmoidal shape is considered to reflect the relative effects of combined nucleation and growth processes.

The Avrami equation is a general representation of the Johnson-Mehl equation[11]:

$$X = 1 - \exp\left(-\frac{\pi}{3} N G^3 t^4 \right) \tag{2.13}$$

which was developed to describe the isothermal austenite-to-pearlite transformation, which occurs by nucleation and growth process. In this equation, N and G are nucleation and growth rates, respectively, and both are assumed constant. Eqs. 2.12 and 2.13 were developed for transformations which exhibit linear growth such as the austenite-to-pearlite transformation. The Avrami equation (Eq. (2.12)), has been applied to long-range diffusion-controlled reactions as well, such as the austenite-to-ferrite transformation[7,25]. However, the Avrami equation (Eq. (2.12)), when applied to characterize the complete austenite-to-ferrite transformation, is more of a mathematical tool than an equation of fundamental significance.

The fundamental aspect of the additivity principle is that the reaction rate depends only on instantaneous temperature and fraction transformed. Cahn[13] postulated that this could be satisfied by an isothermal transformation rate equation:

$$\frac{dX}{dt} = \frac{H(T)}{G(X)} \tag{2.14}$$

where $\frac{dX}{dt}$ is the rate of change of fraction transforming, $H(T)$ is a function of temperature only and $G(X)$ is a function of fraction transformed only. This equation was seen to be sufficient for describing an additive reaction. It can be shown that the Avrami equation (Eq. (2.12)) obeys the criterion proposed by Cahn[13], if certain assumptions are made. Rearranging the Avrami equation (Eq. (2.12)):

$$\begin{aligned} \exp(-b\,t^n) &= 1-X \\ -b\,t^n &= \ln(1-X) \\ t &= \left\{ \ln\frac{(1-X)}{-b} \right\}^{\frac{1}{n}} \end{aligned} \tag{2.15}$$

Differentiating Eq. (2.12) with respect to t,

$$\frac{dX}{dt} = -\exp(-b\,t^n)(-n\,b\,t^{n-1}) \tag{2.16}$$

Substituting Eq. (2.15) into (2.16),

$$\begin{aligned} \frac{dX}{dt} &= (1-X)(b\,n)\left\{ \frac{\ln(1-X)}{-b} \right\}^{\frac{n-1}{n}} \\ &= (1-X)(n)(-b)^{\frac{1}{n}}\{\ln(1-X)\}^{\frac{n-1}{n}} \\ &= \frac{n\,(-b)^{\frac{1}{n}}}{\left(\frac{1}{1-X}\right)\left(\frac{1}{\ln(1-X)}\right)^{\frac{n-1}{n}}} \end{aligned} \tag{2.17}$$

Thus, if b is a function of temperature only and n is a constant, Eq. (2.17) satisfies Cahn's equation (Eq. (2.14)).

Avrami[8,9,10] also examined the requirements for applying isothermal reaction kinetics to describe continuous cooling transformation behaviour, i.e., the use of the additivity principle. He postulated a range over which the additivity principle could be used for a transformation which includes both nucleation and growth processes. This range, known as the isokinetic range, is defined as the temperature range over which the ratio of the nucleation rate, N, to growth rate, G, remains a constant.

Cahn[13] recognized that the isokinetic condition, N/G being constant over a temperature range, is a fortuitous circumstance as both the nucleation and growth rates vary independently with temperature and possibly with time. Since the isokinetic condition will

rarely be satisfied, Cahn introduced an alternative criterion for establishing the existence of an additive reaction. He observed that many systems in which nucleation is heterogenous exhibit the property that all nucleation occurs early in the reaction. This may be due to the fact that only a limited number of sites for nucleation, such as impurity particles, grain corners, grain edges or grain boundaries exist and these sites can be consumed very early in the reaction. Cahn called this phenomenon *"early site saturation"*.

If the nucleation sites saturate early in the reaction, the course of the reaction will be dependent solely upon the growth rate. If the growth rate is a function of instantaneous temperature only, then the reaction will be additive. Cahn[12] derived conditions under which sites will be saturated, for a reaction in which both the growth rate and the specific nucleation rate are independent of time. As shown in Fig. 2.2, based on a space filling tetrakaidecahedron grain shape model, the following conditions were derived for site saturation to be realized:

$$N_c(corner) > 2.5\times 10^2 \frac{G}{d^4} \tag{2.18}$$

$$N_e(edge) > 10^3 \frac{G}{d^4} \tag{2.19}$$

$$N_s(surface) > 6\times 10^3 \frac{G}{d^4} \tag{2.20}$$

where N is the nucleation rate of a particular site, G is the growth rate and d is the grain diameter. Cahn went further and proposed rate laws for different sites after early site saturation. However, experimental verification of these rate laws is not an easy task due to the fact that, in an opaque system, the grain boundary area, grain edge, grain length or number of corners is difficult to measure.

A second criterion for site saturation proposed by Cahn[12] was based upon the nucleation of at least one pearlite nodule per grain. He proposed that site saturation will occur if,

$$\frac{G\, t_{0.5}}{d} \leq 0.5 \tag{2.21}$$

where G is the growth rate, d is the grain diameter and $t_{0.5}$ is the time to complete 50% of the transformation.

It is clear from the above discussion that in order to use the Avrami equation (Eq. (2.12)) to describe a continuous cooling transformation using isothermal data, the transformation event must be additive. Kuban et al.[15] recently examined the criteria for applicability of additivity as postulated by Avrami[8,9,10] and Cahn[12,13,14] for the austenite-to-pearlite transformation in a eutectoid plain-carbon steel. It was shown that, although the theoretical criteria are sufficient they are not always necessary for additivity to be realized. It was found that the ratio N/G did not remain constant over a temperature range. Instead, the nucleation rate increased more with decreasing temperature than did the growth rate. Hence, for the pearlite reaction in a eutectoid carbon steel, the isokinetic condition proposed by Avrami[8] did not hold.

An assessment of the site saturation criterion proposed by Cahn[13] was also made by Kuban et al.[15]. As it is very difficult experimentally to measure nucleation rates for the individual surface, edge and corner sites, the comparison was made using the corner nucleation rate. It was shown that the experimental nucleation rate observed over the initial 20% of transformation, which is the combined effect of corner (N_c), edge (N_e) and surface (N_s) nucleation rates, was consistently less than that required for corner site saturation and therefore must have been less than that required for edge or grain boundary saturation.

Cahn's [12] alternative early site saturation condition (Eq. (2.21)) of at least one pearlite nodule per grain was also examined. Metallographic observations, as well as calculated values of $\frac{G\,t_{0.5}}{D}$, were not consistent with early site saturation. Relatively few pearlite nodules were observed to be growing in a large number of austenite grains. Although the criteria proposed by Avrami[8] and Cahn[13] did not hold for the austenite-to-pearlite reaction in a 1080 eutectoid steel, at the temperatures examined by Kuban et al.[15], it was possible to describe the continuous cooling transformation kinetics using the isothermal transformation data.

In the light of failure to satisfy the criteria for defining additive reactions, Kuban et al.[15] proposed yet another condition for additivity to hold. This new criterion called *"effective site saturation"*, was based on the assumption that the material nucleating early in a transformation reaction accounts for the major portion of transformation volume in later stages of the reaction. This criterion is based upon the empirically derived relation:

$$t_{20} \geq 0.37\, t_{90} \tag{2.22}$$

where t_{20} is the time required to reach 20% of transformation and t_{90} is the time to reach 90% transformation. Equation (2.22) was derived for $t = 0$ at T_{A_1} and $n = 4$ [J-M equation (Eq. (2.13))]. For the case of the transformation event only, i.e., $t = 0$ at the start of the transformation and the experimentally observed[23] $n = 2$, the authors derived the following effective site saturation condition:

$$t'_{20} \geq 0.28\, t'_{90} \tag{2.23}$$

Here, t'_{20} and t'_{90} refer to transformation times only. The observed time exponent, $n = 2$, was attributed to grain edge nucleation and early site saturation. Whereas, using the J-M equation[11] and $n = 4$, reflected the random nucleation site described in the development of

the J-M equation. The authors[15] examined the effective site saturation criterion using reported austenite-to-pearlite isothermal kinetic data and observed that the criterion is satisfied in each case, thereby explaining the observed additivity in these steels.

2.3 Application of the Principle of Additivity

The application of the additivity principle to predict non-isothermal transformation kinetics using isothermal transformation data has been recognized as a powerful metallurgical tool. In 1940 Grange and Kiefer[16] addressed the need for correlating the transformation phenomena during continuous cooling with isothermal data. They derived a simple relationship between isothermal and continuous cooling transformation kinetics for a given cooling rate. Although the study had some erroneous assumptions and examined only one steel (S.A.E. 4340), it was one of the first studies that attempted to relate isothermal and non-isothermal transformation behavior.

In 1946, Manning and Lorig[17] examined the relationship between the start of transformation during cooling and the start of the isothermal transformation for five 0.30 wt.% carbon steels of various chromium contents. The authors presented a method to calculate the start of the transformation on cooling, based essentially on the method proposed by Scheil[6]. The validity of the assumption of additivity for the incubation event was examined using step tests at two different isothermal temperatures. It was observed that the incubation event was additive for the equiaxed ferrite range (from $T_{A_{e_3}}$ to $649°C$), and for the mixed microstructure of acicular ferrite and bainite, in the range of $593°C$ to $371°C$. In the latter case, the incubation events were additive individually as well as for the acicular ferrite to bainite transition. However, tests started in the equiaxed ferrite range and completed in either the acicular ferrite or bainite range were not additive. The authors also used experimental cooling curves obtained from end-quench bars to compare experimental start times with calculated start times. It was found that the experimental and calculated data differed appreciably for two of the five steels investigated.

In 1954, Moore[18] assessed the validity of Scheil's fractional incubation theory under step-quench and continuous cooling conditions. Comparing experimental results and predictions made with the Scheil[6] theory for the step-quench conditions, he found poor agreement for the start of the transformation. On the other hand, a much better correspondence between predicted and observed transformation start times was found for the continuous-cooling experiments. The discrepancy between the step-quench and continuous-cooling predictions in terms of the Scheil[6] theory was attributed to a difference in nucleation mechanisms for the two different cooling regimes.

In 1973, Kirkaldy[19] proposed a simple algorithm for the calculation of hardenability of low alloy eutectoid steels, based upon thermodynamic and kinetic data and theories of nucleation and growth of pearlite. The unique feature of Kirkaldy's method was the calculation of a realistic pearlite growth velocity as a function of undercooling and the diffusion coefficient of carbon. The TTT 'start times' were also predicted, based upon the diffusion coefficient, the degree of undercooling and a summation effect for each alloying element. Similar to an approach due to Grange and Kiefer[16], the conversion of TTT to CCT start times was accomplished by assuming that if a given continuous cooling curve intersects a TTT start curve at temperature, T_s, and time, τ_s, and intersects the CCT start curve at a different temperature, T_c, and time, τ_c, then the two intersections can be related by the equation:

$$\tau_{\left(\frac{T_s+T_c}{2}\right)} = \tau_c - \tau_s \qquad (2.24)$$

Using predicted TTT and CCT curves, Kirkaldy[19] performed a sample calculation of hardenability for a 4068 steel and compared the results with experimental data, obtaining reasonable agreement.

In subsequent studies[20,21], Kirkaldy and co-authors refined their earlier approach by attempting to improve the method of predicting TTT and CCT curves. They evaluated the

$T_{A_{e3}}$ temperatures using published standard free energy changes and activity data for iron and its binary and ternary alloys. The incubation period was obtained through use of a nonlinear formula derived to fit a set of TTT curves. This formula included the grain size effect, the effect of degree of undercooling and the effect of individual alloying elements. It was expressed as:

$$\tau_{TTT}^{(0.1\%)} = \exp\left[\frac{Q_{eff}/RT}{2^{(p-1)/2}\Delta T^3}\right]\sum_{j=1}^{m}\alpha_j C_j \qquad (2.25)$$

where Q_{eff} is the empirically determined effective activation energy for diffusion, p is the ASTM grain size of the austenite, ΔT is the degree of undercooling, and α_j and C_j are the activity coefficient (empirically determined) and concentration of alloying element, respectively. With the exception of very high carbon and very high alloy steels, the agreement between predicted and experimental TTT 'start times' was quite good.

The calculation of CCT start time based upon TTT start times was done using the Scheil equation. Instantaneous nucleation site saturation was assumed in addition to the assumption of linear consumption of fractional incubation times. A comparison of predicted CCT and experimental CCT curves was quite satisfactory. Although the predictions were not exact, the authors asserted that the technique was successful in view of the semi-empirical nature of the procedure.

Shimizu and Tamura[26] studied the effect of discontinuous cooling on the austenite-to-pearlite transformation in a hypereutectoid steel. The transformation behavior was affected by changing the continuous cooling rate and was related to the amount of incubation period consumed or to the amount of transformation occurring up to the time of changing the cooling rate. Applying the Scheil approach to the consumption of incubation period (Eq. (2.9)), the authors concluded that if there is no difference in the fraction of incubation-period consumed by either continuous cooling or isothermal holding, then the

transformation behavior is unchanged during subsequent cooling, if the cooling starts from the same temperature. This result suggests that the incubation period of the pearlite transformation is an additive event.

Umemoto et al.[27] related grain size, section size and fraction transformed to predict hardenability in a eutectoid steel. The Avrami equation (Eq. (2.12)), modified to include a prior austenite grain size term, was used to describe the isothermal transformation kinetics:

$$X = 1 - \exp\left\{ -k(T)\frac{t^n}{d^m} \right\} \tag{2.26}$$

where d is the grain size, $k(T)$ is a temperature dependent constant, and n and m are reaction constants which depend on the type of predominant nucleation site and the growth morphology. The Scheil equation (Eq. (2.9)) was used in conjunction with the assumption that the reaction is additive over the complete transformation range. Two sets of experiments were carried out to study both the effect of incubation period on the transformation and the additive nature of the pearlite reaction. As shown in Fig. 2.3(a), the percent pearlite transformed as a function of isothermal ($670°C$) transformation time is independent of the temperature ($670°C$ or $715°C$) at which the incubation period is consumed. Since the incubation period can be defined as the time at which the first small fraction of pearlite nodules are observed (0.1% transformation) , the subsequent constant rate of transformation at $670°C$ can be taken as an indication of the reaction being additive. The second set of experiments clearly established the additive nature of the pearlite reaction. As shown in Fig. 2.3(b), samples were partially transformed at one temperature and the transformation was completed at a second temperature. As seen, for both the $715°C$ to $670°C$ and the $670°C$ to $715°C$ transformations, the kinetics at the second temperature were similar to the isothermal transformation kinetics obtained at that temperature.

The first model reported in the literature which combined the reaction kinetics, the heat of transformation and heat flow considerations to describe the phase transformation in a continuously cooled steel was presented by Agarwal and Brimacombe[22]. This model, based on the controlled cooling of wire rod, such as in the Stelmor process, examined a eutectoid plain-carbon steel. The Avrami equation (Eq. (2.12)) was used to determine the fraction transformed, assuming additivity. The n and b parameters in the Avrami equation were determined from published TTT start and finish curves for a eutectoid plain-carbon steel. The experimental and the model-predicted cooling curves showed good agreement as far as shape and relative amount of recalescence was concerned. However, the small observed over-estimation of the time predicted for the start of the reaction under continuous cooling conditions was attributed to the poor accuracy of published isothermal transformation data.

Hawbolt et al.[23] examined the kinetics of the austenite-to-pearlite transformation of a 1080 eutectoid steel under isothermal and continuous cooling conditions. Previous authors[20,21,22,28,30], in calculating n and lnb, used a start time based on $t = 0$ and $X = 0$ at T_{A_1}. However, Hawbolt et al.[23] used start time, $t = 0$, at the start of the transformation (end of the incubation period) and designated it as t_{av}. The authors found that by using $t = 0$ at t_{av}, the value of n remains constant and the kinetic parameter b, is a function of temperature only, satisfying Cahn's additivity condition[13] (Eq. (2.17)). The authors confirmed the additivity of the transformation by comparing the continuous cooling transformation kinetics obtained from dilatometer measurements with calculations using: (1) n and lnb determined by assuming $t = 0$ and $X = 0$ at t_{av} and (2) n and lnb determined by assuming $t = 0$ and $X = 0$ at T_{A_1}. As seen in Fig. 2.4, the agreement was excellent for the first condition and was poor for the second condition; the predicted start time for the second case was considerably longer than that observed from the dilatometer measurements.

The validity of the Scheil equation (Eq. (2.9)) for predicting continuous cooling transformation from isothermal data was also tested. A numerical integration of the Scheil equation was performed at three stages in the transformation i.e., for the transformation stage only, for the incubation period only and for the combined incubation-plus-transformation stages. Based on the values calculated for these integrals, the authors concluded that the transformation stage is an additive event, whereas the incubation stage is not.

Umemoto et al.[29] applied the additivity principle to the bainite reaction in a high carbon(0.99 wt.%) high chromium(1.39 wt.%) steel. The progress of the bainite transformation during isothermal and continuous cooling conditions was measured using a longitudinal dilatometer. Equation (2.26) was employed to characterize the isothermal transformation kinetics. The authors, assuming the combined incubation plus transformation events to be additive for the bainite reaction, calculated the fractions transformed for three different cooling rates. Figure 2.5 shows that the calculated and experimental fraction transformed as a function of temperature, decreases with increasing cooling rate. Only low cooling rates were employed and the agreement for the faster of the three cooling rates is not as good as that obtained at the slower cooling rates. The paper did not address the question of recalescence during the isothermal or continuous-cooling transformation. The authors attributed the additive nature of the bainite transformation to a nucleation rate controlled reaction.

Application of the additivity principle for predicting kinetics of the austenite-to-ferrite plus austenite-to-pearlite sequential transformation has been limited. Hawbolt et al.[25] successfully applied the additivity principle for predicting the continuous cooling transformation kinetics in a 1025 plain-carbon steel. Using a diametral dilatometer, the isothermal and continuous-cooling transformation kinetics, $\gamma \rightarrow \gamma' + \alpha$ and $\gamma' \rightarrow P$ (pearlite), were measured and the isothermal transformation kinetics for each reaction was described using the Avrami equation, (Eq. (2.12)). The authors in their earlier study[23] had shown that

the incubation period is not an additive event. A similar approach was taken in this work and the CCT start times for the ferrite and pearlite and the completion time for the pearlite transformation was experimentally determined for a range of cooling rates. This information was used in predicting the continuous cooling transformation kinetics for cooling rates of 2 to $23°C/s$. As shown in Fig. 2.6, the agreement between predicted and experimental results is excellent for the $23°C/s$ cooling rate.

The authors also used the experimentally determined TTT and CCT data to check the validity of applying the Scheil equation to predict incubation and transformation behavior in a hypoeutectoid (1025) steel. Five integrations were performed over the ferrite transformation, the pearlite transformation, the combined ferrite plus pearlite transformation, the incubation period and the incubation plus ferrite transformation. From the results, it was observed that the Scheil equation adequately described the transformation results, but not the incubation period.

Umemoto et al.[31] studied the overall kinetics of the austenite-to-proeutectoid ferrite reaction under isothermal and continuous cooling conditions in 0.2 and 0.43 wt.% C plain-carbon steels. The isothermal kinetics were measured using a dilatometer and were described by an equation based upon the Johnson-Mehl equation (Eq. (2.13)) and an empirical equation proposed by Hickley and Woodhead[32]. The equation was derived with the assumption that the transformation rate could be modified to include soft impingement effects by multiplying the time derivative of Eq. (2.26) by $(1-X)^p$. The resulting equation was given as:

$$X = 1-\left\{1+\frac{1}{d^m}0.5\,k(T)\,(t-t_0(T))^n\right\}^{-2} \tag{2.27}$$

where $k(T)$ is the rate constant, d is the austenite grain diameter, $t_0(T)$ is the incubation period at temperature T, and m characterizes the nucleation site viz., 3, 2, 1 and 0 for corner, edge, boundary and homogeneous nucleation, respectively.

The experimental results revealed that the rate of transformation of ferrite decreased with increase in the austenite grain size. The additivity principle was applied over the combined incubation plus transformation period for the ferrite reaction, and isothermal transformation kinetics were used to predict the continuous cooling transformation kinetics. The agreement between the predicted and experimental data was quite good, as can be seen in Fig. 2.7. However, only two slow cooling rates ($0.1°C/s$ & $0.5°C/s$) were considered and the calculations were restricted to temperatures above T_{A_1}.

The authors observed that at temperatures below $680°C$ the isothermal transformation curves were smooth and sigmoidal, attributable to the pearlite reaction. Between T_{A_1} and $680°C$, the isothermal transformation curve exhibited a plateau which did not correspond to the incubation period of the pearlite reaction. The authors attributed this plateau to the latter stages of the ferrite transformation overlapping with the early stages of the pearlite transformation. The region of overlap was treated with a modified form of Eq. (2.27). The isothermal transformation curves for pearlite at temperatures below $600°C$ were characterized using the Avrami equation (Eq. (2.12)).

Recently, Campbell and co-authors[33,34] applied the principle of additivity to a range of hypoeutectoid and eutectoid plain-carbon steels from 0.18 to 0.79 wt.% C, to develop a mathematical model describing the microstructure evolution during controlled cooling of steel rod on a Stelmor line. The isothermal transformation kinetics were characterized using the Avrami equation (Eq. (2.12)), a mean constant n, and a temperature dependent b. The authors assumed the $\gamma \rightarrow \gamma' + \alpha$ and $\gamma' \rightarrow P$ transformations to be additive and predicted continuous cooling transformation kinetics over a broad range of cooling rates (0.2 *to* $50°C/s$) using isothermal transformation data and experimentally determined transformation start times. Release of latent heat was estimated and was coupled with the phase transformation kinetic calculations. Predictions of the austenite-to-pearlite

transformation kinetics under continuous cooling conditions showed very good agreement with measured values in eutectoid steels. Agreement between measured and predicted austenite-to-ferrite kinetics was reasonable.

The foregoing literature review has shown that there has been a substantial amount of work reported on the application of the additivity principle to predict non-isothermal transformation kinetics in steels using isothermal data. This work has been carried out mainly using plain-carbon steels and examining the austenite-to-pearlite reaction. The use of the additivity principle to describe the austenite-to-ferrite, austenite-to-ferrite plus pearlite reaction in plain-carbon and in alloy steels has been limited. The additivity of the incubation event has not yet been resolved conclusively.

2.4 The Proeutectoid Ferrite Transformation

The austenite-to-ferrite transformation in steels is one of the most important reactions, since the bulk of steel produced is low carbon, hypoeutectoid grade. From the work of Carpenter and Robertson[35] in 1931, in which the microstructural changes in continuous cooled hypoeutectoid steels were studied, to Aaronson's exhaustive review[36] on proeutectoid ferrite reaction in 1960, experimental studies of the austenite-to-ferrite transformation were limited to the measurement of nucleation and growth kinetics. In Aaronson's review, emphasis was placed upon detailed morphological studies of the proeutectoid ferrite reaction product. A general theory of precipitate morphology was proposed and was shown to be capable of providing a qualitative accounting for the experimental observations. In 1983 Reynolds, Enamoto and Aaronson[37] reviewed the literature placing emphasis on studies conducted on high-purity Fe-C and Fe-C-X alloys. Data on the nucleation and the growth kinetics of grain boundary allotriomorphs in both Fe-C and Fe-C-X alloys and on the growth kinetics of ferrite sideplate in Fe-C alloys were presented and analysed using available theory. The authors concluded that although considerable progress had been made, no single fundamental mechanism could be applied to

describe the ferrite reaction. Part of the difficulty in understanding the proeutectoid ferrite reaction is due to the variety and intricacy of the ferrite morphologies formed. Dube[38] classified ferrite into several distinctive morphologies based on microstructural shapes. Figure 2.8 shows the components of this morphological classification system. However, very little attention has been given to the study of the transformation kinetics of ferrite under conditions of decreasing temperatures, which relates to the applicability of the additivity principle. Hence, the following sections will review the literature on the nucleation and growth kinetics of ferrite.

2.4.1 Nucleation Kinetics

In general, two distinct types of nucleation are possible: homogenous and heterogenous. In homogenous nucleation, the nucleus forms within a grain independent of grain boundaries, dislocations, impurities etc. In heterogenous nucleation, the nucleus forms at a high energy site, such as a grain boundary, where the available boundary free energy can be used to lower the required activation free energy for nucleation. Although the number of sites for homogenous nucleation is much greater, heterogenous nucleation dominates most phase transformations because of the much lower activation energy required. In the case of ferrite, homogenous nucleation is very rare and heterogenous nucleation occurs at grain boundaries, grain edges, grain corners, or at inclusions. Over the last 3 to 4 decades a considerable amount of data on the nucleation and growth kinetics of ferrite has been acquired, most of which has been restricted to grain boundary allotriomorphs growing under isothermal transformation conditions.

It has been recognized that the rate of nucleation ($\frac{\text{number of nuclei}}{\text{time} \quad \text{volume}}$) of ferrite increases considerably with decreasing temperature and decreasing austenite grain size[36]. Mazanec and Cadek[39] found that the nucleation rate, expressed in terms of the number of nuclei of proeutectoid ferrite formed per unit area of unreacted γ grain boundary, decreased

continuously with time, as shown in Fig. 2.9. Early site saturation becomes a possibility under these conditions. The authors also found that the nucleation rate increased with decreasing austenitizing temperature, although data obtained by Simcoe et al.[40] and Dube[38] shows the reverse trend, as seen in Fig. 2.9. This apparent conflict is probably the result of measurements being made at different reaction temperatures at different stages of transformation in steels with varying composition and different γ grain sizes. Mazanec and Cadek[39] also measured the ferrite nucleation rate in a more slowly reacting steel. These experiments were performed to examine the question of the time dependency of the nucleation rate. It was observed that the nucleation rate increases initially and then decreases with time, consistent with initial nucleation progressing to site saturation.

A more complete evaluation of the effects of carbon content and temperature upon ferrite nucleation kinetics was made by Hickley and Woodhead[32]. Using plain-carbon steels the authors were unable to evaluate the nucleation rate at sufficiently early stages of transformation due to the high reaction rates. They obtained nucleation rate data through a semi empirical analysis which involved the measurement of the fraction of the austenite transformed to ferrite as a function of the isothermal reaction time and the number of ferrite grains present at the conclusion of the transformation. Figure 2.10 shows the increasing nucleation rate with decreasing transformation temperature obtained for each of the four steels studied. However, it should be emphasized that any grain growth within the ferrite phase and the possibility of unrevealed ferrite:ferrite boundaries could have resulted in appreciable errors in the metallographic determination of the nucleation rates.

Lange and Aaronson[41] investigated the nucleation kinetics of ferrite allotriomorphs at austenite grain faces and edges in three Fe-C alloys. Very thin coarse γ grained specimens (0.025 cm thick) were used so that nearly all of the austenite grain boundaries were perpendicular to the specimen surface. Adequate delineation of the prior austenite grain boundaries through careful etching resulted in differentiation of allotriomorphs nucleated at

austenite grain faces from those nucleated at grain edges. As shown in Fig. 2.11, the results agreed with predictions made by Cahn[13], with nucleation occurring predominantly at grain edges when undercooling is small and grain boundaries becoming more important as the undercooling is increased. The ratio of the number of edge to grain boundary nucleated particles is largely a direct reflection of the relative time-integrated nucleation kinetics at the two types of sites, at least until diffusion field impingement becomes important.

Figure 2.11 also shows that the nucleation ratio initially decreases and then increases slightly with reaction time. The initial decrease was attributed to such factors as a possible longer incubation time for the grain boundary nucleated allotriomorphs, slower growth rates of these nuclei to detectable sizes and/or continuing nucleation at grain boundaries after the available edge nucleation sites have been saturated. The later slow increase in the edge to surface nucleated particles was attributed to erroneously counting grain boundary nucleated allotriomorphs, which had sufficient time to grow into contact with a grain edge, as edge nucleated.

In a subsequent paper, Obara et al.[42] measured the fraction transformed vs. time under isothermal conditions and extrapolated the curves to obtain the time for 1% transformation. This data was compared with predicted values obtained using Cahn's analysis for ferrite growth at austenite grain boundaries. The analysis was modified to replace spheres growing with linear kinetics (as for pearlite) with oblate ellipsoids growing with parabolic kinetics (as for ferrite). Also, it was assumed that steady state nucleation was achieved in times much less than that required for 1% transformation at all reaction temperatures and compositions studied. As shown in Fig. 2.12, the agreement between calculated and experimental TTT curves for 1% transformation was good, especially for lower carbon steels. Although only grain boundary nucleation was considered, with the

assumption that edge nucleation contributes little except at the highest temperature, this study[42] was the first quantitative study to examine Cahn's analysis[13] of nucleation kinetics as applied to the proeutectoid ferrite transformation.

Figure 2.13 shows data on the ferrite allotriomorph number density per unit unreacted austenite grain boundary area as a function of isothermal reaction time at three reaction temperatures, as reported recently by Lange et al.[43] for a 0.13 wt.% C steel. The appearance of a maximum density in these plots was attributed to the difficulty of revealing grain boundaries between impinged ferrite crystals and grain growth within these aggregates. The authors obtained the variation of nucleation rate with time by taking slopes of the plots shown in Fig. 2.13. As seen in Fig. 2.14, only at the smallest undercooling (825°*C*) was the steady state nucleation rate achieved before the particle number density reached a maximum value and the measurement of slope was terminated. With higher degrees of undercooling (larger driving force) there are more and more available nucleation sites (grain corners, edges, boundaries etc.) becoming active growth centers within a short reaction time. When the undercooling is small, steady state nucleation is achieved quickly, because the number of sites available for nucleation for that particular driving force are limited.

In a recent study, Enamoto et al.[44] obtained data on the rate of ferrite nucleation at austenite grain edges in Fe-C and Fe-C-X alloys, where X is Mn, Ni, Co and Si. The data was analyzed using classical nucleation theory and modelling critical nuclei as equilateral trigonal prisms. Figure 2.15 illustrates calculated and experimental nucleation rates per unit volume for three of the Fe-C alloys studied. It is worth noting that the representation of nucleation rate on a logarithmic scale may have narrowed the apparent difference between calculated and experimental observations. The authors concluded that low nucleus matrix interfacial energies, consistent with fully or partially coherent interfacial structures, are required, and that only a very small proportion of the total number of atomic nucleation sites in contact with austenite grain edges is actually usable for nucleation. For a given alloy, there was

surprisingly little difference in the nucleation rate at grain faces and edges compared on a per unit volume basis. The authors rationalized this observation by speculating that at grain edges the advantage of forming a smaller critical nucleus is reduced by the problems involved in developing low energy interfaces with two or even three austenite grains.

2.4.2 Growth Kinetics

Once ferrite has nucleated, its continued growth will proceed, being driven principally by the difference in free energy between the austenite and ferrite phases. Growth of proeutectoid ferrite proceeds under long range diffusion control with carbon diffusing away from the advancing ferrite and enriching the remaining austenite phase. Grain boundary allotriomorphs are the predominant ferrite morphology observed in steels and are the subject of most of the research[36-38,45-47,52]. Measurements on ferrite plates have been reported to a lesser extent[36,37,48,49,58,61,62,63]. In this section the discussion of ferrite growth will be limited to grain boundary allotriomorphs.

As shown schematically in Fig. 2.16, the elongated shape of grain boundary allotriomorphs results from the rate of lengthening along the boundary being appreciably greater than the rate of thickening. This requires that the kinetics of growth be separated into thickening and lengthening components, as shown in Fig. 2.16. Measurement of the lengthening and thickening kinetics of grain boundary allotriomorphs poses significant stereological problems. Bradley and Aaronson[50] concluded that using thin specimens, austenitized for sufficient time at a high enough temperature to allow the austenite grain boundaries to grow perpendicular to the broad faces of the specimens, was the best solution to this problem. Simple measurements of the length of the longest and the thickness of the thickest ferrite allotriomorphs on a plane of polish parallel to the specimen broad face were sufficient for obtaining the lengthening and thickening kinetics. The large austenite grain size (ASTM Nos. 1-2) obtained in these samples also prevented the early overlap of diffusion fields around the growing allotriomorphs.

Purdy and Kirkaldy[51] devised a novel technique to observe the controlling mechanism of proeutectoid ferrite thickening. The authors used decarburization and slow cooling into the austenite + ferrite region to establish essentially planar layers of polycrystalline ferrite at both surfaces of an Fe-0.56 wt.% C alloy. After a homogenization anneal at a constant temperature in the austenite + ferrite region to eliminate concentration gradients, the bar was isothermally reacted at a higher temperature in order to grow austenite at the expense of ferrite. An accurate measurement of the true austenite layer thickness as a function of isothermal reaction time was accomplished by periodic quenching and polishing on a plane parallel to the diffusion direction. The parabolic rate constant obtained from these measurements was compared with that calculated from the appropriate constant-diffusivity solution to the diffusion equation. As shown in Fig. 2.17, the experimental and calculated ferrite-austenite movement (x') plotted against time$^{1/2}$ shows good agreement. The observations provide strong evidence for the volume-diffusion control of the motion of an incoherent ferrite-austenite interface, the type which must exist on at least one side of a grain boundary ferrite allotriomorph.

Kinsman and Aaronson[45,52] used thermionic electron emission microscopy to measure ferrite allotriomorph growth kinetics in Fe-C and Fe-C-X alloys. Both investigations were aimed at evaluating the effects of Mo and Mn[45] and Al, Co and Si[52] upon the kinetics of grain boundary ferrite allotriomorph growth (and thus upon hardenability). The authors used the technique to obtain a metallographic-like image of allotriomorphs which were photographed at short time intervals whilst growth was taking place. However, despite the authors' contention that the individual data sets were very precise, there were significant differences between parabolic rate constants determined in a single specimen during transformation at a given temperature. Bradley and Aaronson[50] attributed part of this

scatter to grain boundaries lying at an angle to the specimen surface and stereological problems resulting from measuring the growth kinetics of an allotriomorph on a plane lying above or below the centerline of the ferrite precipitate.

Bradley et al.[47] obtained data from optical metallographic measurements of growth kinetics in three high purity Fe-C alloys containing 0.11, 0.23 and 0.42 wt.% C, after isothermally reacting and quenching the specimens. Figure 2.18 shows a typical plot of maximum half thickness, S/2, and maximum half length, L/2, of grain boundary allotriomorphs as a function of the square root of the reaction time for the Fe-0.23 wt.% C steel. Although for greater accuracy, the half thickness and the half length should be plotted against the growth time instead of the reaction time, the authors found the difference to be small, as well as difficult to ascertain. Some of the experimental problems in obtaining such measurements are due to the assumption that the specimens take negligible time to attain the isothermal temperature of the lead bath and the likelihood of transformation occurring during either quenching to, or quenching from, the reaction temperature is small. The straight line appearance of these plots (Fig. 2.18) reflects the parabolic nature of the thickening as well as lengthening kinetics of the grain boundary allotriomorphs. The authors assessed the validity of the data by determining the slopes of the ln S/2 and ln L/2 vs. ln t plots as a function of reaction temperature, as shown in Fig. 2.19. The slope remains equal to 1/2 independent of temperature for both lengthening and thickening kinetics, within the limits of scatter. This is the slope predicted for long-range diffusion controlled growth. However, the ratio of the experimentally measured parabolic rate constants for thickening, and lengthening, $\frac{\alpha}{\beta}$, to those calculated from a computer- based solution, is less than unity at all temperatures studied for all three steels, as seen in Fig. 2.20. The computer-based solution was developed by Atkinson[53] by generalizing the morphology of an idealized allotriomorph as an oblate ellipsoid and solving Fick's second law under the condition of a concentration-dependent carbon diffusivity in the matrix phase. The slower than calculated growth kinetics for the

experimental data shown in Fig. 2.20 was attributed by the authors[47], not to the use of an oblate ellipsoid as a model for allotriomorphic growth, but to the presence of a distribution of partially coherent facets amongst the disordered interfacial structure of the allotriomorph faces. Furthermore, it was postulated that such facets will grow by means of the erratically operating ledge mechanism and will thus migrate at lesser rates than those permitted by uniform atomic attachment and detachment at disordered austenite:ferrite boundaries.

Bradley et al.[47] found the average aspect ratio of the allotriomorphs to be roughly one-third and independent of reaction time, reaction temperature and carbon content in the three Fe-C alloys studied. On the other hand, the dihedral angle at the edges of the allotriomorphs shaped as double spherical caps should have an aspect ratio of 0.47. Although the authors[47] have considered a number of possible explanations for these observations, a satisfactory explanation is not yet available.

In their review, Reynolds et al.[37] concluded that the growth kinetics of ferrite with partially coherent facets are much more complex than those treated using planar or ellipsoidal analyses. Hence, in order to develop an exact treatment of allotriomorph growth kinetics, it would be necessary to secure information on the proportions and distribution of any partially coherent facets present at the austenite-ferrite interphase boundaries and their variation with time. The authors pointed out that the destruction of the austenite matrix by the martensite transformation during quenching to room temperature makes it difficult to determine the presence of partially coherent facets. Hence, either a highly alloyed steel has to be used (which complicates the diffusion analysis) or a high-resolution, elevated temperature technique which does not affect the transformation process is required.

2.4.3 Widmanstätten Ferrite

After grain boundary allotriomorphs, the second most commonly observed ferrite morphology is Widmanstätten ferrite. The Widmanstätten ferrite exhibits a number of morphological variants. As shown in Fig. 2.8, these morphologies have been classified by

Dube[38] as: (a) primary side plates which grow directly from austenite grain boundaries (Fig. 2.8b and c (1)); (b) secondary side plates which develop from grain boundary allotriomorphs of ferrite (Fig. 2.8b and c (2)); and, (c) intragranular plates which grow within the austenite grains and are favored by a large austenite grain size and high supersaturation (Fig. 2.8e). Aaronson[36] and recently Reynolds et al.[37] have documented the Dube morphological classification system in great detail.

The most commonly observed Widmanstätten ferrite morphology is the secondary side plate. Hence, the discussion of Widmanstätten ferrite will be limited to secondary side plates. Although secondary side plates appear in at least small numbers throughout most of the ferrite transformation range in plain-carbon steels, they form most readily under conditions of large austenite grain size[36,38,58,61-63] and intermediate reaction temperatures[36,38] in steels containing less than 0.3-0.4 wt.% C. At carbon contents appreciably below 0.2 wt.% C, early impingement of the plates largely obscures the individual plates, unless the transformation is halted by quenching. Aaronson[36] speculated that as the carbon content increases above 0.3-0.4 wt.% the pearlite transformation becomes much more efficient in preventing the development of side plates at a given transformation temperature.

Shown in Fig. 2.21 is the temperature-composition region of the Fe-C phase diagram in which side plates are the dominant ferrite morphology at late reaction times in plain-carbon steels for two different austenite grain sizes. As can be seen, for a carbon steel with a coarse austenite grain size, the side plates are dominant at higher transformation temperatures than those obtained for the finer grained steel. Although nucleation and growth of Widmanstätten side plates has been discussed over the years[36,37,48,49,58,61-63], there is no clear consensus about the mechanisms at work due to the complexities involved. Townsend and Kirkaldy[61] presented a theory describing how the allotriomorph interface becomes unstable

and the array of Widmanstätten side plates evolve. They supported the theory with metallographic evidence. However they emphasized that their model is to be regarded as representative rather than definitive in light of the complexity of the system.

The growth of Widmanstätten plates has received considerable attention and this has been summarized by Reynolds et al.[37] in their review on the proeutectoid ferrite reaction. There are two components important to overall growth of Widmanstätten plates, i.e. lengthening and thickening. It is generally agreed that lengthening occurs by the volume diffusion of carbon in austenite, while thickening is slower than that expected for full diffusion control, as a consequence of the lower mobility of the interfaces bounding the sides of the precipitate. Also, lengthening is enhanced by the point effect of diffusion. Purdy and Hillert[64] in their overview on the nature of bainite transformation, point out that the application of theoretical models for volume diffusion controlled lengthening of Widmanstätten plates give quite good agreement with experimental results. Furthermore, the authors suggest that any discrepancies between the observed and predicted lengthening could be the result of uncertainties in phase equilibria, volume diffusion coefficients and interfacial free energies.

Kinsman et al.[49] used thermionic electron emission microscopy to measure the thickening kinetics of Widmanstätten ferrite side plates in Fe-C alloys. The experimental data was compared to model predictions assuming volume diffusion controlled growth of a disordered interphase boundary. Shown in Fig. 2.22 are the plots comparing experimentally measured thickening kinetics to model predictions. As can be seen, the experimental growth kinetics are consistently less than model predictions and the observed kinetic behaviour is erratic. The authors showed the presence of ledges on the broad faces of the ferrite side plates by means of electron microscopy, and concluded that the broad faces of ferrite side plates are immobile and are displaced only through the lateral movement of ledges.

2.4.4 Theoretical Considerations in Applying the Principle of Additivity to Proeutectoid Ferrite Transformation

The application of the additivity principle, permitting the use of isothermal data to predict the continuous cooling transformation kinetics of the austenite-to-ferrite transformation, has been demonstrated by various authors[25,31,33,34]. However, proper assessment of the additivity principle as applied to the proeutectoid ferrite reaction must take into account theoretical considerations. Referring to the hypoeutectoid section of the iron-carbon equilibrium diagram (Fig. 2.23), once the temperature of the austenite decreases below the A_{e_3} line, proeutectoid ferrite allotriomorphs will nucleate and grow. The discussion of the theoretical growth of ferrite has been restricted to the formation of ferrite allotriomorphs. Since the carbon content of the ferrite, C_{α_1} (Fig. 2.23), is much lower than that of the parent alloy C_0, the carbon is rejected to the austenite with increasing ferrite formation, creating a gradient of carbon at the growing ferrite interface. Because the carbon does not have sufficient time to diffuse uniformly throughout the austenite matrix, the growth of the ferrite phase is controlled by long-range diffusional transport of carbon in austenite. For isothermal growth of ferrite at T_1 (Fig. 2.23), the ferrite precipitation stops when all the remaining austenite reaches the equilibrium composition, C_{γ_1}, on the A_{e_3} line. This assumes that local equilibrium is maintained at the phase boundary during the austenite-to-ferrite transformation.

The size and shape of the diffusion gradient in the γ phase for a given initial alloy content C_0, and an initial γ grain size d_0, is affected by time and temperature. The gradient, which is initially steep, becomes shallower thereby reducing the driving force for carbon redistribution. The growth follows a parabolic law of the form[36],

$$S/2 = \beta t^{1/2} \tag{2.30}$$

where $S/2$ is the thickness of a planar ferrite precipitate, β is the temperature dependent parabolic rate constant and t is the growth time. The effect of γ grain size is seen in determining the time at which a decreasing growth rate of ferrite occurs due to overlapping of carbon-enriched regions of austenite associated with other ferrite precipitates in the grain, i.e., *soft impingement.*

The effect of transformation temperature on the growth kinetics is realized through its effect on the diffusion gradient, which is dependent on the equilibrium carbon content of the austenite (C_γ) and ferrite (C_α), as shown in the iron-carbon equilibrium diagram (Fig. 2.23) and the magnitude of the temperature- and composition-dependent diffusion coefficient. The instantaneous ferrite growth rate has been shown to be dependent on the diffusion flux of carbon in the austenite[36], i.e.,

$$J = -D_C^\gamma \frac{\partial C}{\partial x} \tag{2.31}$$

where D_C^γ is the diffusion coefficient for carbon in austenite (γ) and $\frac{\partial C}{\partial x}$ is the carbon gradient ahead of the growing ferrite. Thus, as shown in Fig. 2.23 for two different growth temperatures (T_1 & T_2), the same ferrite thickness (S) can result from two different carbon gradients ahead of the growing ferrite, the triangular and rectangular shaded areas being equal at each temperature.

Since the size and shape of the carbon gradient in the austenite ahead of the growing ferrite is dependent on the temperature and the time at temperature for a given carbon content and austenite grain size, diffusion gradients having different boundary conditions and different shapes would be expected for the ferrite growth at each temperature. For example, assume that the alloy of composition C_0 is held at a temperature T_1 for partial transformation (Fig. 2.23) and is then rapidly cooled to another temperature T_2, above A_{e_1} for completion of the transformation. The rate of growth of a ferrite precipitate at each stage would be

determined by the appropriate diffusion coefficient D_C^{γ}, and the composition gradient. In other words, the rate of growth of ferrite is dependent on the thermal path of the transformation. In particular, the instantaneous growth rate of a ferrite grain after growing at T_1 and being rapidly transferred to T_2 would result from the diffusion gradient appropriate to temperature T_1. For continued equilibrium growth at T_2, a rapid adjustment to the new boundary conditions characteristic of T_2 would be required and the associated diffusion gradients would have to adjust to those required by the new temperature, T_2. Thus a different growth rate would be expected at least during the initial stages of growth at T_2. The transformation would then be path dependent and hence the general additivity condition given in Eq. 2.1 would not be valid. However, as discussed earlier, the studies of Hawbolt et al.[25] and Umemoto et al.[31] demonstrated that the continuous-cooling transformation kinetics of the proeutectoid ferrite reaction can be predicted using isothermal data by assuming that the ferrite reaction is additive.

This apparent conflict between theoretical predictions and experimental observations may be explained, at least for the slow cooling rates (0.1 and $0.5°C/s$) employed in the work of Umemoto et al.[31], by the fact that the diffusion gradients would have sufficient time to adjust to the new temperature and thereby effectively satisfy the additivity requirement. However, the continuous-cooling rates employed by Hawbolt et al.[25] were much higher ($23°C/s$), and yet the system exhibited additive behaviour.

The effect of change in ferrite morphology on the ferrite transformation kinetics is also of importance in light of applying of the additivity principle to austenite-to-ferrite transformation. For example, if the morphology of ferrite isothermally transforming at one temperature is allotriomorphic, and if the temperature of the steel is rapidly changed to another isothermal temperature, such that the predominant morphology at the second temperature is Widmanstätten, then the resulting growth rate may be path dependent and therefore not additive.

2.5 Scope and Objectives

Phase transformation theory would suggest that the long-range diffusion controlled austenite-to-ferrite transformation should be path dependent and therefore not additive. However, research has shown that the transformation is experimentally additive. It is the objective of this study to examine and analyze the applicability of the principle of additivity to the ferrite transformation.

The study has been carried out in two parts. First, the applicability of the additivity principle has been experimentally assessed by measuring the austenite-to-proeutectoid ferrite transformation kinetics isothermally and after rapid change from one temperature to another using stepped-isothermal tests. In addition, the additive nature of the proeutectoid ferrite reaction has been examined with the aid of mathematical models which take into account the relevant theoretical factors for isothermal and stepped-isothermal transformation conditions.

The second part of the research relates to the effect of changing morphology on the additivity of the ferrite transformation. Allotriomorph and Widmanstätten morphologies are the most commonly observed ferrite morphologies in steels. Appropriate experimental conditions have been established to obtain allotriomorph and Widmanstätten ferrite morphologies and isothermal transformation kinetics have been measured for those conditions. In the second series of tests, the effect of changing the ferrite morphology during the stepped-isothermal test has been evaluated to assess the experimental additivity of the ferrite transformation under conditions of changing morphology.

In summary, it is the purpose of this research to assess experimentally whether the austenite-to-ferrite transformation is additive under conditions of changing temperature with and without varying ferrite morphology and to examine the effect of changing temperature, soft impingement and prior austenite grain size on ferrite growth kinetics through the development of appropriate mathematical models based on diffusion theory.

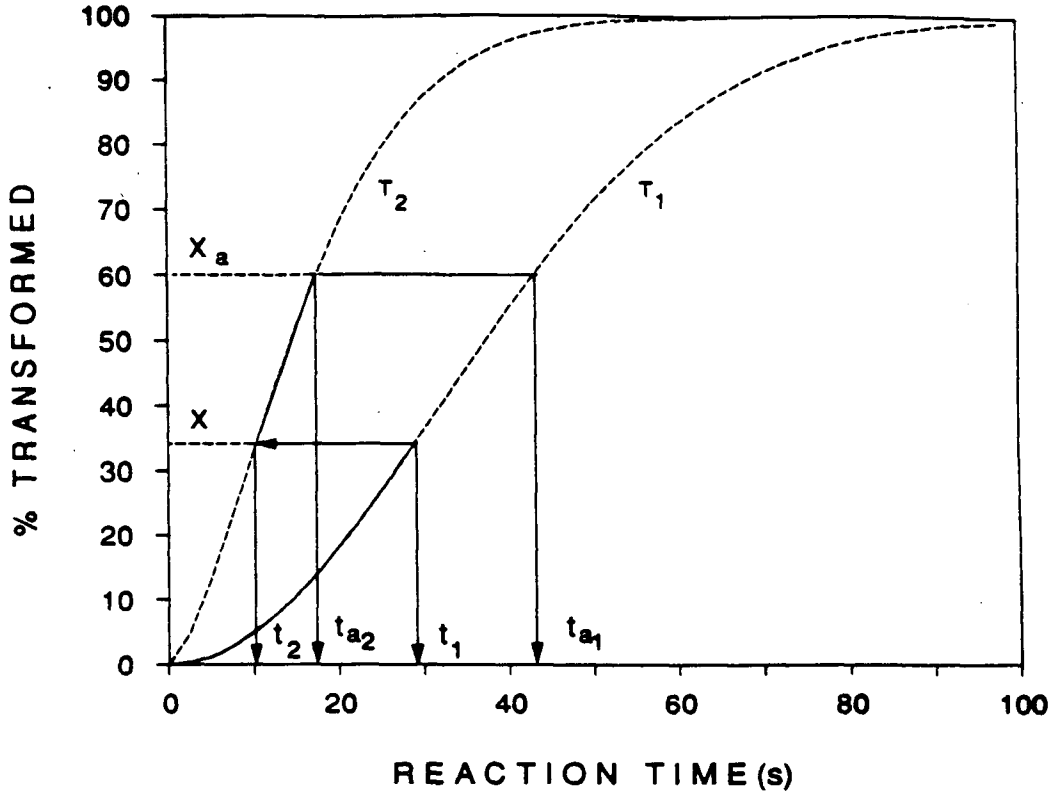

Fig. 2.1 - Schematic diagram illustrating the Principle of Additivity.

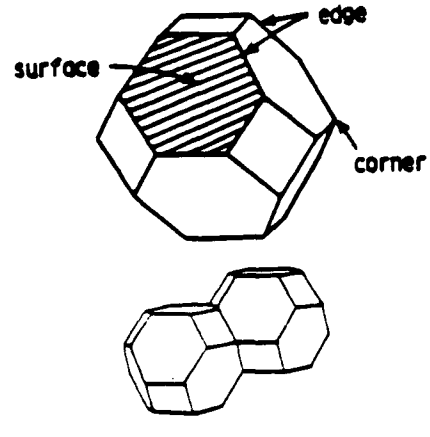

Fig. 2.2 - Schematic diagram of austenite grain as a tetrakaidecahedron and showing three types of nucleation sites of ferrite.

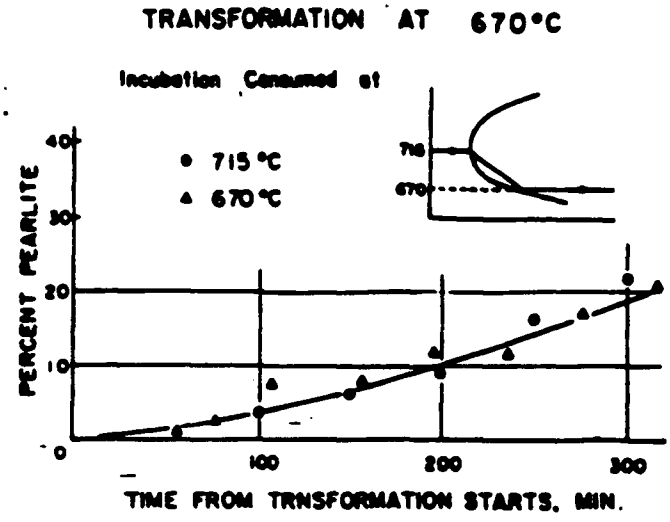

Fig. 2.3(a) - Percent pearlite as a function of the time after transformation starts at 670°C, O; incubation period was consumed at 715°C, Δ; incubation period was consumed at 670°C from Umemoto et al.[27].

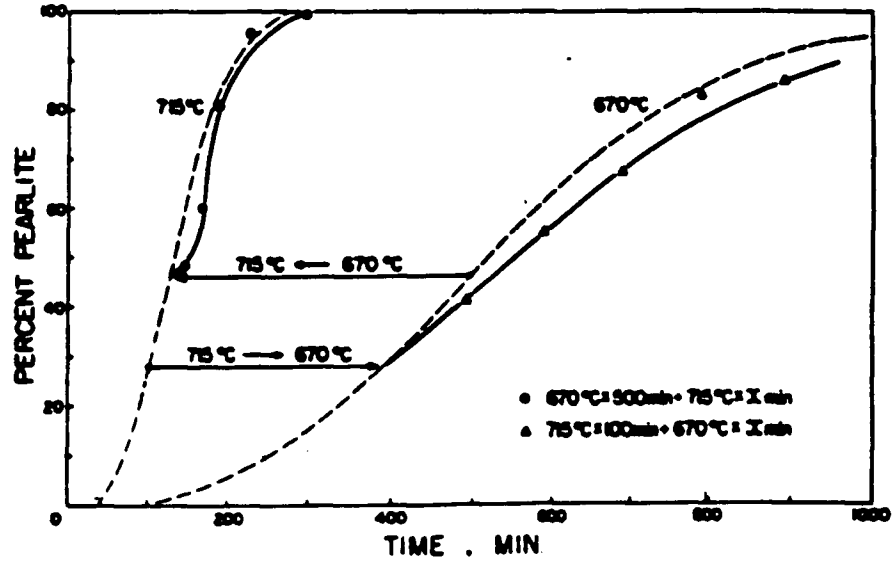

Fig. 2.3(b) - Step quench experiments showing that the transformation is nearly additive after a partial transformation at the first holding temperature from Umemoto et al.[27].

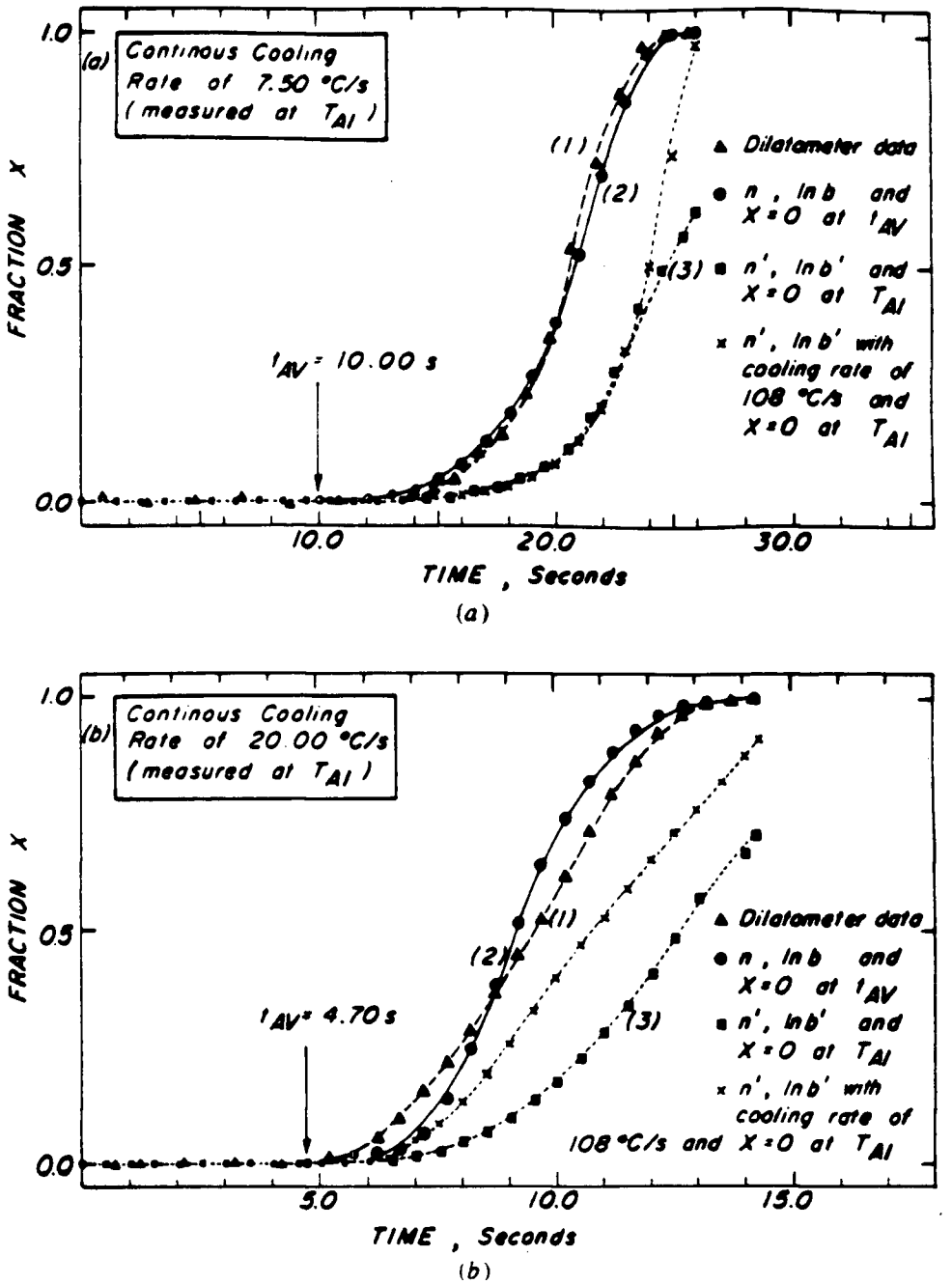

Fig. 2.4 - Measured and predicted fraction of pearlite transformed versus time for two cooling rates in a 1080 plain-carbon steel from Hawbolt et al.[23]; (a) 7.5°C/s, and (b) 20°C/s.

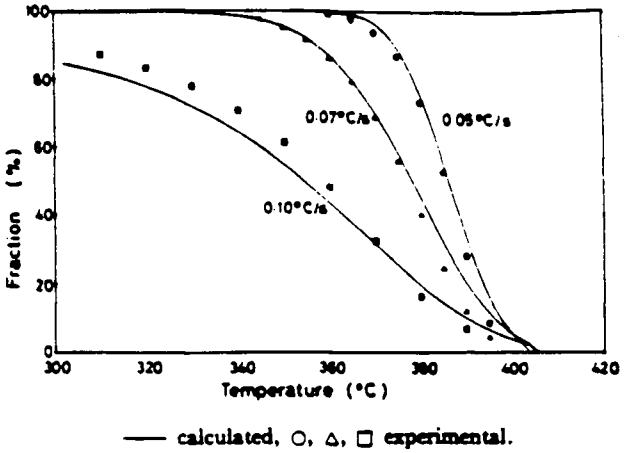

Fig. 2.5 - Measured and calculated fraction of bainite transformed versus temperature at three cooling rates from Umemoto et al.[29].

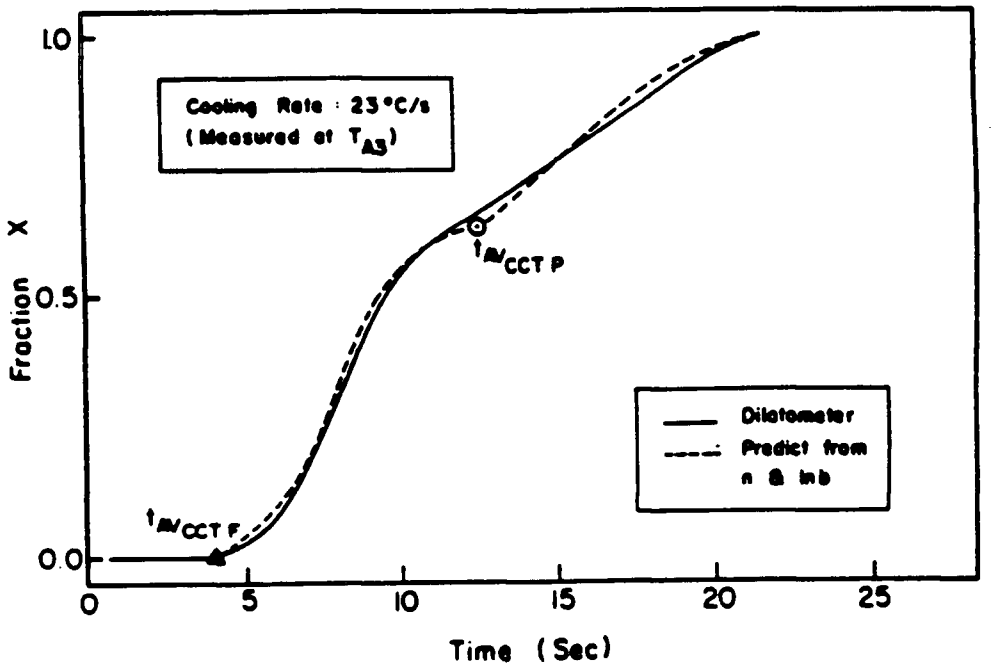

Fig. 2.6 - Measured and calculated fractions of ferrite and pearlite transformed versus time at 23°*C/s* in a 1025 plain-carbon steel from Hawbolt et al.[25].

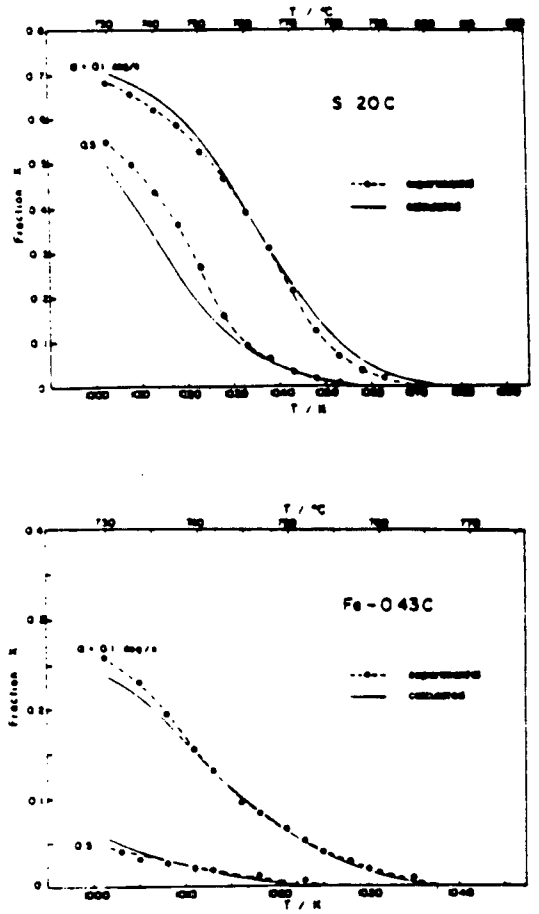

Fig. 2.7 - Measured and calculated fractions of ferrite transformed versus temperature at two cooling rates in 0.2 and 0.43 wt.% C steels, from Umemoto et al.[31].

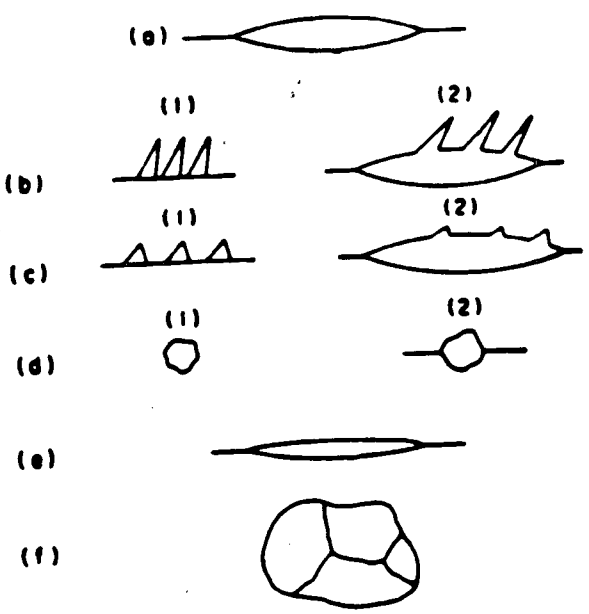

(a) Grain boundary allotriomorph

(b) (1)Widmanstätten primary side plates

(2)Widmanstätten secondary side plates

(c) (1)Widmanstätten primary saw teeth

(2)Widmanstätten secondary saw teeth

(d) (1)Idiomorphs

(2)Grain boundary idiomorphs

(e) Intergranular Widmanstätten plates

(f) Massive structure

Fig. 2.8 - The components of the ferrite morphological classification system according to Dube[38].

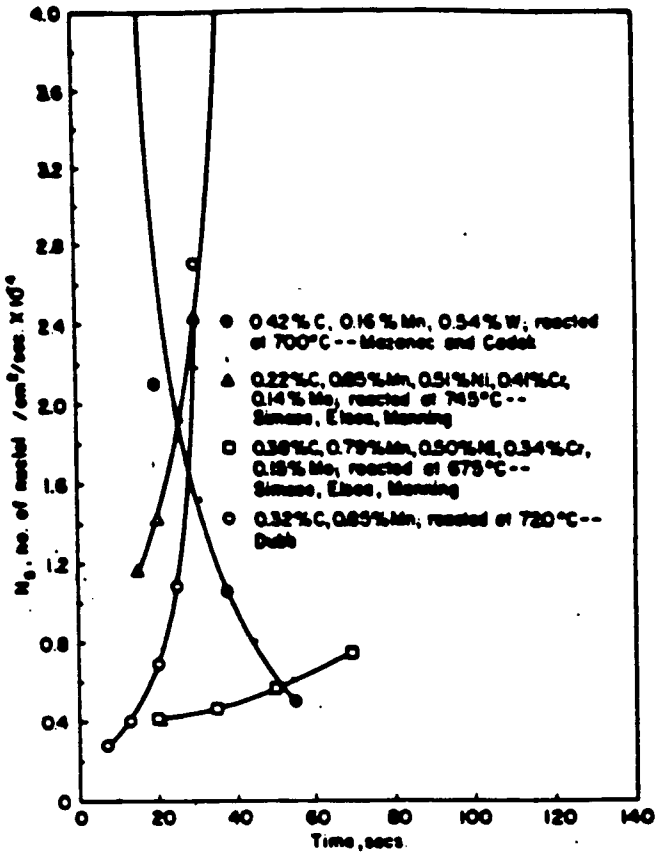

Fig. 2.9 - Time dependence of the rate of ferrite nucleation in several steels from Aaronson[36].

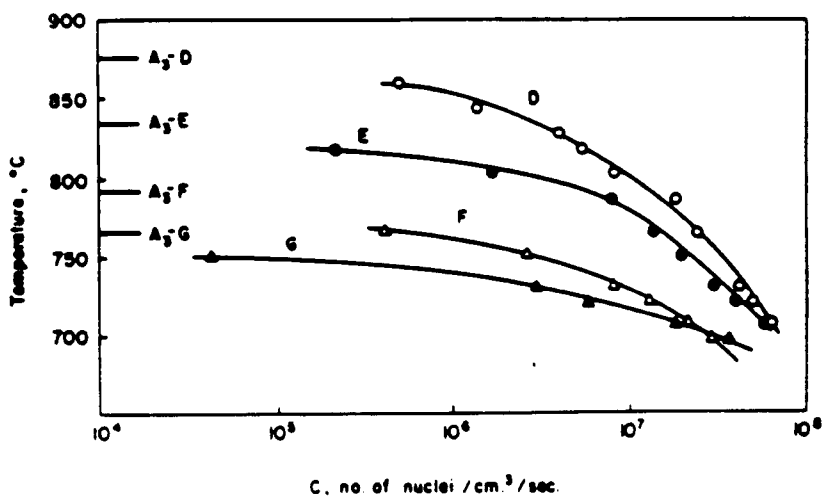

Fig. 2.10 - Variation of ferrite nucleation rate with temperature in four carbon steels D(0.08 wt.% C), E(0.19 wt.% C), F(0.33 wt.% C) and G(0.47 wt.% C) from Hickley and Woodhead[32].

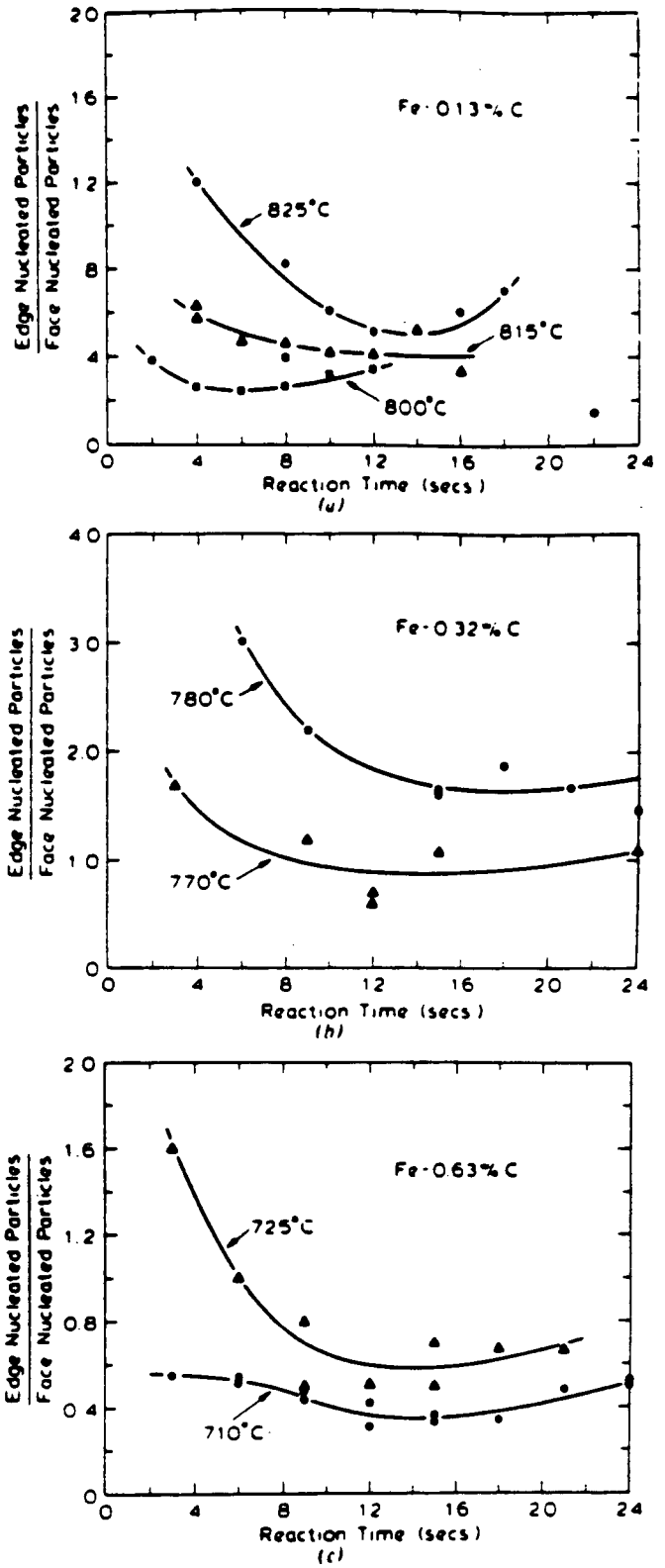

Fig. 2.11 - Variation of the ratio of edge-nucleated to face-nucleated ferrite precipitates with isothermal reaction times at various reaction temperatures in three plain-carbon steels: (a)Fe-0.13 wt.% C, (b)Fe-0.32 wt.% C and (c)Fe-0.63 wt.% C from Lange and Aaronson[41].

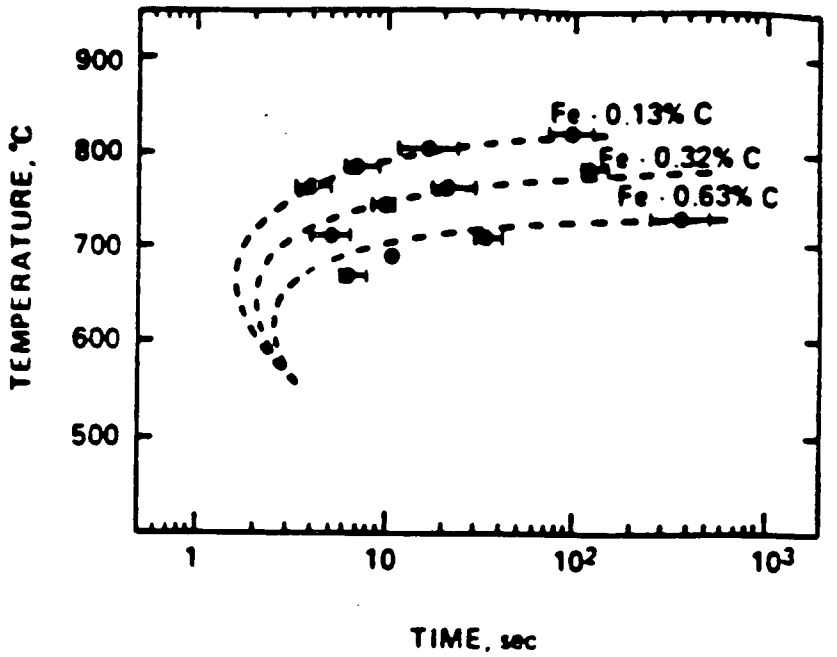

Fig. 2.12 - Comparison of measured and calculated transformation start times for isothermal transformation of austenite to ferrite in three plain-carbon steels from Obara et al.[42].

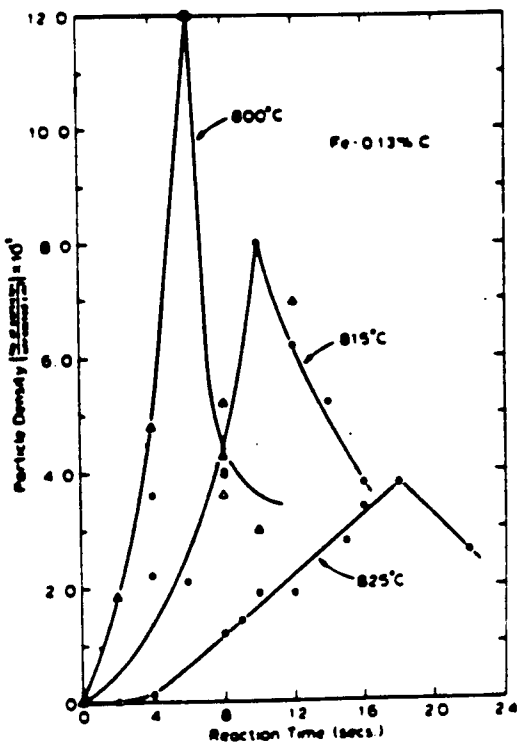

Fig. 2.13 - Number density of face-nucleated ferrite precipitates versus reaction time at three temperatures in Fe-0.13 wt.% C steel from Lange et al.[43].

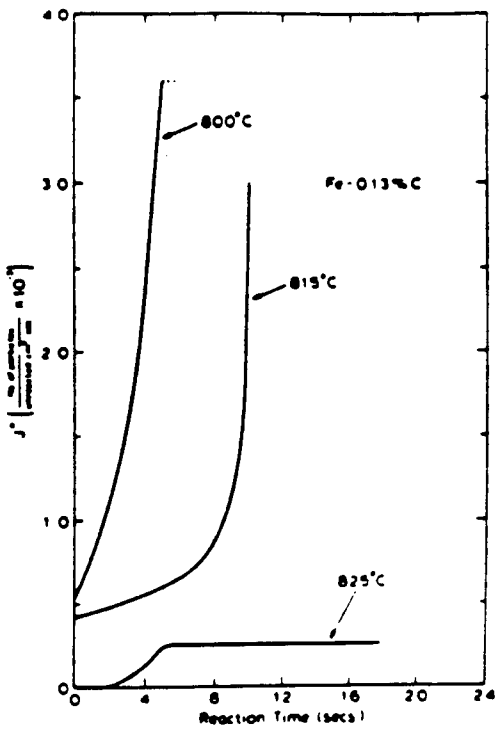

Fig. 2.14 - Nucleation rate of ferrite at austenite grain faces versus reaction time at three temperatures in Fe-0.13 wt.% C from Lange et al.[43].

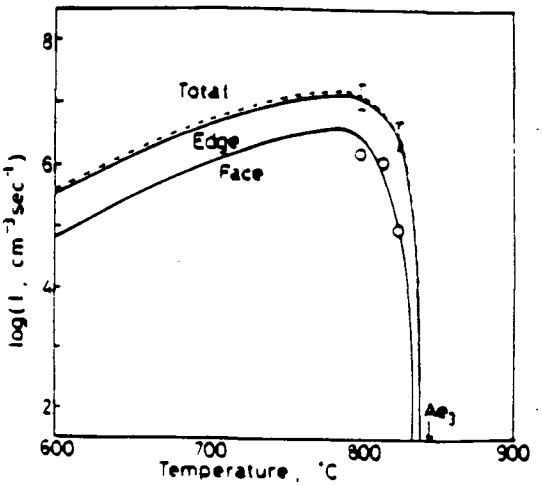

(a)

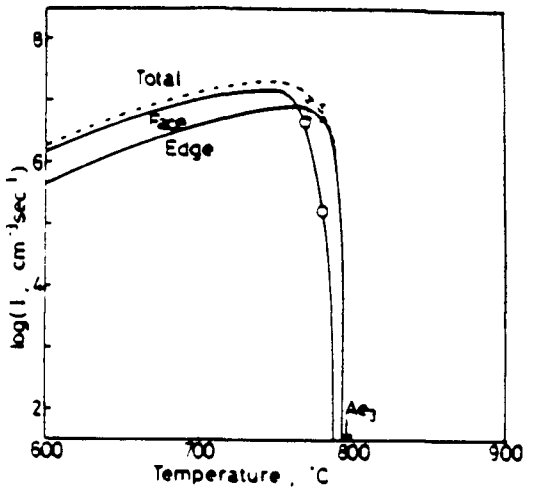

(b)

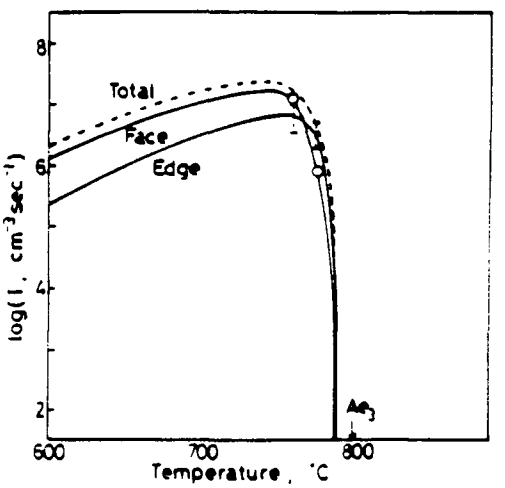

(c)

Fig. 2.15 - Measured and calculated nucleation rate per unit volume at grain faces, at grain edges, and total nucleation rate for (a)Fe-0.13 wt.% C, (b)Fe-0.32 wt.% C and (c)Fe-0.63 wt.% C alloys from Enamoto et al.[44].

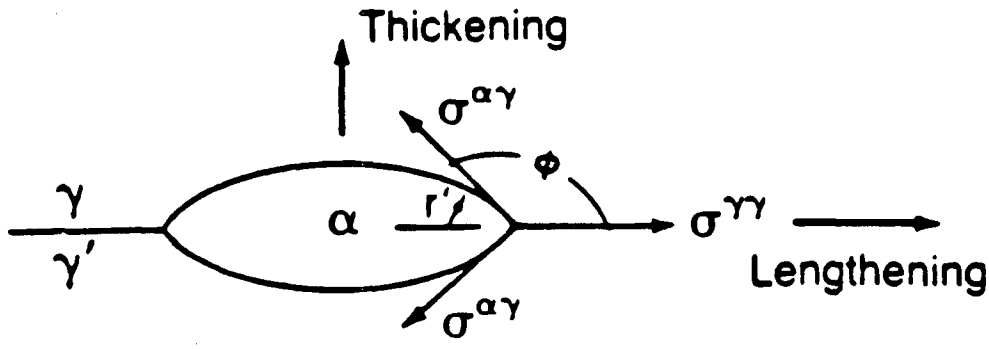

Fig. 2.16 - Schematic diagram illustrating the thickening and lengthening of grain boundary allotriomorph.

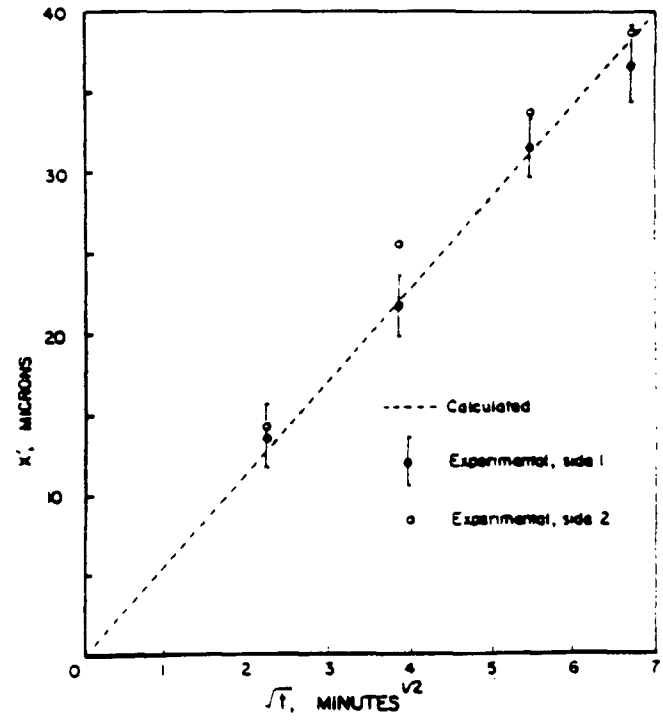

Fig. 2.17 - Comparison of measured and calculated austenite growth data for ferrite-austenite diffusion couple at 792°C from Purdy and Kirkaldy[51].

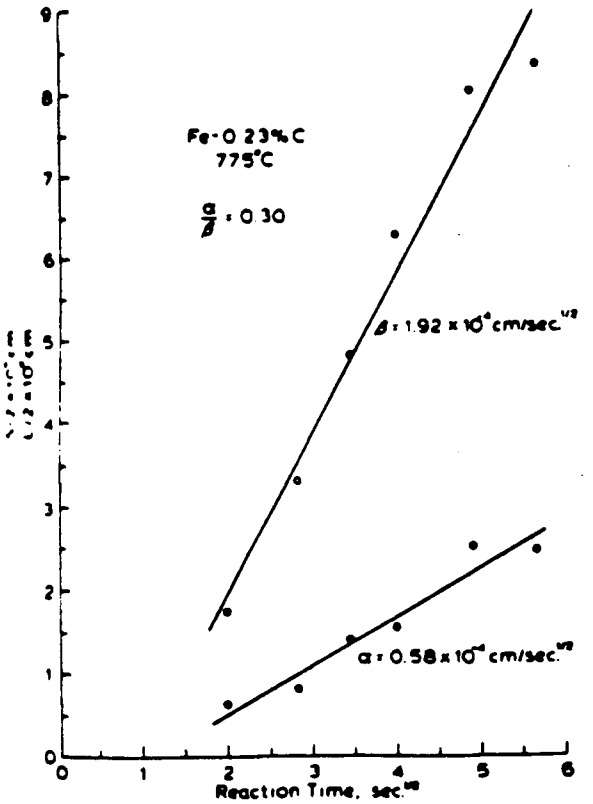

Fig. 2.18 - Typical plots of maximum half-thickness, S/2, and maximum half-length, L/2, of grain boundary ferrite allotriomorph vs. (reaction time)$^{1/2}$ in Fe-0.23 wt.% C from Bradley et al.[47].

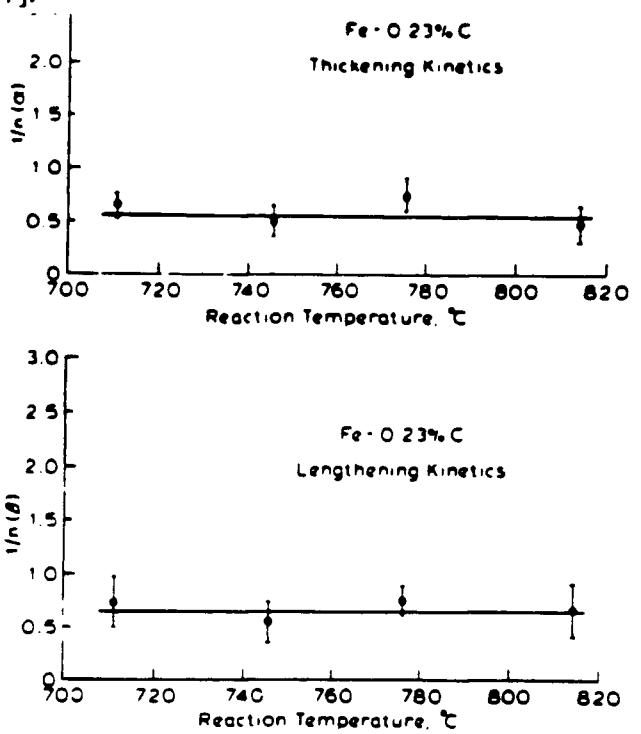

Fig. 2.19 - Typical plots of the slope, 1/n, of (a) ln S/2 and (b) ln L/2 vs. ln (reaction time)$^{1/2}$ as a function of reaction temperature in Fe-0.23 wt.% C from Bradley et al.[47].

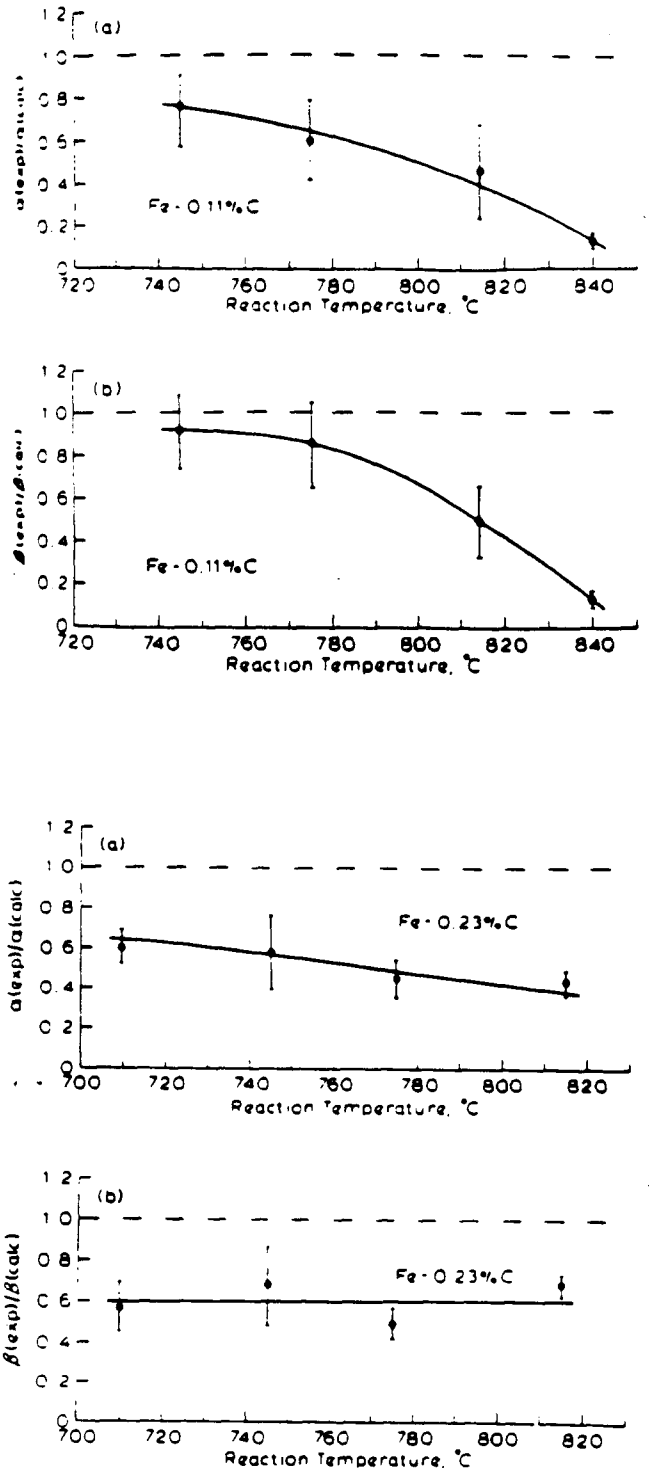

Fig. 2.20 - Ratio of experimental to calculated parabolic rate constants for thickening (α) and lengthening (β) of grain boundary ferrite allotriomorphs vs. temperature in Fe-0.11 wt.% C and Fe-0.23 wt.% C from Bradley et al.[47].

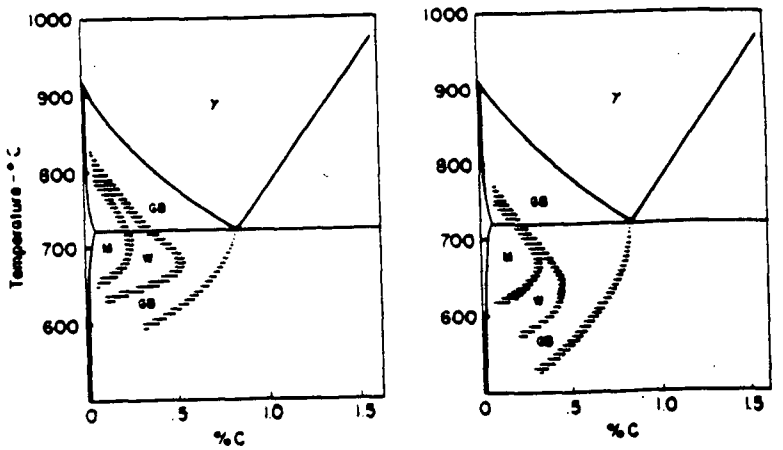

Fig. 2.21 - Temperature-composition regions in which various morphologies of the ferrite are dominant at late reaction times in coarse-grained (left-hand diagram; ASTM Nos. 0-1) and fine-grained (right-hand diagram; ASTM Nos. 7-8) specimens. GB = grain boundary allotriomorphs, W = Widmanstätten plates, and M = massive ferrite, according to Dube[38].

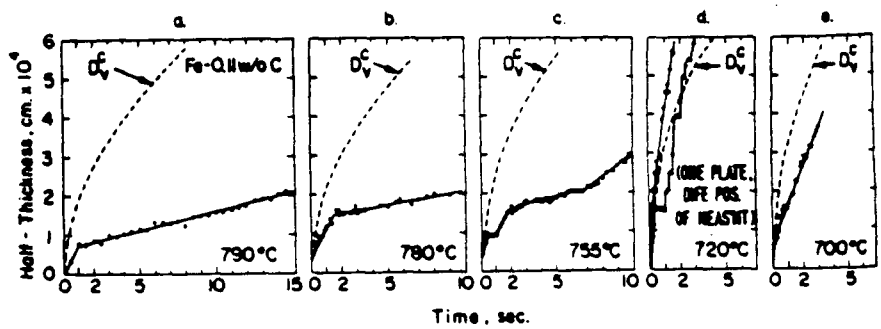

Fig. 2.22 - Representative plots of half-thickness vs. time for proeutectoid ferrite plates in the Fe-0.11 wt.% C steel . The dashed lines marked "D_V^C" indicate the theoretical result for the case of uniform advance of a planar disordered interface controlled by volume diffusion of carbon in austenite from Kinsman et al.[49].

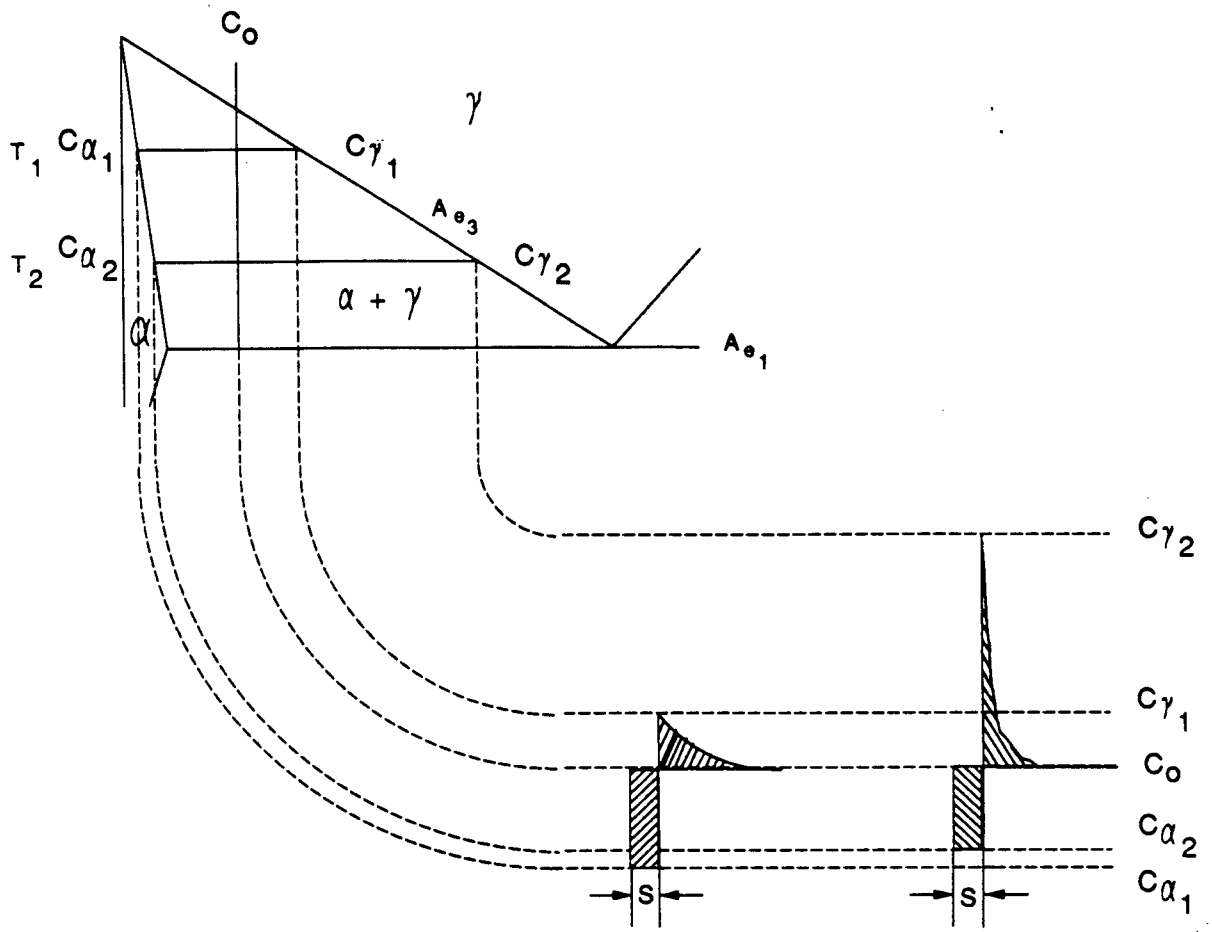

Fig. 2.23 - Schematic diagram of the hypo-eutectoid section of the iron-carbon equilibrium diagram showing the carbon diffusion gradients associated with two different temperatures.

Chapter 3 - EXPERIMENTAL WORK

3.1 Materials Used

Three plain-carbon AISI 1010, 1020 and 1040 hypoeutectoid steel grades having the composition shown in Table 3.1 were provided by Stelco Inc. for use in this study. Samples of the three steels were analyzed for chemical composition and the analyses agreed with those provided by Stelco Inc., as shown in Table 3.1.

3.2 Apparatus

Isothermal, stepped-isothermal and continuous-cooling tests on the 1010 grade and isothermal and stepped-isothermal tests on the 1040 grade were performed to measure the austenite-to-ferrite transformation kinetics using the diametral dilatometer device shown in Fig. 3.1. This apparatus has been described in detail in a previous paper[23]. The device was designed to maximize the accuracy of temperature control and the accuracy of the dilation measurement during the phase transformation event. The dilatometer incorporates resistive heating of a thin-walled tubular specimen (8 mm O.D., 0.8 mm wall thickness by 100 mm in length) with a thermocouple (0.25 mm diameter wire, intrinsic, chromel-alumel) spot welded onto the specimen surface at the midpoint. The thermocouple is used for feedback control to monitor and control the temperature of the specimen. Diametral dimensional changes in the plane of the temperature-controlling thermocouple were monitored with a modified water-cooled, quartz-tipped extensometer. The measurement of diametral, rather than axial dimensional changes, eliminated errors arising from temperature gradients along the axis of the specimen.

Controlled cooling was provided by a time-controlled helium or water flow along the length of the tubular specimen. In order to minimize decarburization, the dilatometer chamber was evacuated and back-filled with argon gas which had been passed over titanium

turnings at 850°C to strip oxygen from the gas. Each test was run to obtain the desired thermal history, the thermocouple and dilatometer data being recorded simultaneously as a function of time using a Zenith PC data-acquisition system and a two-pen chart recorder. The dilation signal was passed through an isolation amplifier before being recorded on the PC in order to minimize noise and to amplify the data signal independently for maximum resolution. The data-acquisition system allowed selection of a broad range of data sampling rates, the choice depending on the type of test being run and the total test time.

The second set of experiments to measure the isothermal and stepped-isothermal austenite-to-ferrite transformation kinetics of a 1020, plain-carbon steel was accomplished using the same diametral dilatometer attached to a Gleeble 1500 thermomechanical simulator. The tubular test specimen was resistively heated using the sophisticated computer control of the Gleeble machine. Specimens of the same diameters (I.D. and O.D.) were employed but were only 25 mm in length. The specimen temperature was controlled and monitored using a 0.25 mm diameter, intrinsic chromel-alumel thermocouple spot welded to the surface of the tube at its midpoint.

The Gleeble computer-controlled feedback system allowed precise control of specimen temperature during the heating, holding, step-quenching and cooling cycle of each test. In order to minimize decarburization, the specimen chamber was evacuated and back-filled with argon gas which had been passed over an oxygen getter (R3-11, a copper oxide catalyst) heated to 150°C to strip oxygen from the gas. Cooling of the specimens at desired cooling rates was accomplished by current control and by time-controlled flow of helium or water through the tubular specimen. Data acquisition was obtained using a Zenith PC, as previously described for the dilatometer.

3.3 Specimen Preparation

Specimen preparation for the tests consisted of mechanical straightening of commercial rod coil samples using a hand-press, followed by precise straightening through hot tension on

an Instron testing machine, and finally careful machining to produce tubular specimens of uniform wall thickness of 0.80 ± 0.10 mm. Samples were fully annealed after hot straightening. The stringent tolerance on specimen wall thickness resulted in temperature variations of less than $2°C$ around the periphery of the specimen, as measured in preliminary tests using multiple thermocouples on test specimens of known wall thickness variation.

3.4 Procedure

All test specimens were sealed in a quartz tube under vacuum and homogenized for 20 hours at $1200°C$, prior to any transformation measurements. Isothermal, stepped-isothermal and continuous-cooling experiments using the 1010 steel and isothermal and stepped-isothermal experiments using the 1020 and 1040 steel were performed. The isothermal experiments are illustrated schematically in Fig. 3.2(a) for the 1010 steel. Each specimen was first austenitized for 3 minutes at $950°C$, then cooled and held at $920°C$ for 1 minute, prior to rapidly cooling to the desired isothermal test temperature. The continuous-cooling transformation tests involved the same austenitization treatment followed by cooling of the specimen at a desired rate.

Specimens of the 1020 steel were austenitized in the Gleeble for 30 seconds at $1200°C$, then cooled and held at $850°C$ for 30 seconds, prior to rapidly cooling to the desired isothermal test temperature, as illustrated schematically in Fig. 3.2(b). A sufficient number of isothermal transformation tests were conducted to establish the temperature range for producing the allotriomorph and the Widmanstätten morphologies. The 1040 steel specimens were austenitized at $880°C$ for 3 minutes and rapidly cooled to the desired isothermal test temperature and held for the transformation to occur. A time-controlled jet of helium gas provided rapid cooling of the specimen. Dilatometer response and specimen temperature were monitored continuously throughout the test using both the PC and the two-pen chart recorder.

A number of stepped-isothermal tests were performed on the 1010, 1020 and 1040 steels. Figure 3.3 illustrates schematically the thermal histories of the stepped-isothermal tests performed on the 1010 and 1020 steels. A stepped-isothermal test typically consisted of rapidly cooling the austenitized specimen to an initial test temperature within the austenite plus ferrite phase field, partially transforming to ferrite, and then rapidly cooling to a second temperature where the transformation was completed. In the case of the 1010 and 1040 steels, all the tests were performed above A_{e_1}, whereas, for the 1020 steel, isothermal tests were also performed below A_{e_1} (Fig. 3.2(b)). Typically, sampling rates of 10 to 20 Hz. were employed to acquire the temperature and dilation data on the PC.

Some specimens were water-quenched at various stages and subjected to metallographic procedures of cutting, mounting and mechanical polishing. Specimens were then etched with 2% Nital solution. Metallographic analyses involved estimation of prior austenite grain size, volume fraction of ferrite, assessment of ferrite nucleation sites and identification of ferrite morphology. A Leitz Image Analyzer was used to estimate volume fraction of ferrite. Photomicrographs were obtained using a Carl Zeiss Ultraphot Camera microscope. Some of the 1020 steel specimens were subjected to surface examination using a Scanning Electron Microscopy (SEM) and a Scanning-Transmission Electron Microscopy (STEM). Also, thin foil electron microscopy was employed and a number of thin foils of isothermally transformed 1020 steel specimens were prepared and examined using SEM, TEM and electron diffraction procedures on the STEM.

Chemical Composition (In wt. %)	1010		1020		1040	
	As Rec'd	From Analysis	As Rec'd	From Analysis	As Rec'd	From Analysis
C	0.11	0.10	0.19	0.201	0.39	0.40
Mn	0.40	0.37	0.48	0.46	0.79	0.74
S	0.018	0.012	0.008	0.008	0.020	0.012
P	0.009	0.010	0.007	0.007	0.013	0.014
Si	0.014	0.012	0.012	0.014	0.26	0.27
Cu	0.011	-	0.008	0.007	0.009	-
Ni	0.004	-	0.004	0.003	0.005	-
Cr	0.009	-	0.018	0.022	0.025	-
Al	0.030	0.032	0.030	0.042	0.032	0.045

Table 3.1- Comparison of steel composition provided by Stelco Inc. with that obtained from a laboratory chemical analysis.

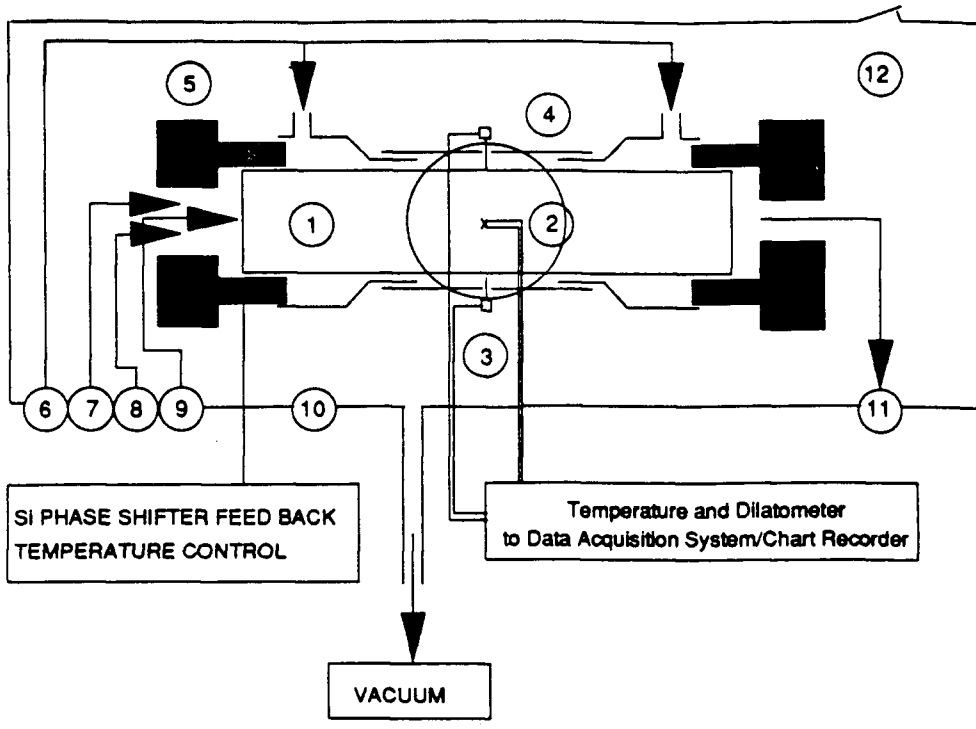

1 SAMPLE
2 THERMOCOUPLE
3 DIAMETRAL DILATOMETER
4 QUARTZ TUBE
5 ELECTRICAL BLOCKS
6 OUTSIDE ARGON INLET
7 INSIDE ARGON INLET
8 HELIUM QUENCHING
9 WATER QUENCHING
10 CHAMBER
11 INSIDE GAS OUTLET
12 WINDOW

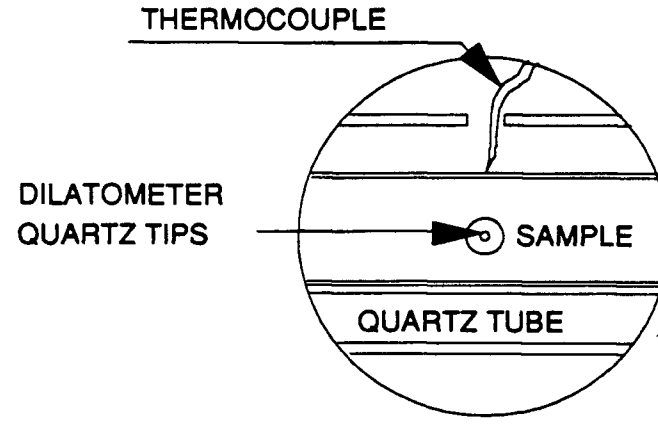

Fig. 3.1 - Schematic diagram of diametral dilatometer.

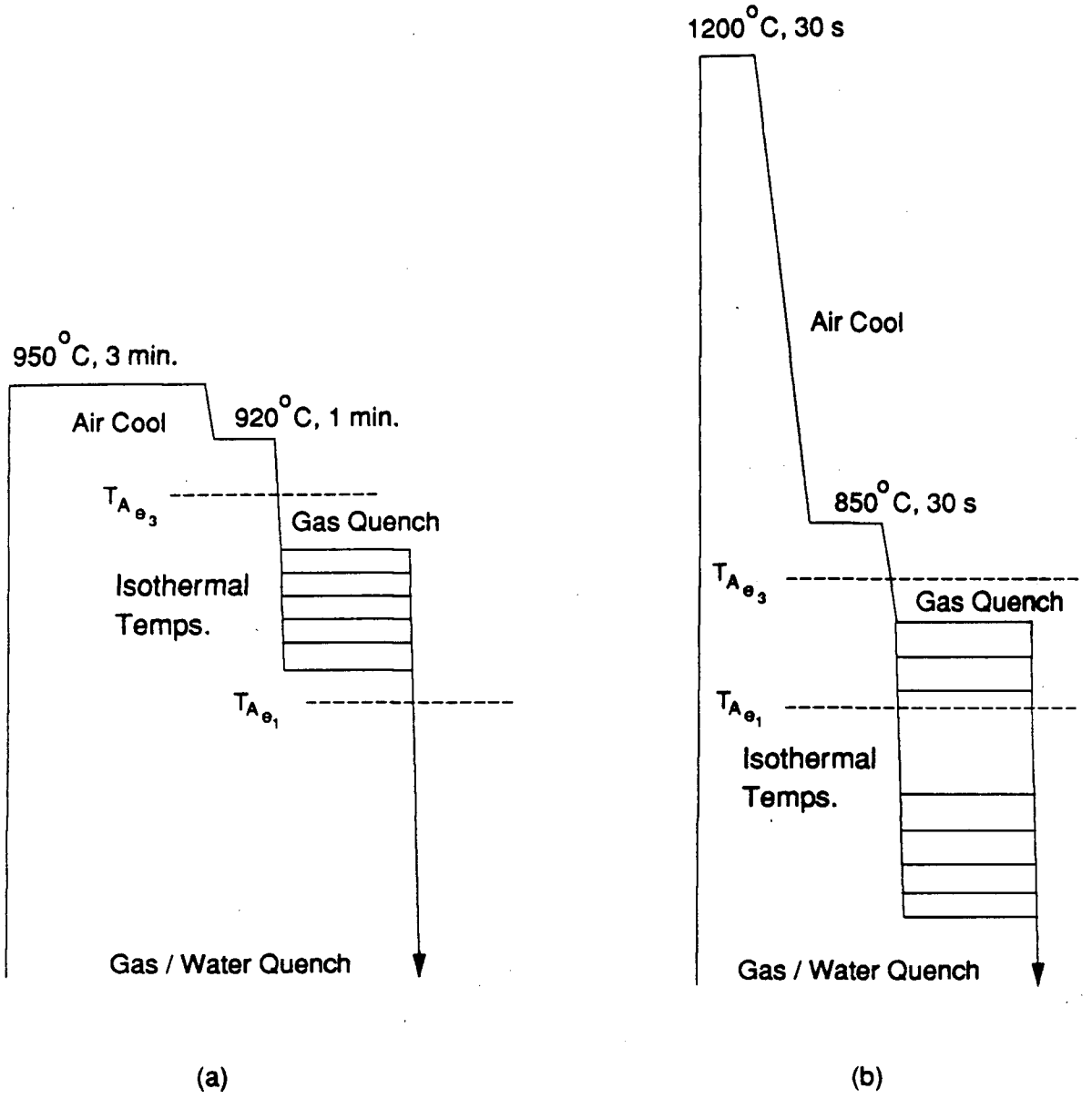

Fig. 3.2 - Schematic diagram illustrating isothermal transformation experiments for:(a) 1010 grade steel and (b) 1020 grade steel.

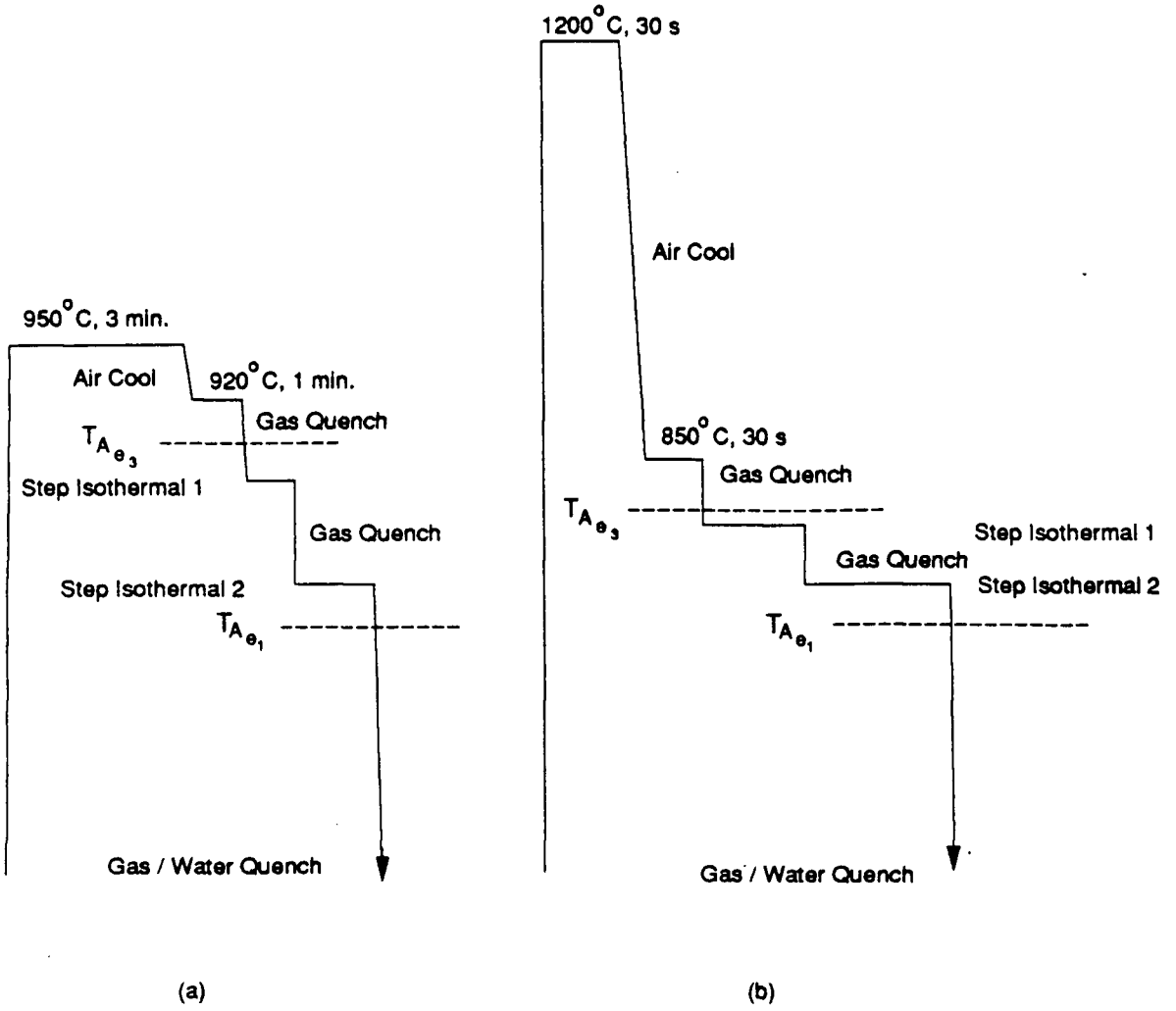

Fig. 3.3 - Schematic diagram illustrating stepped-isothermal transformation experiments for:(a) 1010 grade steel and (b) 1020 grade steel.

Chapter 4 - EXPERIMENTAL RESULTS

Experiments were conducted using AISI 1010, 1020 and 1040 steel grades, having the chemical composition shown in Table 3.1. The U.B.C. dilatometer was employed for the tests on 1010 and 1040 grade steel and the Gleeble 1500 was used for the 1020 grade. Isothermal and stepped isothermal transformation kinetics were measured for all three grades. In addition, continuous-cooling kinetics were measured for the 1010 grade.

Slow heating tests were performed on the three steel grades to determine the $T_{A_{c_1}}$ and $T_{A_{c_3}}$ temperatures. An example is shown in Fig. 4.1 of the temperature and dilatometer response of a 1020 specimen which was heated at a rate of $0.75°C/s$. With increasing temperature above $T_{A_{c_1}}$, the specimen progressively transforms to austenite at the expense of dissolving ferrite, causing an overall contraction of the specimen, although the specimen is also undergoing thermal expansion. When the temperature passes $T_{A_{c_3}}$, the specimen has become fully austenitic and expands due to thermal expansion. $T_{A_{c_3}}$ and $T_{A_{c_1}}$ values were also calculated from the following equations, developed by Andrews[59] and based on a regression analysis of published data for a number of steel compositions.

$$\begin{aligned} T_{A_{c_3}}(°C) = {} & 910 - 203(\sqrt{wt.\%C}) - 15.2(wt.\%Ni) + 44.7(wt.\%Si) + 104(wt.\%V) \\ & + 31.5(wt.\%Mo) + 13.1(wt.\%W) - 30(wt.\%Mn) - 11(wt.\%Cr) \\ & - 20(wt.\%Cu) + 700(wt.\%P) + 400(wt.\%Al) + 120(wt.\%As) \\ & + 400(wt.\%Ti) \end{aligned} \tag{4.1}$$

and

$$\begin{aligned} T_{A_{c_1}}(°C) = {} & 723 - 10.7(wt.\%Mn) - 16.9(wt.\%Ni) + 29.1(wt.\%Si) \\ & + 16.9(wt.\%Cr) + 290(wt.\%As) + 6.38(wt.\%W) \end{aligned} \tag{4.2}$$

Table 4.1 shows good agreement between the experimental and calculated values of $T_{A_{c1}}$ and $T_{A_{c3}}$ for the three steels used in this study. This set of experiments not only confirmed the composition of the steel grades used in this study, but was also used to check the accuracy of the temperature measurements.

The austenite grain size estimated for each steel is also shown in Table 4.1. This was assessed using specimens water quenched after partial transformation in the proeutectoid ferrite plus austenite ($\alpha + \gamma$) two-phase field. This procedure facilitated easy identification of the γ grain boundaries, as they were outlined by the proeutectoid ferrite. The lineal intercept technique[60] was employed on photomicrographs of these specimens to estimate the average γ grain size.

4.1 Characterization of Isothermal Transformation Kinetics

The isothermal transformation results were obtained from measurements of specimen temperature and dilation as a function of time. Figure 4.2 shows a typical dilatometer and temperature response for a 1010 specimen isothermally transformed from austenite-to-proeutectoid ferrite at 803°C. Typically, the dilatometer signal was in the range of 0 to 100 millivolts. As shown in Fig. 4.2, the 1010 specimen was initially cooled rapidly from the 920°C austenitizing temperature to the 803°C isothermal test temperature over a period of one second. On attaining the isothermal temperature, the dilatometer exhibits an expansion due to the austenite to proeutectoid ferrite transformation. A sampling rate of 10 Hz. was adopted for both the thermocouple and the dilatometer. The signal from both the thermocouple and the dilatometer exhibit a certain amount of noise in spite of using a noise isolation device. To smooth the results, the data points were averaged with care being taken to retain important data points such as those at the start of the transformation.

The isothermal transformation kinetics were characterized with the Avrami equation (Eq. (2.12)). D_{MIN} in Fig. 4.2 represents the diameter of a fully austenitic specimen and D_{MAX}

the diameter of a partially austenitic specimen containing the equilibrium fraction of proeutectoid ferrite, assuming zero or negligible transformation during the quench to the isothermal test temperature. To use the Avrami equation to describe the $\gamma \rightarrow \alpha + \gamma'$ partial transformation, the equilibrium fraction of ferrite formed was normalized to unity. This was accomplished by dividing the measured volume fraction transformed at each time by the total volume fraction transformed, ΔD_{TOT}, as measured at the end of the transformation, where

$$\Delta D_{TOT} = D_{MAX} - D_{MIN} \tag{4.1}$$

and the normalized fraction of ferrite formed, X is:

$$X = \frac{D - D_{MIN}}{\Delta D_{TOT}} = \frac{\Delta D_F}{\Delta D_{TOT}} \tag{4.2}$$

where D represents the diameter of the specimen at a given time. Figure 4.3 shows the results of the conversion of the dilatometer data shown in Fig. 4.2 to a plot of the normalized fraction transformed (X) and the true fraction ferrite transformed as a function of time. The true fraction ferrite was obtained by multiplying the dilational fraction by the equilibrium fraction calculated from the iron-carbon equilibrium phase diagram. The equilibrium ferrite fraction for each steel was confirmed by quantitative metallographic procedures.

The final step in characterizing the data involved the calculation of the parameters n and b in the Avrami equation. This was accomplished by performing a least-squares analysis of the kinetic data plotted as ln ln[1/(1-X)] vs. ln (t-t_s). The start of transformation, $t = t_s$, was selected initially as the time at which the sample cooled below the $T_{A_{c3}}$ temperature. The initiation time then was increased by small increments (0.1 second) until the best fit for the ln ln[1/(1-X)] vs. ln (t-t_s) line was obtained over the range of 2 to 98 pct. X transformed. Figure 4.4 shows the best fit line for the data of Fig. 4.3, where the slope of the line is n and the y-intercept the value of lnb. For reference, the plot also includes values of 2, 50 and 98 % transformed. After rapidly quenching the specimen to the isothermal test temperature, its

initial temperature may not match the programmed isothermal temperature for a short time, as a result of under-quench or over-quench. This potential error in the initial dilation data is avoided by using the 2 to 98 pct. X transformation range for the kinetic analysis.

The Avrami equation, when applied to characterize the complete austenite-to-ferrite transformation, is more of a mathematical tool than an equation of fundamental significance because it was not developed to account for soft impingement. Figure 4.5 illustrates a comparison of experimental isothermal data with that predicted by the Avrami equation (Eq. (2.12)). It can be seen that the Avrami equation describes the experimental results very well.

4.2 Characterization of Stepped Isothermal Transformation Kinetics

The true test of the additive nature of the proeutectoid ferrite reaction is obtained by studying the kinetics of the ferrite transformation under conditions where partial transformation is permitted at one temperature, after which the transformation temperature is rapidly changed to a new temperature to complete the transformation. A number of tests were performed to assess the additive nature of the proeutectoid ferrite reaction in 1010, 1020 and 1040 steels by measuring the transformation kinetics after rapid change from one temperature to another by helium quenching ($100°/s$).

Figure 4.6 shows typical stepped-isothermal test data consisting of thermal history and the dilatometer response as a function of time for the 1020 steel specimen. The specimen was cooled from the austenite phase field to the first isothermal temperature of $760°C$ and held there until it was partially transformed. The specimen was then cooled rapidly to the second isothermal temperature of $730°C$ and held until the transformation was completed. As described earlier, the isothermal test data was converted to fraction dilation first and then to true fraction ferrite by multiplying the dilational fraction by the equilibrium fraction obtained from the iron-carbon equilibrium phase diagram. The stepped-isothermal data was treated in a slightly different manner. First the data was corrected for the thermal expansion or contraction (step-up or step-down quench) by using the slope of the dilatometer vs.

temperature curve obtained during the step-change. Then the total dilation, ΔD_{TOT}, due to the isothermal transformation at each temperature was used to obtain D_{MAX} and D_{MIN} at the first and second temperatures of a stepped-isothermal test respectively. Using these values, the dilatometer data was converted to fraction dilation. The fraction dilation was then converted to true fraction ferrite by multiplying the dilational fraction by the equilibrium fraction as determined from the boundaries of the equilibrium iron-carbon phase diagram.

4.3 Characterization of Continuous-Cooling Transformation Kinetics

Continuous-cooling transformation tests were performed using the 1010 grade steel to examine the application of the principle of additivity to the continuous decomposition of austenite-to-proeutectoid ferrite. The continuous-cooling transformation kinetics were predicted by applying the principle of additivity and using the isothermal data and experimentally determined continuous-cooling transformation start times. The predictions were compared with the experimental results which consisted of dilatometer and specimen temperature responses. Typical thermal and dilatometer responses for a cooling rate of $0.53°/s$ are shown in Fig. 4.7. It can be seen that a constant cooling rate was maintained until the completion of the transformation. Also shown in the figure are the $T_{A_{c3}}$ and $T_{A_{c1}}$ temperatures for the steel. The initial linear dilatometer response, plotted in Fig. 4.7, is due to thermal contraction. Once the austenite begins to transform to proeutectoid ferrite, expansion occurs, which is reflected in the change of slope of the dilatometer curve.

The transformation start time and temperature for the continuous-cooling transformation were determined from the change in slope of the dilatometer vs. time curve. First, the thermal contraction coefficient of austenite as a function of temperature was determined by calculating the slope of the initial part of the dilatometer vs. temperature curve. With this coefficient, the contraction of the specimen as a function of specimen temperature was predicted, assuming only austenite to be present. The difference between the predicted and the actual dilatometer responses was compared, as shown in Fig. 4.8. This

difference remains essentially zero during initial cooling of the austenite, but changes as the transformation begins, thereby defining $t_{s_{CCT}}$. In order to determine the transformation completion time, the final portion of the dilatometer-temperature curve shown in Fig. 4.7 was used to calculate the thermal contraction coefficient of the combined ferrite plus austenite phase. From this coefficient, the completion times were calculated in a manner similar to that adopted to define the start time.

Calculation of continuous-cooling transformation kinetics in terms of ferrite fraction vs. time (or temperature) was accomplished by using the measured diametral expansion data and the thermal history of each CCT curve. This involved first correcting ΔD by subtracting the thermal contribution due to continuous cooling. The contraction coefficient for the mixed $(\alpha+\gamma')$ phase was expressed in terms of the weight fractions of the two phases present. The transformation was initiated at the experimentally determined start time. The fraction of austenite transformed to ferrite was obtained by first approximating the extent of transformation, then incrementing the degree of transformation until a fit was obtained with the dilatometer response curve as a function of temperature.

4.4 1010 Grade Steel

The low carbon 1010 steel was chosen to obtain the widest possible proeutectoid ferrite plus austenite $(\alpha+\gamma')$ two-phase field. This made it possible to measure the proeutectoid ferrite transformation kinetics, first for the stepped-isothermal transformation temperatures separated by a reasonably large temperature difference, ΔT, and second, for the continuous-cooling transformation to be initiated and completed above $T_{A_{c_1}}$. The large ΔT meant that a significant difference could be obtained between the boundary conditions maintained at the two test temperatures, especially the equilibrium carbon contents of the austenite (C_γ) and the carbon diffusivities (D_C^γ) at each isothermal temperatures. These factors made the stepped-isothermal experiments stringent tests of the principle of additivity for this steel composition.

4.4.1 Isothermal Transformation Kinetics

A number of isothermal transformation tests were performed using the dilatometer, including several to examine the reproducibility of the data. Figure 4.9 shows the results of a reproducibility test. It can be seen that the dilatometer response plotted as a function of time for both 800°*C* isothermal tests shows reasonable agreement.

Figure 4.10 shows typical results obtained for isothermal tests performed at three temperatures. The normalized fraction for each temperature obtained by Avrami analysis has been converted to true fraction using the iron-carbon equilibrium diagram. From the Figure it can be seen that as the temperature decreases, the amount of ferrite and the transformation rate of the austenite-to-proeutectoid ferrite increases.

The effect of austenitizing temperature on the rate of isothermal ferrite transformation was also measured. Figure 4.11 shows the isothermal transformation kinetics measured at 800°*C* for three different austenitizing temperatures of 950°*C*, 1000°*C* and 1100°*C*, for three minutes each. As can be seen in Fig. 4.11, the overall ferrite transformation rate decreases with increase in austenitizing temperature, i.e., with increase in austenite grain size. The decrease in the transformation rate in large-grained specimens is due to the reduction in γ grain boundary area per unit volume and the associated decrease in number of nucleation sites per unit volume contributing to the overall transformation kinetics. All three specimens were water-quenched after completion of the transformation and subjected to metallographic examination. The ferrite morphology in all three specimens was predominantly allotriomorphic.

The results of the Avrami characterization of the isothermal transformation kinetics are shown in Table 4.2. As expected, the incubation time decreases with decreasing temperature. Except for the highest temperature of 812°*C*, the magnitude of the parameter n is relatively constant and b is a function of the transformation temperature. Obtaining a reasonably constant n value implies that the growth kinetics and site saturation conditions are similar

over the temperature range examined. In addition, a constant n and a temperature dependent b satisfies Cahn's general condition for the transformation event to be additive[13] and makes the Avrami equation a useful tool for predicting transformation kinetics during non-isothermal treatment.

Most isothermal test specimens were water-quenched at the end of the test and some were subjected to quantitative metallographic examination to measure the volume fraction ferrite transformed for comparison with the equilibrium fraction ferrite calculated using the iron-carbon equilibrium diagram. The equilibrium weight fraction of ferrite, as determined using the phase boundaries, was converted to volume fraction using reported measurements of the ferrite and austenite densities[64]. As shown in Fig. 4.12, the agreement between the two is excellent. The error bars on the measured volume fraction ferrite reflect the range of measurements obtained on the 10 areas analyzed for each specimen using the Leitz Image Analysis System. Each specimen was heavily etched (~ 20 s in 2% Nital) to improve the visible difference between the ferrite and martensite in the quenched microstructure. This assisted the Image Analysis System to discriminate the light ferrite from the dark martensite.

In an opaque system it is experimentally very difficult to assess nucleation behavior for the individual surface, edge and corner sites. Metallographic examination of specimens water-quenched at early stages of isothermal transformation revealed that all the prior austenite grain boundaries are covered with ferrite. Based on energy considerations, a surface such as an austenite grain boundary is the least favored site for ferrite nucleation, relative to grain edge and corner sites[12]. Hence, it can be expected that the grain edges and corners are saturated with ferrite nuclei prior to grain boundary nucleation and that general site saturation conditions prevail early in the transformation for the temperatures and γ grain sizes examined. Figure 4.13 shows an example of early site saturation. The isothermal transformation at $812°C$ was arrested by a water-quench after approximately 25 pct. ferrite had formed. This is the highest isothermal transformation test temperature examined in this

study and still indicates that early site saturation prevails. At temperatures below $812°C$, site saturation would be expected and was observed. Once the nucleation rate reaches zero, the transformation will be dependent solely upon the growth rate.

4.4.2 Continuous-Cooling Transformation Kinetics

A number of continuous-cooling transformation tests were performed over a range of cooling rates. The cooling rates were chosen to initiate and complete the proeutectoid ferrite transformation within the proeutectoid ferrite-plus-austenite ($\alpha + \gamma$) two-phase field to ensure that the equilibrium phase boundaries are maintained. Typical dilatometer traces for four of the tests are shown in Fig. 4.14. As can be seen, the time for transformation start decreases and the transformation rate increases with increasing cooling rate.

The Scheil[6] equation (Eq. 2.10) was applied to examine the additivity of the incubation period for the $0.53°C/s$ cooling rate test. The results of the isothermal and the continuous-cooling tests are presented in Fig. 4.15. As shown, the isothermal start time, $t_{st}(1\%)$, data was described using an exponential type equation based on the extent of undercooling below $T_{A_{c3}}$ and extrapolated to describe temperatures above $812°C$. By applying the Scheil equation in conjunction with the experimental incubation times of the isothermal tests, the start time for the continuous-cooling ($0.53°C/s$) transformation of austenite-to-ferrite was estimated. As can be seen from Fig. 4.15, the Scheil equation underestimates the transformation start time. This result is in contrast to that reported by Hawbolt et al.[25] who obtained an overestimation of start time of ferrite for the continuous-cooling transformation of a 1025 steel using the Scheil approach. However, it should be emphasized that the present assessment was done by extrapolation of TTT data.

The continuous-cooling transformation data also was used to assess the additivity of the ferrite transformation. Based on the Avrami characterization of the isothermal transformation data shown in Table 4.2 with average $\bar{n} = 1.19$ and b as a function of undercooling below $T_{A_{c3}}$, the fraction ferrite was calculated as a function of temperature. The

calculation was initiated at the experimental continuous-cooling transformation start temperature. The calculation method has been described in detail in previous papers[23,25]. The calculated and experimental fraction ferrite under continuous-cooling conditions for a cooling rate $0.53°C/s$ are compared in Fig. 4.16. The Avrami equation used in conjunction with the principle of additivity, underestimates the initial stages of the transformation, although the predicted duration of the transformation compares reasonably well with that experimentally observed. The results of a similar analysis of the $0.2°C/s$ and $0.77°C/s$ cooling rate data showed a similar underestimation of calculated fractions in the initial stages of transformation. The disagreement between predicted and experimental fraction transformed in the early stages of continuous-cooling transformation may be attributed to the lack of accurate n and b values for the high temperature range which necessitated an extrapolation of the lower temperature isothermal data. High temperature isothermal transformation tests were attempted but the amounts of ferrite transformed were not sufficient to generate significant and clear dilation signals for meaningful analyses.

All the continuous-cooling transformation test specimens after completion of transformation were subjected to quantitative metallographic examination using the Leitz Image Analysis system. On average, 89 pct. of ferrite was measured to be transformed at each cooling rate which matches very well with the predicted value of 88.5 pct. obtained using the lever rule and assuming that the equilibrium amount of ferrite had formed.

4.4.3 Stepped Isothermal Transformation Kinetics

Two types of tests were performed with the 1010 steel. Both involved the austenite being partially transformed to ferrite at one temperature and the temperature being changed rapidly to either a *lower* or a *higher* temperature and allowing the transformation to proceed to completion at the second temperature. These two experiments are considered as critical tests of the principle of additivity and should assess the effect of the previous temperature on

the transformation kinetics at the second temperature. Complete isothermal transformation kinetics were measured for the temperatures used for each of the stepped-isothermal transformation experiments.

In the first series of tests, two isothermal temperatures (803°C and 764°C), separated by a temperature drop of 39°C, were selected for the step-change experiment. The austenite was partially transformed to approximately 31 pct. ferrite at 803°C, the temperature was changed rapidly to 764°C and the transformation was completed. In Fig. 4.17, the complete isothermal transformations at 803°C and 764°C are shown as well as the partial, stepped-isothermal results obtained at 803°C and 764°C. As mentioned earlier, the data was compared on the basis of true fraction transformed. The agreement between the partial and full transformation kinetics at the lower temperature (764°C), is reasonable, although slightly higher transformation kinetics are observed after step quenching to 764°C. This supports the experimental additivity of the proeutectoid ferrite reaction under a decreasing temperature in that the reaction kinetics at a lower temperature are quite similar to the isothermal kinetics obtained at that temperature.

The effect of soft impingement on the applicability of the principle of additivity was also assessed. During isothermal transformation of ferrite, the growth kinetics of ferrite decreases with increasing time due to long range diffusion control and overlapping of carbon-enriched regions of austenite from other ferrite precipitates. This latter effect is called soft impingement. The extent of soft impingement varies with the γ grain size. The smaller the grain size, the earlier will be the soft impingement. Step-down quench tests were performed which involved extensive isothermal transformation of the specimen at 800°C, thereby ensuring soft impingement, followed by completion of transformation at 760°C. The complete isothermal transformations at 800°C and 760°C are shown in Fig. 4.18, as well as the partial, step-down results obtained at 800°C and 760°C. The data was compared on the basis of true fraction transformed, the agreement between the partial and full transformation

kinetics at the lower temperature ($760°C$), being reasonable. The transformation appears to be experimentally additive, given the extent of experimental variability in reproducibility of the test data (shown in Fig. 4.9). The soft impingement due to the higher temperature transformation did not much influence the lower temperature transformation kinetics, although the overall transformation kinetics after the step-down are consistently lower than those obtained during the isothermal transformation.

The overall transformation from austenite-to-ferrite is due to the combined effect of nucleation and growth processes. However, if the nucleation rate becomes zero due to site saturation, only the growth kinetics dictate the overall transformation rate. As discussed in the previous sections, metallographic examination has shown definite evidence for early site saturation at all temperatures studied. Hence, only growth kinetics can be expected to govern the overall transformation kinetics at a given temperature.

The effect of temperature on the ferrite growth kinetics is realized through the carbon gradient (based on C_γ and C_α) and the carbon diffusion coefficient in austenite (D_C^γ) due to the long-range diffusion of carbon in γ. Thus, when the temperature of the partially transformed system ($803°C$), with its associated equilibrium boundary conditions and carbon gradients, is rapidly changed to a new temperature ($764°C$), two possibilities emerge in terms of kinetics at the second temperature. Initially, one would expect the growth kinetics to be affected by the carbon gradients of the previous temperature ($803°C$), at least for a short time during the attainment of the new equilibrium boundary conditions at $764°C$. If it is assumed that at $764°C$ the equilibrium boundary conditions are attained instantaneously, then a very large carbon gradient can be expected to be present ahead of the growing ferrite/austenite (α/γ) interface. Both these possibilities would make the growth kinetics at the second temperature dependent on the thermal path and hence non additive. No well defined evidence of this effect is apparent in Figs. 4.17 and 4.18.

Figure 4.19 compares the rate of transformation as a function of time for the isothermal and the stepped-isothermal situations shown in Fig. 4.17. The data was corrected for thermal contraction of the specimen by using the slope of the temperature vs. dilation data for the step-down period. As shown in Fig. 4.19, the rate of transformation for the stepped-isothermal test exhibits a sudden increase due to the temperature change and the rate decreases thereafter very quickly to that characteristic of the lower temperature isothermal data. This increase in transformation rate signifies rapid attainment of the new equilibrium carbon concentrations, C_γ and C_α, in the austenite and ferrite respectively, as dictated by the equilibrium phase boundaries at $764°C$. During the initial transformation at $803°C$, the rate of transformation increases, reaching a peak, and then reduces with time. This initial increase in transformation rate is due to the nucleation rate contributing to the growth rate of the transformation. Once all the sites are saturated and the nucleation rate drops to zero, only the growth rate dictates the overall transformation kinetics. On stepping down to $764°C$, after site saturation and partial transformation at $803°C$, the initial high transformation rate is related to the attainment of the new phase boundary equilibria. The rate thereafter decreases steadily as required for long-range diffusion controlled isothermal growth and impingement effects. Thus the rate of transformation does show the effect of thermal path, although for a very short time. The observed agreement between the overall stepped transformation kinetics and the isothermal transformation kinetics at $764°C$ (Fig. 4.17) supports the previously observed experimental additivity of the austenite-to-ferrite transformation[25,31,33,34] under continuous-cooling conditions.

The second type of stepped-isothermal test involved transforming the specimen partially at one temperature and changing the temperature rapidly to a higher temperature. For comparison with the step-down quench test, the same temperatures were utilized ($764°C$ and $803°C$). The complete isothermal transformation kinetics at $803°C$ and $764°C$ are shown in Fig. 4.20 as well as the partial, stepped-isothermal transformation kinetics. The results are

compared on the basis of true fraction transformed. The partial and full transformation kinetics at 803°C agree reasonably well. Unlike the step-down quench, the increase in temperature should result in a reduction of the phase boundary compositions and an associated decrease in the initial carbon gradients. When the data was analyzed for transformation rate, the thermal expansion due to the temperature increase masked the affects of changing the boundary conditions and the resulting carbon gradients.

A number of step-quench test specimens were water-quenched after partial and complete transformation and subjected to metallographic examination. The photomicrograph in Fig. 4.21 is the microstructure obtained in the step-down test from 803°C to 764°C after completion of transformation at 764°C. As can be seen, the proeutectoid ferrite is polygonal. This result is in agreement with the observed morphologies of test specimens water-quenched after completion of individual isothermal transformations at 803°C and 764°C. This signifies that for the 1010 grade, under the condition of a step-down quench, the morphology of ferrite remains the same as that obtained for the isothermal transformations. Also, the transformation is experimentally additive under these conditions.

The ferrite transformation kinetics obtained after rapid change from one temperature to another support the observed experimental additivity of the austenite-to-ferrite transformation. In a very short time interval, the isothermal kinetics at the second temperature are attained. These tests can be examined in the light of continuous-cooling (or heating) transformation kinetics. The experimental step-change tests, with a temperature drop of 39°C, can be described as an exaggerated continuous-cooling (or heating) tests. Based on the experimental evidence presented so far, it is clear that the time taken by the system to adjust to the isothermal transformation kinetics at the second temperature, under step-change conditions, is very small. Hence under continuous-cooling (or heating) conditions, where the

incremental temperature changes are infinitesimally small in magnitude, the time to reach the expected isothermal transformation rates would be expected to be extremely small. This may explain the observed experimental additivity of the austenite-to-ferrite transformation.

4.5 1020 Grade Steel

The tests on the 1010 steel indicated that the austenite-to-polygonal ferrite transformation showed experimentally additive behaviour for austenite grain sizes in the range ASTM No. 5-6. The choice of a 1020 steel with a high austenitizing temperature ($1200°C$) was made with the specific objective of obtaining a range of temperatures in which the transformation from a polygonal ferrite to a Widmanstätten morphology could be attained. It has been recognized that although Widmanstätten ferrite plates appear in small numbers throughout most of the temperature range of the ferrite reaction in plain-carbon steels, they form most readily under conditions of large austenite grain size and in steels containing less than 0.3 wt.%. carbon[38] (Fig. 2.21).

4.5.1 Isothermal Transformation Kinetics

A number of isothermal transformation tests were performed using the Gleeble 1500 for a range of temperatures to examine the effect of ferrite morphology. Reproducibility of the isothermal results is demonstrated in Fig. 4.22 for transformation at $730°C$. Figure 4.23 shows the isothermal transformation kinetic results obtained at four temperatures, $730°C$, $740°C$, $760°C$ and $780°C$. The total fractions, normalized to unity, have been converted to equilibrium fraction transformed using the iron-carbon equilibrium diagram. As can be seen, the amount of ferrite formed and the transformation rate decrease with increasing temperature. The quantitative metallographic determination of fraction ferrite transformed at $730°C$ was 74 ± 2 pct., comparing favorably with the value of 75.3 pct. calculated using the iron-carbon phase diagram. Table 4.3 summarizes the incubation time and the measured values of the Avrami parameters n and lnb. The parameter n is a maximum for the highest temperature ($780°C$) studied; this higher n value can be attributed to nucleation contributing

to the transformation event for relatively long times. Whereas, the n value for the other three temperatures remains almost constant. As mentioned before, a constant n value implies comparable nucleation and growth conditions. Also, a constant n and a temperature-dependent b satisfies the conditions for a transformation event to be additive. Since the transformation kinetics being measured include soft impingement, the kinetic characterization also includes soft impingement effects, making it possible for the system to exhibit experimental additivity even though theoretical additivity is not conceivable.

4.5.2 Morphological Observations

Metallographic analyses of the isothermal test specimens identified the two basic morphologies of polygonal proeutectoid ferrite and Widmanstätten ferrite. With decreasing temperature, the ferrite changed from nearly all grain boundary polygonal to predominantly Widmanstätten morphology. Figure 4.24 shows a typical photomicrograph of partially transformed ferrite at $780°C$. It can be seen that almost all ferrite is present as polygonal grain boundary allotriomorphs. The dark phase is martensite transformed from the remaining austenite. With decreasing transformation temperature below $780°C$, the proeutectoid ferrite changed from polygonal allotriomorph to a Widmanstätten morphology. Figures 4.25 to Fig. 4.27 are typical photomicrographs of the ferrite isothermally formed at temperatures from $760°C$ to $730°C$. It can be seen that over this temperature range the proportion of Widmanstätten ferrite increases with decreasing temperature. The Widmanstätten ferrite plates were observed to originate from the grain boundary allotriomorphs. Figure 4.28 (a) shows a photomicrograph of ferrite allotriomorphs nucleating at the austenite grain boundaries of a specimen reacted isothermally for 10 s at $730°C$. When this specimen is viewed at a higher magnification (Fig. 4.28 (b)) it can be seen that in most instances the Widmanstätten ferrite plates develop from pre-formed grain boundary allotriomorphs. Such plates have been referred to as secondary sideplates[36], as opposed to primary sideplates

which grow directly from austenite grain boundaries. As seen in Fig. 4.28 (b), the Widmanstätten ferrite sideplates are invariably located on one side of the allotriomorphs, the other side remaining relatively planar.

A common microstructural feature observed throughout the temperature range of this investigation was that at early stages of the transformation, ferrite allotriomorphs rapidly nucleated and spread along the austenite grain boundaries (Fig. 4.24 and 4.28(a)). Widmanstätten ferrite plates were found invariably to grow from those grain boundary allotriomorphs. With decreasing temperature, the frequency of Widmanstätten ferrite sideplate formation not only increased but the sideplates appeared in groups with several plates evolving from the same allotriomorph (Fig. 4.28(b)). At lower transformation temperatures, the Widmanstätten sideplates physically impinged, as shown in Fig. 4.29. Within a group of sideplates, the entire set of plates was often aligned parallel to each other at a fixed angle to the allotriomorph axis. At lower temperatures, a number of Widmanstätten sideplates developing from both sides of the allotriomorph were observed, as shown in Fig. 4.30. The microstructures presented here are generally consistent with those reported by previous authors[36,61,62], although some of the published work is based on steel compositions other than the 1020 grade.

4.5.3 Stepped Isothermal Transformation Kinetics

As discussed earlier, this particular grade of steel was used to examine the effect of morphology change on the experimental additivity of the proeutectoid ferrite reaction. A number of tests were performed to determine the transformation kinetics measured after partially transforming the specimen at one temperature and allowing the transformation to go to completion at a second temperature. These two isothermal transformation temperatures were generally selected such that a different predominant ferrite morphology would be obtained at each temperature. However, some tests were performed at two temperatures where a common ferrite morphology was obtained at both temperatures.

Figure 4.31 shows the complete isothermal transformation kinetics obtained at 740°C and 730°C, as well as the partial, step-down isothermal transformation kinetics, compared on the basis of true fraction transformed. Both temperatures produced a predominantly Widmanstätten ferrite morphology. As can be seen, the agreement between the partial and full transformation kinetics at the lower temperature (730°C), is good. Thus the proeutectoid ferrite reaction between two temperatures having similar morphologies and separated by a step-quench is experimentally additive in the 1020 steel; similar observations were made previously for the 1010 steel having polygonal ferrite.

The complete isothermal transformation results obtained at 760°C and 730°C are shown in Fig. 4.32, together with the stepped-isothermal transformation results. As discussed in the earlier section, the results of isothermal transformation tests at 760°C showed that the predominant ferrite morphology consists of polygonal allotriomorphs, although some Widmanstätten ferrite is present; while at 730°C, the ferrite is mainly Widmanstätten. As can be seen, the agreement between the partial and full transformation kinetics at the lower temperature (730°C), remains fairly good, in spite of the difference in morphologies between the isothermal transformation temperatures. This confirms the experimental additive nature of the proeutectoid ferrite transformation with dissimilar proportions of ferrite morphologies at two temperatures separated by a step-quench.

The ferrite observed in the specimen isothermally transformed at 780°C was fully allotriomorphic, as can be seen in Fig. 4.24. A step-isothermal test was performed going from fully allotriomorphic at 780°C to predominantly Widmanstätten at 730°C. As shown in Fig. 4.33, the transformation kinetics at 730°C after partial transformation at 780°C agree well with the kinetics of the complete isothermal transformation at 730°C, although the predominant morphology at the completion of transformation at 730°C is Widmanstätten. As mentioned earlier, the Widmanstätten ferrite forms as *secondary* sideplates growing from

already formed ferrite allotriomorphs. Hence after the step-change to 730°C, the morphology of ferrite changes from smooth-sided allotriomorphs to allotriomorphs with secondary Widmanstätten sideplates, the transformation kinetics following the 730°C isothermal kinetics. Figure 4.34 shows the photomicrograph of a specimen with the same thermal history as that of the test displayed in Fig. 4.33, except that the specimen after step-quenching was transformed at 730°C for 30 seconds and water-quenched. It can be seen that the secondary Widmanstätten ferrite sideplates are originating from allotriomorphs formed at 780°C. It is worth noting here that the photomicrograph shown in Fig. 4.28 (b) has similarities with the one shown in Fig. 4.34, with ferrite sideplates originating from the ferrite allotriomorphs, almost all of which had nucleated at austenite grain boundaries. The comparison of the partial ferrite transformation kinetics at two temperatures with those obtained using isothermal tests having two different predominant morphologies should be considered to be a severe test of experimental additivity.

Several step-quench tests were performed to assess the effect of the amount of equilibrium ferrite (with allotriomorphic morphology) on subsequent lower temperature transformation kinetics. Figure 4.35 shows a plot of isothermal transformation kinetics and stepped-isothermal transformation kinetics measured at two temperatures, 780°C and 730°C. Unlike the step-quench tests described earlier, in this test the transformation at the higher temperature, 780°C, was carried to completion and then the specimen temperature was changed to 730°C. It is evident that the kinetics at the lower temperature after step-quenching are slower than those obtained isothermally at that temperature. In this particular case, soft impingement of carbon diffusion fields is believed to have reduced the amount of Widmanstätten ferrite sideplates formed and hence reduced the overall transformation kinetics. This was confirmed metallographically by a qualitative comparison of the relative amounts of Widmanstätten ferrite sideplates formed in this test (Fig. 4.35) with

that formed in an isothermal transformation test at 730°C. The fraction of Widmanstätten ferrite sideplates was considerably less and the ferrite morphology was mostly allotriomorphic in the former case.

The effect on the lower temperature transformation kinetics of equilibration of the ferrite-austenite phase boundaries after formation of equilibrium amount of ferrite at a higher temperature (780°C) was determined. Specimens were held at 780°C for an additional time of 15 minutes after completion of the isothermal transformation at 780°C. This equilibration treatment was undertaken to examine whether α/γ interfaces stabilize and if so, to determine the effect of the stabilization on subsequent lower temperature transformation kinetics. As shown in Fig. 4.36, the transformation kinetics at the lower temperature are much slower indicating that the transformation event at the second temperature is affected by the stabilization of the α/γ interfaces at 780°C, making the transformation path dependent. Metallographic examination of a specimen having the same stepped thermal history as that shown in Fig. 4.36, except that the specimen was water-quenched after partial transformation at 730°C, revealed a significant morphological difference from the other stepped-isothermal test specimens. As can be seen from the photomicrograph shown in Fig. 4.37, the morphology of most of the ferrite formed is allotriomorphic with very little Widmanstätten ferrite visible. This observation is consistent with the findings of Townsend and Kirkaldy[61], who made a detailed investigation of Widmanstätten ferrite formation in three hypoeutectoid plain-carbon steels with 0.235, 0.385 and 0.405 wt.% carbon. The authors equilibrated the α/γ boundaries obtained through a series of decarburization experiments for various times. The results of these experiments showed a smaller number of α/γ interface instabilities and fewer Widmanstätten plates forming in specimens equilibrated for sufficiently long times. Based on these observations, they concluded that ferrite-austenite interfaces which are formed and equilibrated for a sufficient time are appreciably more stable than freshly formed ones. In addition, the equilibration results in the total free energy of the

system reaching a minimum and α/γ boundaries attaining a low surface energy. This explanation is consistent with observations made in the present research (Fig. 4.36 and Fig. 4.37).

4.6 1040 Grade Steel

This steel was used to examine the effect of higher carbon content on the isothermal and step-isothermal transformation kinetics, as determined by the diametral dilatometry tests.

4.6.1 Isothermal Transformation Kinetics

Figure 4.38 shows the results of isothermal tests performed at three different temperatures. The normalized ferrite fraction for each temperature has been converted to true fraction using the iron-carbon equilibrium diagram. From the Figure it can be seen that as temperature decreases, the amount of ferrite formed and the austenite-to-proeutectoid ferrite transformation rate increase. Although the lowest transformation temperature of 714°C falls below $T_{A_{c1}}$, metallographic examination of specimens water-quenched after completion of transformation did not indicate the presence of any pearlite. The ferrite morphology obtained at the three isothermal test temperatures, 714°C, 723°C and 735°C was observed metallographically to be that of grain boundary allotriomorphs.

Values of the Avrami equation parameters, n and lnb, characterizing the isothermal transformation kinetics are shown in Table 4.4. As previously observed in the research on the 1010 and 1020 steels, the value of the parameter n is a maximum for the highest temperature (733°C) studied and can be attributed to continued nucleation during the early stages of transformation. The n value is reasonably constant for the rest of the temperatures. The isothermal start time t_{st} decreases with transformation temperature.

A comparison was made of the n and b parameters obtained from the Avrami analysis of the isothermal proeutectoid ferrite transformation kinetics for all three steels (1010, 1020 and 1040) studied in this investigation. Figure 4.39 shows the results of this comparison for the n values plotted as a function of the isothermal transformation temperature. Within each

grade of steel, the value of n remains almost constant except for the higher temperatures, where it increases significantly especially for the 1010 grade. For the 1020 steel, the n value is not significantly affected by the change in morphology. For all three steels, the n value remains almost constant over the temperature range studied. A constant n value signifies a common nucleation and growth condition, although the average austenite grain size for each steel grade was different.

The b parameter is shown in Fig. 4.40 for each steel studied and increases in each steel with increasing temperature. This increase is significantly greater for the 1010 steel. No systematic variation of b with carbon content was evident. However this could be due to the difference in austenite grain size of each steel.

4.6.2 Stepped Isothermal Transformation Kinetics

A number of step-down quench tests were performed to assess the additivity of the proeutectoid ferrite transformation in a higher carbon steel. Figure 4.41 shows the complete isothermal transformation results at $735°C$ and $714°C$, and the partial, stepped-isothermal transformation results, compared on the basis of true fraction transformed. The data was corrected for thermal contraction. The agreement between the stepped-isothermal transformation kinetics and the isothermal transformation kinetics at the second temperature is good. As mentioned in the earlier section, the specimens water-quenched after completion of transformation at the two temperatures showed the ferrite morphology to be predominantly grain boundary allotriomorphs. This was also observed for the specimen water-quenched after completion of the stepped-isothermal transformation, as shown in the photomicrograph in Fig. 4.42. Pearlite was not observed in the stepped-isothermal test specimen. Compared to the 1010 grade tests, the smaller γ grain size in the 1040 specimens would encourage soft-impingement earlier in the transformation for the same fraction of ferrite transformed. This however did not affect the experimental additivity observed for the ferrite transformation, as indicated by the results of the stepped-isothermal test.

Steel Grade	Experimental $T_{A_{c_1}}$ (°C)	Calculated $T_{A_{c_1}}$ (°C)	Experimental $T_{A_{c_3}}$ (°C)	Calculated $T_{A_{c_3}}$ (°C)	Austenite Grain Size (ASTM No.)
1010	721	719.5	859	857.5	5-6
1020	723	718.5	817	812.2	1-2
1040	725	722.5	780	779.8	8-9

Table 4.1- Experimental and calculated $T_{A_{c_1}}$ and $T_{A_{c_3}}$ temperatures and the austenite grain size of the steel grades used in the study.

Isothermal Transformation Temperature (°C)	Transformation Start Time Relative to $T_{A_{c_3}}$ (s)	Avrami Parameter n	Avrami Parameter lnb
744	0.9	1.08	-1.80
764	1.2	0.95	-1.87
784	1.8	0.97	-2.16
803	2.8	1.21	-3.72
812	3.9	1.75	-5.09

Table 4.2- Values of t_{s1}, n and lnb calculated from Avrami characterization of the isothermal transformation data for the 1010 steel.

Isothermal Transformation Temperature (°C)	Transformation Start Time Relative to $T_{A_{c3}}$ (s)	Avrami Parameter n	Avrami Parameter lnb
730	3.7	0.79	-3.24
740	5.1	0.78	-3.83
760	6.0	0.73	-3.61
780	8.1	1.11	-5.03

Table 4.3- Values of t_{s1}, n and lnb calculated from Avrami characterization of the isothermal transformation data for the 1020 steel.

Isothermal Transformation Temperature (°C)	Transformation Start Time Relative to $T_{A_{c3}}$ (s)	Avrami Parameter n	Avrami Parameter lnb
714	3.5	0.77	-2.61
718	4.3	0.67	-2.87
723	6.8	0.65	-2.90
729	7.7	0.71	-3.25
735	8.3	0.91	-4.24

Table 4.4- Values of t_{s1}, n and lnb calculated from Avrami characterization of the isothermal transformation data for the 1040 steel.

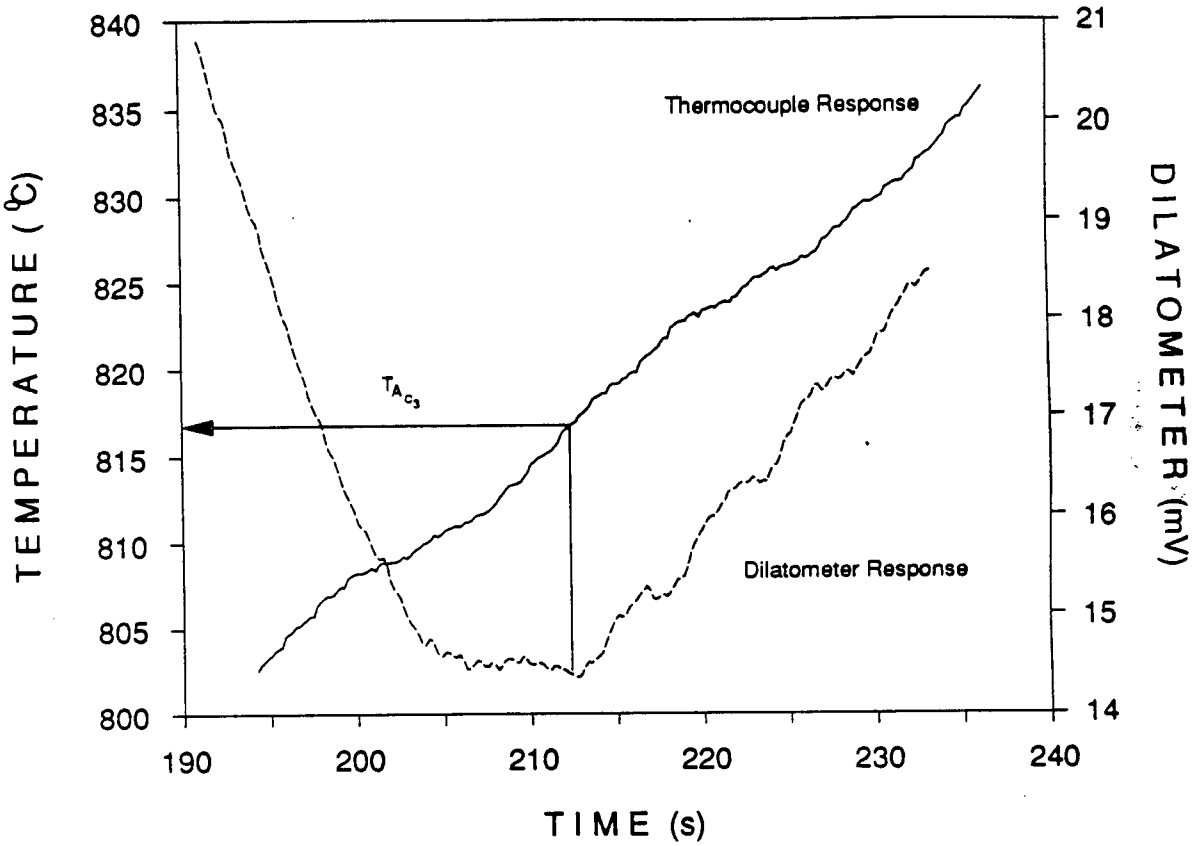

Fig. 4.1 - Thermocouple and dilatometer response for the 1020 steel heated at $0.75°C/s$ to estimate the $T_{A_{c3}}$ temperature.

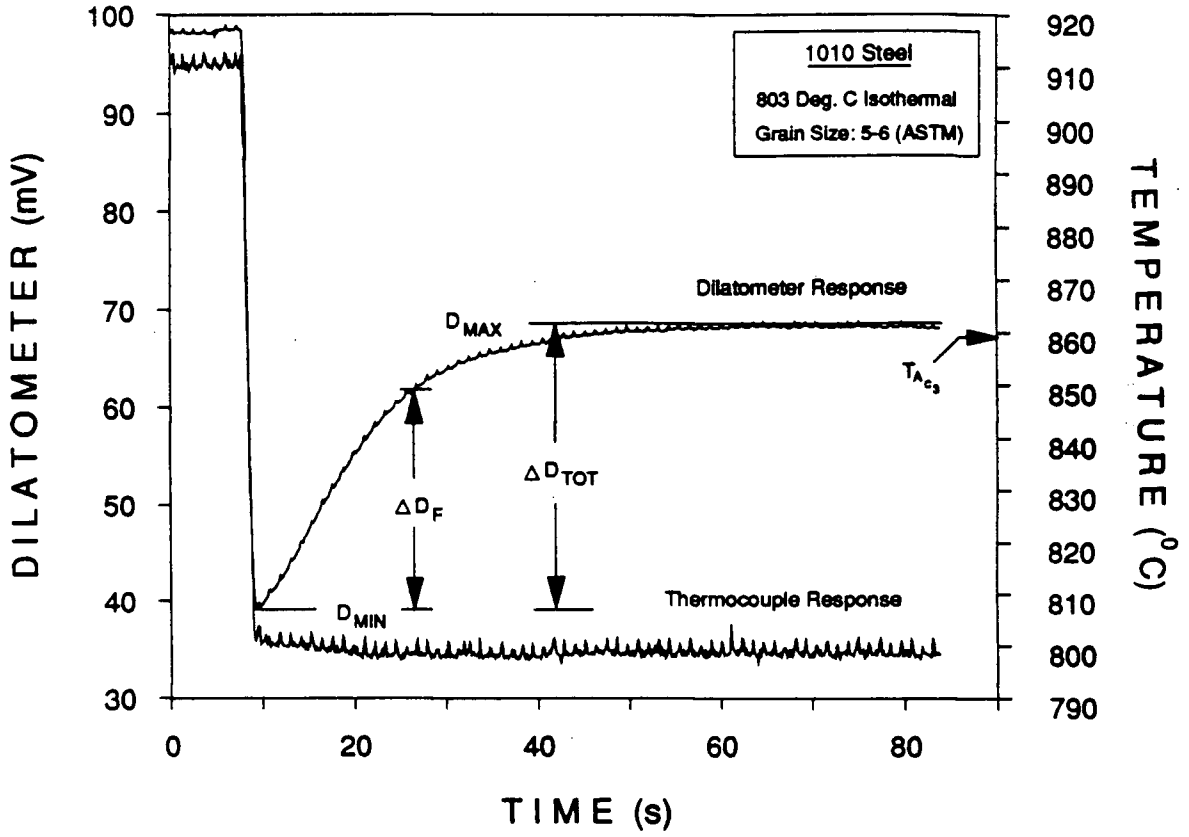

Fig. 4.2 - Dilatometer and temperature response is shown for the 1010 steel isothermally transformed at 803°*C*.

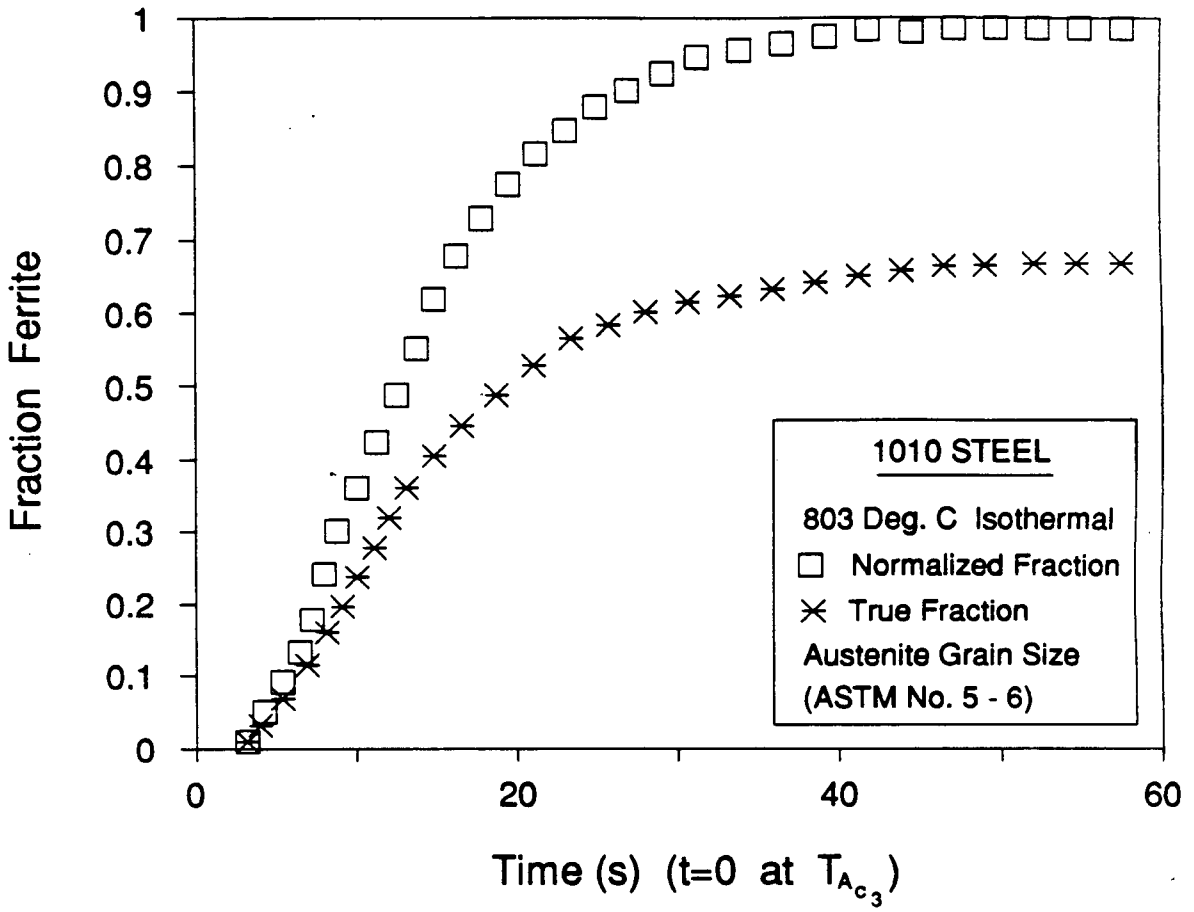

Fig. 4.3 - Normalized and true fraction of ferrite formed isothermally at 803°*C* in the 1010 steel.

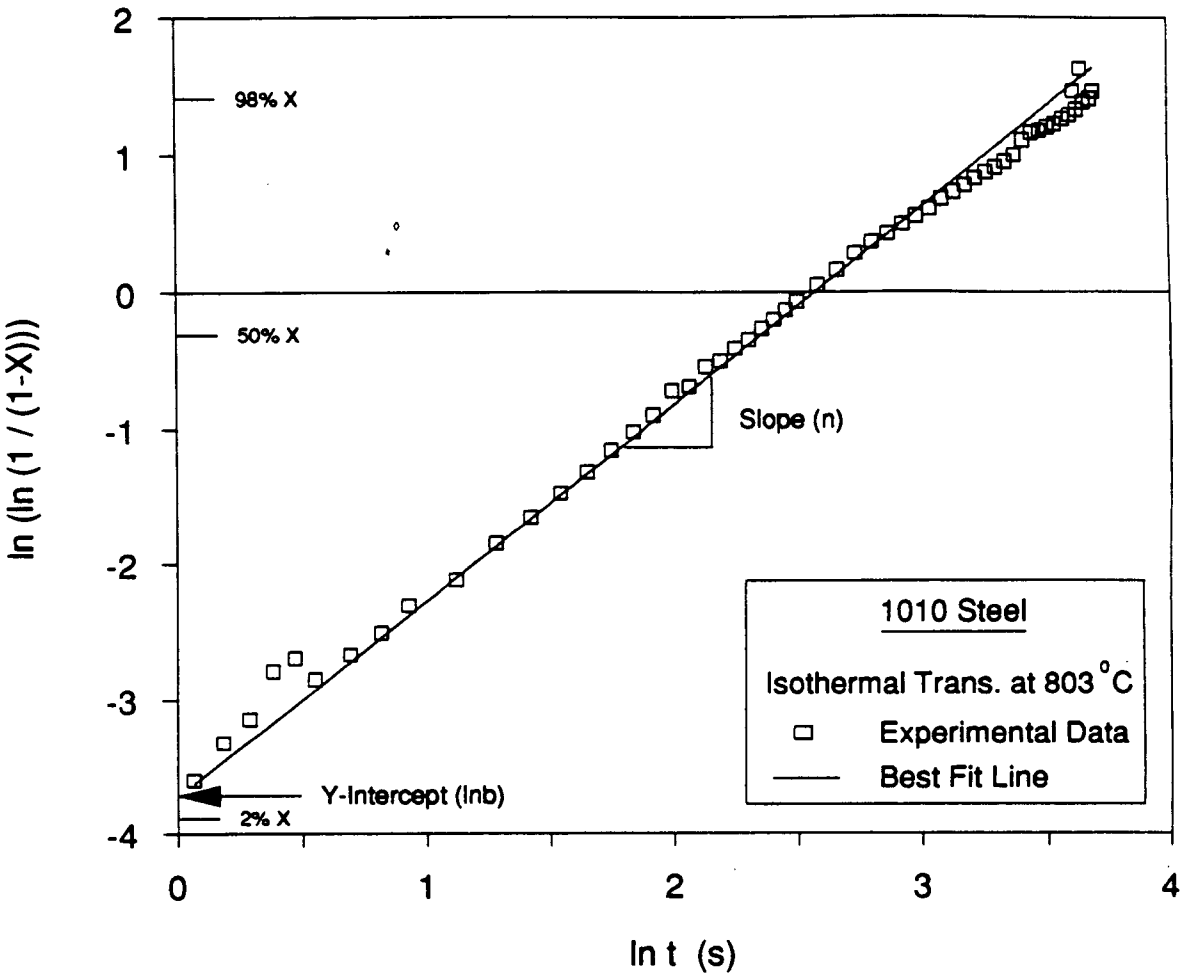

Fig. 4.4 - Linearization of the Avrami equation for determining the constants n and b from the isothermal transformation kinetics obtained at 803°C for the 1010 steel.

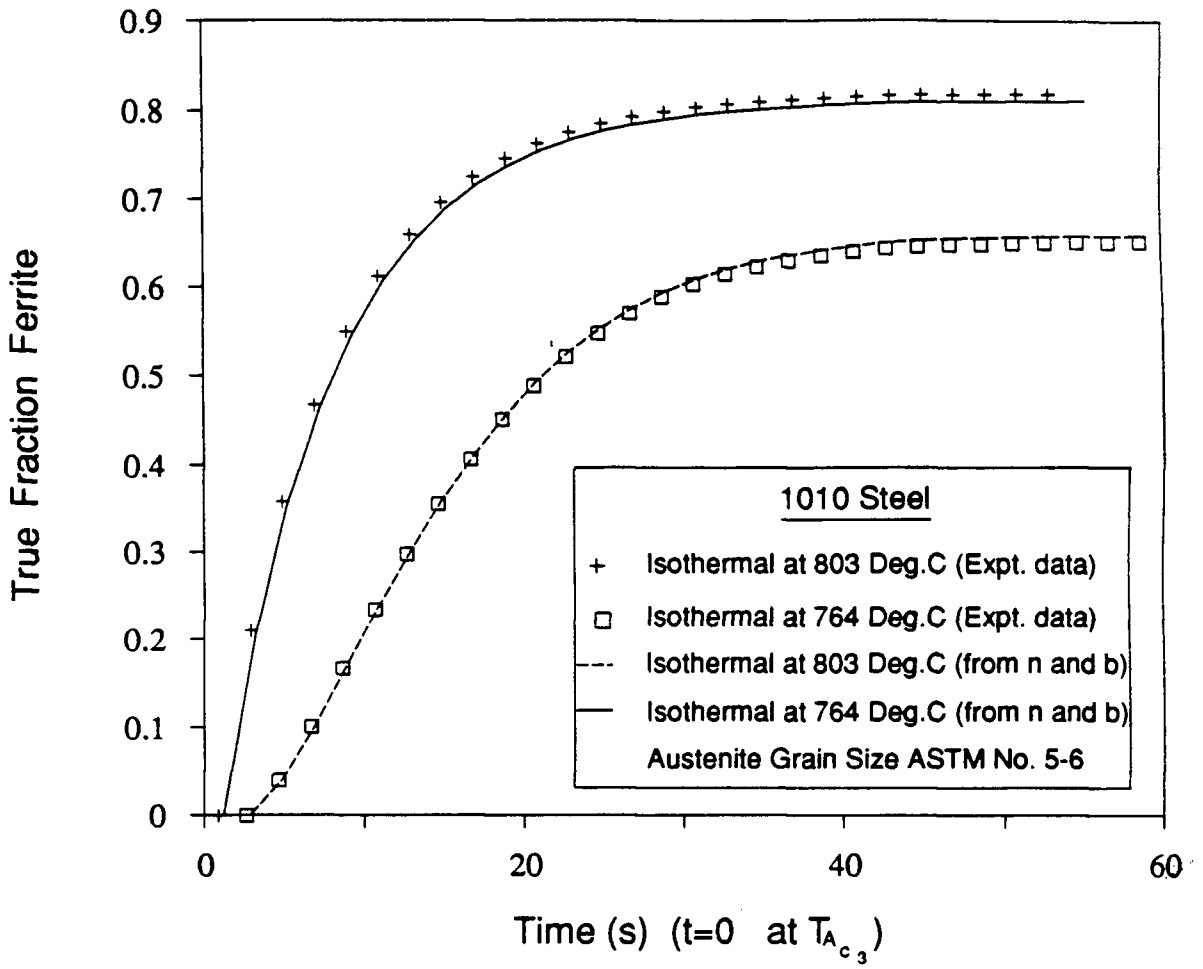

Fig. 4.5 - Comparison of experimental and predicted austenite to ferrite isothermal transformation kinetics obtained at 803°*C* and 764°*C* for the 1010 steel.

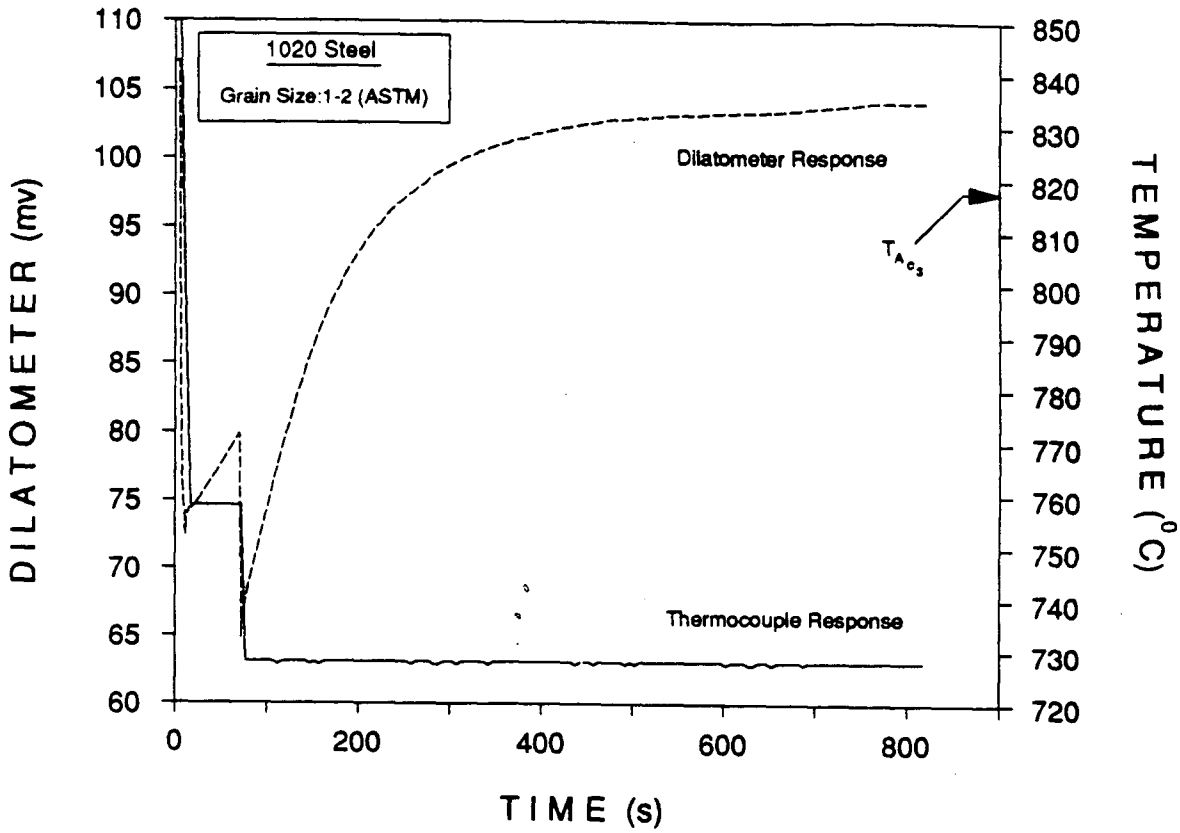

Fig. 4.6 - Typical thermal history and dilatometer response in a stepped-isothermal transformation test.

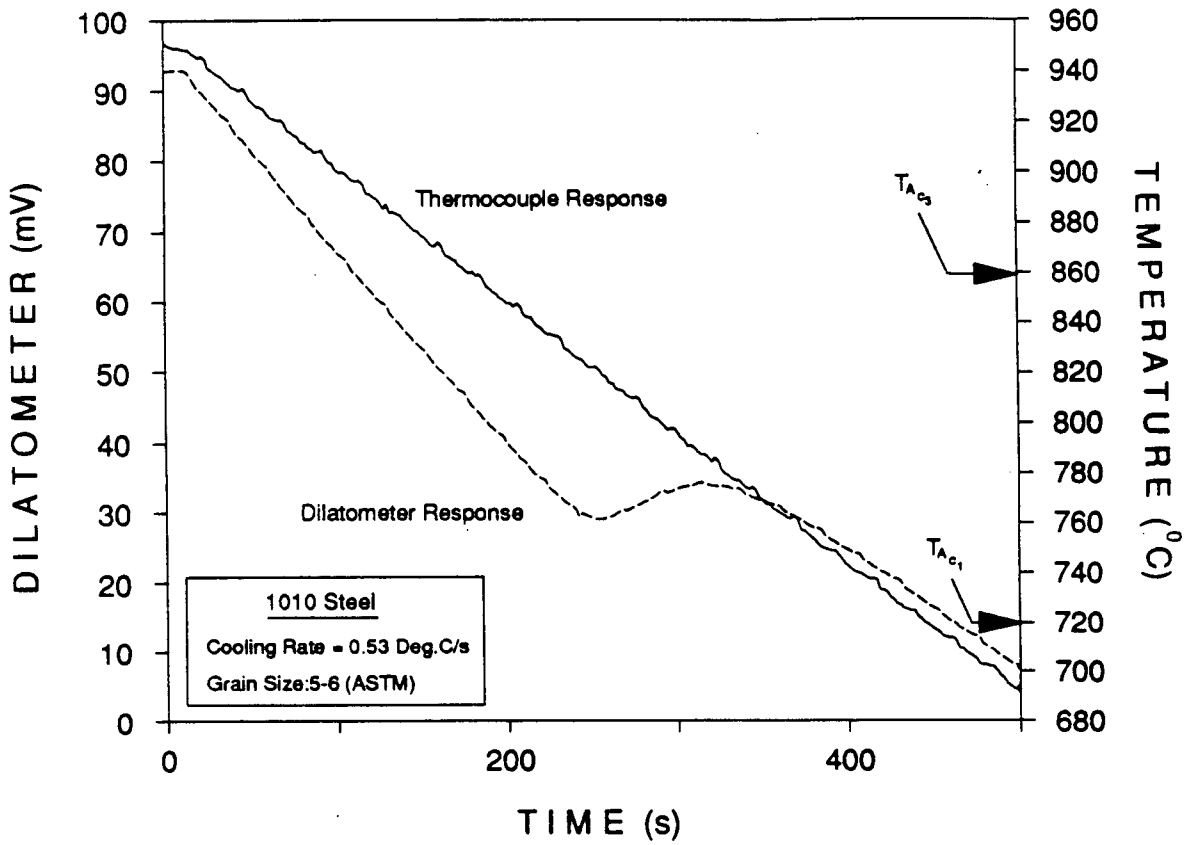

Fig. 4.7 - Typical thermal history and dilatometer response in a 0.53°*C/s* continuous-cooling transformation test on the 1010 steel.

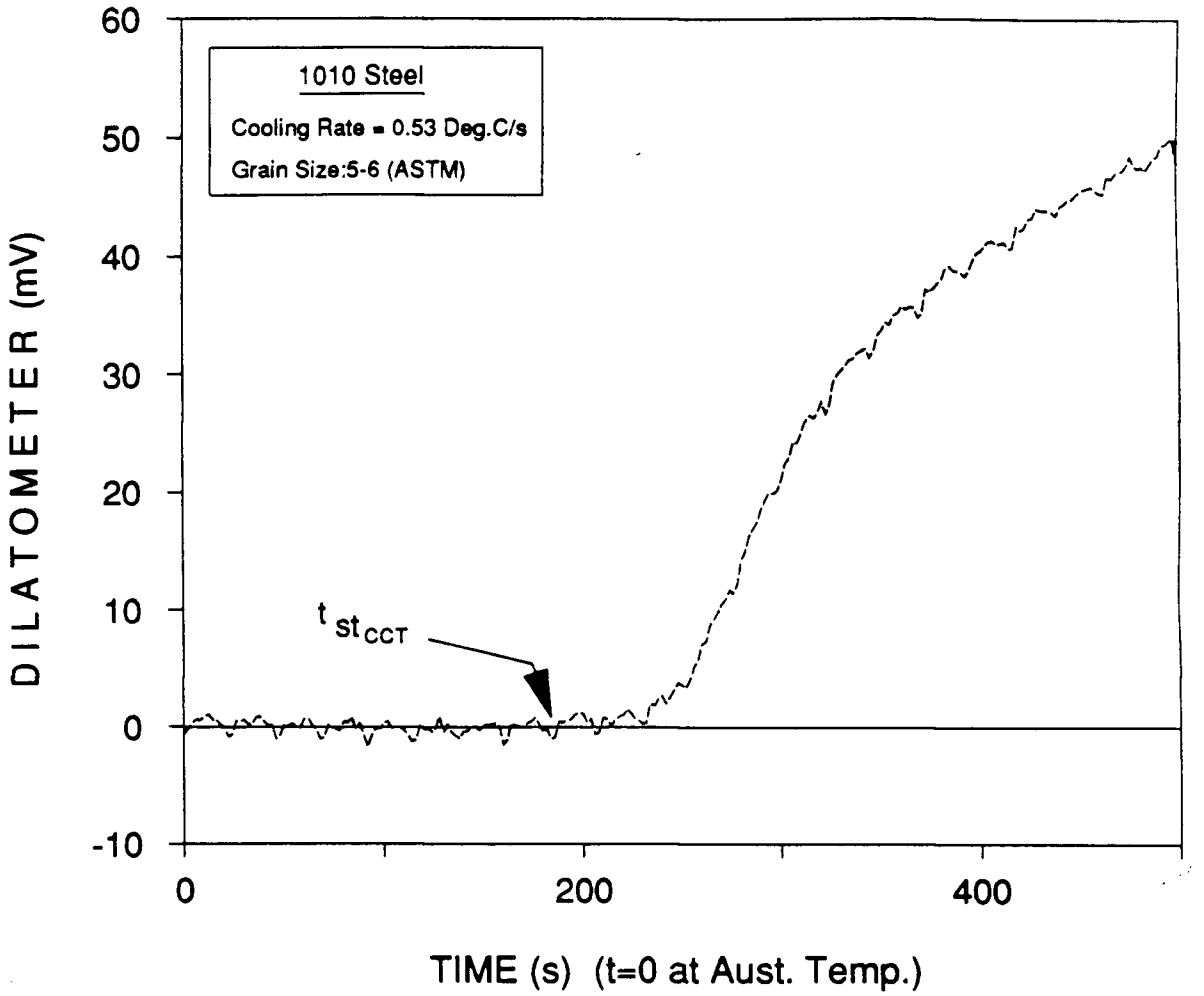

Fig. 4.8 - Measured specimen dilation minus dilation predicted due to temperature change, plotted against total time from a continuous-cooling transformation test.

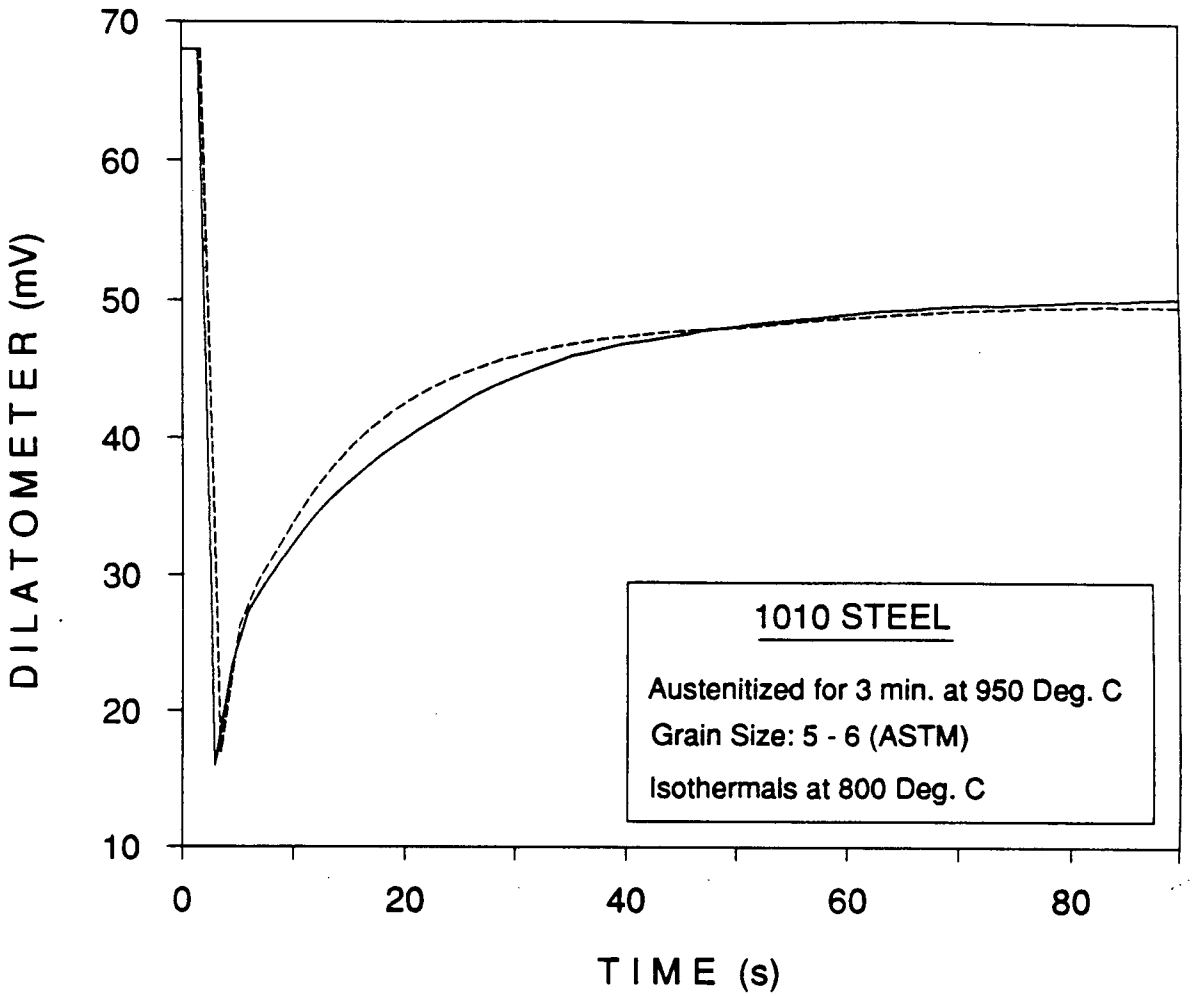

Fig. 4.9 - Dilatometer response plotted as a function of time for two isothermal transformation tests at 800°C for the 1010 steel.

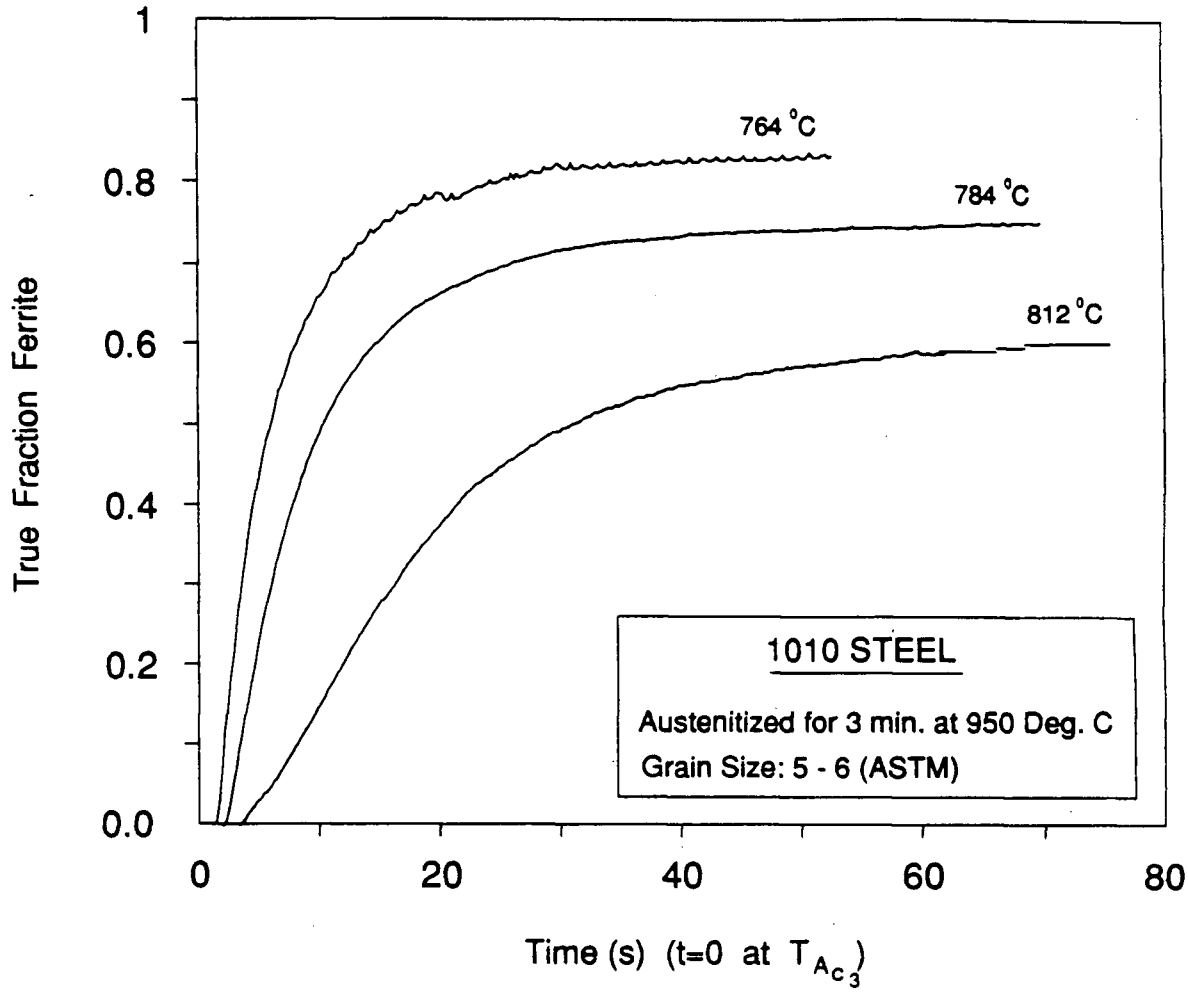

Fig. 4.10 - Typical isothermal transformation data for the 1010 steel.

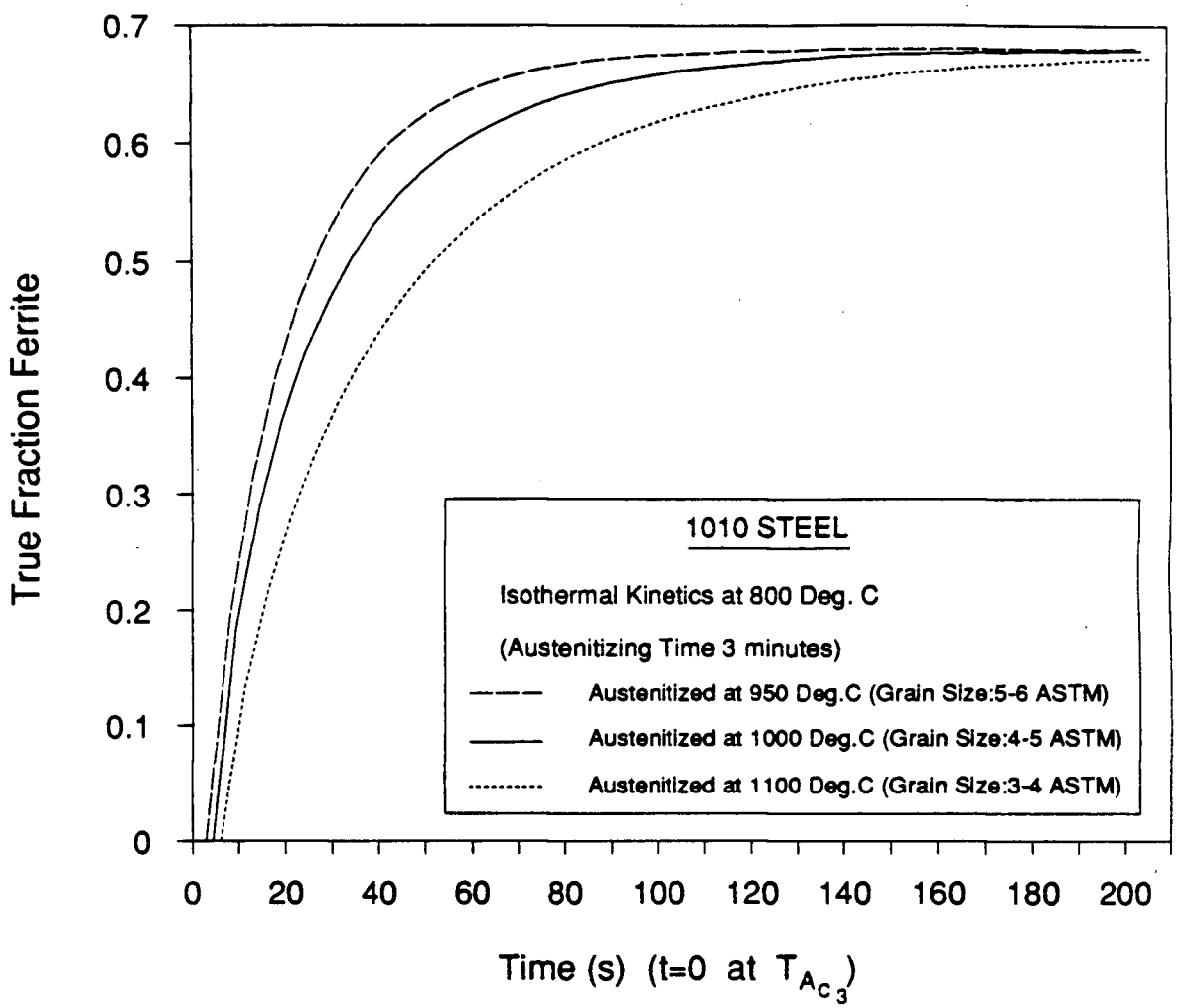

Fig. 4.11 - Effect of austenitizing temperature on isothermal transformation kinetics at 800°*C* for the 1010 steel.

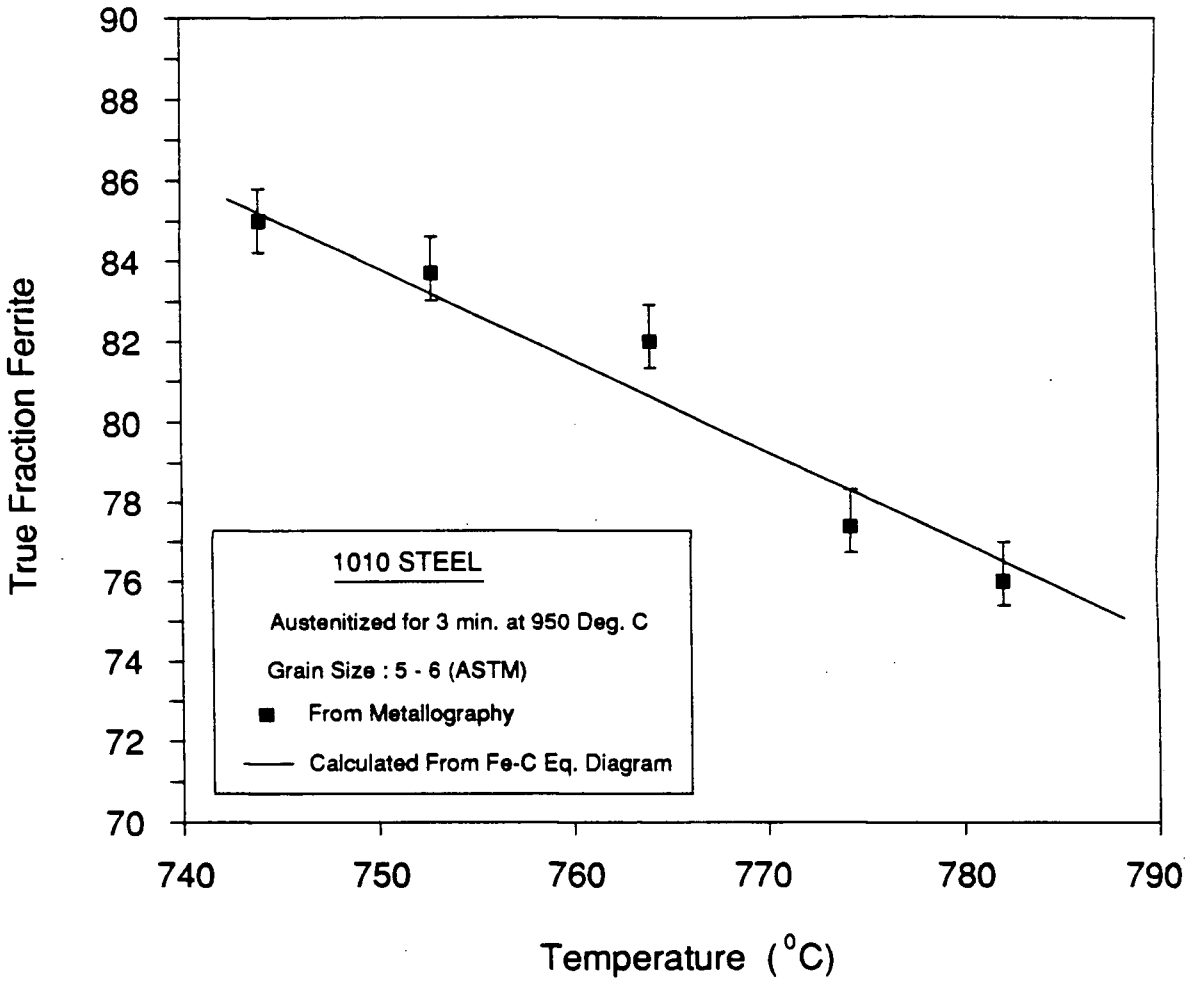

Fig. 4.12 - Comparison of experimental and calculated ferrite fraction plotted as a function of isothermal transformation temperature for the 1010 steel.

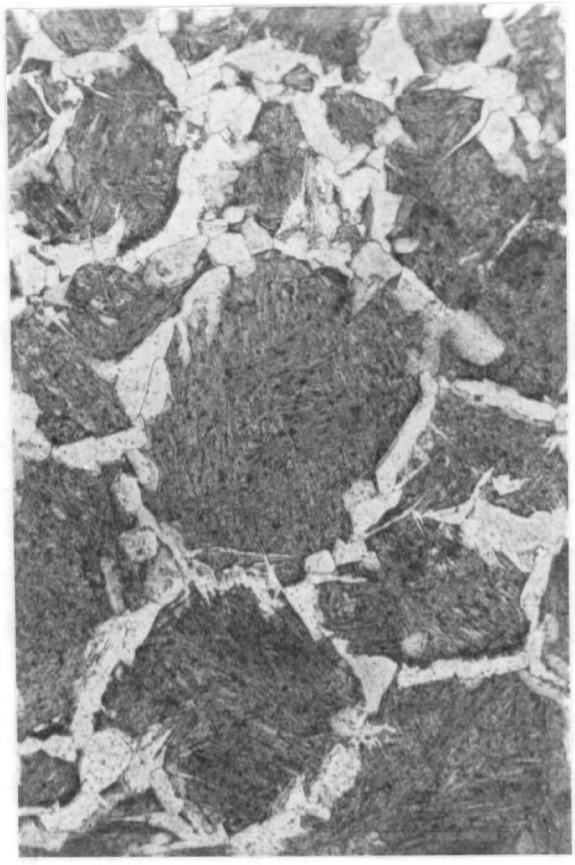

Fig. 4.13 - Photomicrograph of 1010 steel partially transformed at 812°*C* and water quenched, showing proeutectoid ferrite nucleating at the austenite grain boundaries (Magnification 440 times).

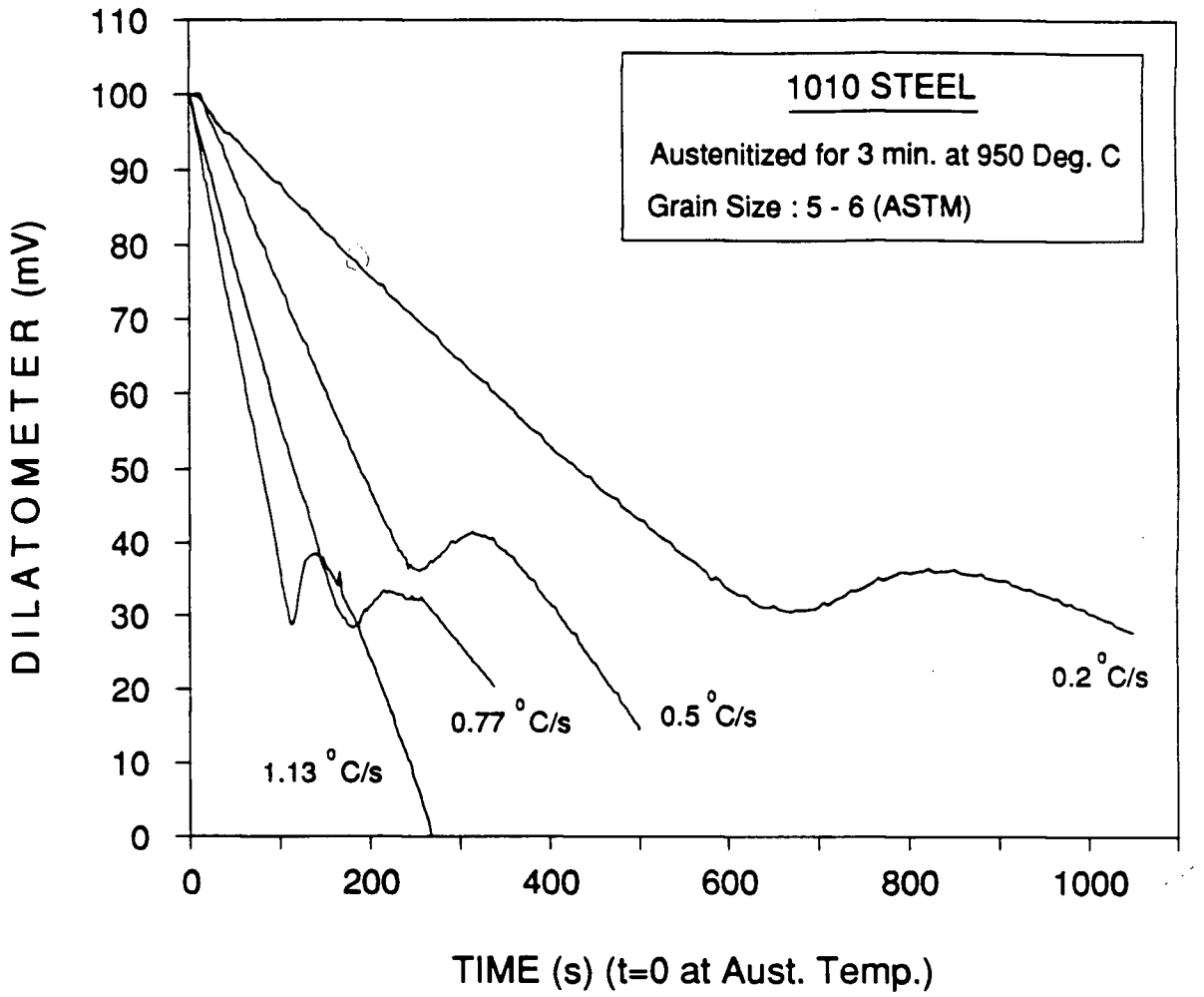

Fig. 4.14 - Typical dilatometer response plotted as a function of time for the continuous-cooling transformation in 1010 steel.

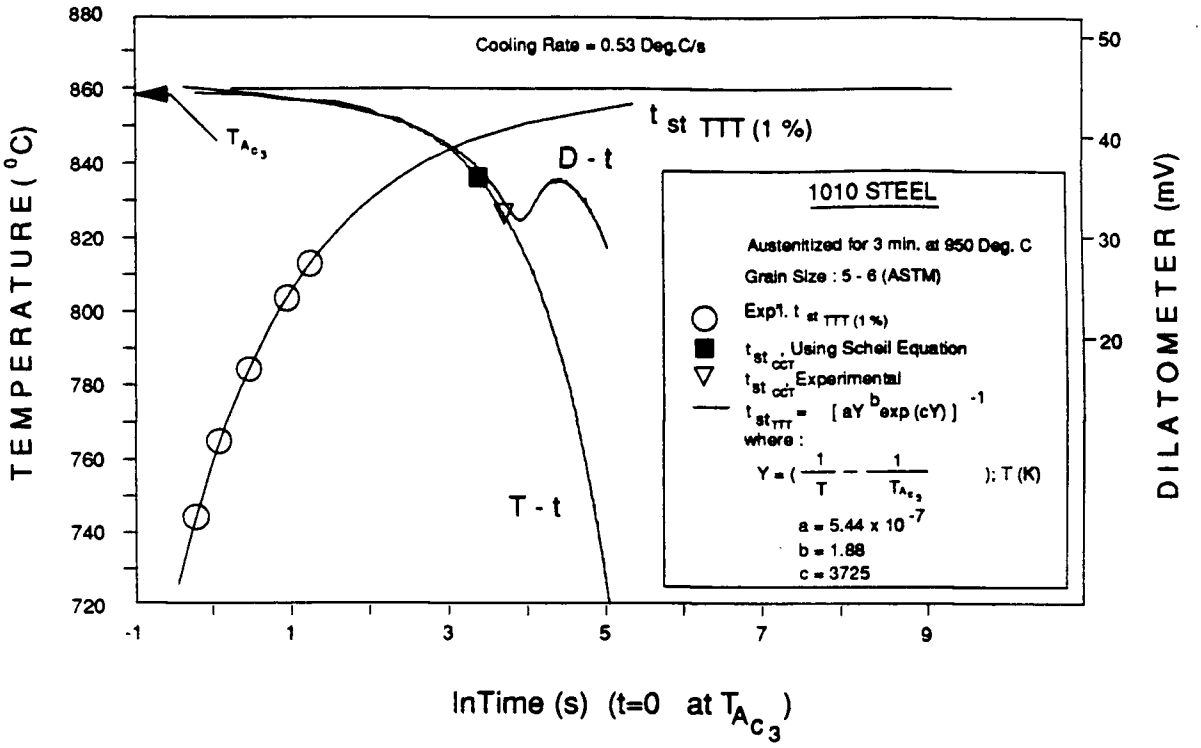

Fig. 4.15 - TTT and CCT data for the 1010 steel showing an assessment of t_{st} for CCT using the Scheil equation.

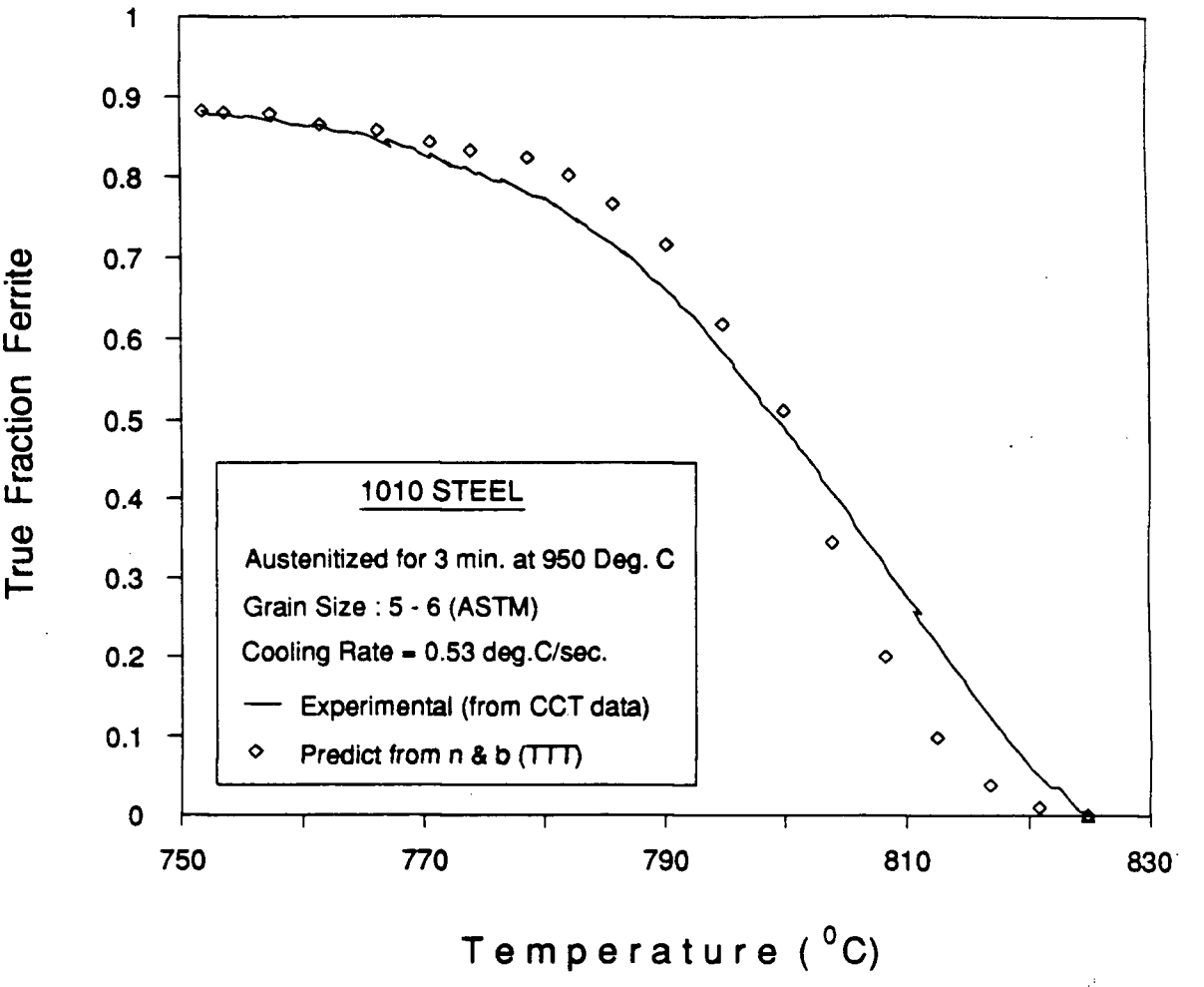

Fig. 4.16 - Comparison of experimental and predicted continuous-cooling transformation kinetics for the 1010 steel.

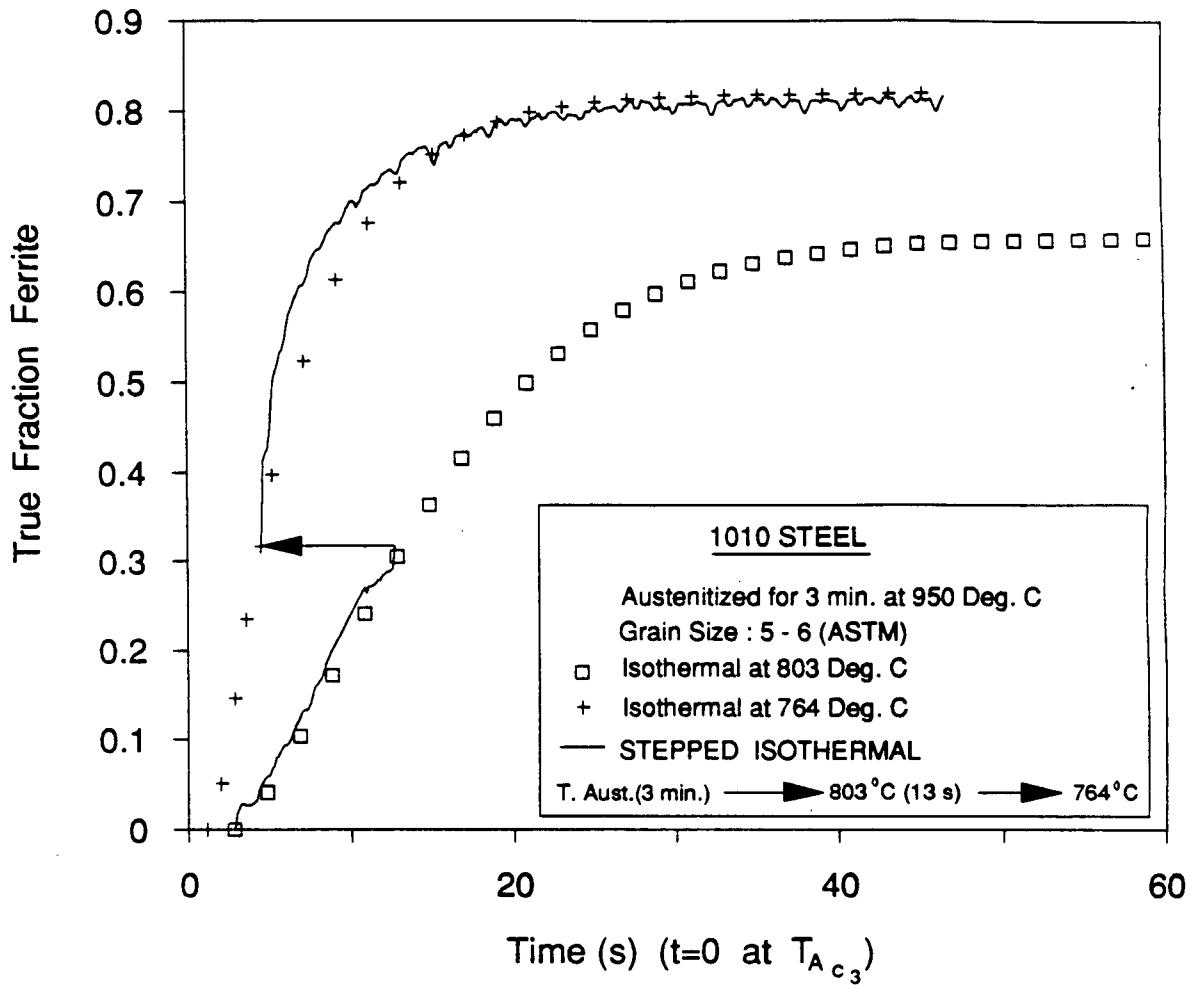

Fig. 4.17 - Experimental isothermal and step-down test data for 1010 steel.

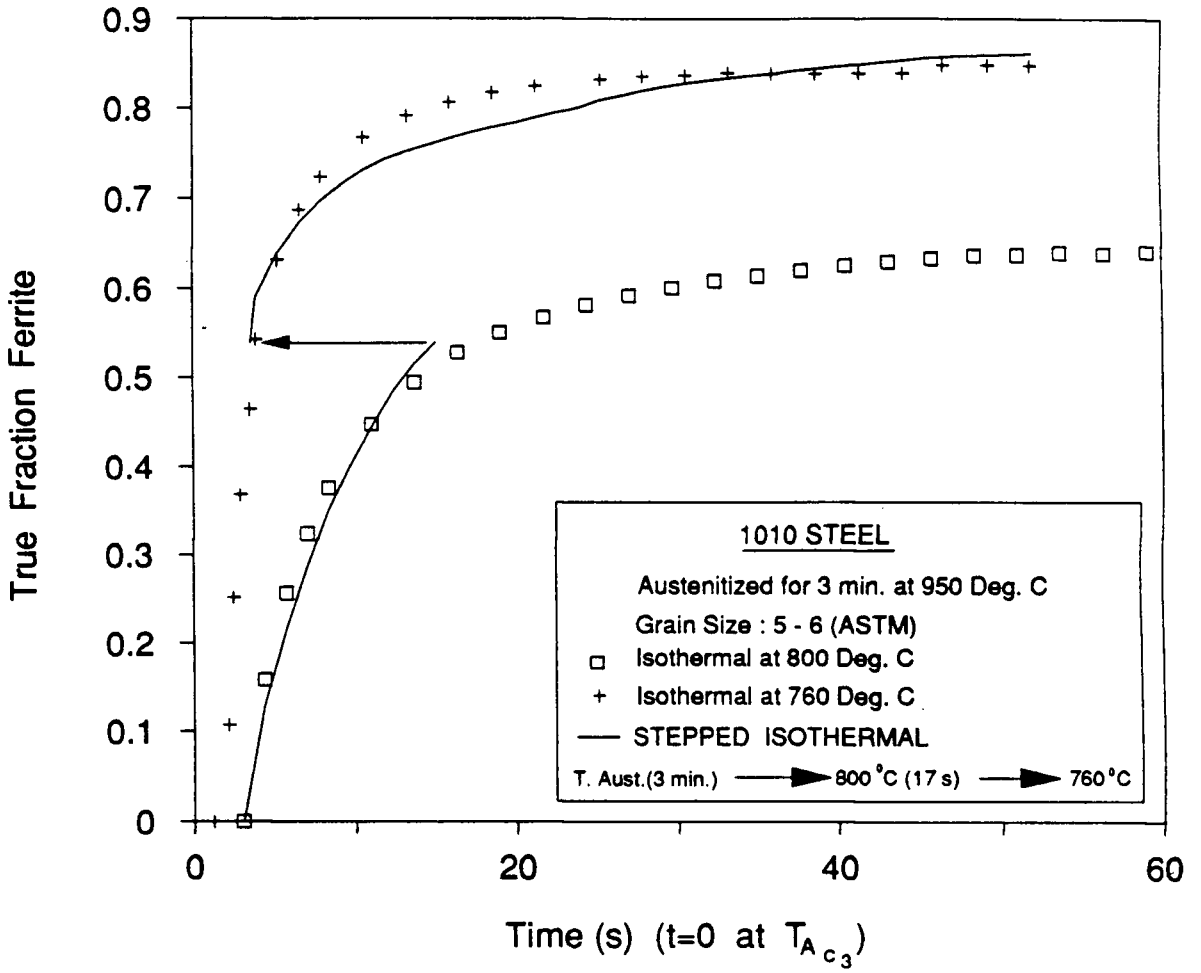

Fig. 4.18 - Experimental isothermal and step-down test data for 1010 steel.

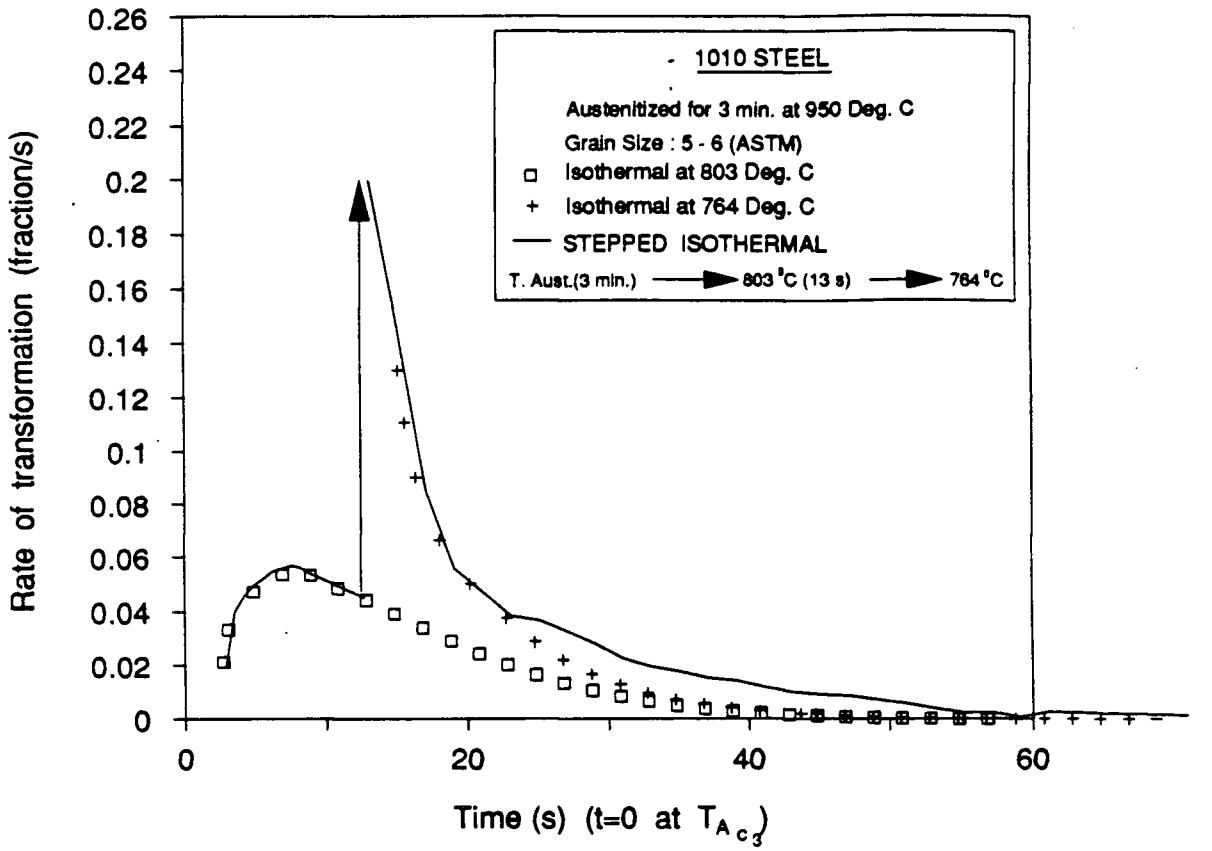

Fig. 4.19 - Experimental isothermal and stepped-isothermal transformation rate as a function of transformation time for the step-down test for 1010 steel.

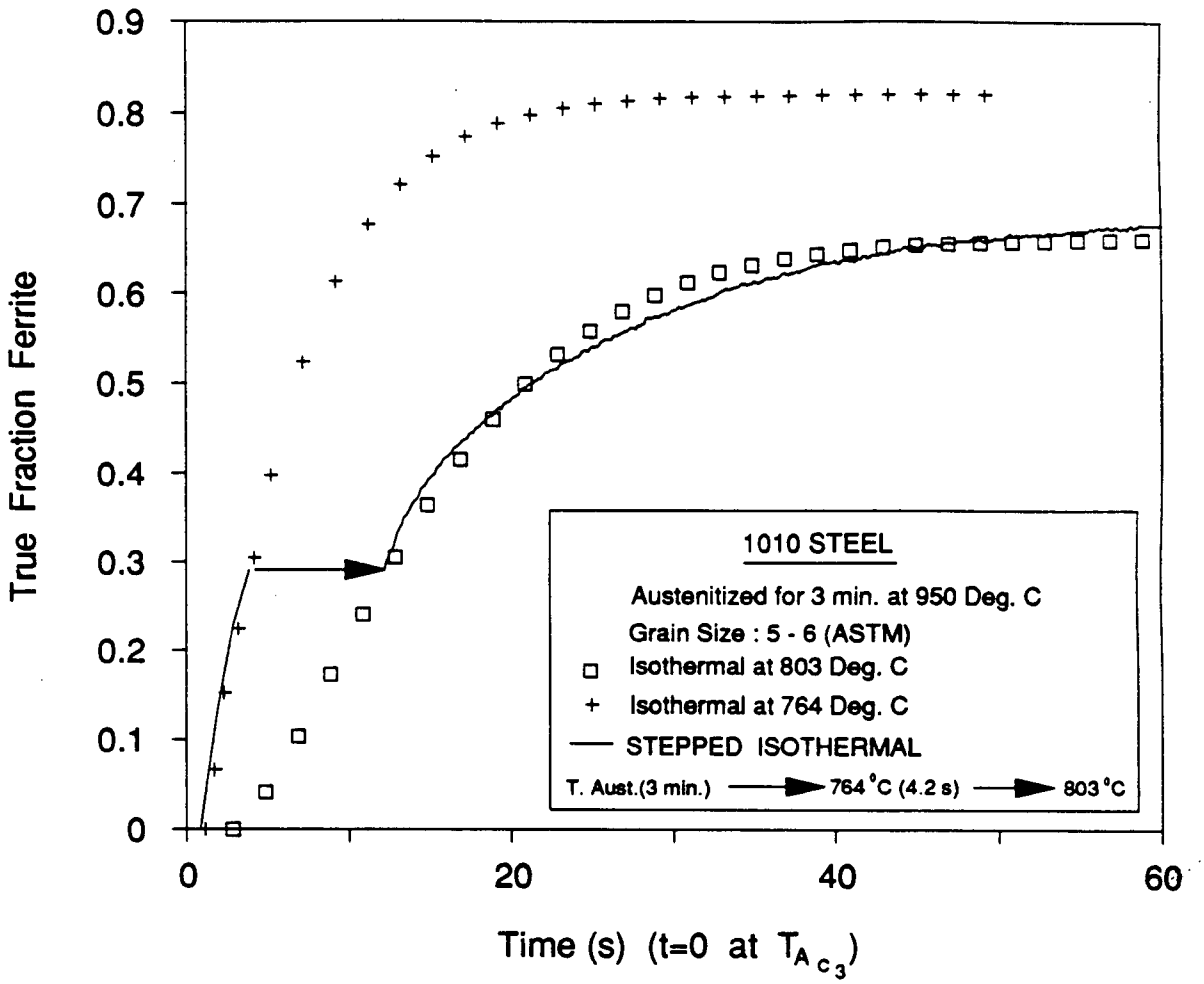

Fig. 4.20 - Experimental isothermal and step-up test data for 1010 steel.

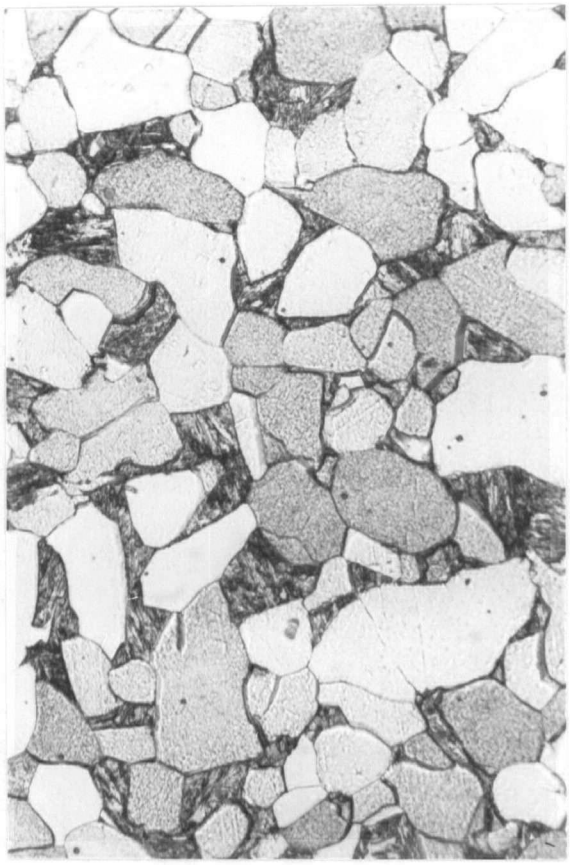

Fig. 4.21 - Photomicrograph of 1010 steel transformed partially at 803°*C*, step-quenched to 764°*C* and transformed completely before being water-quenched, showing polygonal ferrite morphology. (Magnification 440 times).

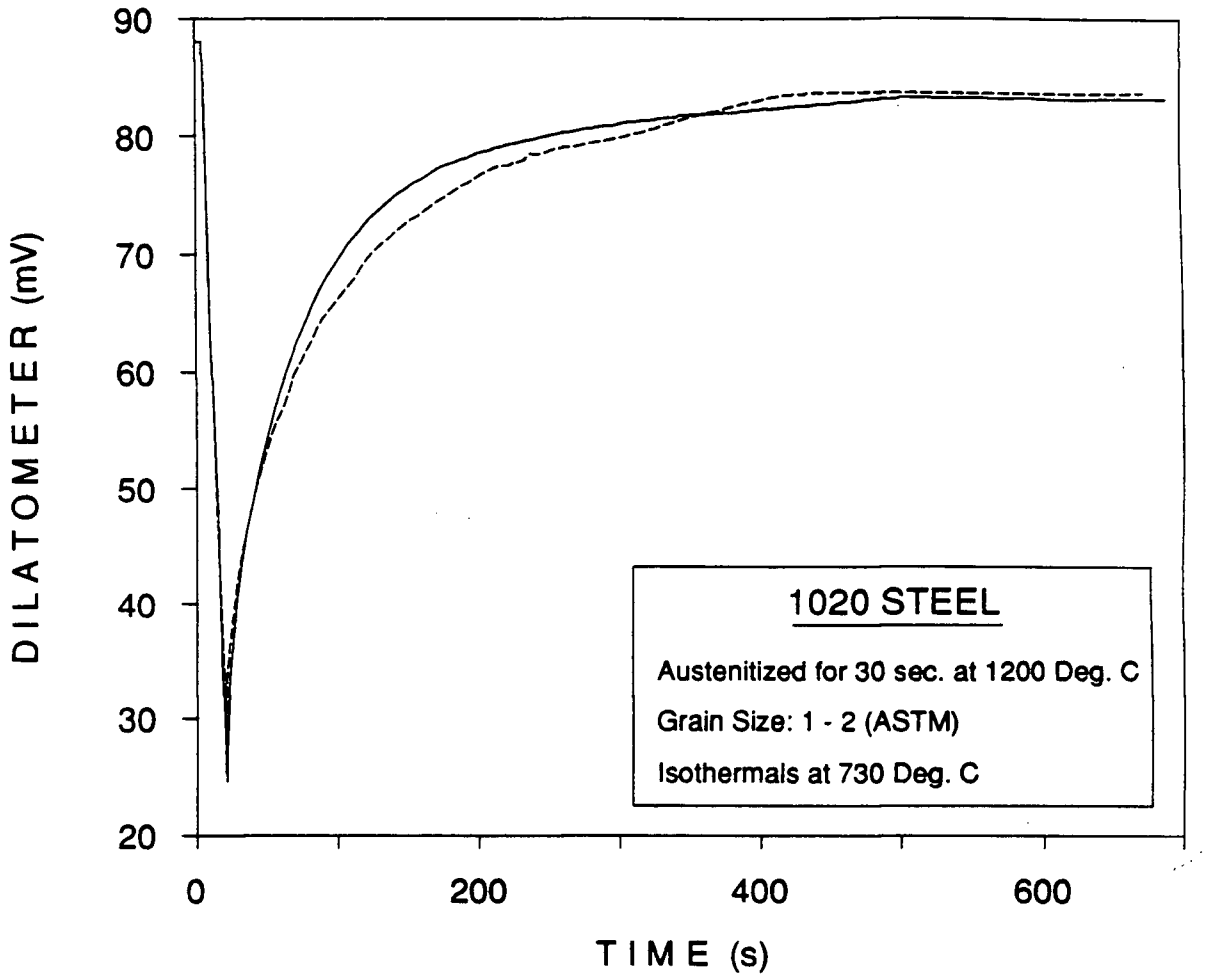

Fig. 4.22 - Dilatometer response plotted as a function of time for two isothermal transformation tests at 730°C on the 1020 steel.

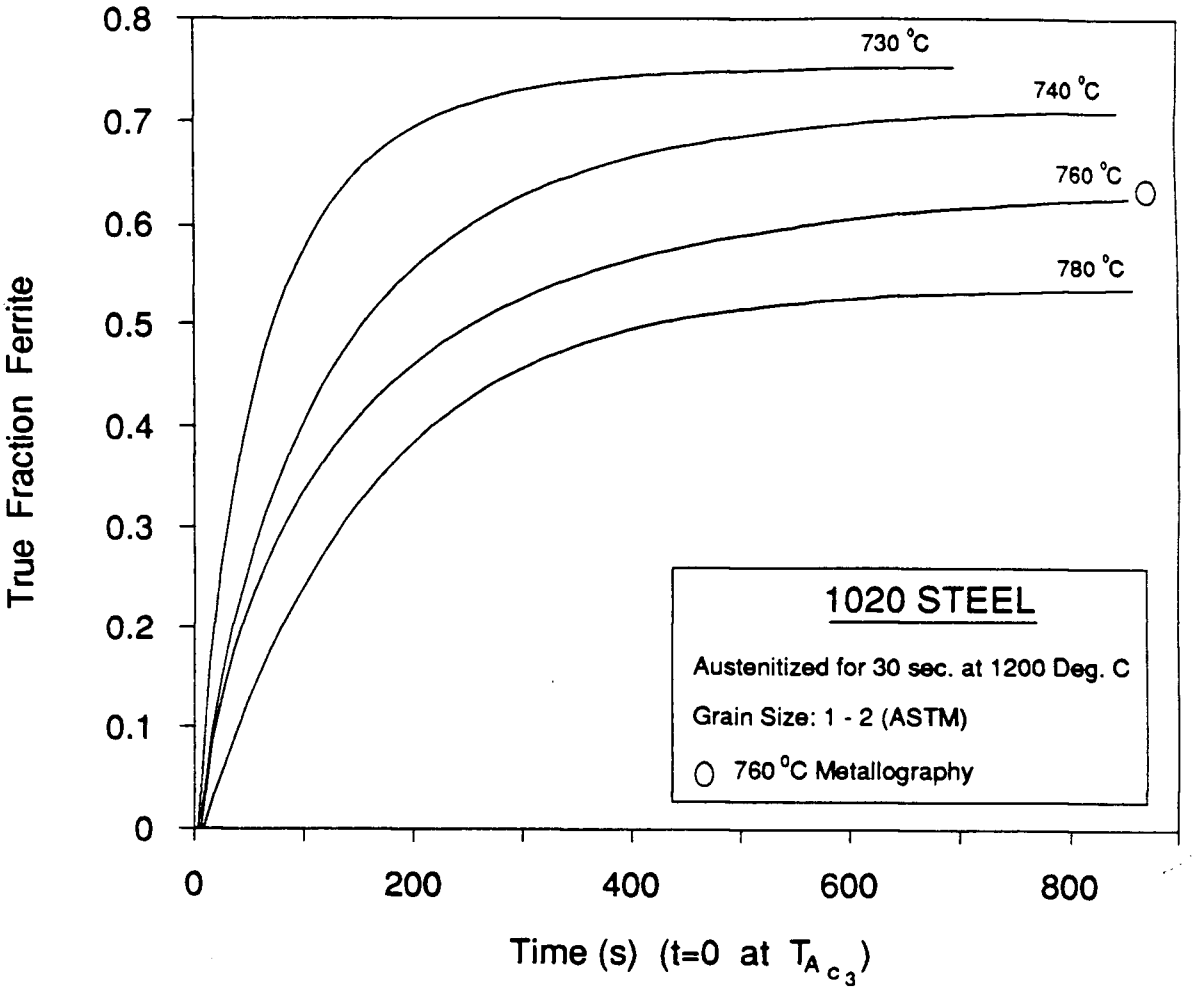

Fig. 4.23 - Typical isothermal transformation data for the 1020 steel.

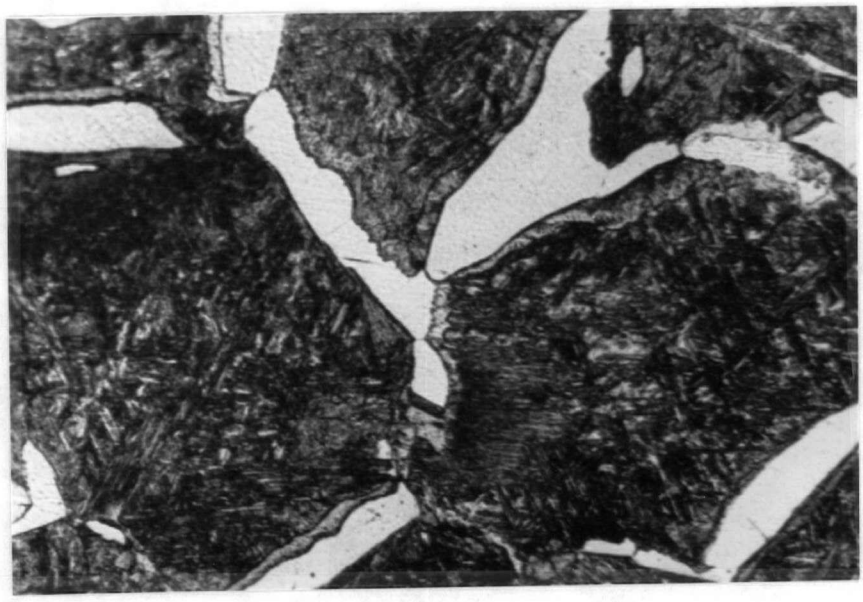

Fig. 4.24 - Photomicrograph of 1020 steel partially transformed at 780°*C* and water quenched, showing a predominantly polygonal ferrite morphology (Magnification 440 times).

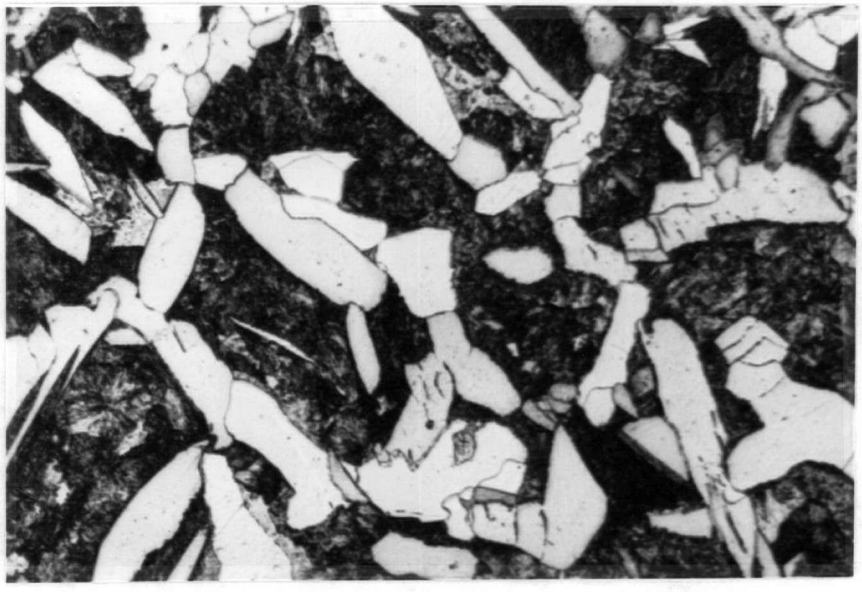

Fig. 4.25 - Typical photomicrograph of 1020 steel partially transformed at 760°*C* and water quenched, showing predominantly polygonal morphology of proeutectoid ferrite with some Widmanstätten ferrite sideplates (Magnification 176 times).

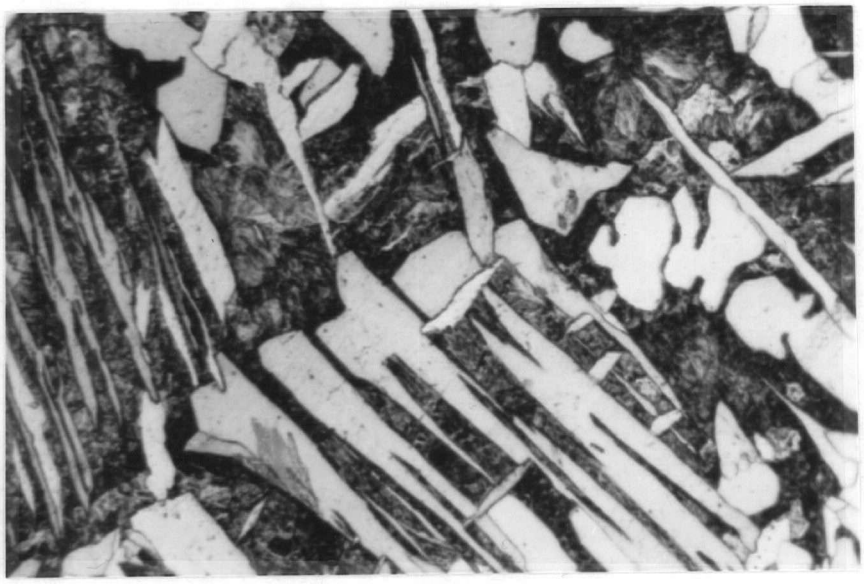

Fig. 4.26 - Typical photomicrograph of 1020 steel partially transformed at 740°*C* and water quenched, showing a mixed polygonal plus Widmanstätten ferrite microstructure (Magnification 176 times).

Fig. 4.27 - Typical photomicrograph of 1020 steel partially transformed at 730°*C* and water quenched, showing a greater fraction of Widmanstätten ferrite (Magnification 176 times).

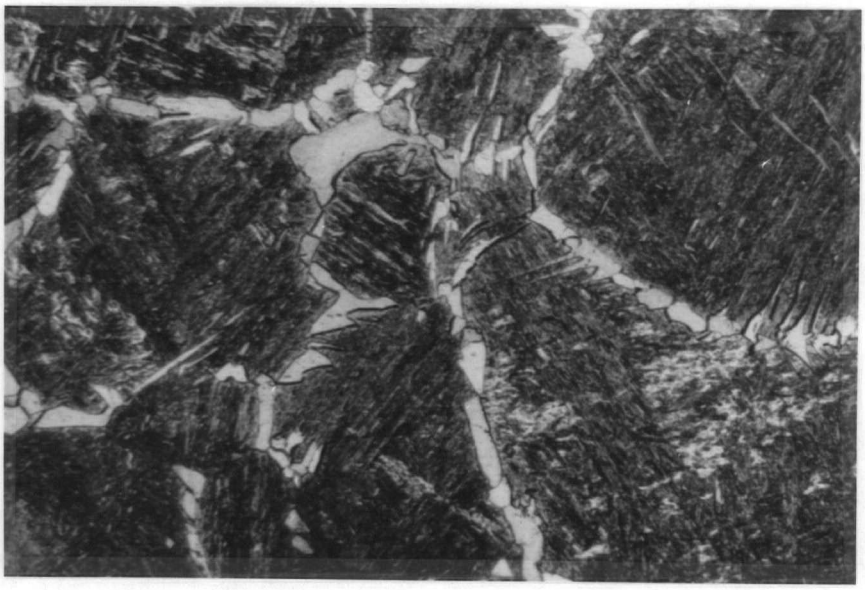

(a)

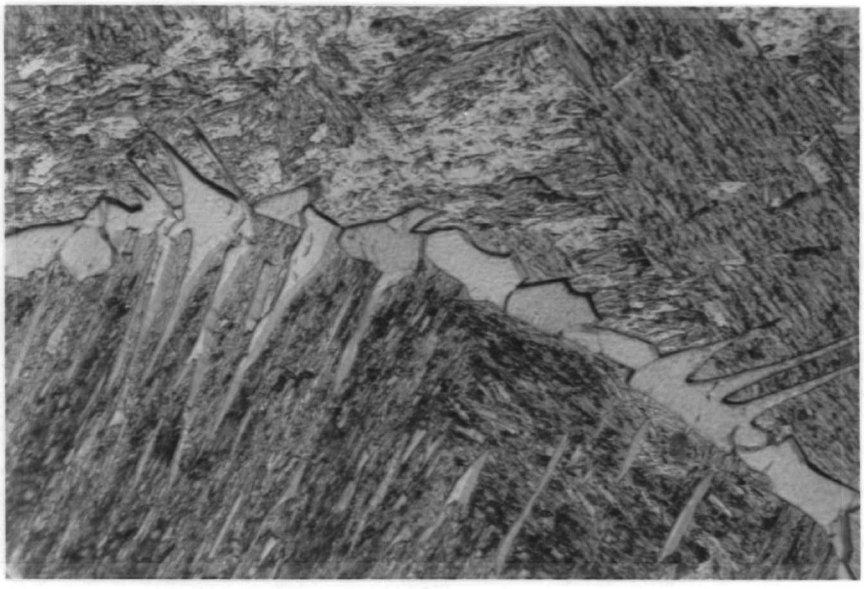

(b)

Fig. 4.28 - Typical photomicrographs of 1020 steel partially transformed at 730°*C* and water-quenched, showing nucleation and growth of proeutectoid ferrite. (a) as grain boundary allotriomorphs nucleating at the austenite grain boundaries (Magnification 200 times) and (b) growth of Widmanstätten ferrite sideplates from the grain boundary allotriomorphs (Magnification 440 times).

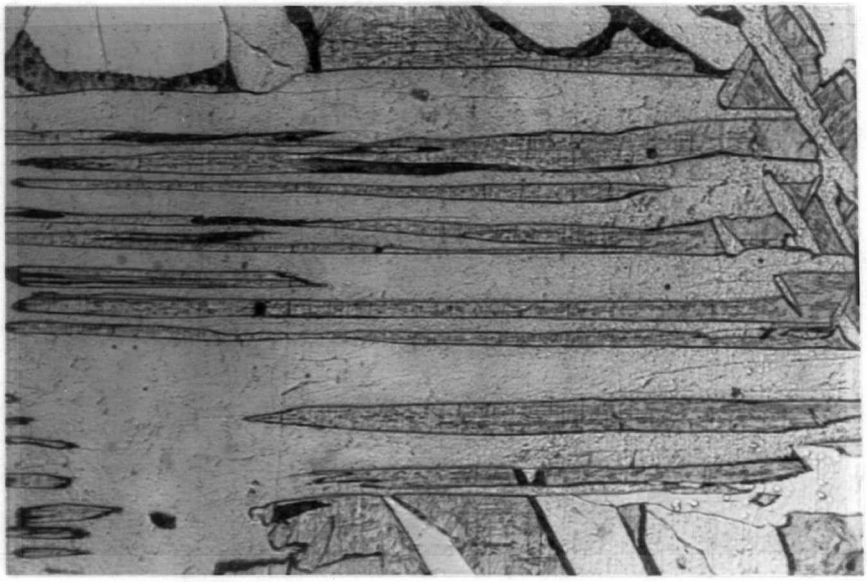

Fig. 4.29 - Typical photomicrograph of 1020 steel transformed completely at 730°*C* and water-quenched showing Widmanstätten ferrite sideplates growing into each other (Magnification 440 times).

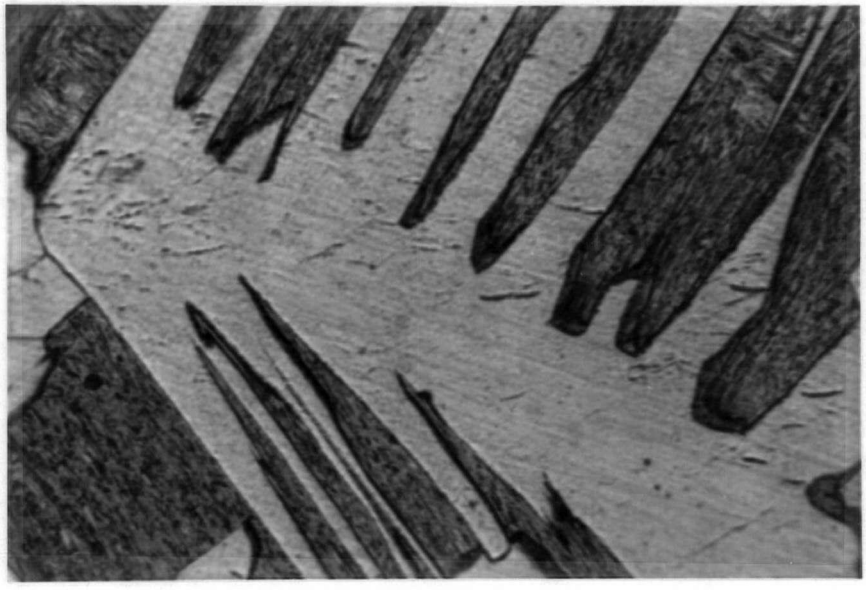

Fig. 4.30 - Typical photomicrograph of 1020 steel transformed completely at 730°*C* and water-quenched showing Widmanstätten ferrite sideplates growing from both sides of an allotriomorph (Magnification 440 times).

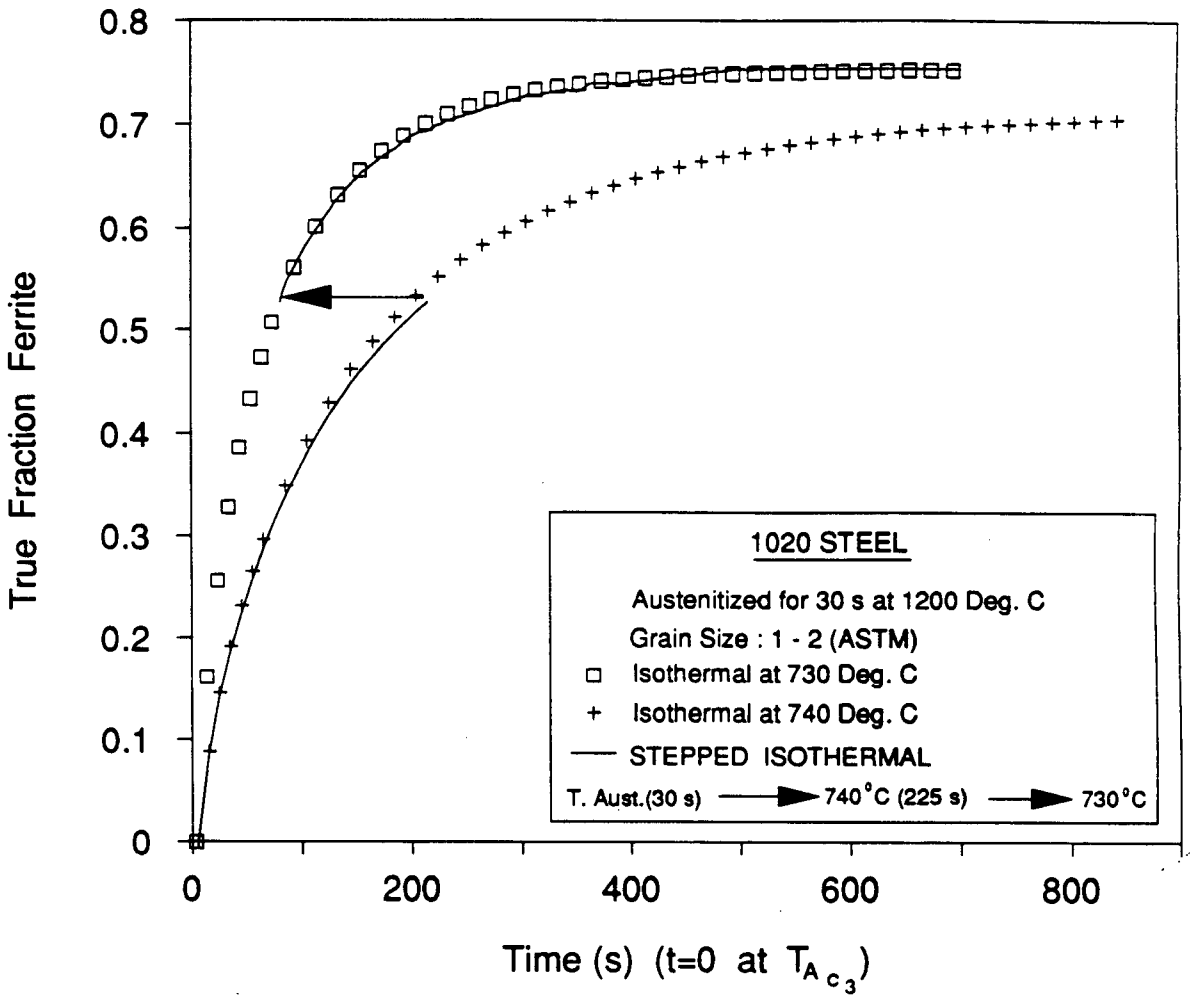

Fig. 4.31 - Experimental isothermal and stepped-isothermal data for 1020 steel.

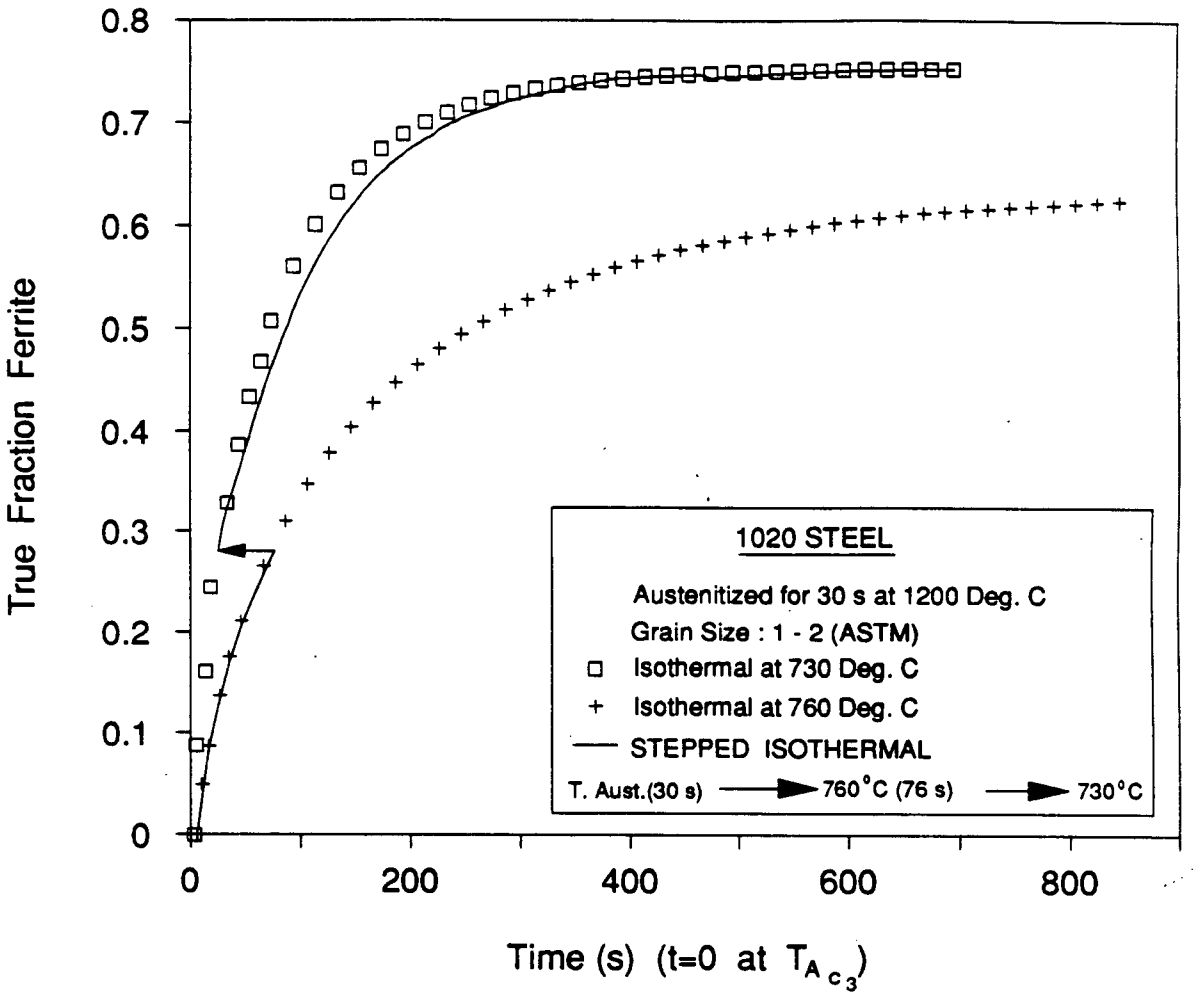

Fig. 4.32 - Experimental isothermal and stepped-isothermal data for 1020 steel.

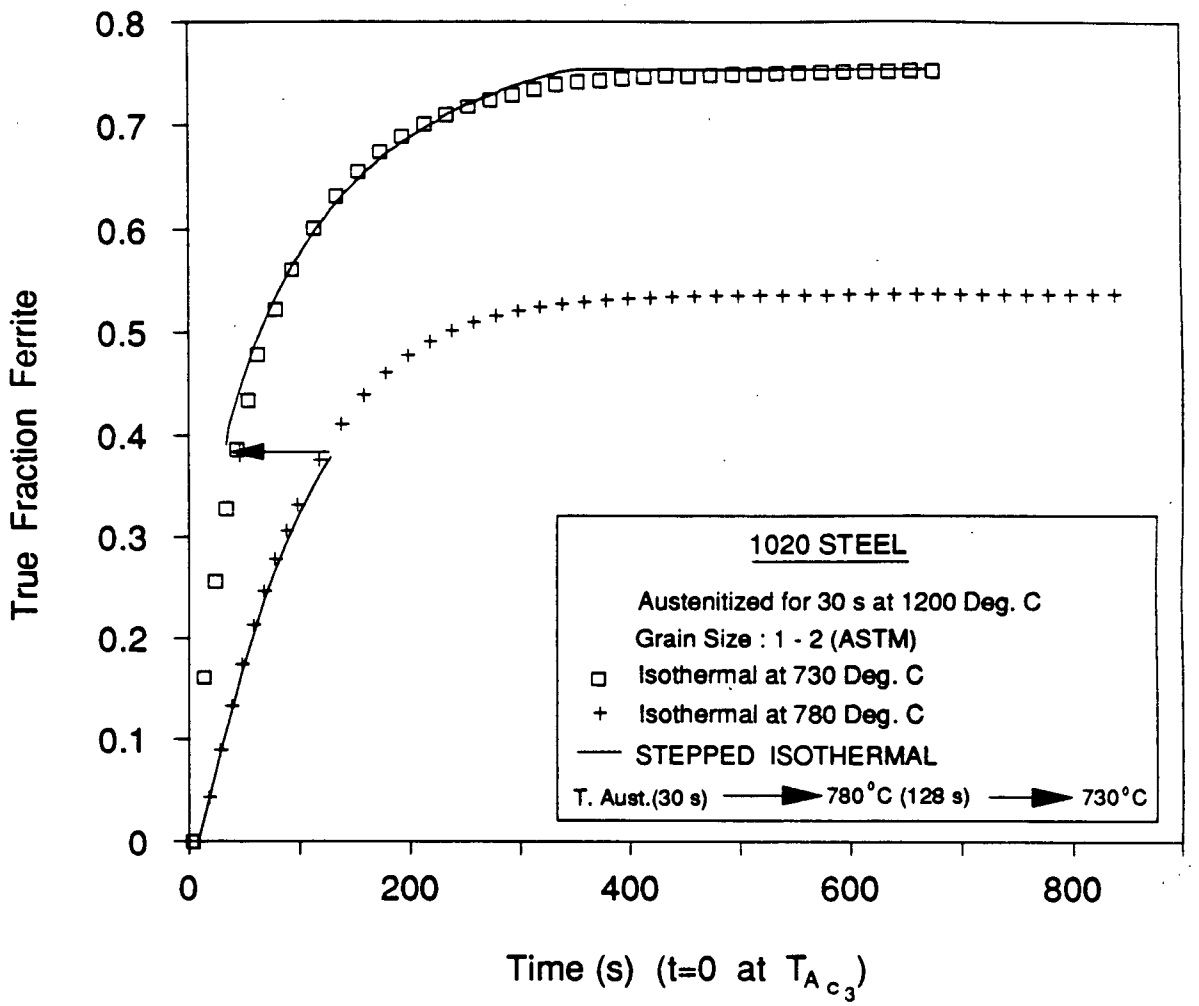

Fig. 4.33 - Experimental isothermal and stepped-isothermal data for 1020 steel.

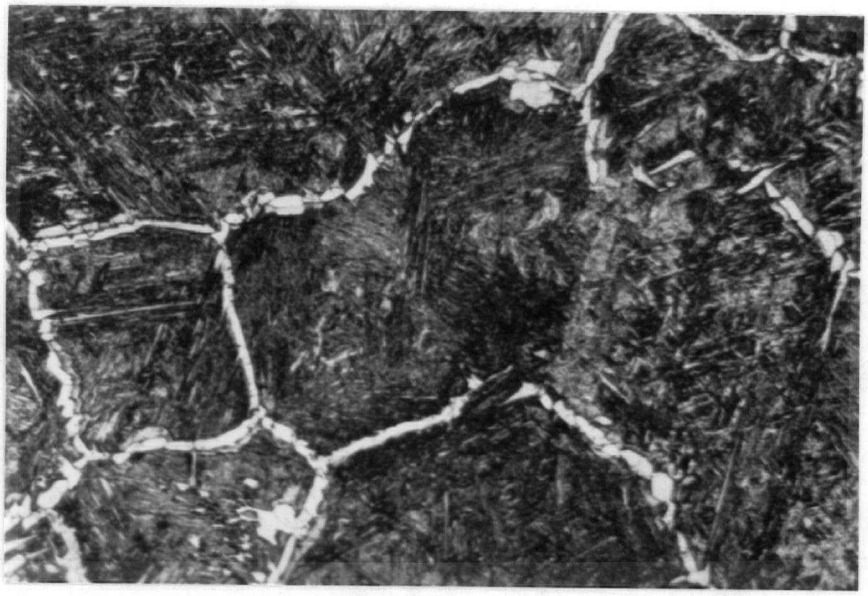

(a)

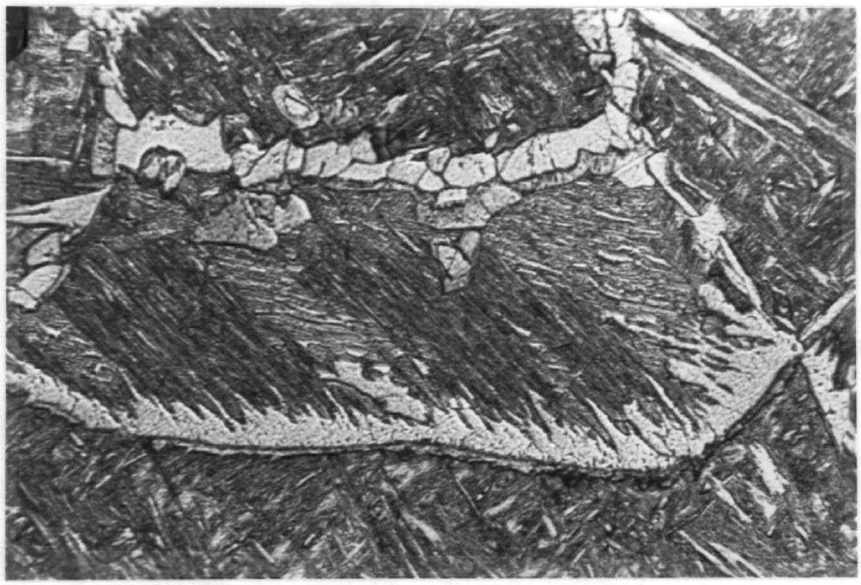

(b)

Fig. 4.34 - Photomicrographs of 1020 steel transformed partially at 780°*C* and step-quenched to 730°*C* and transformed partially before being water-quenched (a) Magnification 176 times and (b) Magnification 440 times.

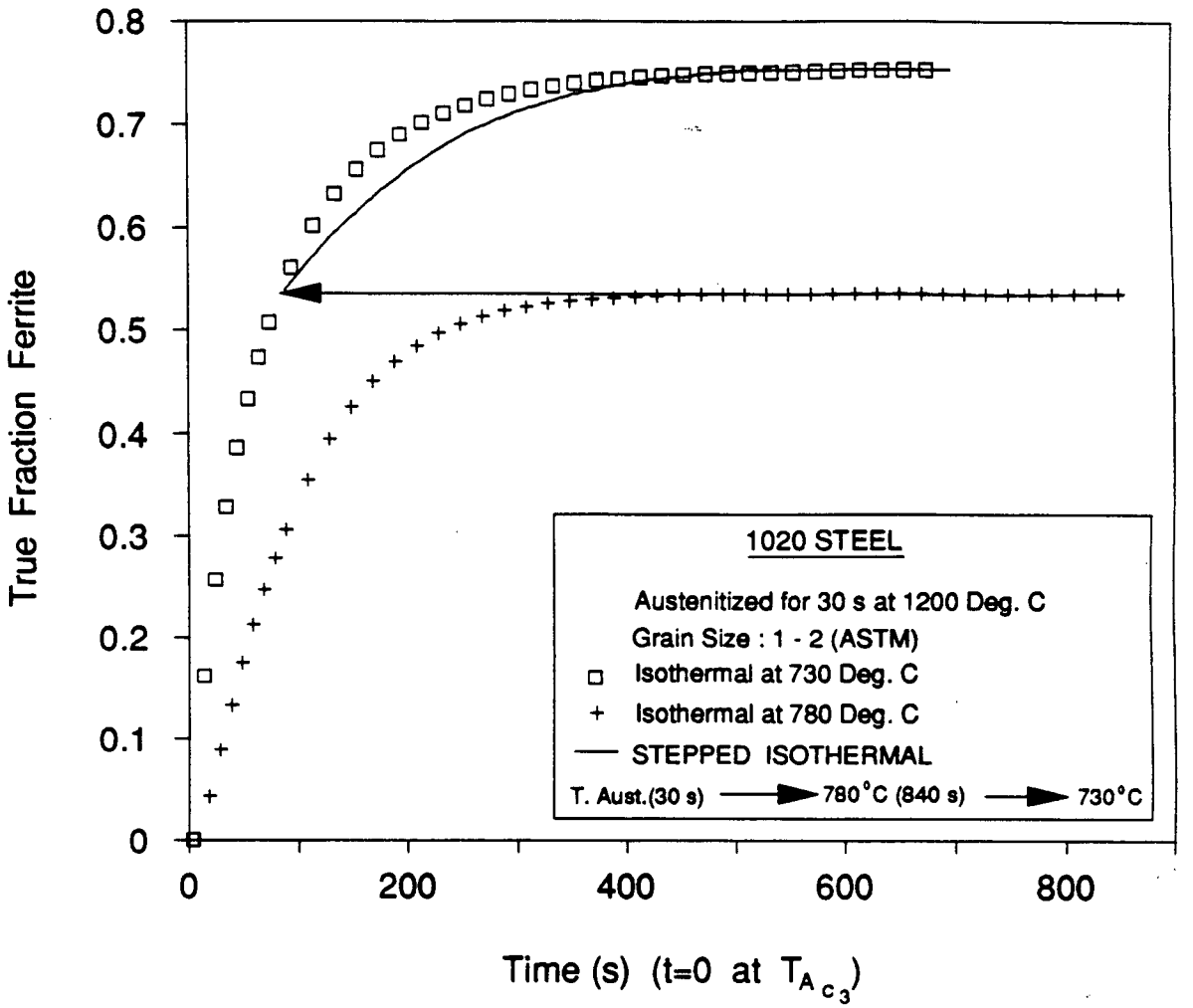

Fig. 4.35 - Experimental isothermal and stepped-isothermal data for 1020 steel.

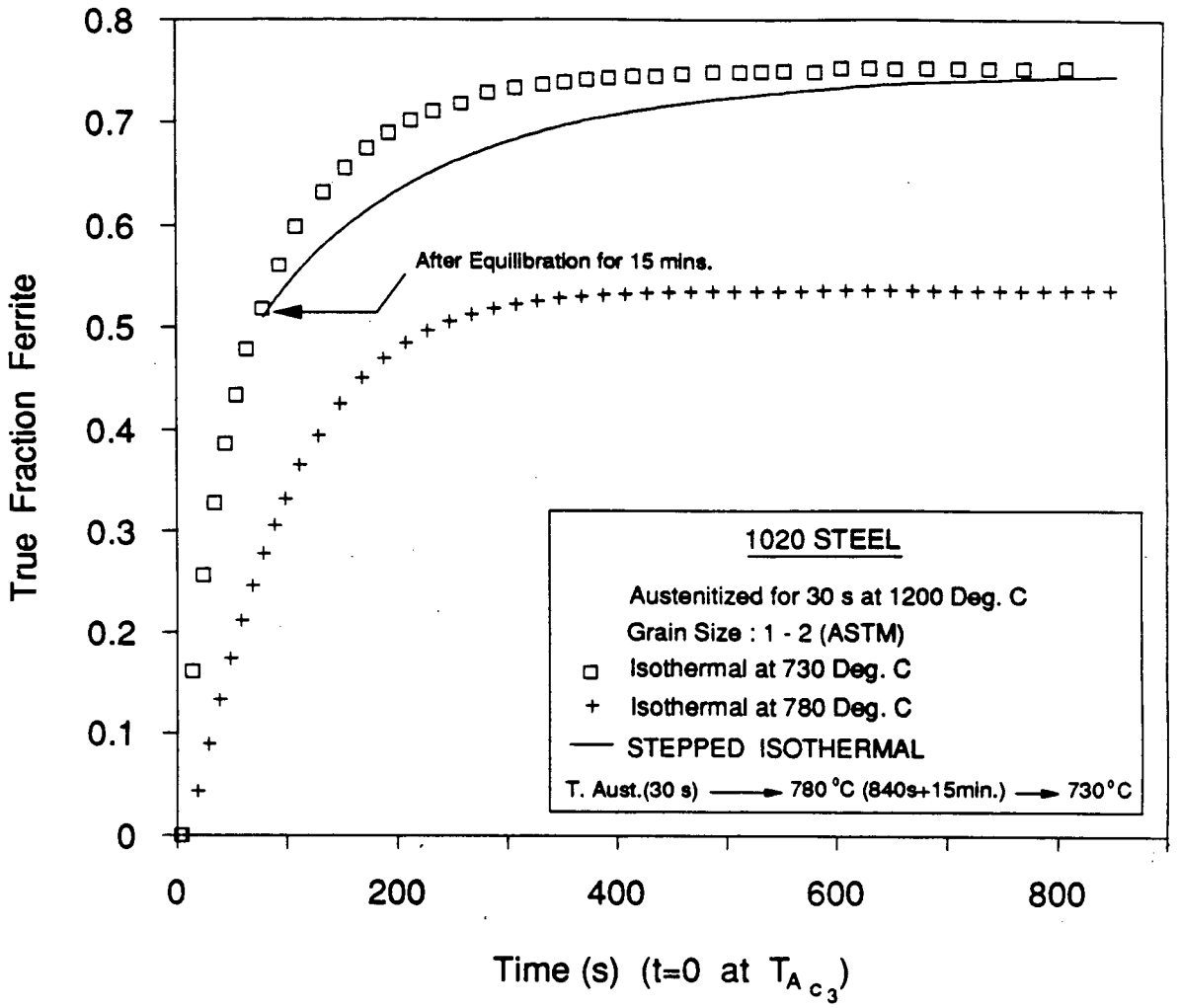

Fig. 4.36 - Experimental isothermal and stepped-isothermal data for 1020 steel.

Fig. 4.37 - Typical photomicrograph of 1020 steel transformed completely at 780°C and equilibrated for 15 mins. before being step-quenched to 730°C, transformed partially and water-quenched (Magnification 184 times).

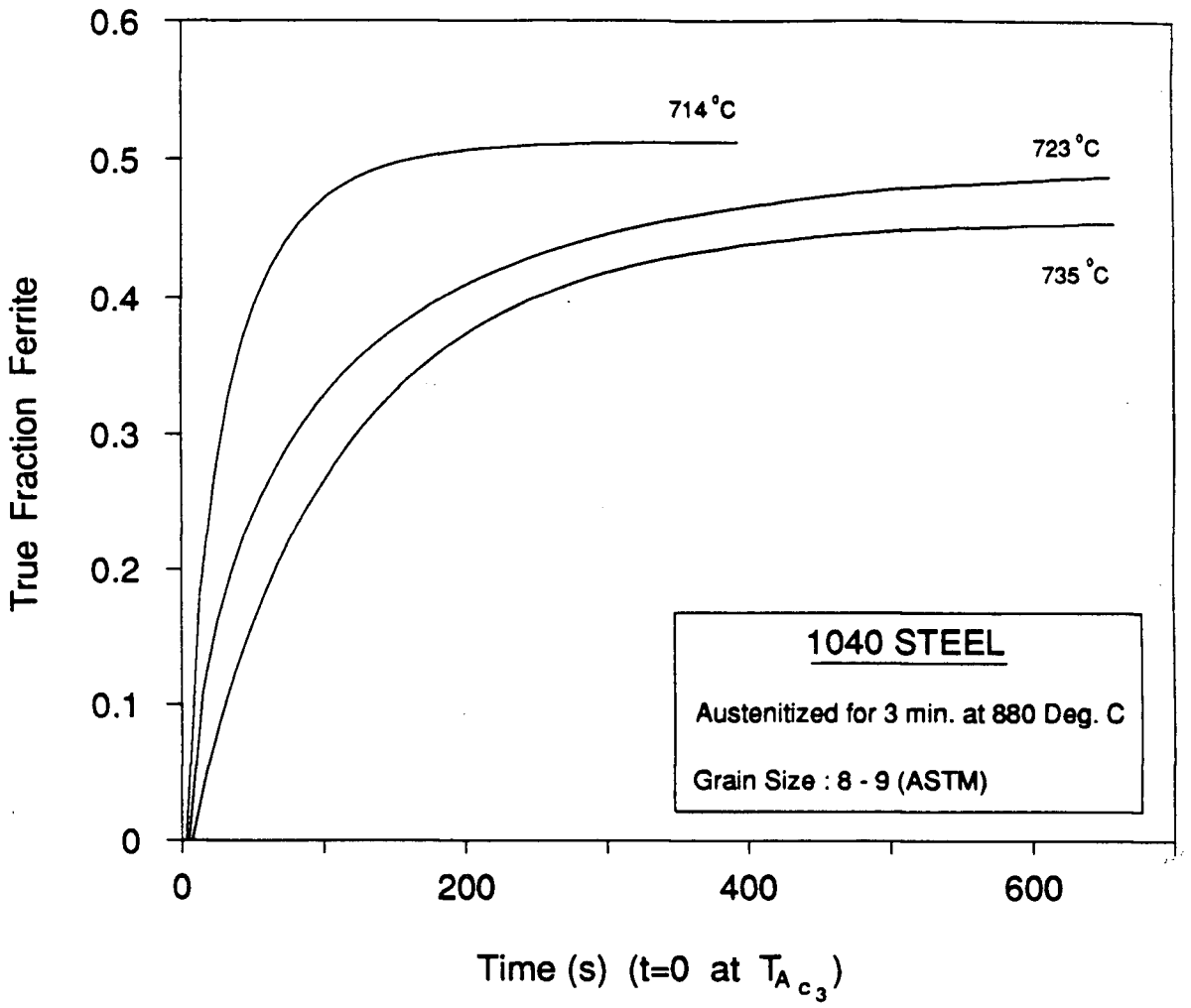

Fig. 4.38 - Typical isothermal transformation data for the 1040 steel.

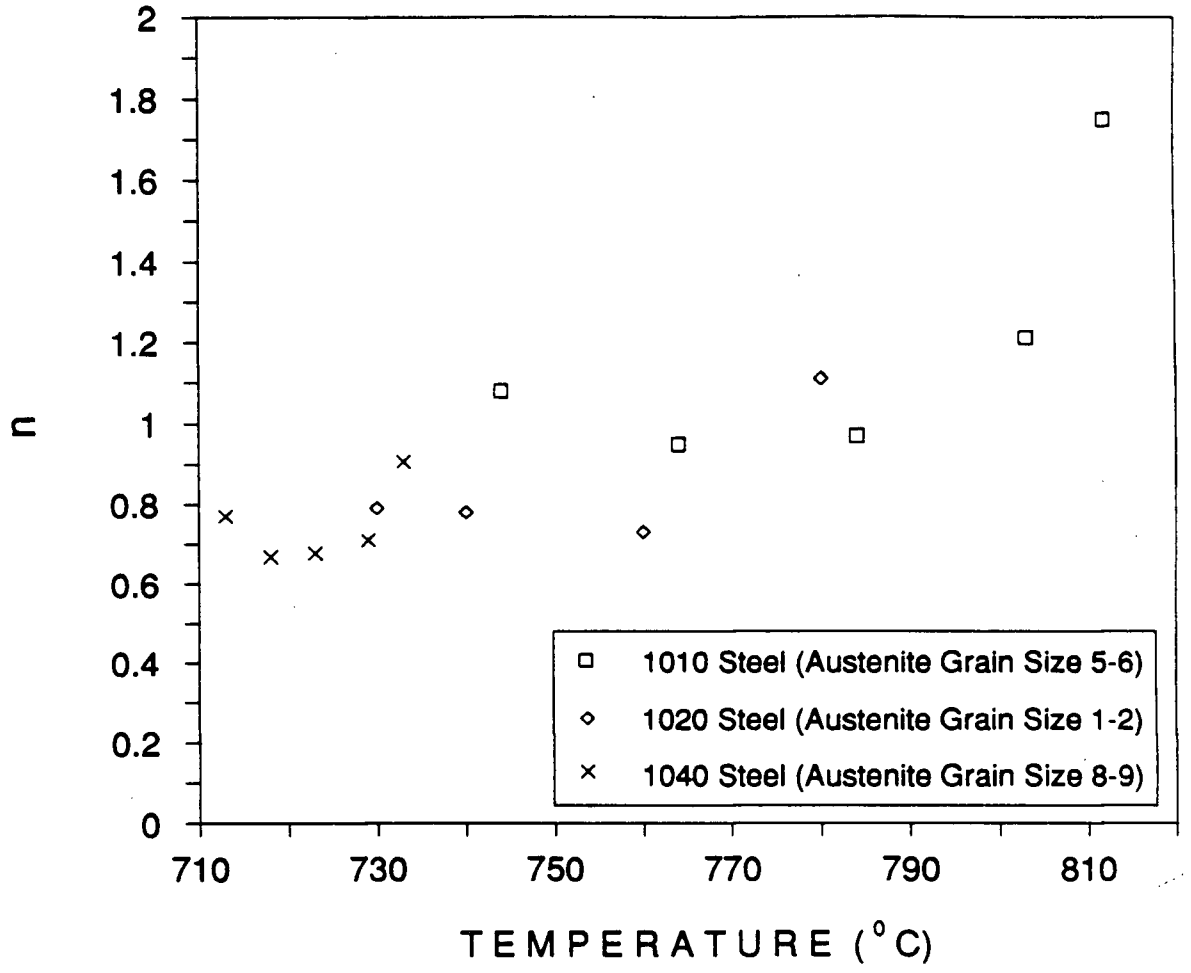

Fig. 4.39 - The n value plotted against isothermal transformation temperature for three steel grades.

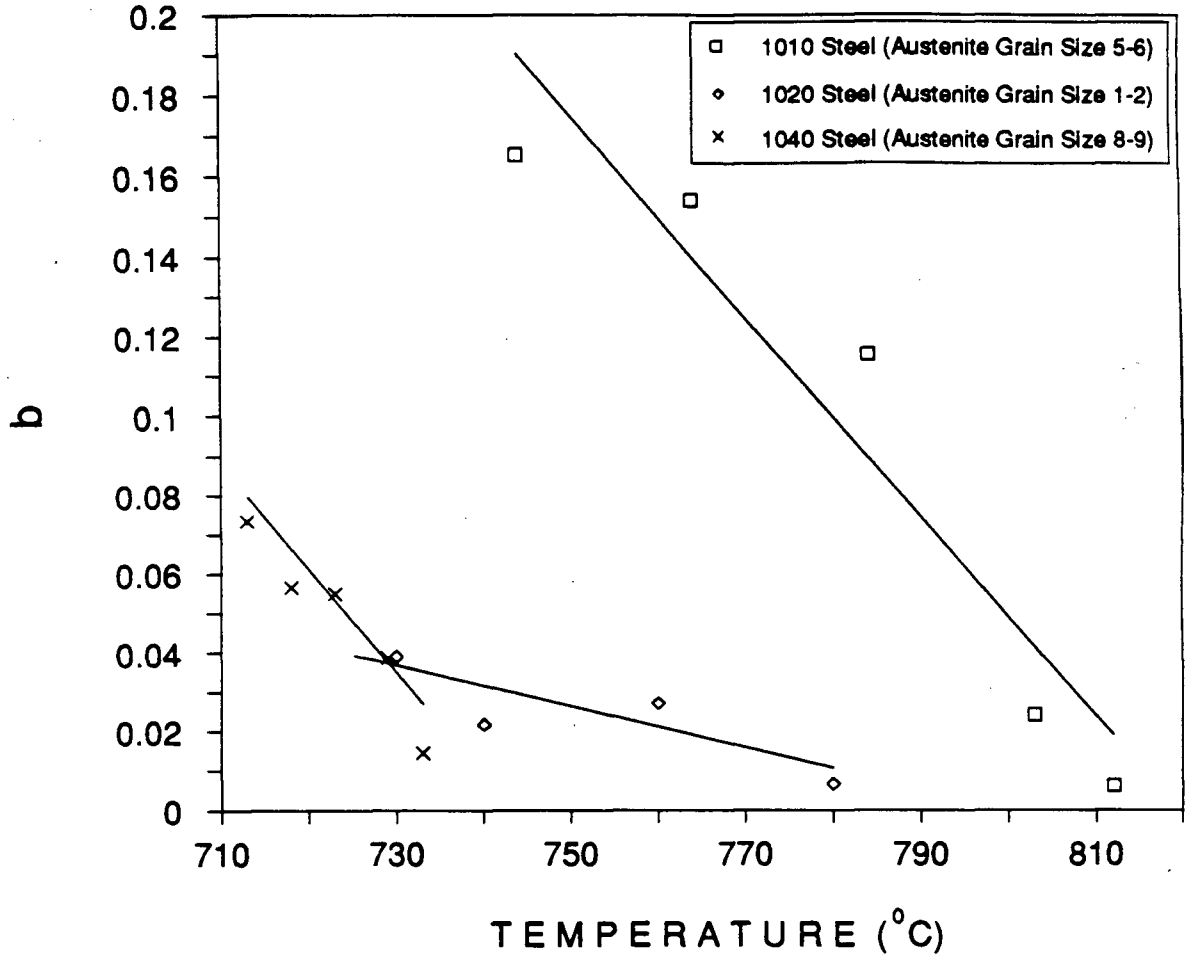

Fig. 4.40 - The b value plotted against isothermal transformation temperature for three steel grades.

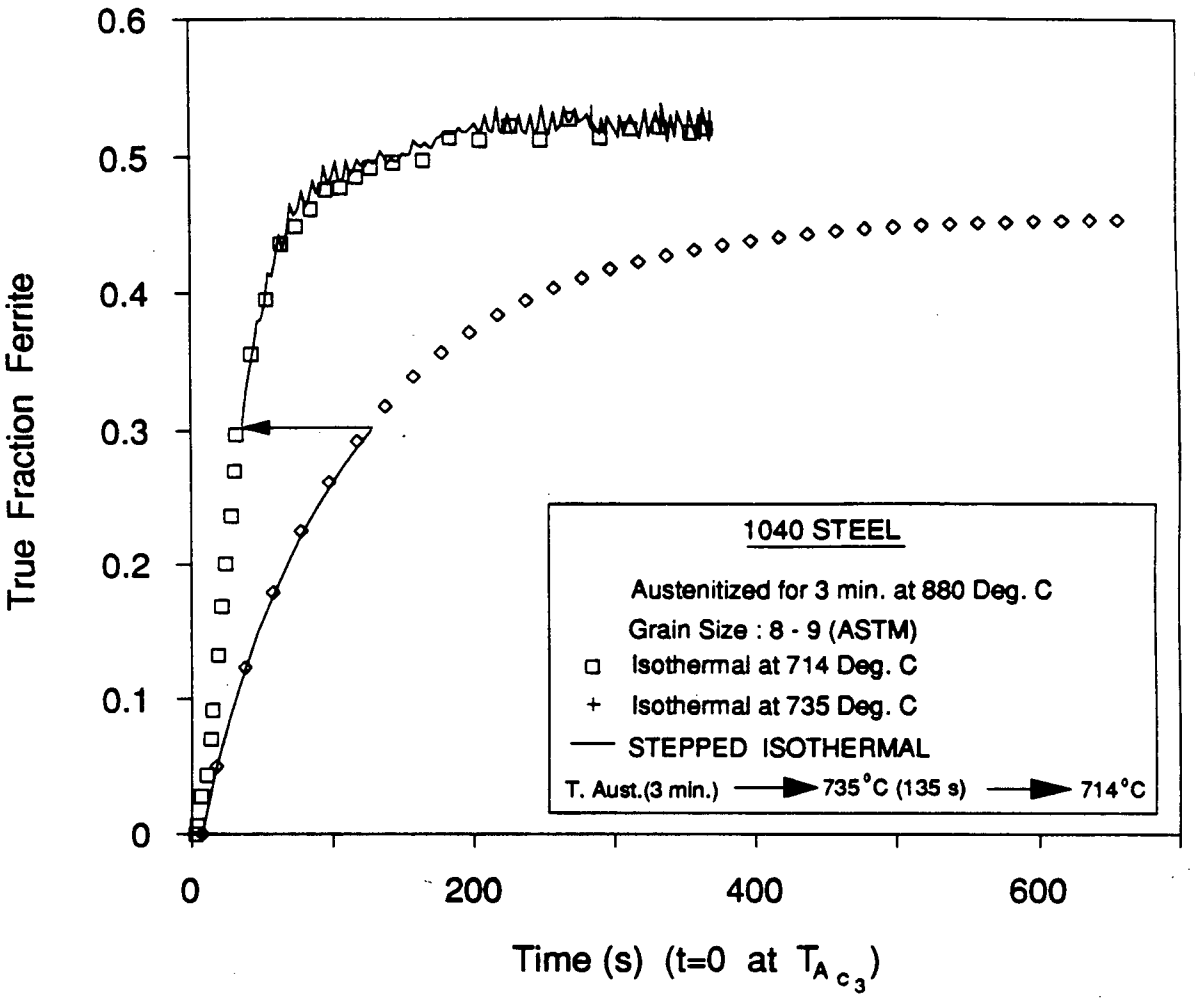

Fig. 4.41 - Experimental isothermal and stepped-isothermal data for 1040 steel.

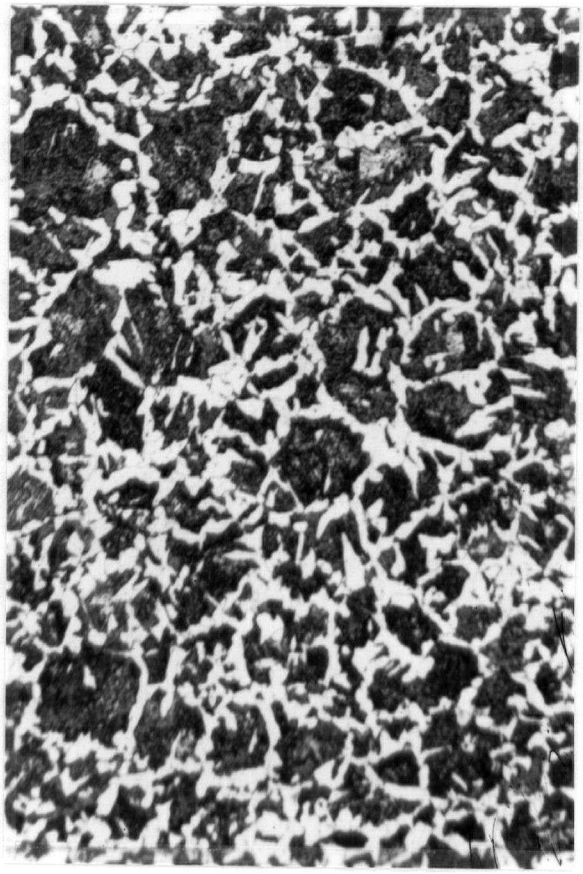

Fig. 4.42 - Photomicrograph of 1040 steel transformed partially at 735°*C*, step-quenched to 714°*C* and transformed completely before being water-quenched, showing ferrite morphology to be predominantly allotriomorphs (Magnification 440 times).

Chapter 5 - MATHEMATICAL MODEL

In order to assess theoretically the applicability of the principle of additivity to the proeutectoid ferrite reaction, two mathematical models have been developed, each of which describes proeutectoid ferrite growth assuming long-range carbon diffusion control, typical of a ferrite grain boundary allotriomorph. Although practically important, exact closed form analytical solutions to diffusion problems with finite boundary systems have not been found as yet. In the present work, finite boundary conditions arise when analyzing proeutectoid ferrite growth in an austenite grain of finite size. Solutions to such problems are possible using numerical techniques. A finite-difference technique based upon the Murray-Landis[54] variable-grid transformation has been used in this work for describing the two-phase, diffusion controlled, austenite-to-ferrite moving-interface problem for a system having finite boundaries.

Mathematical formulation of phase transformations such as the austenite-to-ferrite transformation in steel involves stereological complications. Some of these complications arise due to difficulty in physically describing the varied spatial arrangement of austenite grains and phases present and the precise shape and size of the austenite grain in three dimensions. Estimation of an average grain size can be made by various methods. The austenite grain shape must be space filling, and the interfaces between grains must conform to laws governing surface tension. The optimum space-filling shape with a minimum of surface area is the tetrakaidecahedron shown in Fig. 5.1. This shape is a polyhedron with 14 faces. The surface tension requirements are fulfilled with no more than three grains meeting at an edge and no more than four edges meeting at a corner. However, it does not meet the requirement of 120° dihedral angles between grain boundaries where three adjacent grains

meet an edge. This requirement can be satisfied by introducing a slight double curvature to the faces, which changes the surface area by approximately 4 percent[57]. In practice, the grains in a polycrystalline solid exhibit a range of size, shape, and number of faces. It is not practical to describe growth of ferrite in an austenite grain having a tetrakaidecahedron shape and other more complex shapes. Simple approximations are necessary. Two austenite grain shape geometries are analyzed in the present work, planar and spherical. As shown in Fig. 5.1 these two geometries represent two limiting cases of ferrite growth. The actual shape of the austenite grain as represented by the tetrakaidecahedron would be expected to give growth rates intermediate between these two extremes.

5.1 Model Assumptions

The following simplifying assumptions have been made in developing the two models:

(1) For a given temperature, the equilibrium carbon contents of the γ and α phases at the phase interface, C_γ and C_α, are dictated by the iron-carbon phase diagram and are attained instantaneously.

(2) At a given temperature, the interface concentrations C_γ and C_α, are time independent.

(3) The variation of carbon concentration within the ferrite phase has been considered negligible.

(4) Nucleation has been neglected by assuming that early site saturation occurs.

(5) The densities of both phases, α and γ, are equal (independent of temperature and carbon concentration).

The assumption that early site saturation occurs during the austenite-to-ferrite transformation is a valid one, as was shown earlier. The principle of additivity, as stated earlier, is realized when the reaction rate depends only on the instantaneous temperature and fraction transformed (Eq. (2.14)). Hence, if nucleation sites saturate early in the reaction, the

course of the reaction will be dependent upon the growth rate only. If the growth rate is a function solely of instantaneous temperature, then the reaction will be experimentally additive. Thus, in both models, it is assumed that all of the available sites for nucleation of ferrite are saturated early in the reaction in order to reduce the nucleation rate to zero and ensuring that the growth kinetics govern the overall transformation rate.

Both models incorporate the changing equilibrium concentration of ferrite and austenite (Fig. 2.23) at the phase boundary due to temperature change and the temperature- and concentration-dependence of the carbon diffusion coefficient in austenite[55,66]. As stated earlier, the carbon content within the ferrite phase has been assumed not to vary significantly. Hence, for a given temperature, a constant value of carbon content in the ferrite has been used, as dictated by the iron-carbon equilibrium diagram (schematically shown in Fig. 2.23). Appropriate boundary conditions have been formulated to describe the finite austenite grain size.

5.2 Planar Geometry

A grain of austenite has been modelled as a one-dimensional plane of finite length with ferrite growing from a single boundary. The nodal arrangement is shown in Fig. 5.2 as well as the corresponding initial condition and boundary conditions which constitute a one-dimensional, planar unsteady-state diffusion model coupled with the moving α/γ interface. The unsteady-state diffusion equation for planar geometry is

$$\frac{\partial C}{\partial t} = \frac{\partial}{\partial x}\left(D_C^{\gamma} \frac{\partial C}{\partial x} \right) \tag{5.1}$$

where C is the carbon content in austenite, D_C^{γ} is the carbon diffusion coefficient in austenite, x is the diffusion distance and t is the diffusion time. The temperature and carbon dependency of D_C^{γ} have been evaluated using data from Wells, Batz and Mehl[55], and are incorporated in the form of a mathematical expression[66] in the finite-difference equations. The thickening of ferrite precipitates at γ grain boundaries results in overlapping diffusion

fields within the austenite grain. Hence, the model considers one half of an austenite grain having a central plane which becomes the plane of zero flux, and at which the carbon content builds up as ferrite grows and soft impingement occurs. The movement of the α/γ interface during growth of ferrite was derived by applying a mass balance at the interface[56], giving rise to a ferrite growth velocity (V):

$$V = \frac{D_C^{\gamma}}{C_{\gamma} - C_{\alpha}} \left(\frac{\partial C}{\partial x} \right)_{interface} \tag{5.2}$$

From the above equation it is obvious that for a given temperature, the growth velocity will be high if the interface gradient is steep. Equations (5.1) and (5.2), together with the correct initial condition and boundary conditions, were re-written and incorporated in the model in explicit finite-difference form. Since the velocity of the interface is not known *a priori*, it is necessary to assume a velocity and solve the necessary equations at each increment of time. Based on the assumed velocity, the diffusion equations are solved for every node and the resulting diffusion gradient is used to calculate the new velocity. The procedure is repeated iteratively with a new assumption of growth velocity until the assumed and calculated velocities match. In order to make an intelligent assumption of the ferrite growth velocity, the parabolic growth rate constant determined by Kinsman and Aaronson[45] for various growth temperatures in a 0.11 wt.% C steel, has been utilized. Owing to the finite boundaries involved, the austenite phase shrinks with time at the expense of the growing ferrite. Thus, with every time step, the node size gets smaller as the number of nodes are kept the same.

The explicit finite-difference technique requires that for each time step the following stability criterion is met for all the nodes:

$$\frac{D_C^{\gamma} \ \Delta t}{\Delta x^2} \leq \frac{1}{2} \tag{5.3}$$

where Δt is the time increment (0.01 s) and Δx is the node size. This criterion was continuously evaluated and was always satisfied. The carbon concentration profile in front of the growing ferrite and the interface location was calculated at each instant of time. The effect of changing the temperature and thereby changing the equilibrium boundary conditions, C_γ and C_α, and the diffusion coefficient D_C^γ, on the carbon diffusion gradient and the resulting interface velocity was assessed. At a pre-determined time, or pre-defined thickness of ferrite, the equilibrium boundary conditions were changed from one temperature to another and the resulting carbon diffusion gradient and the α/γ interface velocity were computed throughout.

5.3 Spherical Geometry

This model incorporates a spherical interface, which can be considered as a geometrically limiting case relative to the planar interface. A grain of austenite is assumed to be a sphere with ferrite growing radially inwards from the surface toward the center of the sphere. The approach taken in developing this model is identical to the one described for the planar case. As illustrated in Fig. 5.2, the model constitutes radial, unsteady-state diffusion in a sphere coupled with the moving α/γ interface. The unsteady-state diffusion equation for spherical geometry is:

$$\frac{\partial C}{\partial t} = \frac{\partial}{\partial r}\left(D_C^\gamma \frac{\partial C}{\partial r} \right) + \frac{2 D_C^\gamma}{r} \frac{\partial C}{\partial r} \tag{5.4}$$

where r is the radial diffusion distance. As in the planar case, growth of ferrite results in overlapping diffusion fields within the austenite grain. The model takes into account this soft impingement effect by treating the centre of the spherical austenite grain as a point of zero mass transfer at which the carbon content builds up as ferrite grows. Relevant initial and boundary conditions are shown in Fig. 5.2. The model formulation, including assumptions

and the finite-difference numerical techniques utilized, are the same as those previously described for the planar case. The computing algorithm for both models was written using FORTRAN programming language.

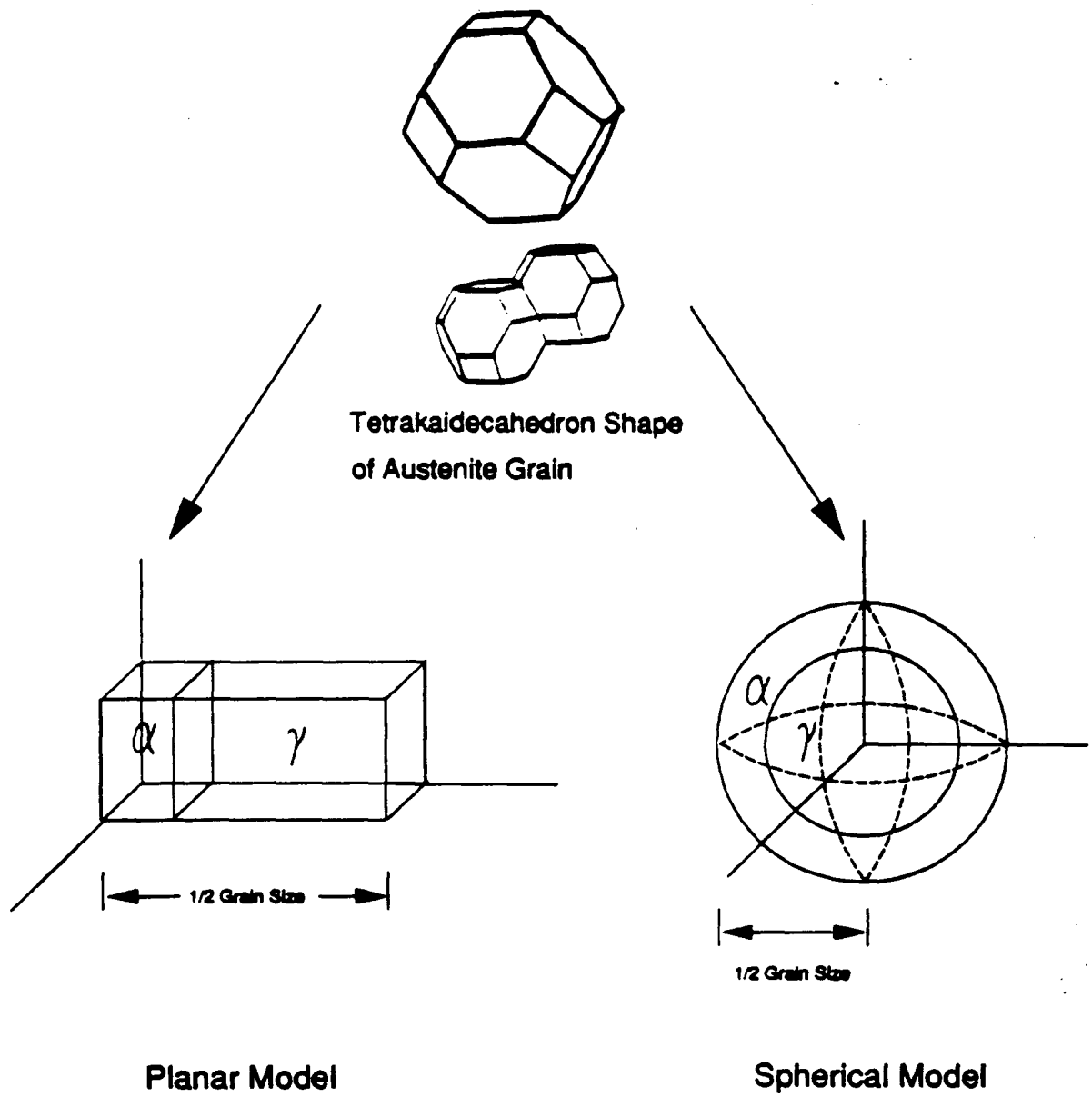

Fig. 5.1 - Schematic diagram illustrating the tetrakaidecahedron shape attributed to an austenite grain and the planar and spherical geometries used in the mathematical models.

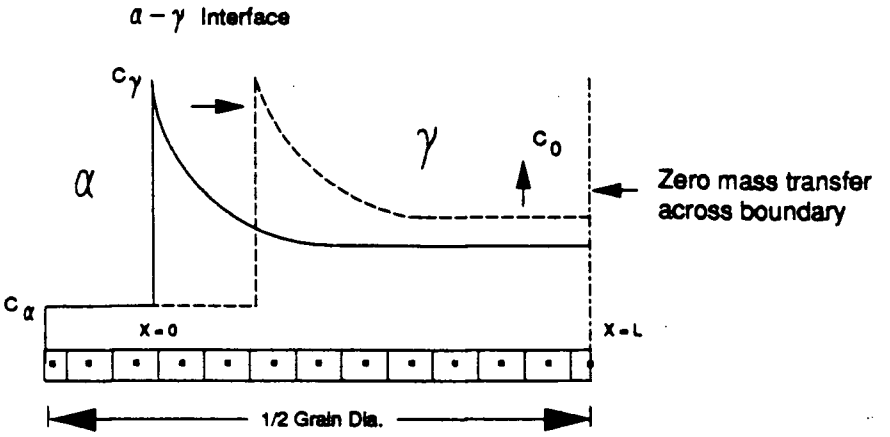

	PLANAR CASE	SPHERICAL CASE
Initial Condition:	At t=0, 0 < X < L C(I)=C_0 (I=1, N)	At t=0, 0 < X < L C(I)=C_0 (I=1, N)
Boundary Conditions:	At t > 0, X=0 For First Node C(1)=C_γ	At t > 0, X=0 For First Node C(1)=C_γ
	At t ⩾ 0, X=L For Last Node dC/dx=0	At t ⩾ 0, X=L For Last Node dC/dr=0

Fig. 5.2 - Schematic diagram illustrating the nodal arrangement and initial and boundary conditions for the planar and spherical diffusion models.

Chapter 6 - MATHEMATICAL MODEL PREDICTIONS

Mathematical models were employed to assess the applicability of the principle of additivity to the proeutectoid ferrite transformation. Planar and spherical geometries were considered as the two limiting cases for ferrite growth. The models were used to predict ferrite growth under isothermal and stepped-isothermal conditions assuming early site saturation. Only one morphology, namely grain boundary allotriomorphs was considered in developing the models. Also, the model predictions are limited to the 1010 grade because, as presented in the experimental results section, the morphology obtained for the range of temperatures studied for this steel is predominantly allotriomorphic.

6.1 Isothermal Conditions

Model predictions for the isothermal growth of ferrite with planar and spherical geometries will be presented in the following sections. In order to obtain a solution of the model with a given specific interface geometry the following input data were specified:

(1) Initial carbon content of the matrix taken as 0.11 wt.%.

(2) Austenite grain size

(3) The equilibrium carbon contents of the γ and α phases, C_γ and C_α, for a given temperature, as determined from the iron-carbon equilibrium phase diagram

(4) Diffusion coefficient of carbon in austenite, D_γ^C, as a function of temperature T in K and carbon content (C_M) in mole fraction given by the following mathematical expression[66]:

$$D_{\gamma}^{C} = 4.53\times10^{-7}\left[1+\frac{C_M}{1-C_M}\left(1-\frac{C_M}{1-C_M}\right)\frac{8339.9}{T}\right]\exp\left\{-\left(\frac{1}{T}-2.221\times10^{-4}\right)\left(17767-\frac{C_M}{1-C_M}26436\right)\right\} \quad m^2 s^{-1} \tag{6.1}$$

(5) Internal node size

(6) Time step

Using this information the models were run to predict the transient concentration profiles and the interface location. The computation was terminated either after a pre-determined time had elapsed or a pre-determined thickness of ferrite had been reached.

6.1.1 Planar Geometry

The mathematical model with a planar α/γ interface was applied to analyze the additivity of the proeutectoid ferrite transformation. The accuracy of the model was evaluated by two different methods. First, the model was modified to incorporate a fixed interface and a constant D_{γ}^{C}, and the carbon gradients were predicted at early times. Under these conditions the model satisfies the semi-infinite condition and hence the model-predicted carbon gradients can be verified against the gradients calculated from the analytical solution:

$$C(x,t) = C_{\gamma} - (C_{\gamma} - C_0)\, erf\left(\frac{x}{2\sqrt{D_{\gamma}^{C} t}}\right) \tag{6.2}$$

where C_0 is the original carbon content (0.11 wt.% in this case), x is diffusion distance and t is time. A negligible error (< 0.5 pct.) was found when the model-predicted carbon gradients were compared with the gradients calculated using the analytical solution for early growth times. The model was then modified to include the moving interface problem and once again the model-predicted carbon gradients for early times were compared with those calculated from the following analytical solution modified to include a moving interface.

$$C(x,t) = C_0 + (C_\gamma - C_0)\left(\frac{1 - erf\frac{x}{2\sqrt{D_\gamma^C t}}}{1 - erf\frac{S}{2\sqrt{D_\gamma^C t}}}\right) \quad (6.3)$$

where S is the ferrite thickness at time t. Figure 6.1 shows that the agreement between the model-predicted and the analytical profiles at 800°C is good, especially at early times. However, the analytical profiles deviate from the model-predicted profiles at longer times due to the use of finite boundary conditions in the model.

The following analytical solution for the movement of the planar interface was adopted to calculate the growth of ferrite[67]:

$$\frac{C_\gamma - C_0}{C_\gamma - C_\alpha} = \frac{S}{2}\sqrt{\frac{\pi}{D_C^\gamma t}}\left\{1 - erf\frac{S}{2\sqrt{D_C^\gamma t}}\right\}\exp^{\frac{S^2}{4D_C^\gamma t}} \quad (6.4)$$

Model-predicted ferrite growth at different temperatures was compared with values calculated from the analytical solution. Figure 6.2 shows an example of such a comparison for 800°C. The agreement between the two is good until the model-predicted result shows the effect of soft impingement due to the finite size of the γ grain considered in formulating the model. The model-predicted carbon profiles are shown in Fig. 6.3. As can be seen, the increase in the matrix carbon composition from 0.11 wt.% occurs during the time interval 20 to 30 s; this being the same time as the model-predicted growth rate deviates from the analytical growth rate (Fig. 6.2). This shows the importance of the soft impingement effect taken into account by the model.

The second method to check the accuracy of the model predictions was applied at programme termination, after reaching equilibrium conditions. This method consisted of performing a carbon mass balance on the ferrite-austenite two-phase system. As shown in Fig. 6.4, if the carbon mass balance is maintained between the austenite and ferrite, then the areas representing the redistribution of carbon in the austenite and the ferrite must be equal. This also can be deduced from the lever rule. Based on these areas and the chosen γ grain

size, the isothermal ferrite thickness was calculated. As shown in Table 6.1, the calculated and model-predicted ferrite thicknesses show very good agreement, thereby confirming the accuracy of the model.

The mathematical model was also validated using experimental data available in the literature for the same steel grade. Fig 6.5 compares the model predictions and the ferrite growth calculated with the experimentally determined parabolic rate constant (α) obtained by Kinsman and Aaronson[45] for a 0.11 wt.% C steel. The comparison of the planar model predictions with experimental results was considered valid because the ferrite growth was predominantly planar in the experimental work. The authors[45] used thin specimens austenitized at a sufficiently high temperature for a long time causing the austenite grain boundaries to grow perpendicular to the broad faces of the specimens. This resulted in ferrite growing as grain boundary allotriomorphs with effectively planar α/γ interfaces. The authors'[45] measured growth kinetics show some scatter and an average value has been considered for the purpose of comparison. Since the experimental results were obtained for a γ grain size of ASTM No. 1-2 (254-180 μm), the model was run for an ASTM grain size No. 1.5 (214 μm), one half the grain size being considered. As shown in Fig. 6.5, agreement between the initial stages of the growth of the model-predicted and the experimentally observed ferrite thickness is very good. The apparent discrepancy, which increases with increasing growth time, is a reflection of the fact that a parabolic rate constant was used to describe ferrite growth, implying that the system is semi-infinite and not subject to soft impingement. The model on the other hand, being formulated for a finite γ grain size, predicts the growth of ferrite taking into consideration the effect of soft impingement. As shown in Fig. 6.5, after 1000 seconds, the ferrite growth rate decreases significantly and approaches zero due to soft impingement.

The model-predicted carbon profiles, as a function of distance at various times, are shown in Fig. 6.6. The carbon gradients are initially steep and decrease in slope with increasing time as more and more carbon is rejected ahead of the growing ferrite. After long times, the carbon profile is almost flat and all of the remaining austenite attains a carbon composition, C_γ, as dictated by the iron-carbon equilibrium diagram for that particular temperature. It is worth noting that the soft impingement effect on the austenite-ferrite interface mobility is not felt until a sufficient amount of carbon build-up in front of the interface has taken place.

6.1.2 Spherical Geometry

The second mathematical model which incorporates a spherical α/γ interface, was also used to assess the applicability of the additivity principle to the proeutectoid ferrite transformation. As in the case of the planar interface model, the spherical model was first assessed for accuracy of the solution. This was accomplished by first comparing the solutions predicted for the planar and the spherical model, as shown in Fig. 6.7. During the very early stages of ferrite growth, the spherical model is identical to the planar model as the curvature effect of the spherical interface on the carbon gradients is not felt. Also, at early growth times, both the spherical and the planar models satisfy the semi-infinite condition. With increasing time, the spherical model predicts more shallow carbon gradients ahead of the growing ferrite due to the curvature of the spherical interface. Carbon is being supplied to the remaining austenite from a 3-D surface and therefore the local carbon concentration is higher at any growth time and soft impingement effects occur more rapidly.

The second check on the accuracy of the spherical model predictions was accomplished, as in the case of the planar model, by performing a carbon mass balance on the ferrite-austenite two-phase system, at the end of the model run. Knowing the equilibrium carbon content of the ferrite and the austenite, it is possible to calculate the final volumes of ferrite and austenite for a given diameter of the sphere and therefore determine the degree of

carbon redistribution in each phase. This can also be deduced from the lever rule. Based on these volumes and for a given γ grain size, the isothermal ferrite shell thickness was calculated. As shown in Table 6.2, the calculated and model predicted ferrite thicknesses are in very good agreement, thereby confirming the accuracy of the model.

The isothermal ferrite growth and the associated carbon gradients were predicted using the spherical model. The effect of γ grain size on the ferrite growth kinetics was assessed for different grain diameters. Figure 6.8 shows the ferrite shell thickness predicted as a function of time for ASTM Grain Sizes No. 5 and 1.5. As can be seen, the rate of ferrite growth is initially high and decreases with time due to the overlapping carbon diffusion fields. The model-predicted carbon diffusion profiles for grain sizes 5 and 1.5 are shown in Figs. 6.9 and 6.10, respectively. For the large γ grain size, impingement of diffusion fields occurs at a significantly later stage, as compared to that obtained for the small grain.

The ferrite growth rate as a function of growth time for the two grain sizes ASTM 5 and 1.5 were compared, as shown in Fig. 6.11. The growth rates for both grain sizes are the same at early growth times and deviate from one another at the onset of soft impingement. The growth rate for a given grain size is controlled by the carbon gradient in front of the α/γ interface, this being reduced by increasing soft impingement. A comparison of the carbon profiles at any instant of time, as shown in Figs. 6.9 and 6.10, indicates that soft impingement causes the growth rate within the smaller austenite grain to decrease earlier and to be smaller in magnitude than the growth rate observed for the larger grain.

The experimental 800°*C* isothermal transformation results converted to fraction ferrite vs. time, were compared with the planar and spherical model predictions, as shown in Fig. 6.12. Neither model completely agrees with the experimental results. However, the spherical model in general gives closer agreement than the planar model.

6.2 Stepped Isothermal Condition

A true test of the observed experimental additivity of the proeutectoid ferrite transformation can be made by assessing the ferrite growth kinetics under conditions of changing temperature. As discussed earlier, a change in temperature will change the equilibrium boundary conditions (C_γ and C_α) and D_C^γ, which in turn will affect the ferrite growth kinetics. Early site saturation is assumed in both models and was experimentally observed for the test conditions being examined, making it possible to neglect the effect of nucleation kinetics on the ferrite transformation behaviour. The planar and spherical models were employed to assess the effect of changing temperature on the growth kinetics of the proeutectoid ferrite, assuming instantaneous attainment of the equilibrium boundary conditions at each test temperature.

6.2.1 Planar Geometry

The planar model was first employed to predict isothermal ferrite growth at two temperatures, 803°C and 764°C. The model was then run at 803°C and, at a predetermined ferrite thickness of 10 μm, the temperature was changed to 764°C to predict the growth kinetics under stepped-isothermal conditions. Figure 6.13 compares the model prediction for ferrite thickness under stepped-isothermal growth conditions with that predicted for isothermal growth at 803°C and 764°C, obtained under test conditions identical to the experimental conditions (Fig. 4.17). The agreement between model-predicted stepped-isothermal and fully isothermal ferrite thickness vs. time (Fig. 6.13) is very good, similar to that obtained in the experimental test results shown in Fig. 4.17.

The plot of model-predicted ferrite growth rate-vs.-time is shown in Fig. 6.14 and exhibits a steep rise in growth rate at the instant of change in temperature from 803°C to 764°C, as found in the experimental test results. However, this enhanced growth rate decays very quickly and soon attains the rate obtained for the 764°C isothermal condition. The time taken to attain the isothermal growth rate after the step quench is of the order of two seconds.

This rapid attainment of the isothermal growth rate at the second transformation temperature supports the observed experimental additivity of the transformation. Thus, although the model-predicted ferrite growth kinetics do show the effect of thermal path, the difference is present for a very short time making the ferrite growth kinetics, to a first approximation, additive under stepped-isothermal conditions, as found experimentally.

Model predictions of carbon concentration profiles in front of the growing ferrite under isothermal and stepped-isothermal conditions one second after the change in temperature were compared, as shown in Fig. 6.15. As can be seen, a steep carbon profile results at the α/γ interface due to changing the boundary conditions from $803°C$ to $764°C$ and should give rise to initially high growth rates. It is also evident from Fig. 6.15 that these steep profiles are spread over just 3 microns from the α/γ interface and that the rest of the profile remains unaffected, matching closely with the isothermal profile at $764°C$. Since the ferrite growth rate is determined by the carbon gradient at the α/γ interface, the system quickly attains the isothermal carbon gradient and therefore the isothermal growth rate as well. Although the effect of changing the equilibrium boundary conditions initially results in enhanced proeutectoid ferrite transformation kinetics, this transient effect is short-lived and the overall transformation kinetics under stepped-isothermal conditions approximate those of the isothermal conditions, thereby supporting the observed experimental additivity of the transformation.

The planar model was also used to predict the stepped-isothermal growth kinetics under conditions of significant soft impingement at the first isothermal transformation temperature. Figure 6.16 shows the model-predicted isothermal and stepped-isothermal ferrite growth at $800°C$ and $760°C$, good agreement between the two being obtained. The carbon profile under stepped-isothermal condition was compared to the isothermal ($760°C$) carbon profile, as shown in Fig. 6.17. The decrease in temperature results in a sudden increase in the carbon gradient just in front of the α/γ interface, which in turn, increases the

ferrite growth rate. The carbon gradient predicted after the step change matches with the isothermal gradient at 800°C in 4 seconds, as shown in Fig. 6.17. However, this transient effect can not be observed in the overall ferrite growth kinetics shown in Fig. 6.16, and thus supports the experimental additivity of the ferrite transformation.

The model was also used to predict the ferrite growth kinetics under conditions of step-up quench, where the initial temperature is less than the final temperature. An increase in the temperature of the system after partial transformation at a lower temperature results in a situation where the ferrite initially shrinks and then starts growing again. The initial shrinking is due to the boundary compositions (C_γ and C_α) being smaller in magnitude at higher temperature. Although the experimental results did not show this shrinkage as the thermal expansion masked the effect, the model predictions were useful in analyzing the situation. As shown in Fig. 6.18, the model-predicted ferrite thickness vs. time for isothermal and step-up isothermal conditions shows good agreement, although the shrinking of the ferrite is seen on a magnified scale. The growth rate for the step-up condition initially showed a negative rate which confirmed some shrinking of the ferrite. However, as shown in Fig. 6.19, the model-predicted ferrite growth rate under step-up conditions very quickly attained the isothermal growth rate at 764°C, thereby illustrating the experimental additivity of the ferrite transformation under the condition of increasing temperature. The model-predicted carbon profiles presented in Fig. 6.20 show the effect of temperature increase, whereby the resulting carbon gradients in front of the α/γ interface initially have positive slopes. These positive gradients result in shrinking of the ferrite phase. Once these gradients become negative, growth of the ferrite resumes. This switch from shrinkage to growth occurs in a short time (< 2 s) making the system experimentally additive.

6.2.2 Spherical Geometry

The spherical model which has been shown to be a closer approximation to the experimental observations, was employed to predict the proeutectoid ferrite growth kinetics

under stepped-isothermal transformation conditions. First, the model was employed to predict isothermal ferrite growth at temperatures identical to those obtained in the experimental stepped-isothermal tests. Figure 6.21 shows the model-predicted isothermal ferrite shell thickness vs. time at 803°C and 764°C, and the ferrite shell thickness for a step-down quench from 803°C to 764°C. As can be seen, good agreement is obtained between the ferrite thickness formed under stepped-isothermal and isothermal conditions at 764°C. The ferrite growth rates for stepped-isothermal and isothermal conditions were also compared, as shown in Fig. 6.22. The growth rate increases significantly compared to the isothermal growth rate at 764°C, when the temperature of the system is changed from 803°C to 764°C. However, this increase in growth rate is present for a short time and the overall ferrite growth rate quickly returns to the isothermal growth rate, as indicated in Fig. 6.21. The carbon profiles for the stepped-isothermal condition were compared to the isothermal profile at the same ferrite shell thickness, as shown in Fig. 6.23. Although the profile after the step change shows a steeper gradient, this profile quickly attains the isothermal carbon profile within 3 seconds.

The spherical model was also used to analyze the effect of soft impingement on the stepped-isothermal ferrite growth kinetics by initiating the temperature change after soft impingement had occurred. In order to compare with the planar model predictions and the experimental observations, the same isothermal test temperatures were selected, i.e., 800°C and 760°C. The model-predicted isothermal and stepped-isothermal ferrite growth is shown in Fig. 6.24. As can be seen, the stepped-isothermal ferrite growth compares moderately well with isothermal ferrite growth at 760°C.

The 760°C isothermal carbon profile was compared with the profile obtained for the stepped-isothermal condition at the same ferrite shell thickness, as shown in Fig. 6.25. The change in temperature from 800°C to 760°C initially gives rise to a steep carbon gradient in front of the α/γ interface. This steep gradient results in an increased ferrite growth rate.

However, with increasing time (within less than 5 seconds) the gradient approaches that of the isothermal profile and the isothermal ferrite growth rate is attained. Since the increase in the ferrite growth rate is only transient, the spherical model predictions are in agreement with the experimentally observed additivity of the ferrite transformation.

The effect of a step-up quench on the ferrite growth kinetics was also analyzed using the spherical model. A temperature increase after partial transformation at a lower temperature results in initial shrinking of the ferrite phase before it starts growing again, as shown in Fig. 6.26. The model-predicted ferrite shell thickness at the higher temperature, after the step-up, compares moderately well with the isothermal ferrite shell thickness. This was seen by plotting the growth rate as a function of time for the step-up condition, giving a negative rate, as can be seen from Fig. 6.27. The growth rate attained the isothermal growth rate at $764°C$ a short time after the temperature change, thereby supporting the observed experimental additivity. The carbon profiles predicted using the spherical model for the step-up condition (Fig. 6.28) were very similar to those predicted using the planar model.

It should be emphasized that the model assumptions of site saturation and instantaneous attainment of equilibrium boundary conditions restrict the model predictions to assessing only the effect of carbon gradient in front of the moving α/γ interface. However, similarity between the model-predicted and the experimentally observed step-isothermal transformation behaviour supports the validity of these assumptions. In addition, the large temperature changes (up to $40°C$) being used in the stepped-isothermal tests exaggerate the experimental continuous-cooling conditions previously employed to examine the additivity of the austenite-to-ferrite transformation[25].

ASTM Grain Size No.	Temperature (°C)	Calculated Ferrite Thickness (μm)	Planar Model Predicted Ferrite Thickness (μm)
1.5	800	73.08	72.97
5	803	22.21	22.22
5	800	23.04	23.01
5	764	27.47	27.47
5	750	28.59	28.57

Table 6.1- Comparison of ferrite thickness, as determined by a carbon mass balance and the planar model for equilibrium transformation conditions.

ASTM Grain Size No.	Temperature (°C)	Calculated Ferrite Thickness (μm)	Spherical Model Predicted Ferrite Thickness (μm)
1.5	800	34.07	34.01
5	803	10.16	10.12
5	800	10.75	10.73
5	764	14.51	14.48
5	750	15.74	15.71

Table 6.2- Comparison of ferrite thickness, as determined by a carbon mass balance and the spherical model for equilibrium transformation conditions..

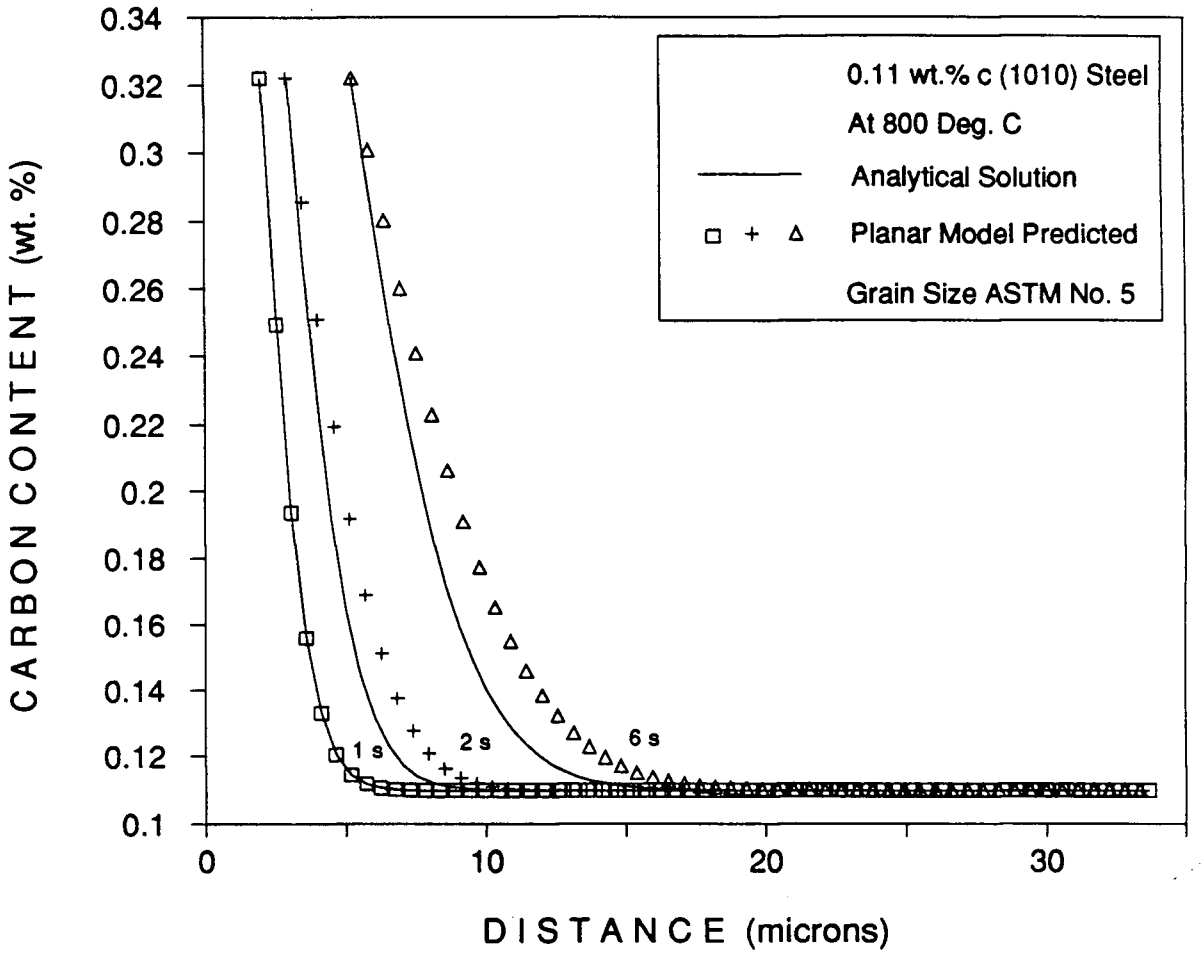

Fig. 6.1 - Comparison of planar model-predicted and analytically calculated carbon concentration profiles in front of growing ferrite at 800°C for the 1010 steel.

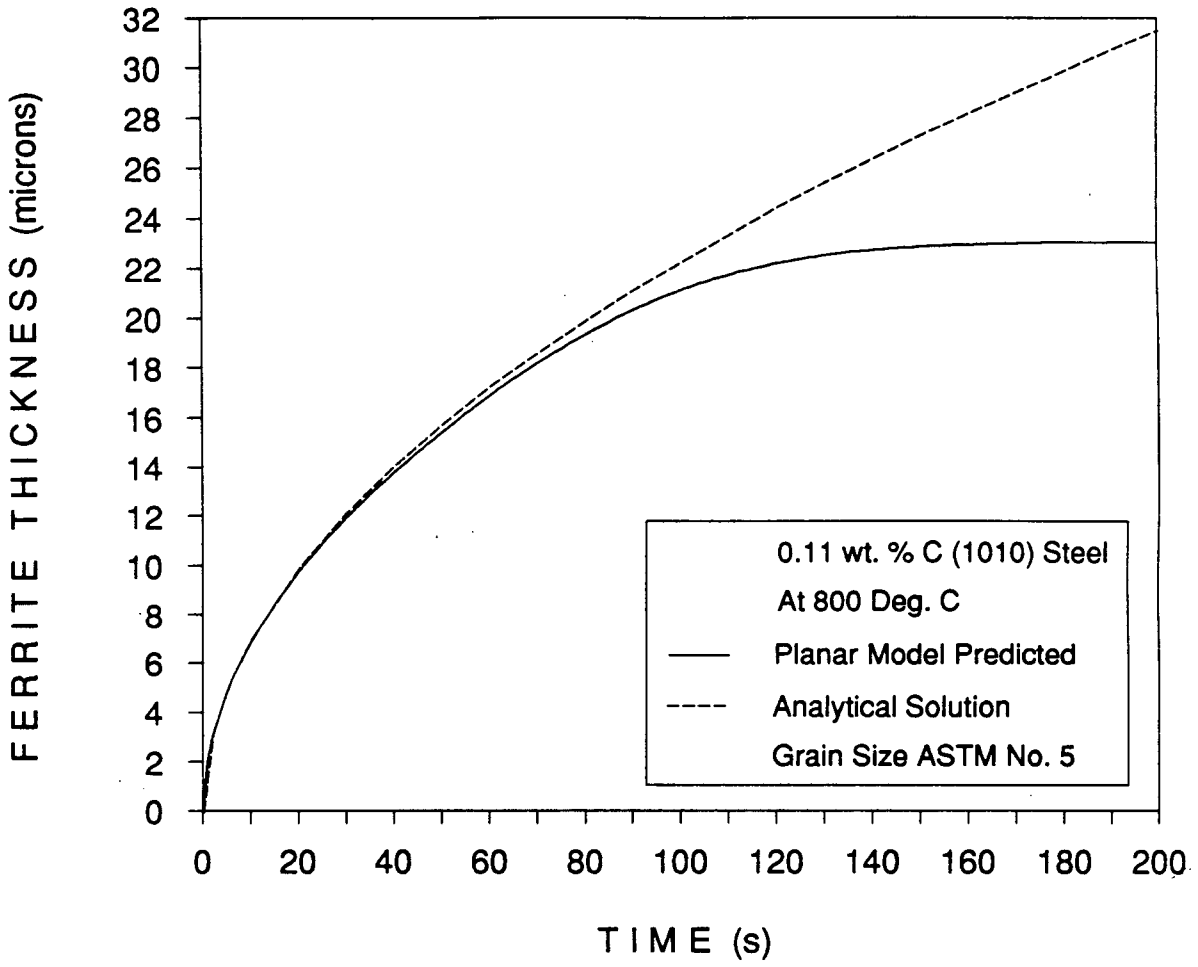

Fig. 6.2 - Comparison of planar model-predicted and analytically calculated ferrite growth at 800°*C* for the 1010 steel.

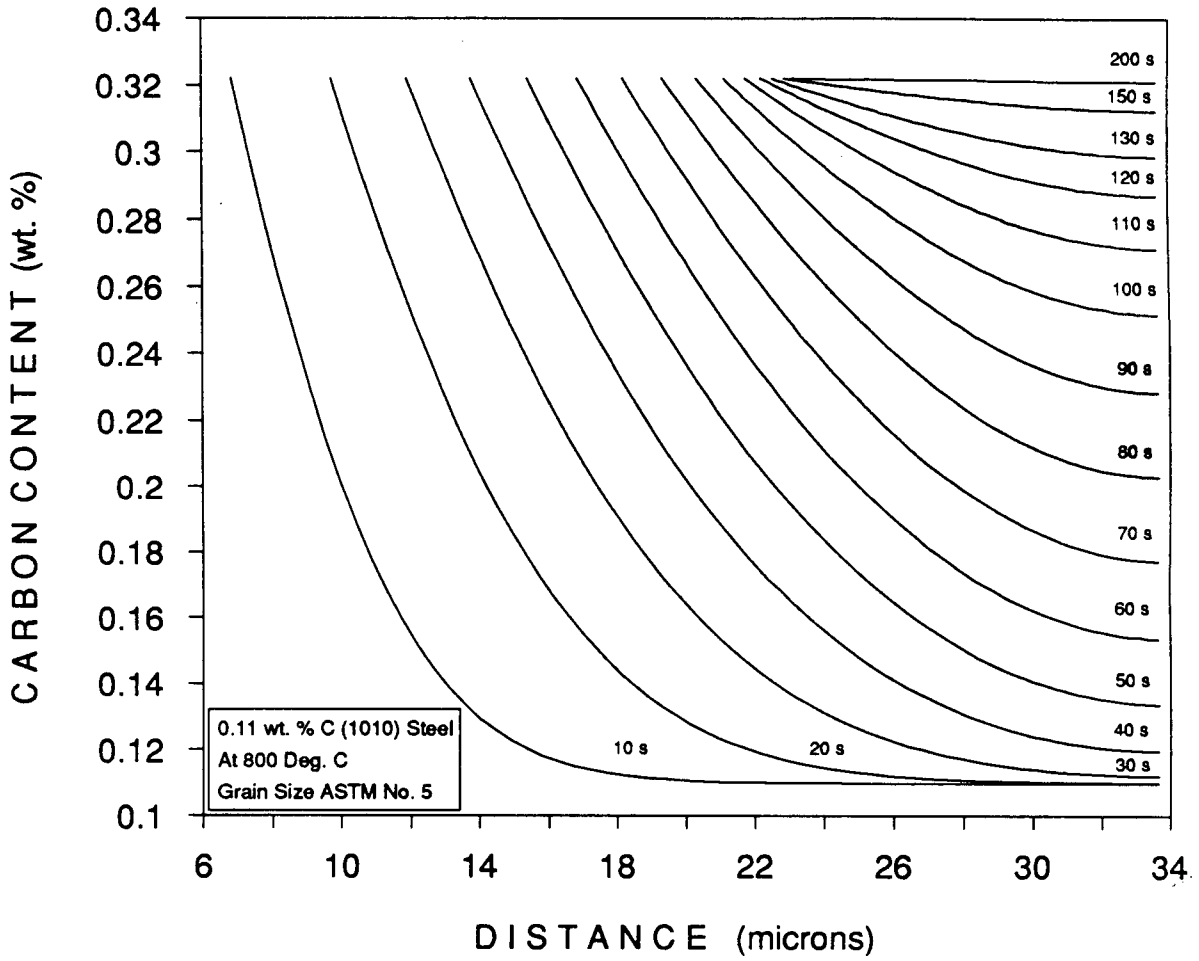

Fig. 6.3 - Planar model-predicted carbon concentration profiles in front of growing ferrite at 800°C for the 1010 steel.

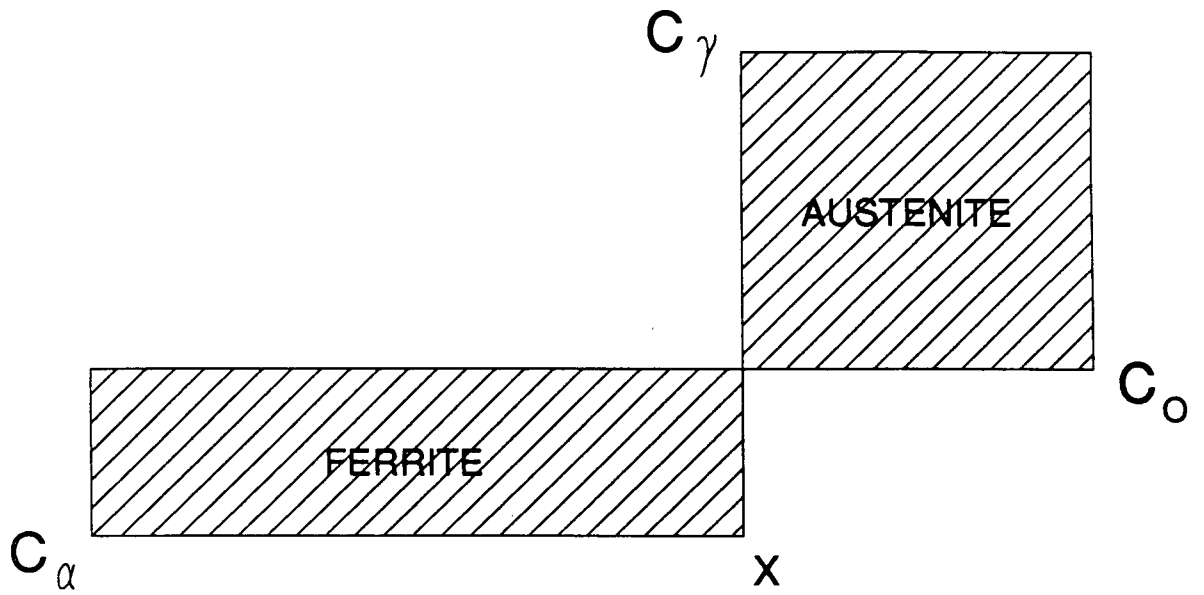

Fig. 6.4 - Schematic diagram showing the redistribution of carbon obtained at the completion of isothermal ferrite growth, upon attaining equilibrium conditions.

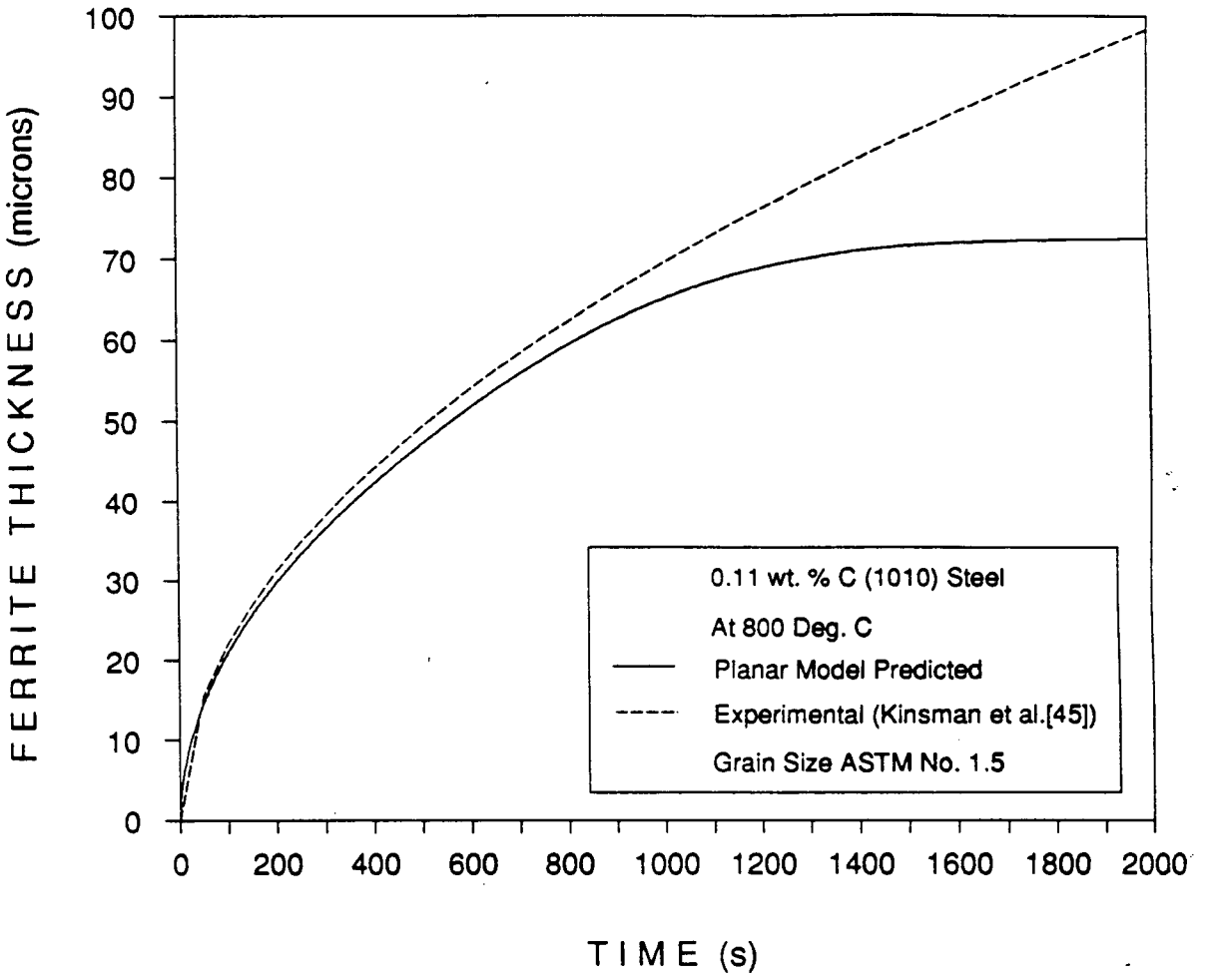

Fig. 6.5 - Comparison of planar model-predicted and experimental (Kinsman et al.[45]) ferrite growth at 800°*C* for the 1010 steel.

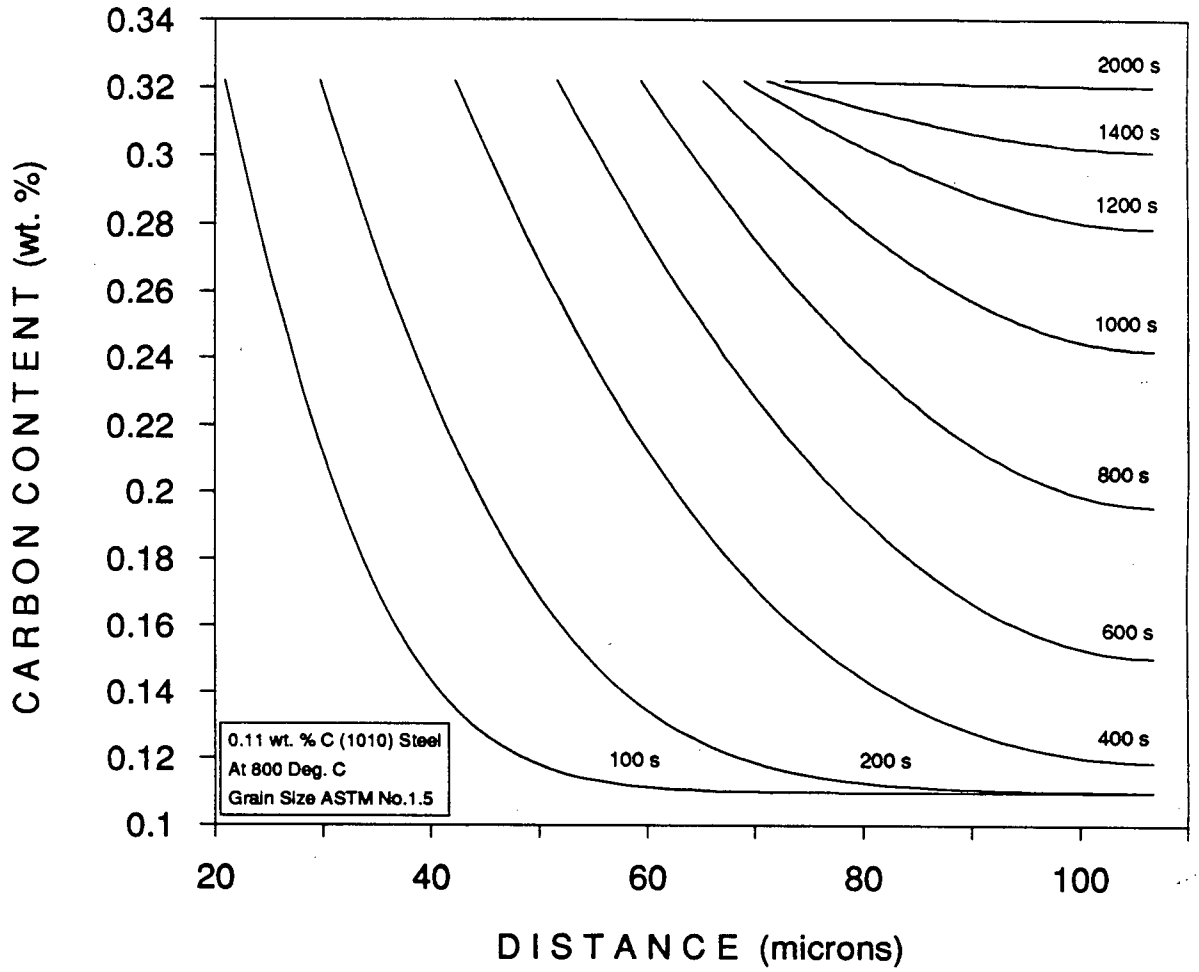

Fig. 6.6 - Planar model-predicted carbon concentration profiles in front of growing ferrite at 800°C for the 1010 steel.

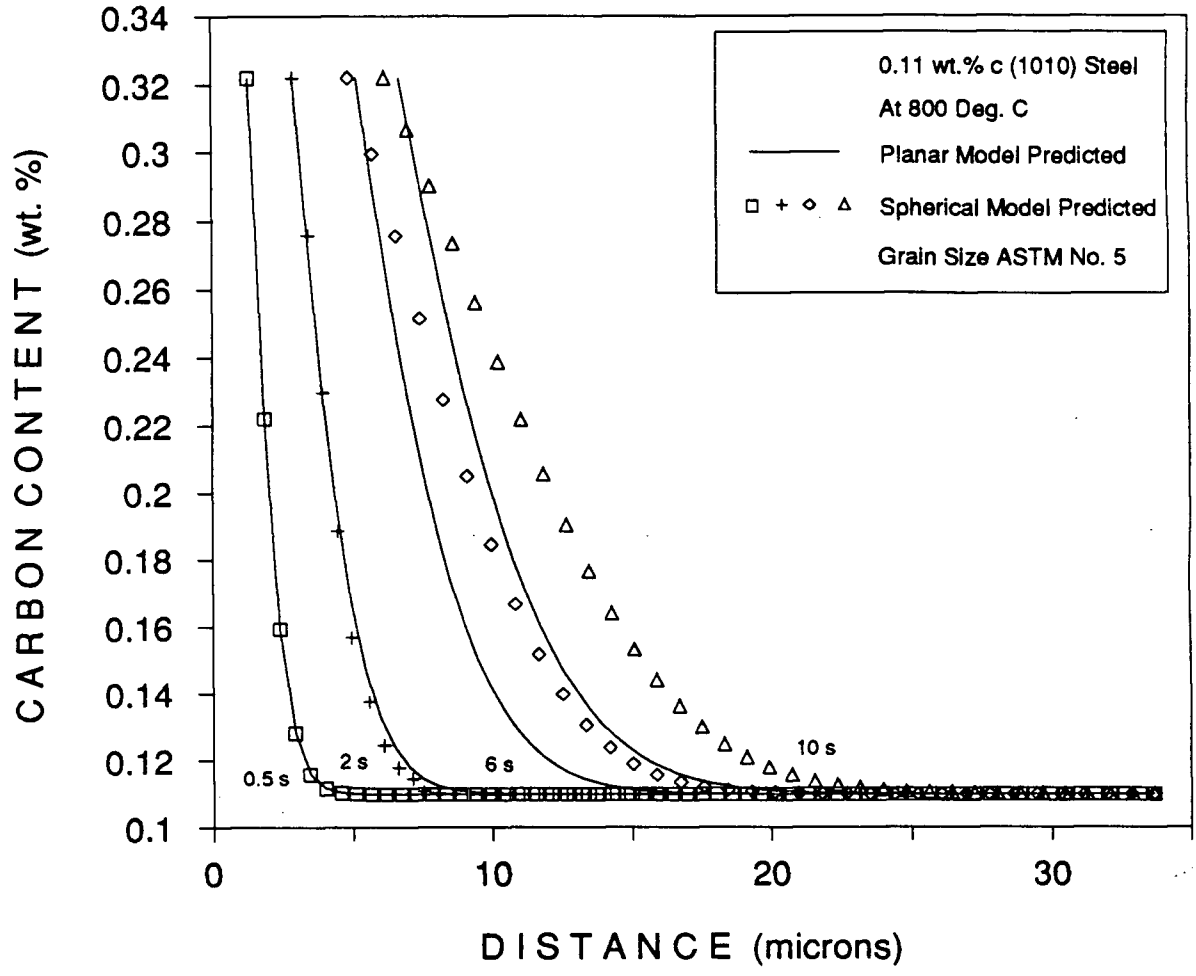

Fig. 6.7 - Comparison of planar and spherical model-predicted carbon concentration profiles in front of growing ferrite at 800°C for the 1010 steel.

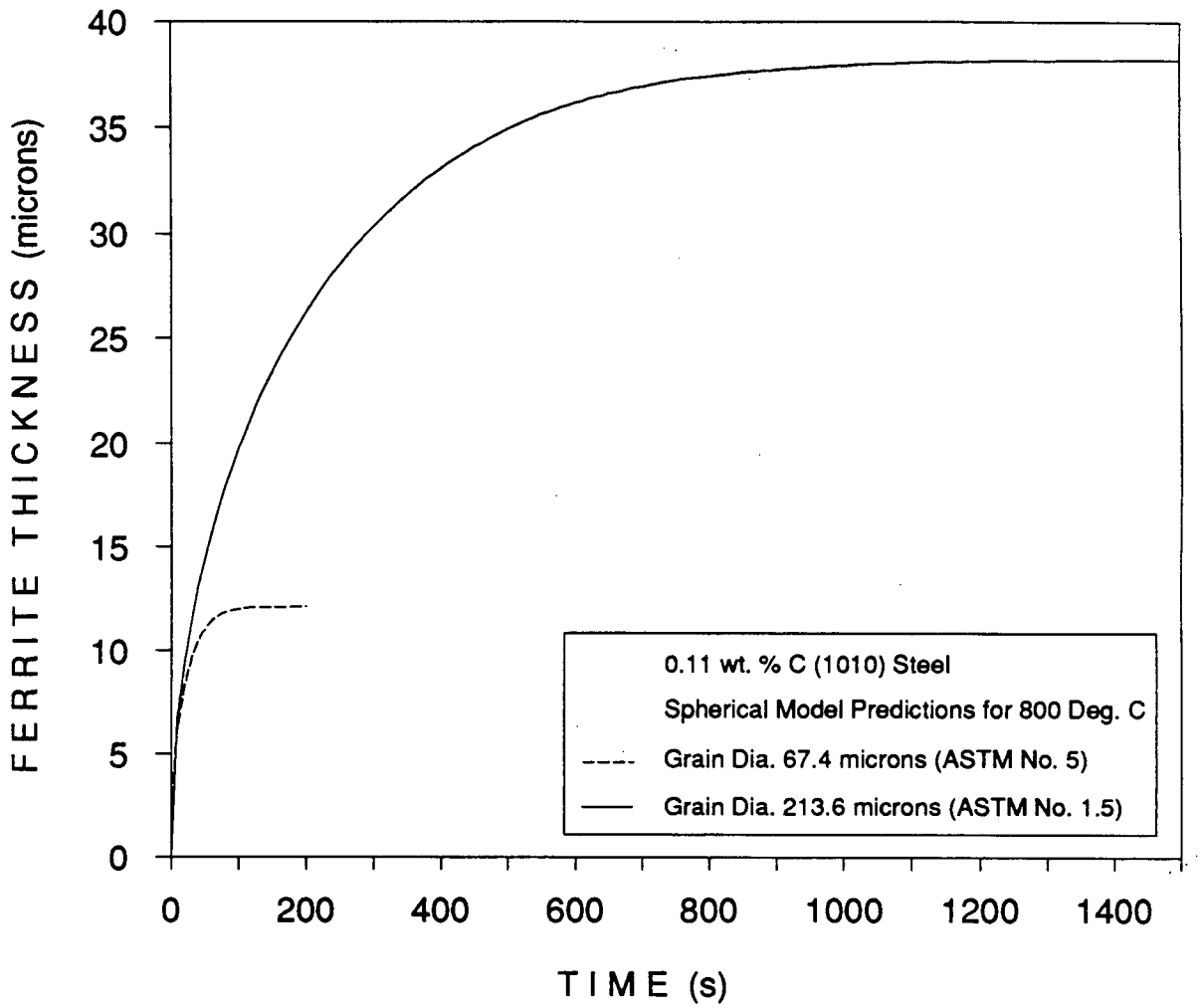

Fig. 6.8 - Spherical model-predicted ferrite growth at 800°*C* for the austenite grain size of ASTM No. 5 and 1.5 in the 1010 steel.

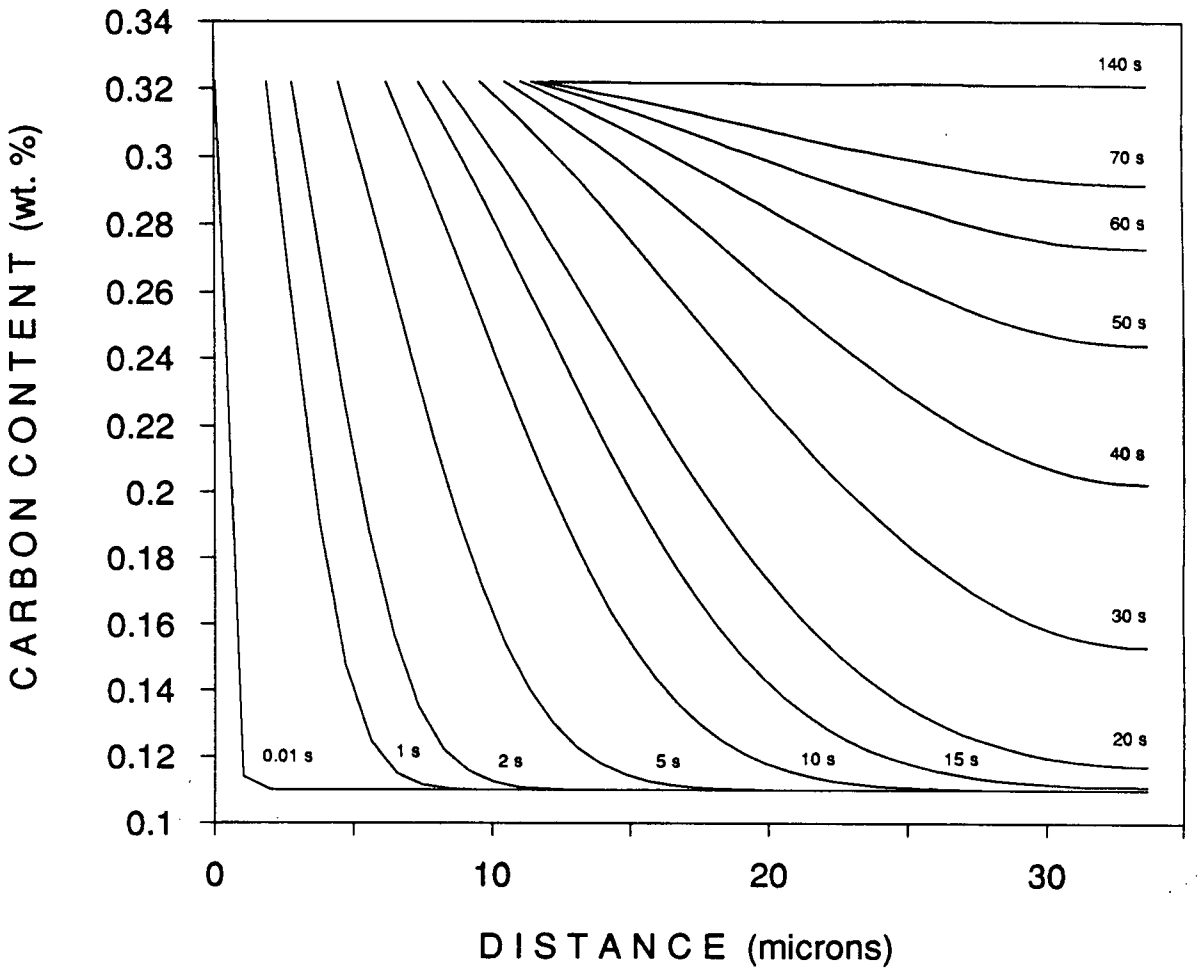

Fig. 6.9 - Spherical model-predicted carbon concentration profiles in front of growing ferrite at 800°*C* for the austenite grain size of ASTM No. 5 in the 1010 steel.

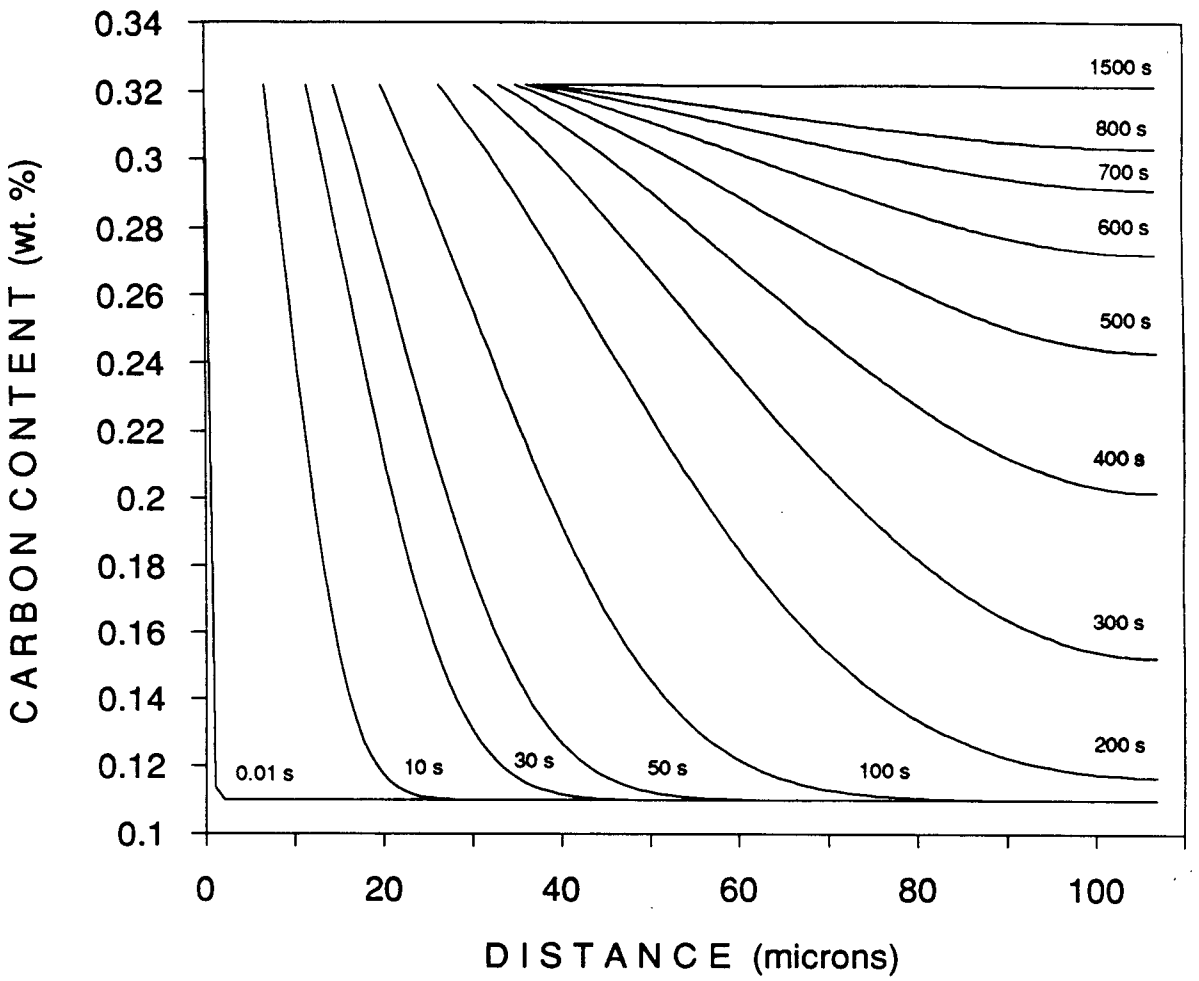

Fig. 6.10 - Spherical model-predicted carbon concentration profiles in front of growing ferrite at 800°*C* for the austenite grain size of ASTM No. 1.5 in the 1010 steel.

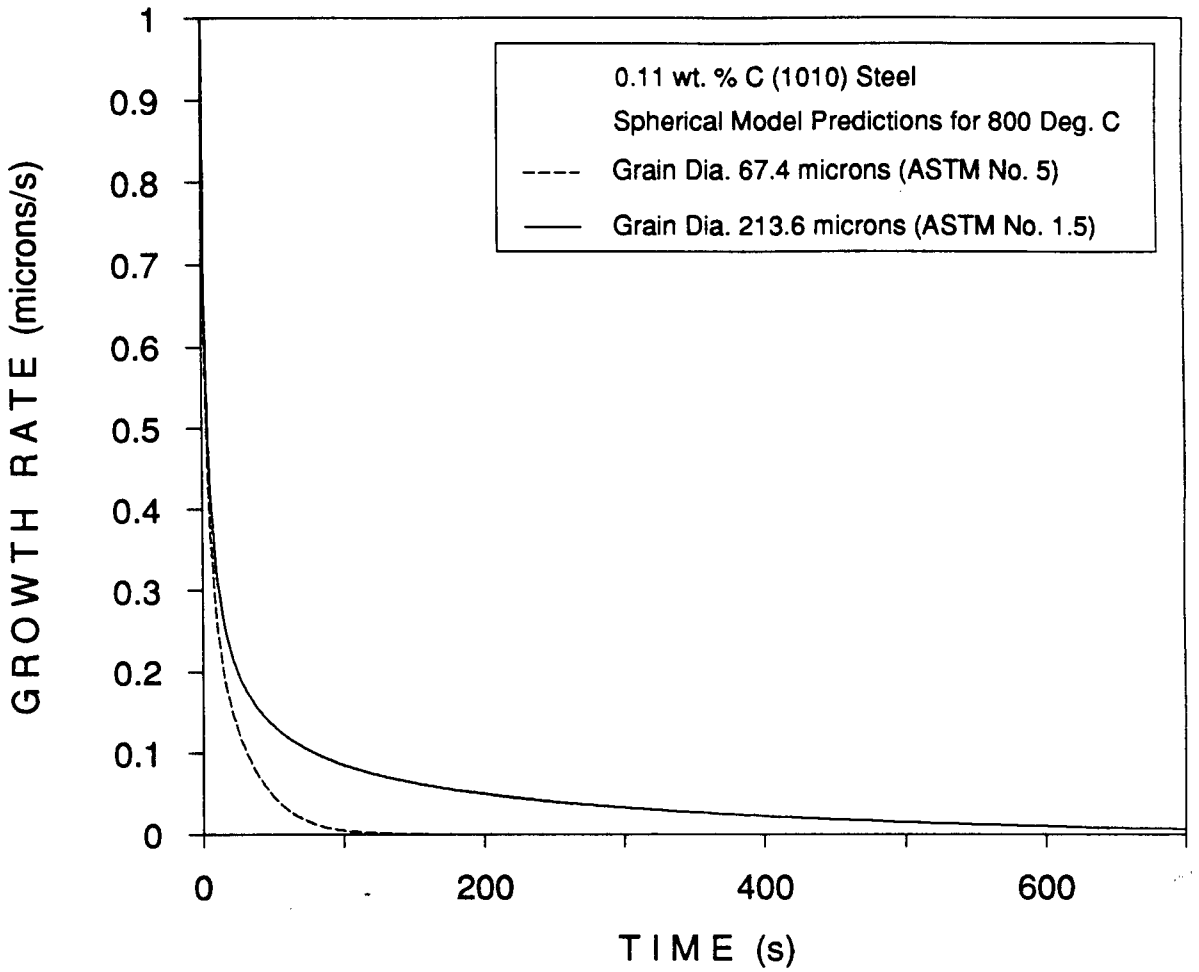

Fig. 6.11 - Spherical model-predicted ferrite growth rate at 800°*C* for the austenite grain size of ASTM No. 5 and 1.5 in the 1010 steel.

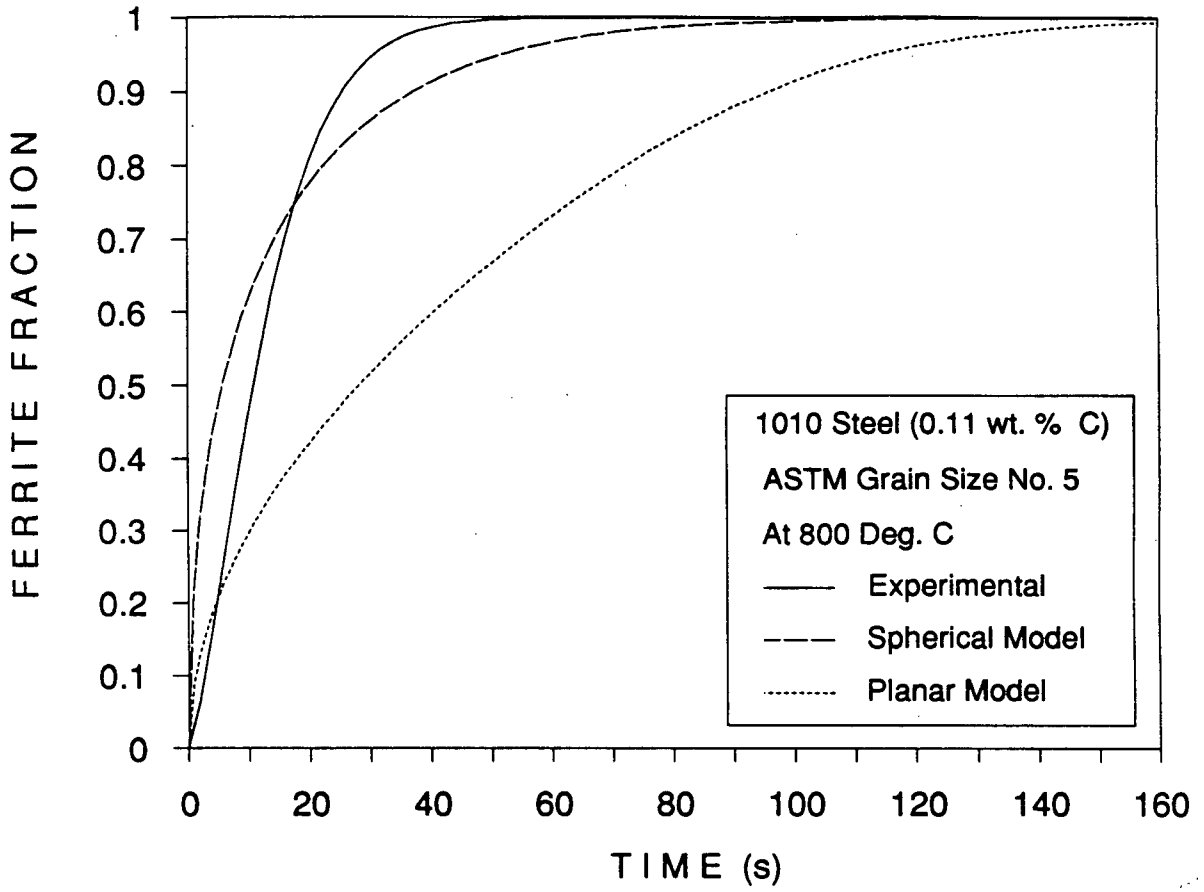

Fig. 6.12 - Comparison of experimental ferrite fraction with the planar and spherical model-predicted ferrite fraction at 800°*C* for the austenite grain size of ASTM No. 5 in the 1010 steel.

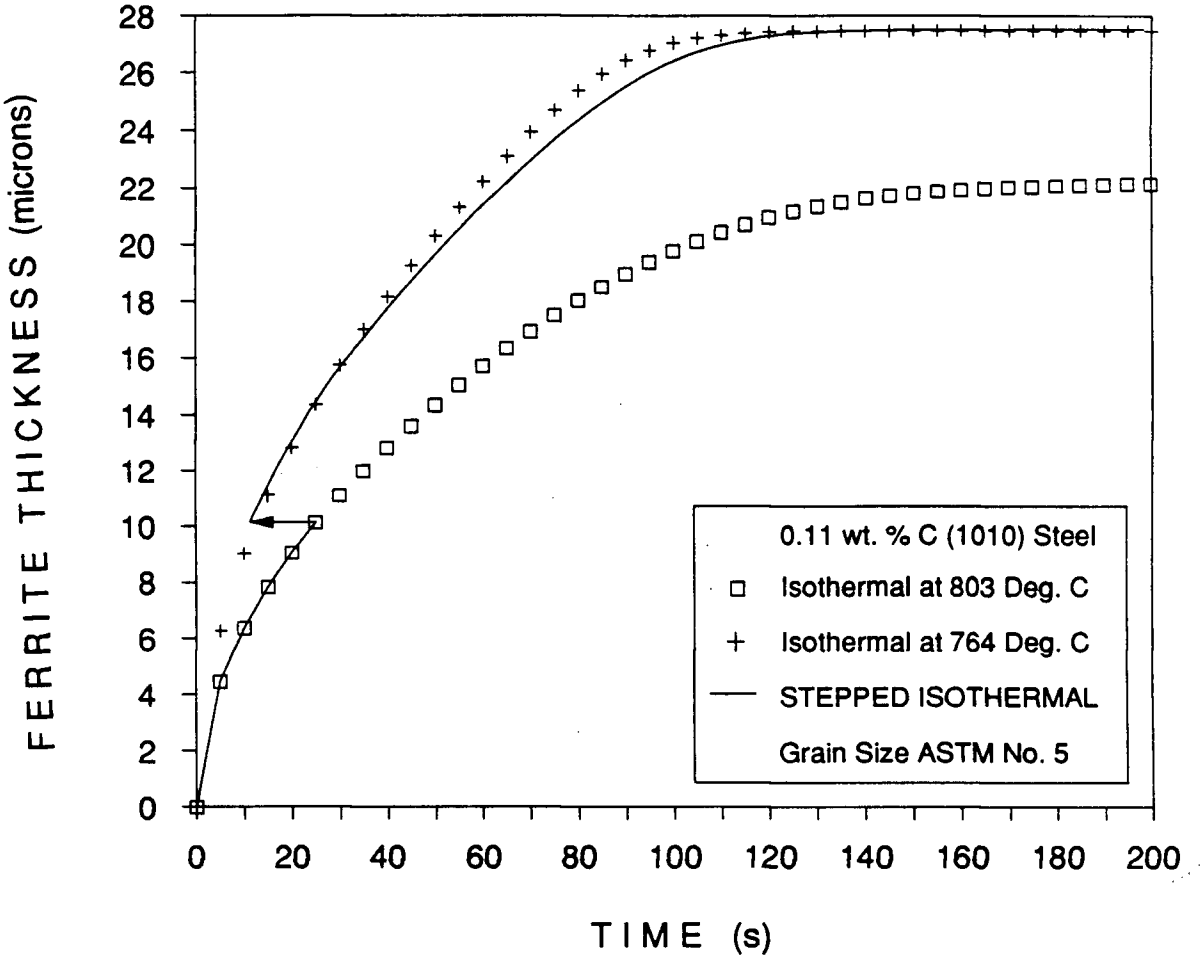

Fig. 6.13 - Planar model-predicted isothermal and step-down isothermal ferrite growth for the austenite grain size of ASTM No. 5 in the 1010 steel.

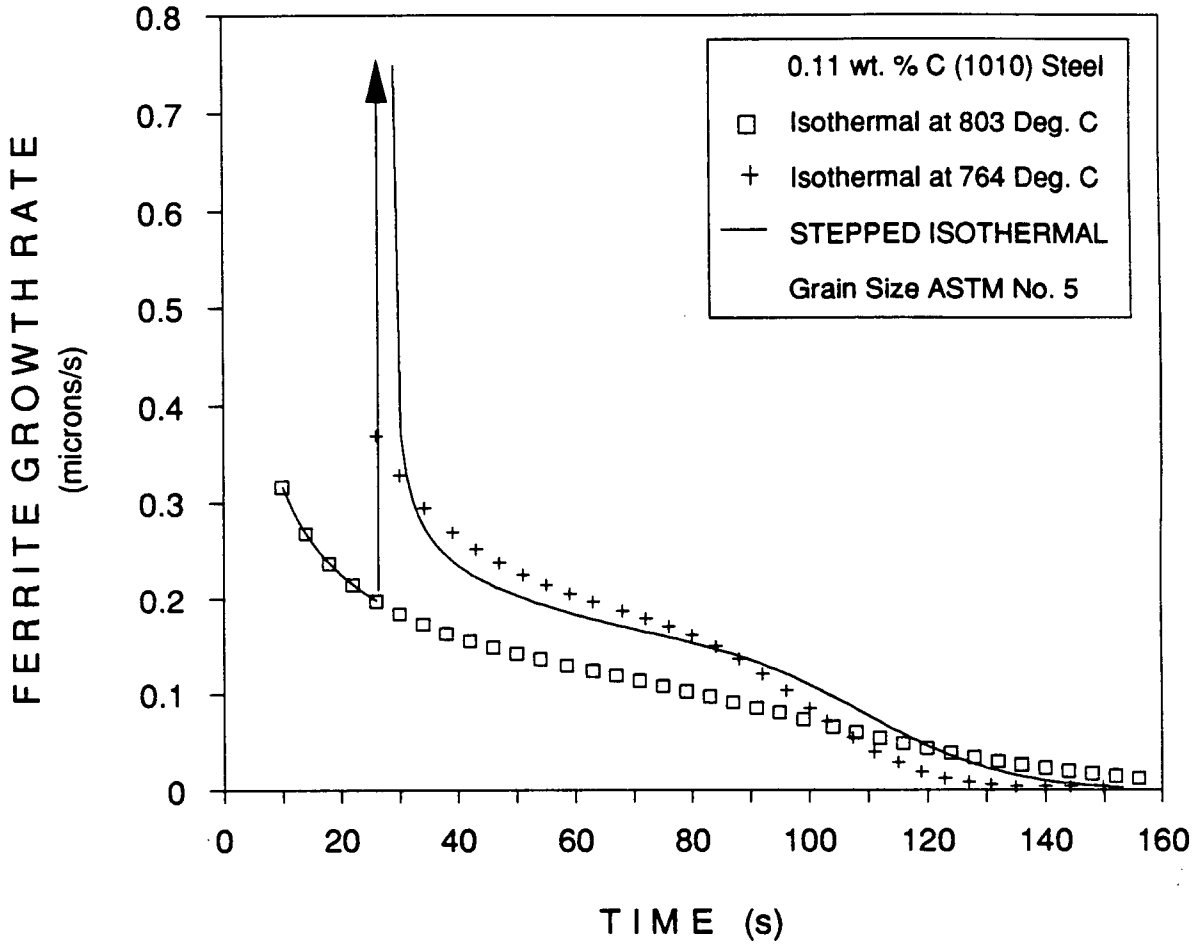

Fig. 6.14 - Planar model-predicted isothermal and step-down isothermal ferrite growth rate for the austenite grain size of ASTM No. 5 in the 1010 steel.

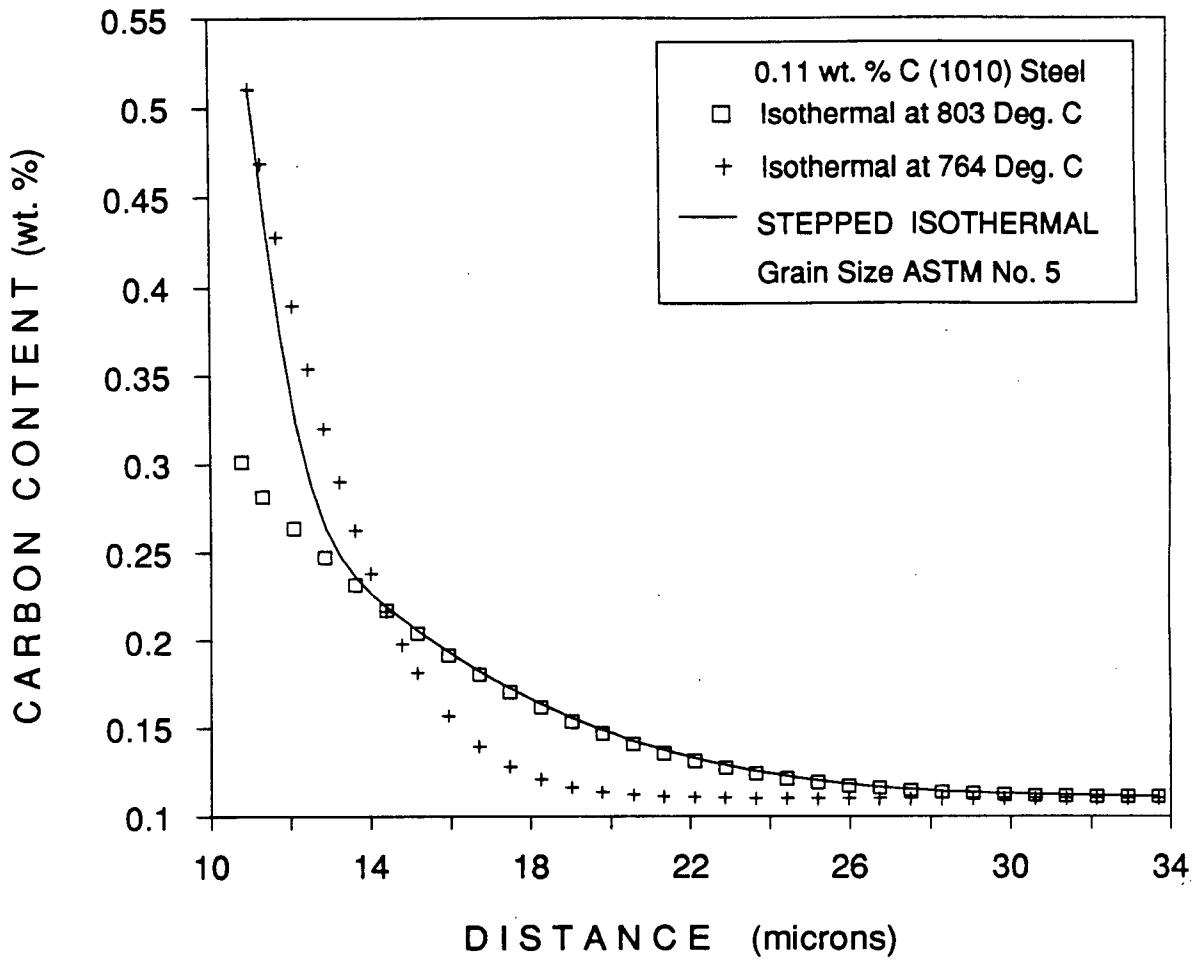

Fig. 6.15 - Planar model-predicted carbon concentration profiles in front of growing ferrite under isothermal and stepped-isothermal conditions one second after the change in temperature for the austenite grain size of ASTM No. 5 in the 1010 steel.

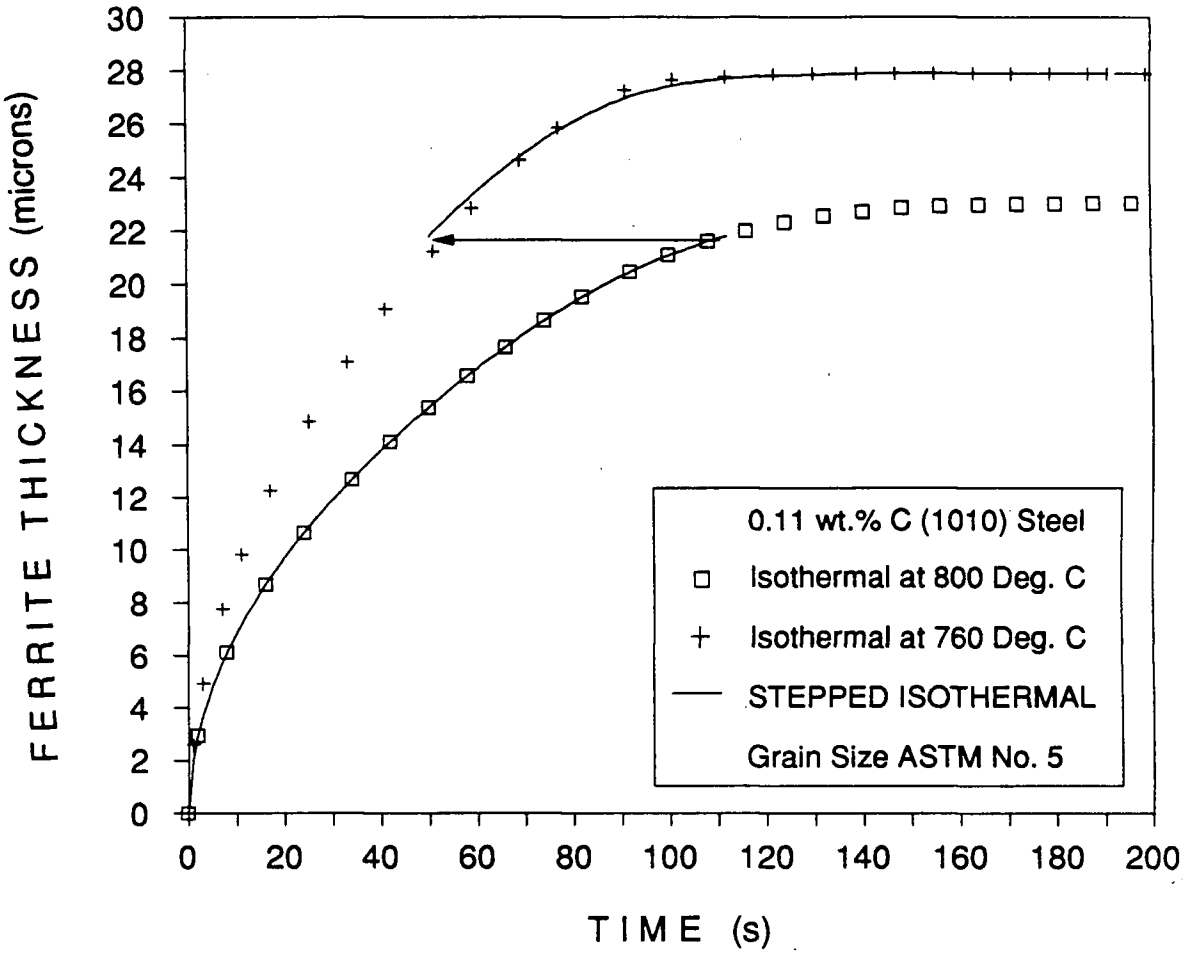

Fig. 6.16 - Planar model-predicted isothermal and step-down isothermal ferrite growth for the austenite grain size of ASTM No. 5 in the 1010 steel.

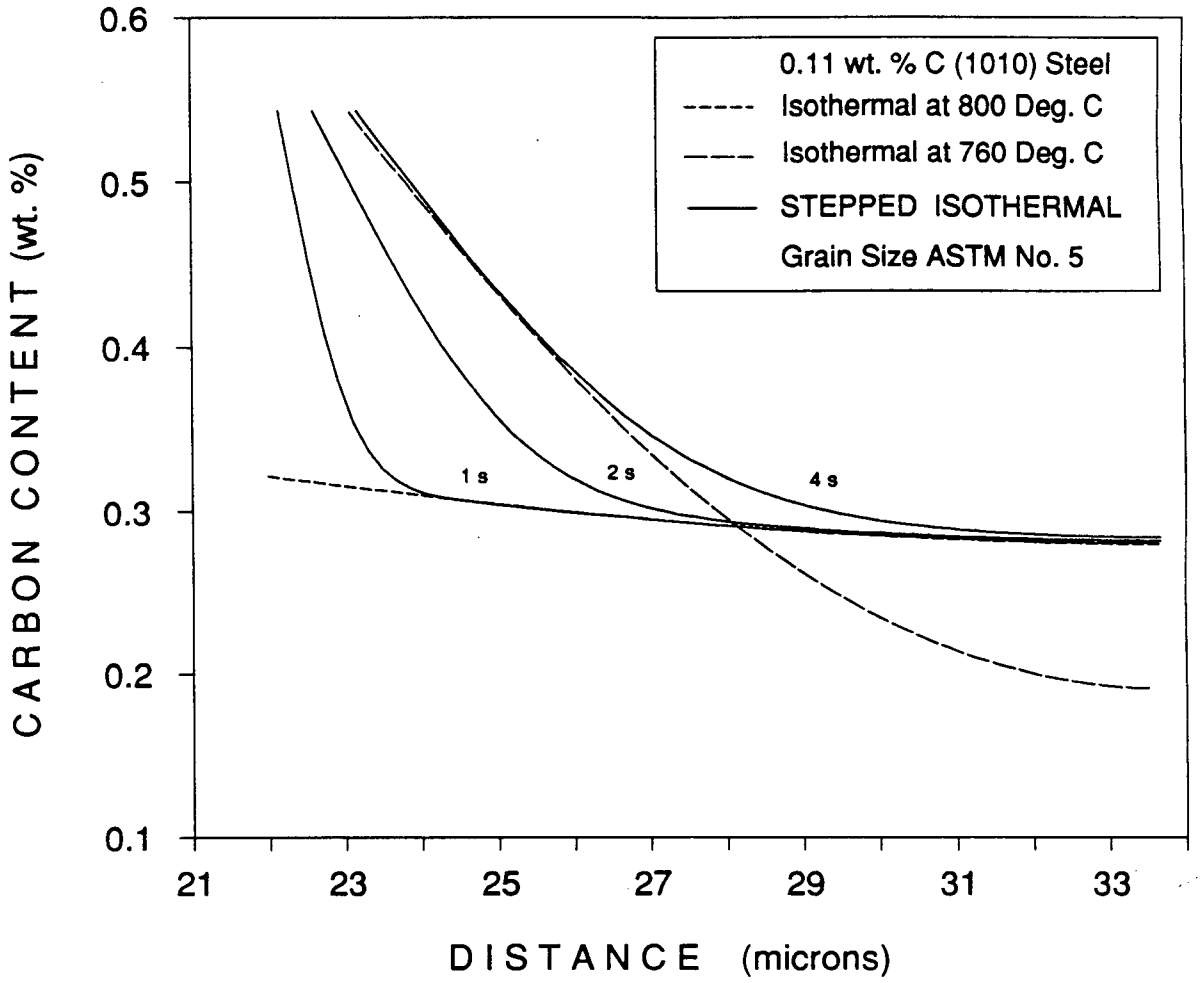

Fig. 6.17 - Planar model-predicted carbon concentration profiles in front of growing ferrite under isothermal and stepped-isothermal conditions for the austenite grain size of ASTM No. 5 in the 1010 steel.

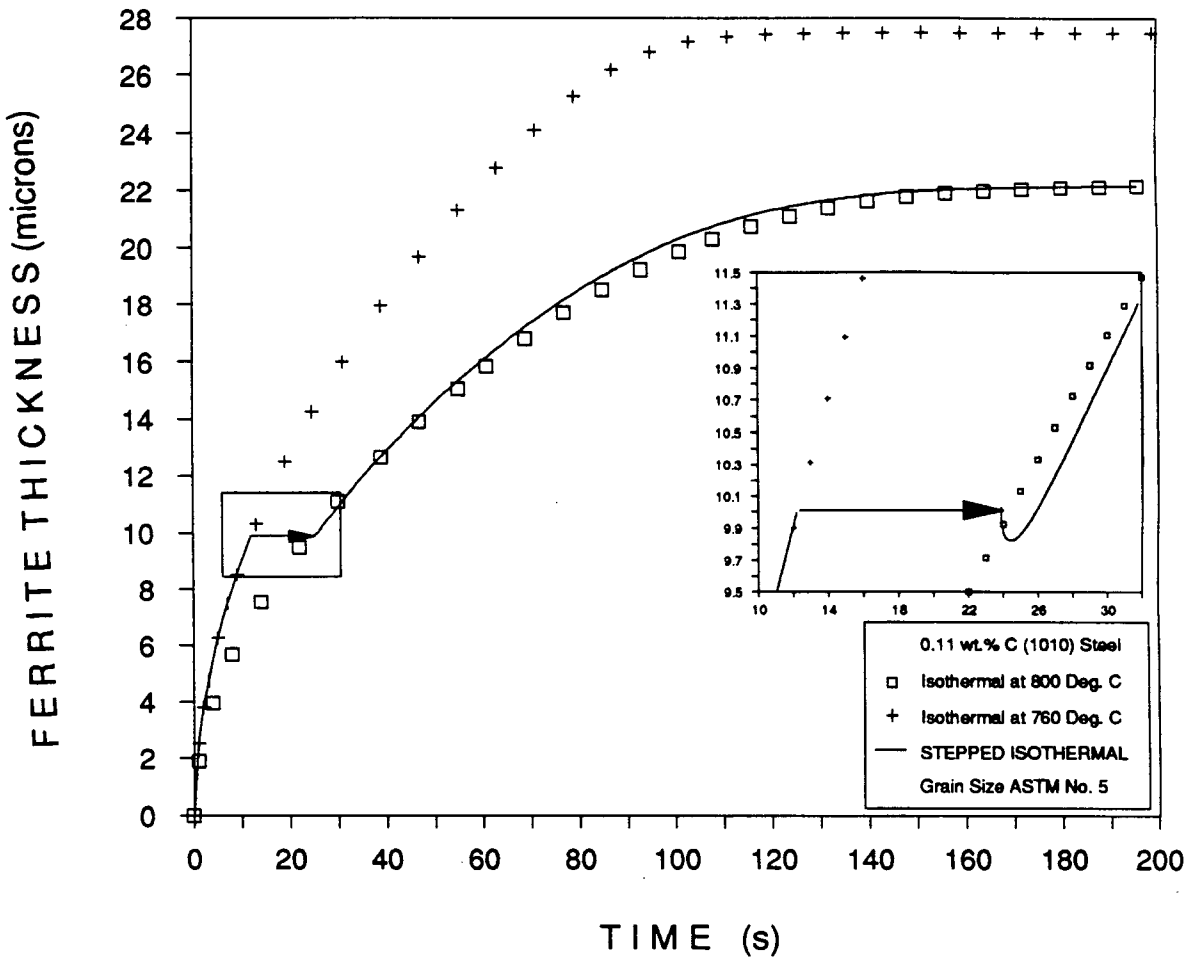

Fig. 6.18 - Planar model-predicted isothermal and step-up isothermal ferrite growth for the austenite grain size of ASTM No. 5 in the 1010 steel.

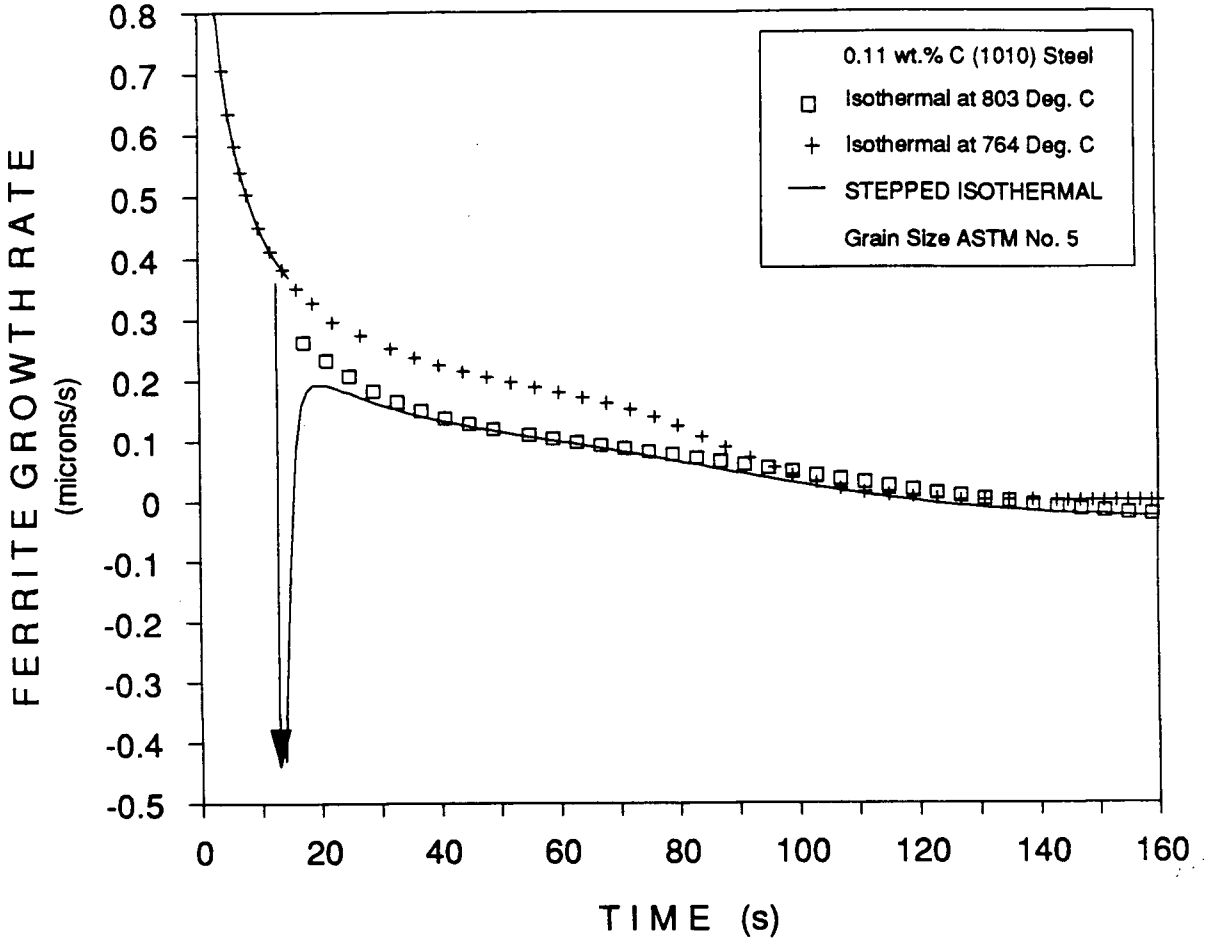

Fig. 6.19 - Planar model-predicted isothermal and step-up isothermal ferrite growth rate for the austenite grain size of ASTM No. 5 in the 1010 steel.

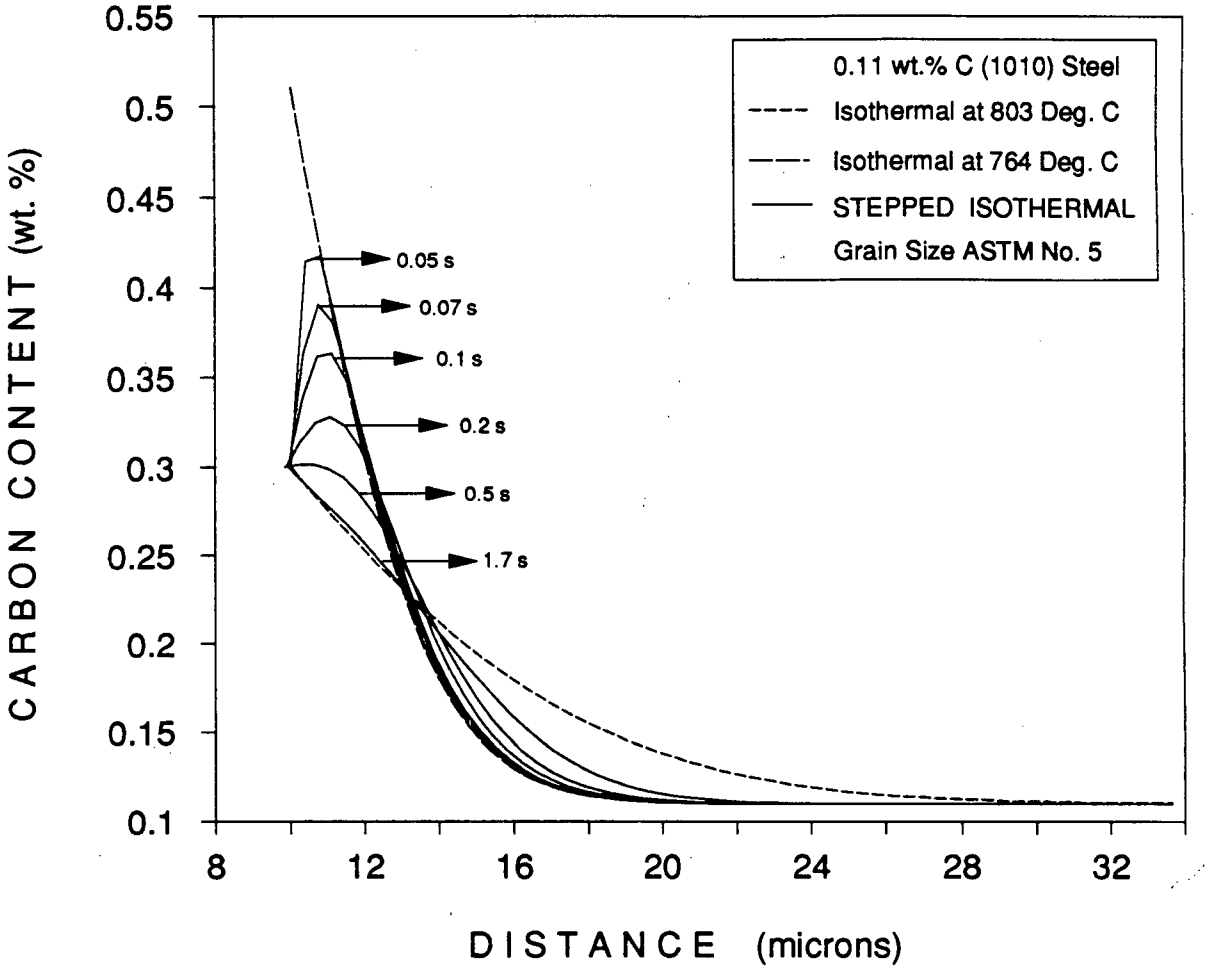

Fig. 6.20 - Planar model-predicted carbon concentration profiles in front of growing ferrite under isothermal and stepped-isothermal conditions for the austenite grain size of ASTM No. 5 in the 1010 steel.

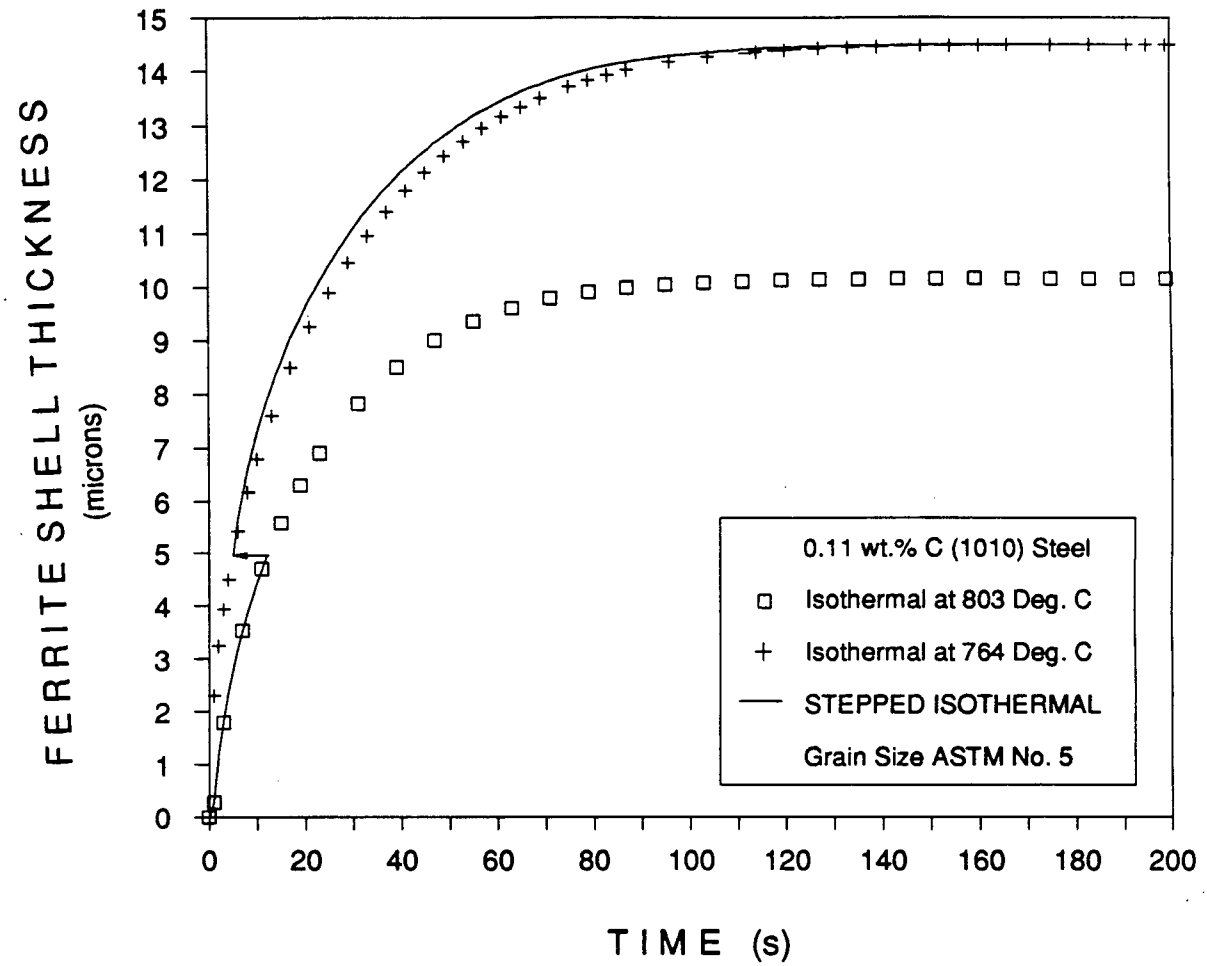

Fig. 6.21 - Spherical model-predicted isothermal and step-down isothermal ferrite growth for the austenite grain size of ASTM No. 5 in the 1010 steel.

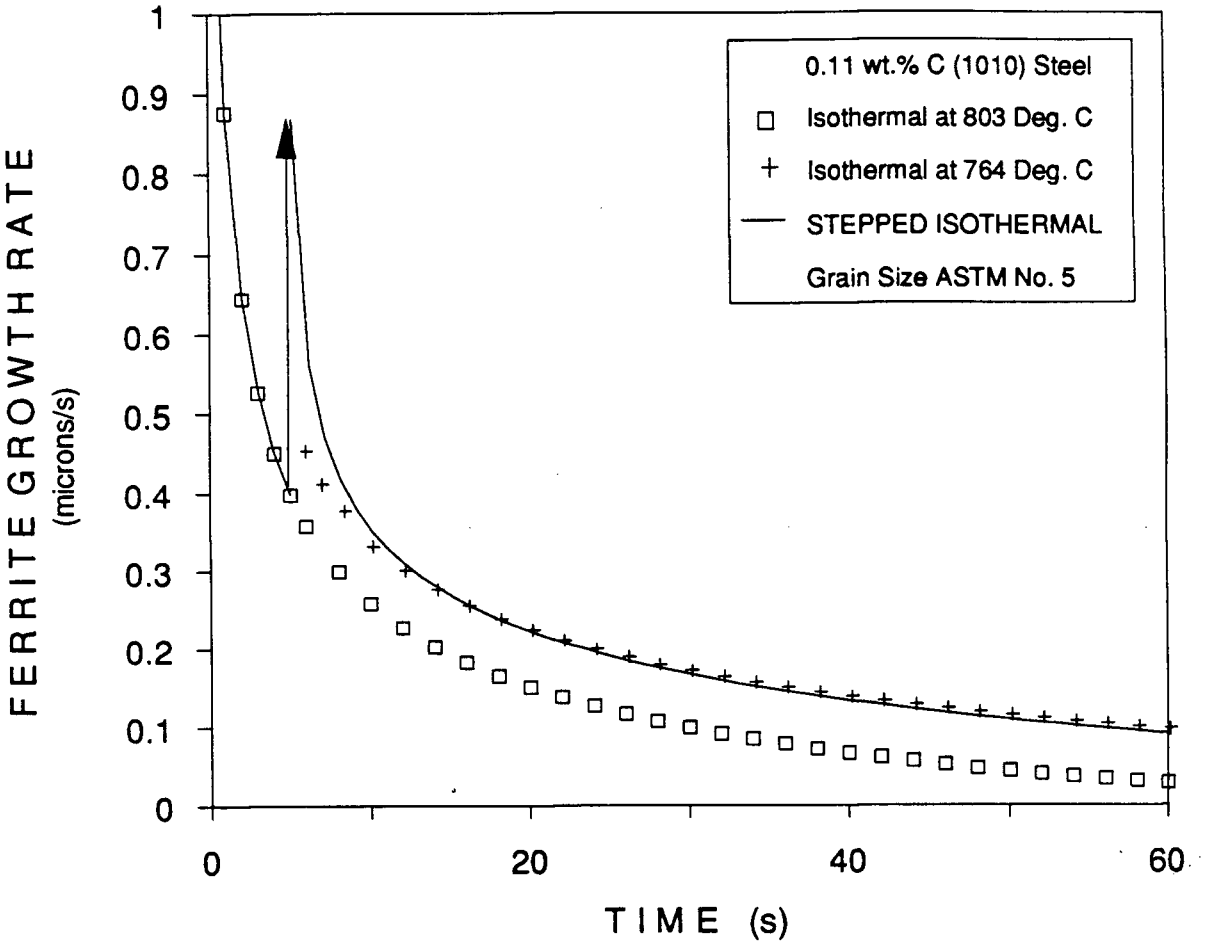

Fig. 6.22 - Spherical model-predicted isothermal and step-down isothermal ferrite growth rate for the austenite grain size of ASTM No. 5 in the 1010 steel.

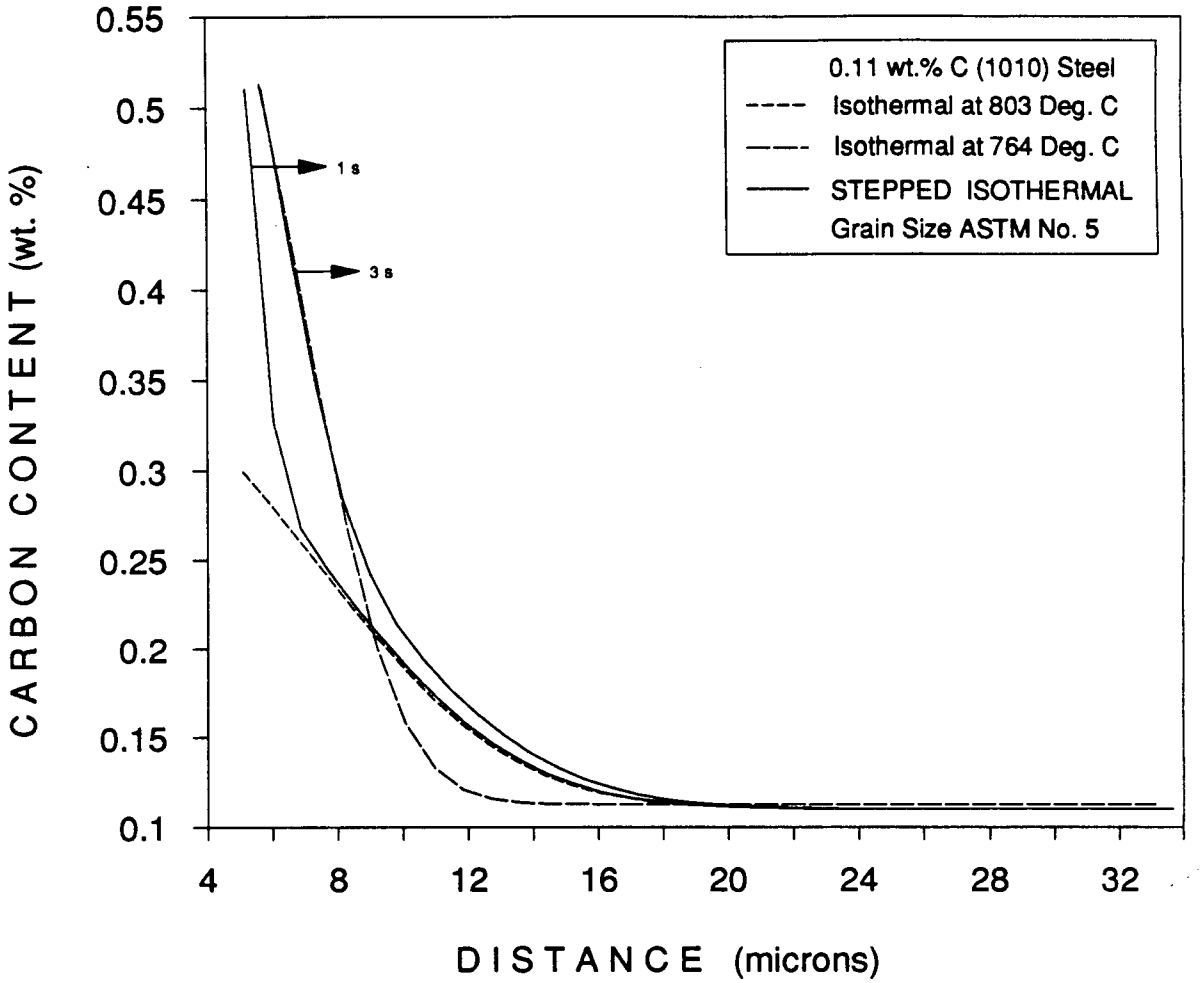

Fig. 6.23 - Spherical model-predicted carbon concentration profiles in front of growing ferrite under isothermal and stepped-isothermal conditions for the austenite grain size of ASTM No. 5 in the 1010 steel.

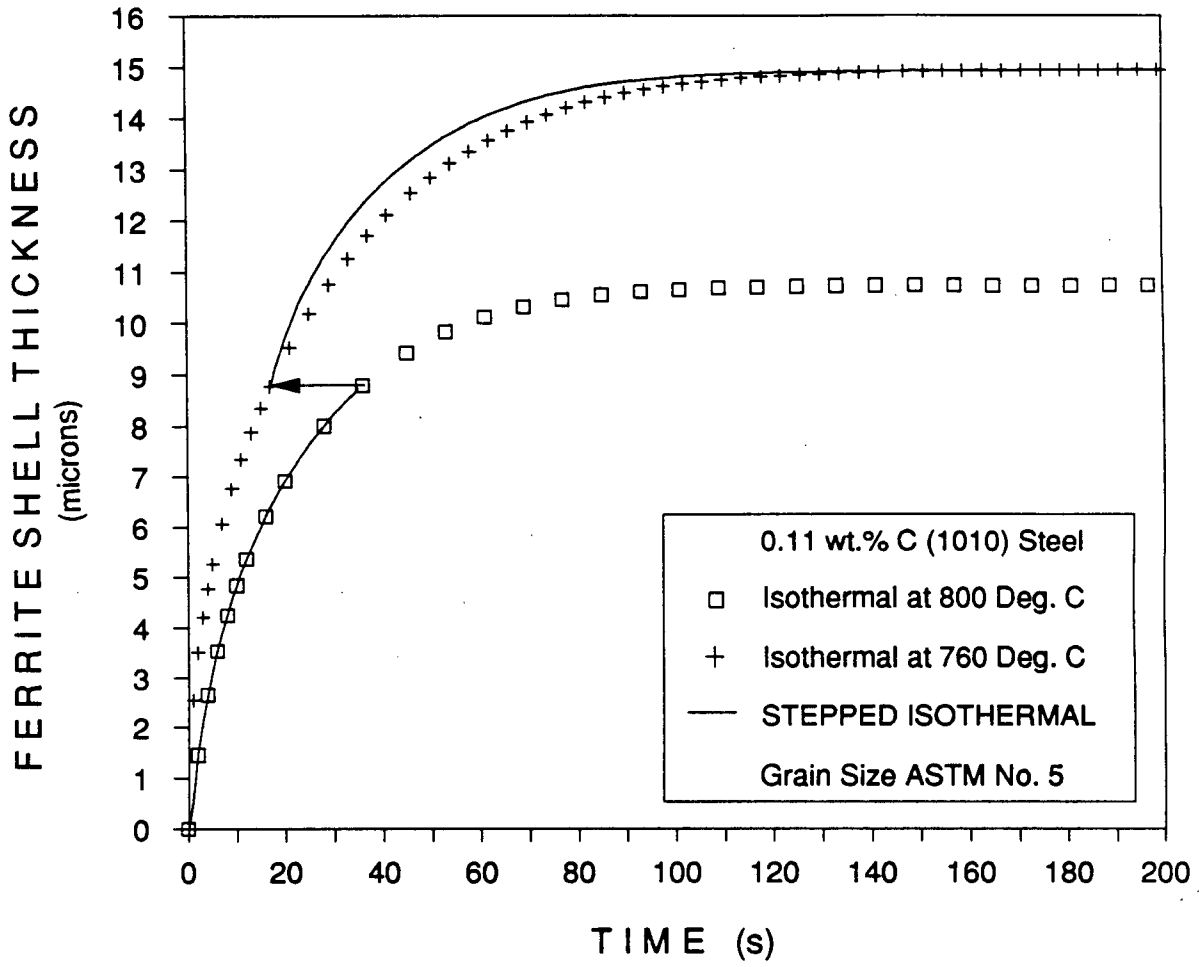

Fig. 6.24 - Spherical model-predicted isothermal and step-down isothermal ferrite growth for the austenite grain size of ASTM No. 5 in the 1010 steel.

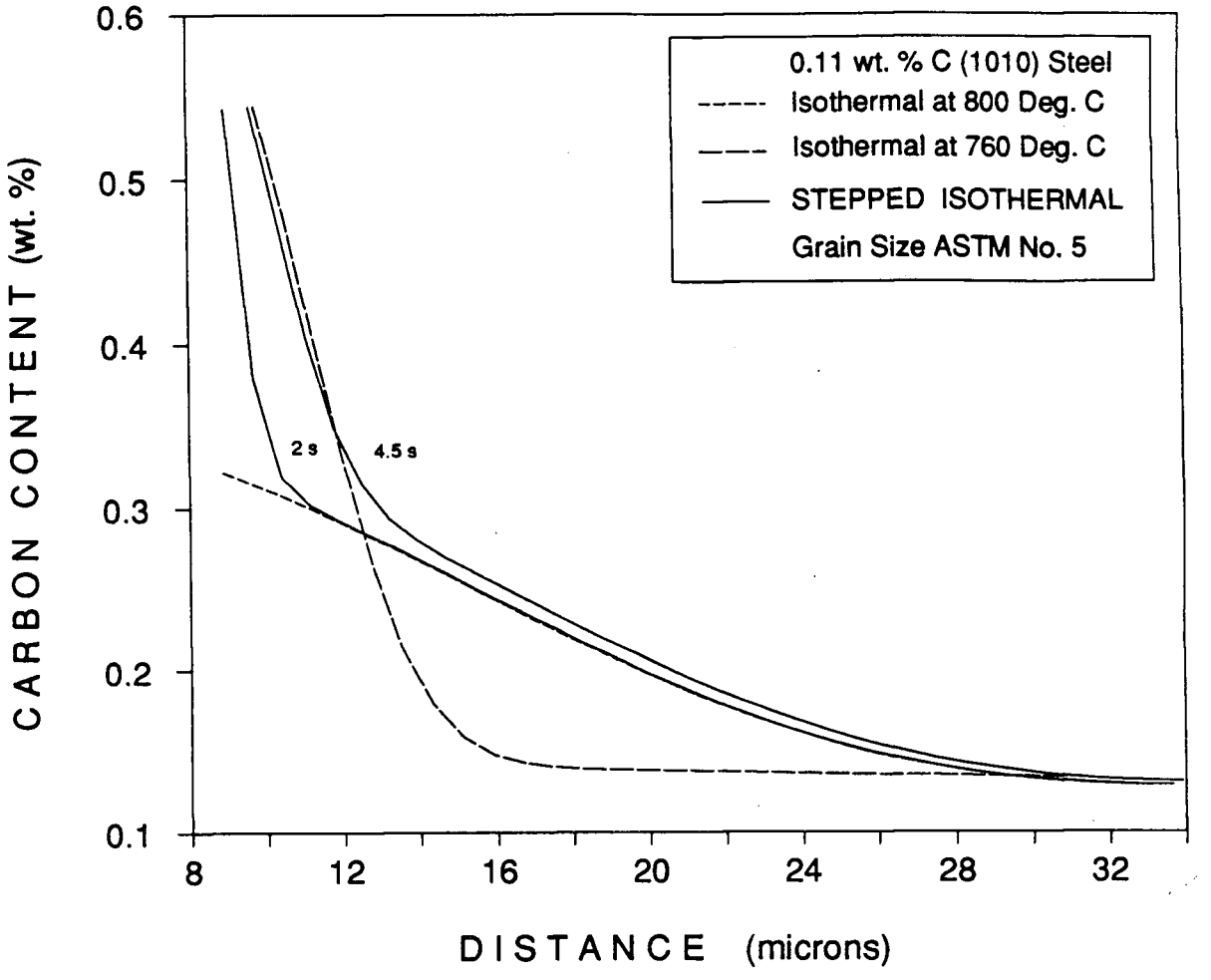

Fig. 6.25 - Spherical model-predicted carbon concentration profiles in front of growing ferrite under isothermal and stepped-isothermal conditions for the austenite grain size of ASTM No. 5 in the 1010 steel.

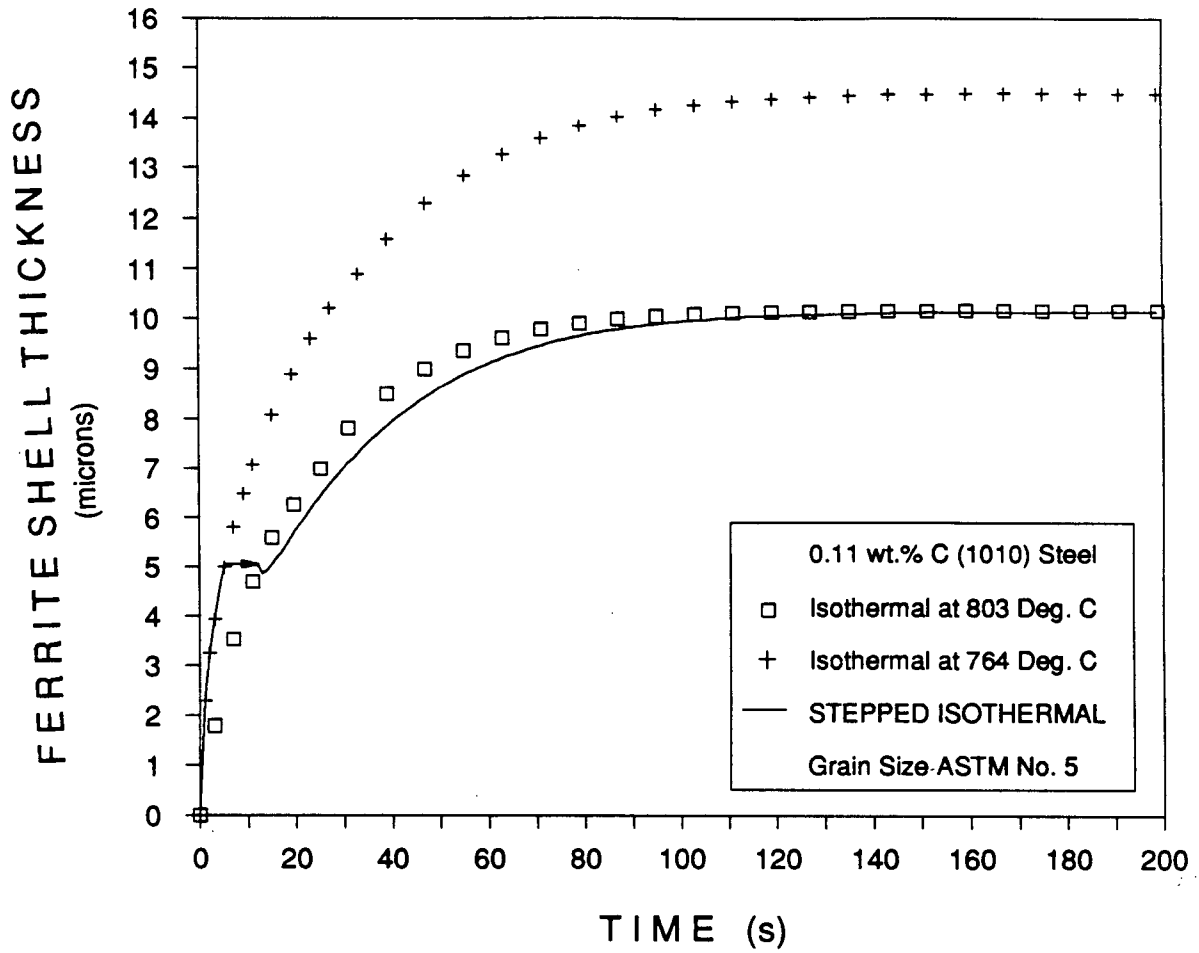

Fig. 6.26 - Spherical model-predicted isothermal and step-up isothermal ferrite growth for the austenite grain size of ASTM No. 5 in the 1010 steel.

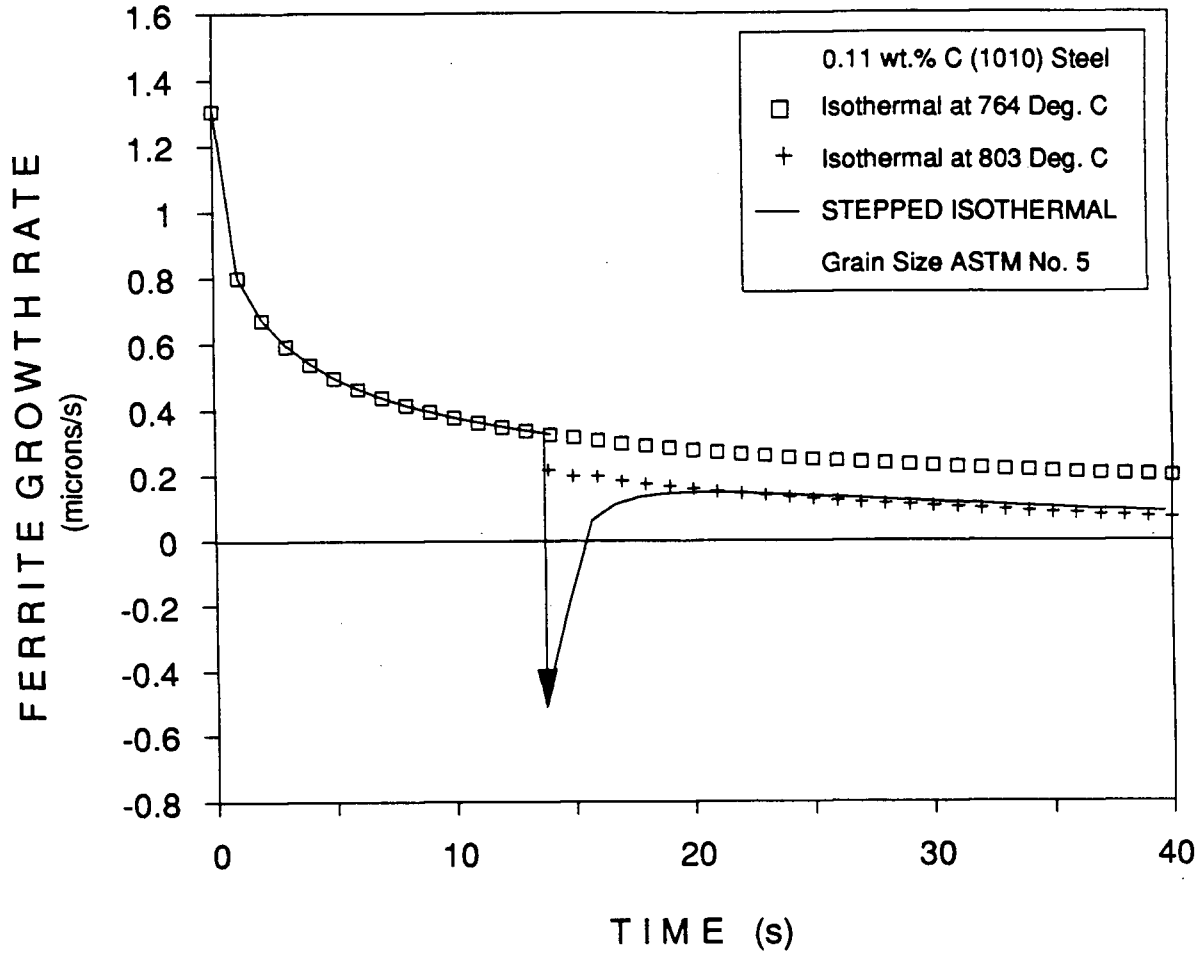

Fig. 6.27 - Spherical model-predicted isothermal and step-up isothermal ferrite growth rate for the austenite grain size of ASTM No. 5 in the 1010 steel.

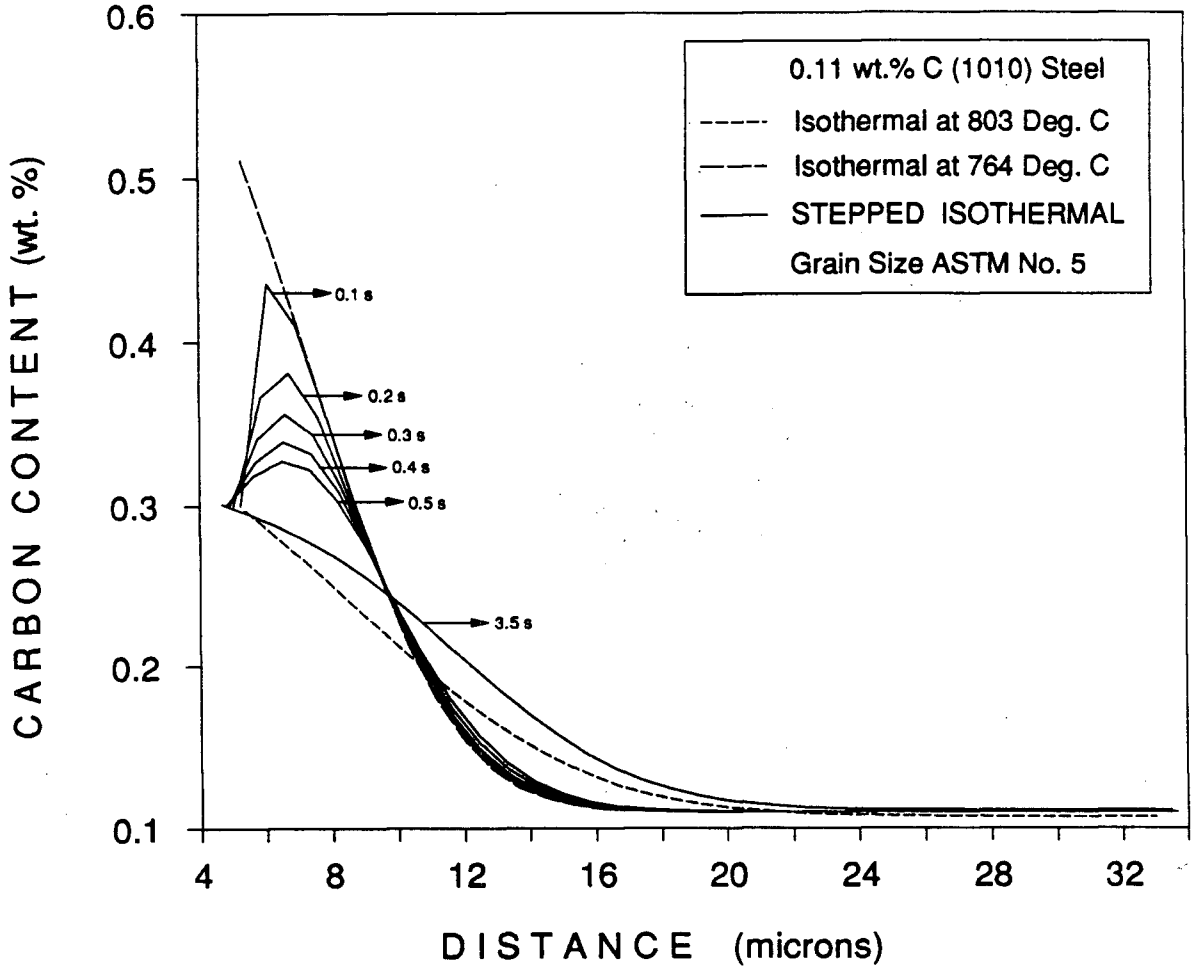

Fig. 6.28 - Spherical model-predicted carbon concentration profiles in front of growing ferrite under isothermal and stepped-isothermal conditions for the austenite grain size of ASTM No. 5 in the 1010 steel.

Chapter 7 - The Bainite Transformation

Several 1020 steel specimens were isothermally transformed and quenched to room temperature using helium gas. The helium gas was employed to obtain high cooling rates (up to 200°C/s) in order to ensure that the remaining austenite did not transform to ferrite and/or pearlite during the quench. However, when these helium-quenched specimens were subjected to metallographic analysis to examine the proeutectoid ferrite microstructure, an additional phase, other than ferrite and martensite was encountered. A typical photomicrograph is shown in Fig. 7.1(a), for a specimen partially transformed at 780°C for 60 s, step-quenched and partially transformed at 730°C for 10 s, before being helium-quenched to room temperature. This new phase is present adjacent to the ferrite and resembles ferrite, but etches differently. It retains a definite interphase boundary and exhibits a different morphology.

The spherical growth model was used to predict the total ferrite thickness obtained for the stepped-isothermal transformation condition mentioned above. It was assumed that negligible ferrite growth occurred during the temperature change from 780°C to 730°C and during the helium-quench from 730°C to room temperature. The model-predicted ferrite thickness of 11.3 μm is close to the ferrite thickness of 13.0 ± 2 μm estimated from the photomicrographs, as shown in Fig. 7.1(a). The same photomicrographs were used to estimate the thickness of the new phase present adjacent to the ferrite; this was found to be 24.0 ± 5 μm. This indicates that the new phase is not formed during the isothermal holding at 780°C and 730°C and therefore must be formed during the cooling of the specimen from 730°C to room temperature. In order to verify this inference, tests were performed in which a number of specimens were helium-quenched directly from the austenite single-phase field, after the normal austenitizing treatment. Figure 7.1(b) shows the photomicrograph of such a specimen helium-quenched from 850°C to room temperature. As can be seen, the new phase has formed on the austenite grain boundaries. The temperature range in which this phase

forms was confirmed from the recorded temperature and dilatometer response as a function of time. As shown in Fig. 7.2, the changes in slopes of both the dilatometer response and the thermal history curve occurs at approximately the same temperature $600°C$. As will be shown later under isothermal conditions the new phase begins to evolve at a temperature of $600°C$ and continues to grow at lower temperatures. Formation of the new phase results in dilation of the specimen, which changes the slope of the dilatometer response curve. The heat evolved due to the transformation results in a change of slope of the thermal history curve.

To examine the origin of this phase, several specimens were water-quenched to room temperature. Figure 7.3(a) shows the photomicrograph of a specimen having a similar thermal history to that of the specimen shown in Fig. 7.1(a), except that it was water-quenched to room temperature. The new phase is not apparent in this photomicrograph. Several specimens were also water-quenched directly from the austenite single-phase field, after the austenitizing treatments. Shown in Fig. 7.3(b) is the photomicrograph of a specimen having a similar thermal history to that of the specimen shown in Fig. 7.1(b), except that it was water-quenched from $850°C$ to room temperature. As can be seen, the new phase is absent and only martensite has formed. These tests confirmed that the high cooling rate obtained by the water quench (in excess of $350°C/s$) was sufficient to avoid the transformation to this new phase.

Various tests were performed to investigate this new phase. However, since this study was not the primary objective of the research programme, the findings will be presented as succinctly as possible.

7.1 Isothermal Transformation Kinetics

A number of isothermal tests were performed to identify the temperature range in which the new phase is formed. Shown in Fig. 7.4 are the normalized isothermal transformation kinetics measured at the four temperatures $600°C$, $575°C$, $550°C$ and $525°C$.

As can be seen, the isothermal transformation kinetics are very rapid at these temperatures. The initial 80 % of the transformation occurs at a very high rate. No incubation period was detectable, which suggests very high nucleation rates.

The transformation kinetics at all five temperatures exhibited a significant amount of recalescence. The isothermal transformation kinetic data shown in Fig. 7.4 was corrected for thermal expansion due to recalescence. Figure 7.5 shows the maximum measured recalescence as a function of isothermal transformation temperature. It can be seen that the magnitude of the recalescence increased with decreasing isothermal transformation temperature. The isothermal transformation tests were repeated with reduced amounts of recalescence by cooling the specimens externally with helium gas during the transformation. As shown in Fig. 7.6 for the 550°*C* "isothermal" test, cooling the specimen during the transformation, to remove the heat of transformation, resulted in negligible difference in the first 80 % of the transformation curve. Strongly exothermic transformation behavior would be expected for the high transformation rate observed and has been reported for massive transformations[68], but not for bainite transformations.

7.2 Morphological Observations

Isothermal transformation test specimens were subjected to metallographic examination. Figures 7.7 to 7.9 are optical photomicrographs of the microstructure of specimens quenched after completion of transformation at 600°*C*, 575°*C* and 550°*C*; all show the same unique structure. The individual grains are equiaxed and often exhibit internal radial lines, as shown in Fig. 7.10 for the specimen transformed at 575°*C*. An increasing amount of a needle-like phase, typical of upper bainite, is apparent with decreasing transformation temperature. At 525°*C*, the microstructure changes from equiaxed to needles or feathers, which resemble conventional upper bainite, as shown in Fig. 7.11.

Specimens which were subjected to isothermal transformation tests in which the heat of transformation was dissipated by external cooling, were also metallographically examined. Figure 7.12 shows the microstructure of the specimen isothermally transformed at 550°C while being subjected to external helium cooling during the transformation to suppress the recalescence. This microstructure compares well with the one shown in Fig. 7.9 for which normal recalescence was permitted. It was also shown in Fig. 7.6 that the transformation kinetics were not significantly affected by the recalescence. It is apparent that there is no significant difference between the transformation kinetics and the microstructures resulting from these two test procedures.

7.3 Activation Energy Analysis

The microstructure of the unknown phase appeared to be equiaxed with almost circular grain boundaries. It was assumed that each grain is a sphere and all the grains nucleated at the same instant. The average number of nuclei per unit volume was calculated using photomicrographs of the specimens transformed at each temperature. From these results, the average growth velocity of the spheres at each temperature from 550°C to 600°C was found to be of the order of 20 mm per s. Such high growth velocities have been observed for massive transformations both in ferrous[69] and non-ferrous alloy systems[70-74]. Massive transformations are thermally activated, non-martensitic, usually composition invariant, and have been described as interface controlled[74].

The activation energy for growth of the transformation product was estimated using the growth velocities, assuming the transformation process to be interface controlled. An Arrhenius-type equation for an interface controlled process having a boundary migration rate (V) has the form[75],

$$V = C \left(\frac{-\Delta F}{R T}\right) \exp\left(\frac{-Q}{R T}\right) \qquad (7.1)$$

where ΔF is the free energy difference between the parent and the product phase, C is a function of the interface width, the lattice vibration frequency and the fraction of interface sites available, T is the absolute temperature, R the gas constant and Q the activation energy for interface transport. Free energy changes (ΔF) for both the austenite-to-massive ferrite (same composition as austenite) and austenite-to-bainite (ferrite plus cementite) were obtained from the work of Kaufman et al.[76] on the thermodynamics of the bainite reaction. A detailed methodology of calculating the activation energy is presented in Appendix I. Figure 7.13 shows the plot of growth velocity (V) as a function reciprocal of absolute temperature (1/T) for the austenite to massive ferrite and austenite to bainite transformations. The activation energies obtained from the slopes for both transformation products are very similar, being approximately 56.5 ± 6 kJ/mole. This value is in agreement with the overall activation energy of 48.6 kJ/mole reported by Umemoto et al.[29] for upper and lower bainite in higher carbon (0.99 wt.%) steel. However, it should be emphasized that this transformation data was obtained over the very small temperature range of $50°C$, with only three temperatures being examined, which limits the accuracy of the measured activation energy. Recognizing these limitations, the value of 56.5 kJ/mole obtained in the present study is closer to the activation energy for the diffusion of carbon in ferrite (about 83 kJ/mole) than it is to that in austenite which is 126 kJ/mole. Overall activation energies of 125 kJ/mole for upper bainite and 75 kJ/mole for lower bainite have been reported by Christian and Edmonds[77] in their review on bainite transformation. On the other hand, values reported for activation energies of massive transformations in some of the non-ferrous alloy systems are comparable to the activation energy determined in this study. For instance in both the Ag-Cd[74] and Cu-Zn[70] systems the activation energy reported is 67 kJ/mole and in Ti-Ag it is 50 kJ/mole[72].

It is worth noting that high transformation rates resulting from high interface growth velocities are not usually observed in diffusional transformations, but are common in massive[68-74] transformations. A growth velocity of 16 mm per s has been reported for the Fe-C system[69], which is close to the growth velocity of 20 mm per s obtained in the present study.

7.4 SEM and STEM Results

A scanning electron microscope (SEM) was employed to examine the microstructure of a number of test specimens at higher magnifications. Specimens were mechanically polished and etched with 2% Nital. Figure 7.14 is an SEM micrograph of the etched microstructure obtained in the 575°*C* isothermally transformed test specimen. Previously presented optical microscopy (Fig. 7.7) indicated the microstructure to be a single phase. However, at the higher magnifications obtained in the SEM photomicrograph, two distinct phases are discernible. These phases were speculated to be equiaxed ferrite with internal oriented cementite rods.

Using the wavelength dispersive X-ray spectrometer on the SEM, a microanalysis was performed to assess the carbon content of the two phases in a number of specimens. Figure 7.15(a) shows a photomicrograph of a specimen partially transformed at 780°*C* and helium-quenched to room temperature to obtain all three phases- grain boundary ferrite, the new phase and martensite. Figure 7.15(b) shows the carbon map of the microstructure shown in Fig. 7.15(a). The ferrite has less carbon than the new phase and the martensite. The new phase and the martensite show a comparable carbon content.

A number of microhardness (Knoop Diamond Indenter) measurements were performed on the specimen to check the relative hardness of the ferrite, the new phase and the martensite. The microhardness data is shown in Table 7.1. On average, the new phase was 40-45 per cent harder than the ferrite, whereas the martensite was almost 100 per cent harder

than the ferrite. These observations indicate that the new phase is not equilibrium ferrite. The observations of hardness and carbon content do not distinguish between bainite and massive ferrite, and massive ferrite which would have a similar carbon content to the austenite matrix.

A number of thin foils of isothermally transformed specimens were prepared and examined using SEM, TEM and electron diffraction procedures on the STEM. Figures 7.16(a) and (b) show the SEM and the TEM micrographs of the thin foil of the specimen isothermally transformed at 575°*C* for 50 s. As can be seen, the new phase appears to consist of carbide precipitates distributed throughout the ferrite matrix. A number of areas with no precipitates were selected for electron diffraction analysis. Figure 7.17 is a selected area diffraction pattern, together with its indexing, which corresponds to a body centered cubic lattice. The analysis of these patterns confirmed that the crystallography of the matrix is that of ferrite. The plane spacings (d), determined from the crystallographic analysis of the diffraction pattern, matched closely with the standard crystallographic data available for ferrite[79], as shown in Table 7.2; the maximum spacing variation between the observed and the reported values was 0.01 $\mathring{A}$. The measured and calculated interplanar angles were in very close agreement; the difference was of the order of 1°, as shown in Table 7.2.

A number of precipitates were examined by electron diffraction. Figure 7.18 shows a selected area diffraction pattern of a precipitate together with its indexing. Crystallographic analysis identified this precipitate to be cementite. The maximum difference between measured and reported[79] plane spacings was 0.04 $\mathring{A}$ and that for measured and calculated interplanar angles was 1.1°, as shown in Table 7.2.

7.5 Discussion

The new phase observed in this steel does not have the appearance of the feathery structure known as upper bainite or the plate-like product known as lower bainite[77]. The alternative variant of bainite, known as granular bainite, consists of relatively coarse ferrite plates or regions of other shapes separated by retained austenite or high carbon martensite.

Granular bainites are more easily produced by continuous cooling than by isothermal holding[78]. It is apparent that the new phase is not the granular bainite observed in medium and low-alloy steels[78]. In the present study, it is suggested that the new phase is a type of bainite, but exhibits some of the characteristics attributed to massive transformation products. For example, the unique radial equiaxed character of the ferrite matrix is unlike conventional bainite and its variants. The observed very high nucleation rates and growth velocities of the interface and the associated high recalescence give the phase change characteristics commonly attributed to massive transformations. On the other hand, the two-phase nature of the microstructure is typical of a bainitic transformation product. These dual characteristics of this particular transformation product make this a unique form of bainitic transformation, not previously reported in the literature.

Phase	Diamond Pyramid Hardness Numbers (DPH)				Average
Ferrite	190.50	176.65	200.65	185.80	188.40
New Phase	296.70	229.90	262.75	274.30	265.91
Martensite	404.93	376.25	400.73	395.40	394.33

Table 7.1- Microhardness data obtained using a 136° Knoop Diamond Pyramid Indenter.

Plane Spacings (d)			Interplanar Angles		
Plane Index	Measured ($\mathring{A}$)	Standard ($\mathring{A}$)	Planes	Measured (°)	Calculated (°)
110	2.01	2.0268	110-101	59	60
101	2.01	2.0268	101-$0\bar{1}1$	61	60
211	1.17	1.1702	110-211	29	30
$0\bar{1}1$	2.01	2.0268	211-101	30	30
$\bar{1}10$	2.01	2.0268	$0\bar{1}1$-$\bar{1}10$	30	30

Table 7.2- Data corresponding to selected area electron diffraction pattern shown in Fig. 7.17, of the ferrite matrix in the $[1\bar{1}1]$ zone of the 1020 steel transformed completely at 575°C and water-quenched.

Plane Spacings (d)			Interplanar Angles		
Plane Index	Measured ($\mathring{A}$)	Standard ($\mathring{A}$)	Planes	Measured (°)	Calculated (°)
113	1.91	1.8716	113-$\bar{1}\bar{2}2$	89	88.84
$\bar{1}\bar{2}2$	1.88	1.8526	$\bar{1}\bar{2}2$-$0\bar{1}5$	44	44.13
$0\bar{1}5$	1.32	1.3035	$\bar{1}\bar{2}2$-$\bar{1}\bar{3}7$	25	26.10
$\bar{1}\bar{3}7$	0.83	0.8236	$0\bar{1}5$-$\bar{1}\bar{3}7$	19	18.03
			113-$0\bar{1}5$	44.5	44.70

Table 7.3- Data corresponding to selected area electron diffraction pattern shown in Fig. 7.18, of the cementite precipitate in the [$2\bar{5}1$] zone of the 1020 steel transformed completely at 575°C and water-quenched.

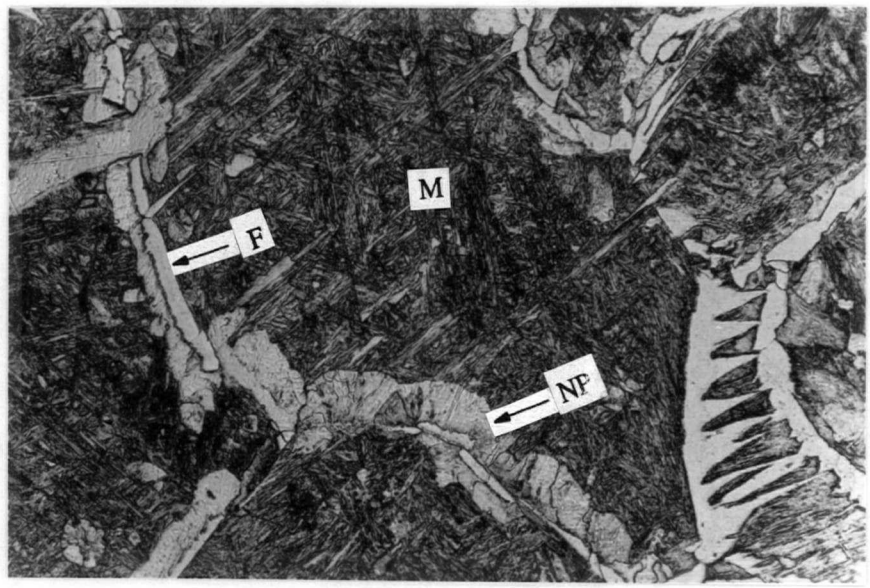

(a)

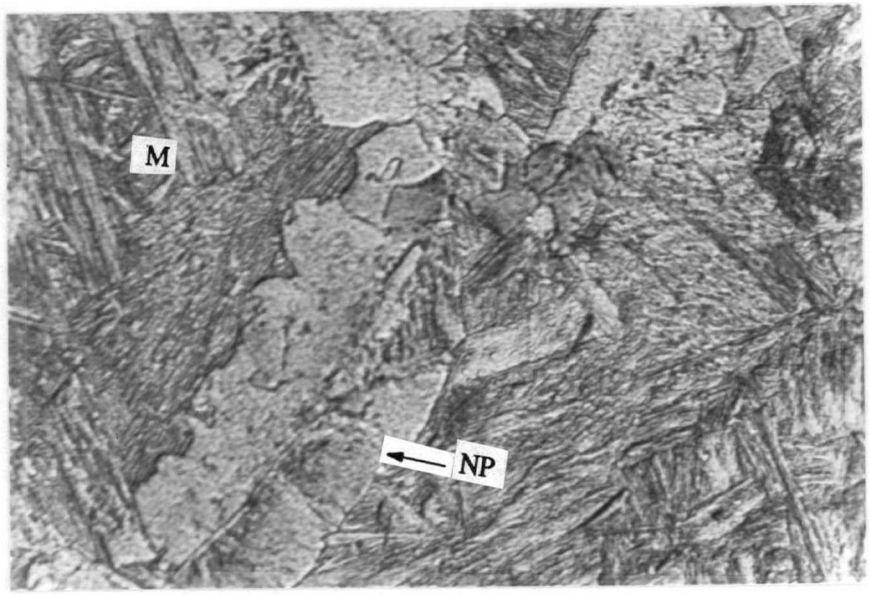

(b)

Fig. 7.1 - Photomicrographs of 1020 steel (a) partially transformed at 780°*C* step-quenched and partially transformed at 730°*C* and helium-quenched to room temperature, showing the equilibrium ferrite (F), the new phase (NP) and the martensite (M) (Magnification 224 times) and (b) austenitized and helium-quenched to room temperature, showing the new phase (NP) and the martensite (M) (Magnification 660 times).

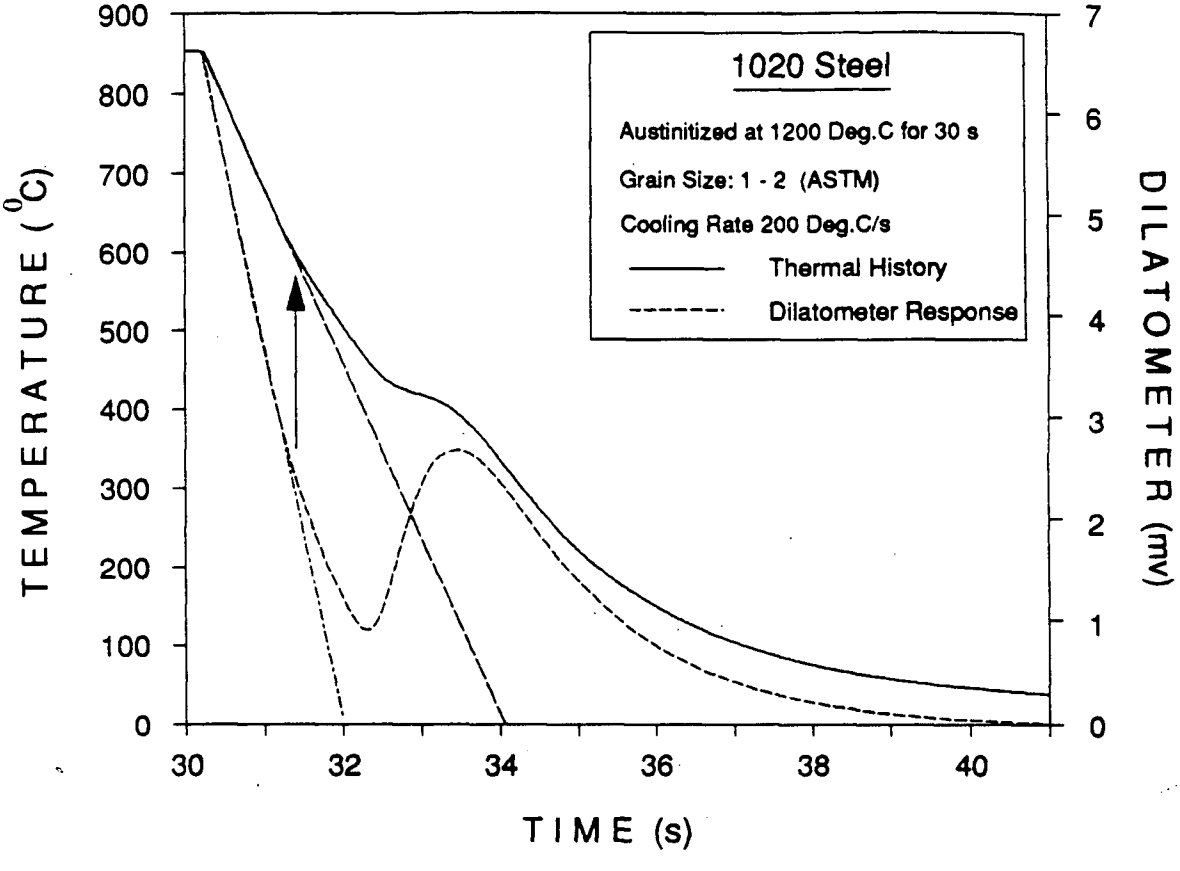

Fig. 7.2 - Temperature and dilatometer response for the 1020 steel helium-quenched from 850°C to room temperature. The arrow shows that the change in slopes of temperature and dilatometer response curves occurs at the same instant.

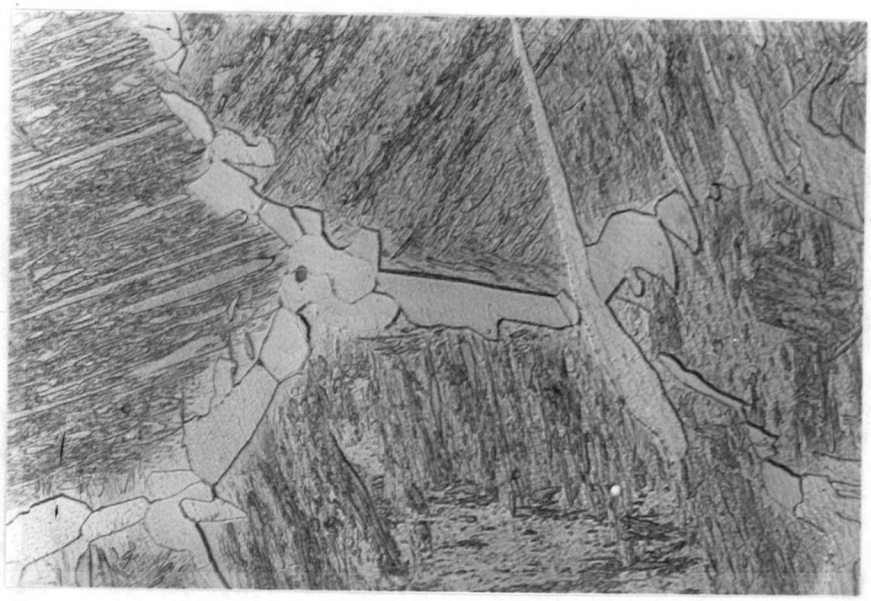

(a)

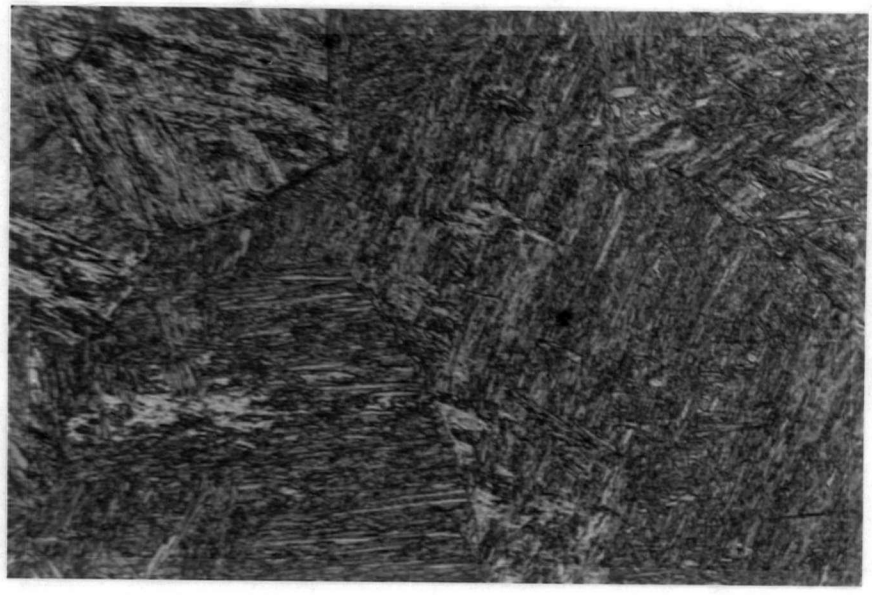

(b)

Fig. 7.3 - Photomicrographs of 1020 steel (a) partially transformed at 780°*C* step-quenched and partially transformed at 730°*C* and water-quenched to room temperature (Magnification 440 times) and (b) austenitized and water-quenched to room temperature (Magnification 264 times).

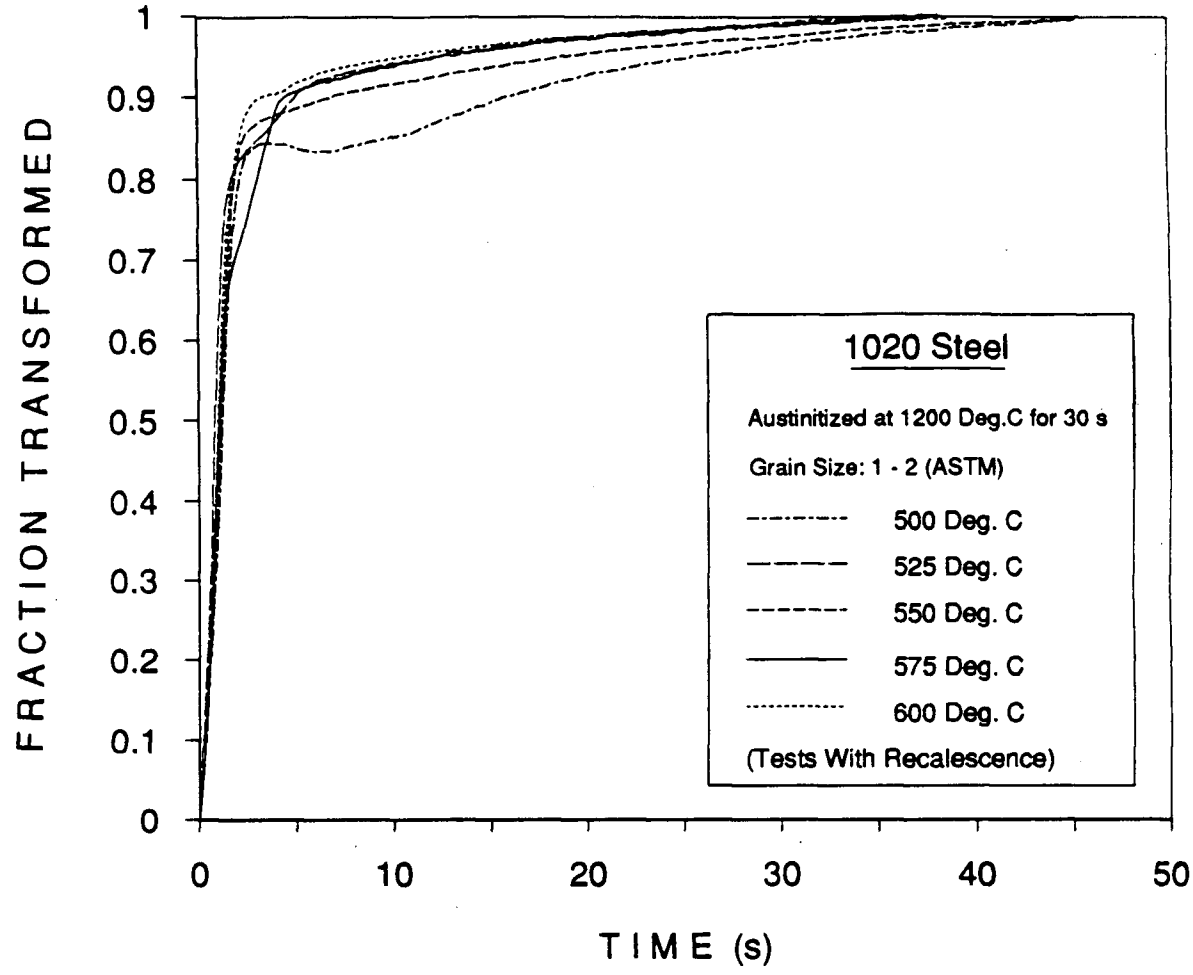

Fig. 7.4 - Isothermal transformation data for the 1020 steel, each test normalized to 100 percent and corrected for recalescence.

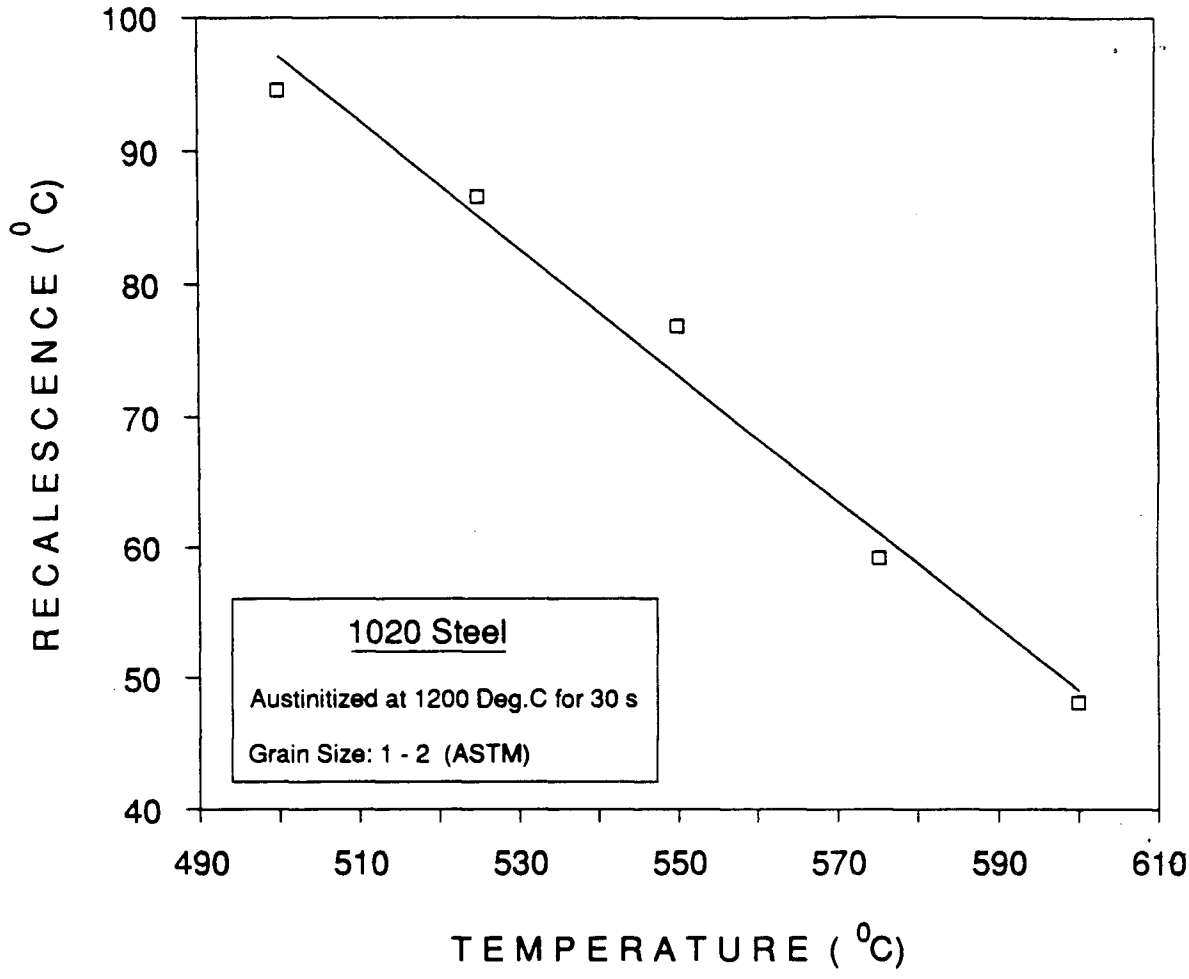

Fig. 7.5 - Recalescence as a function of isothermal transformation temperature for the 1020 steel.

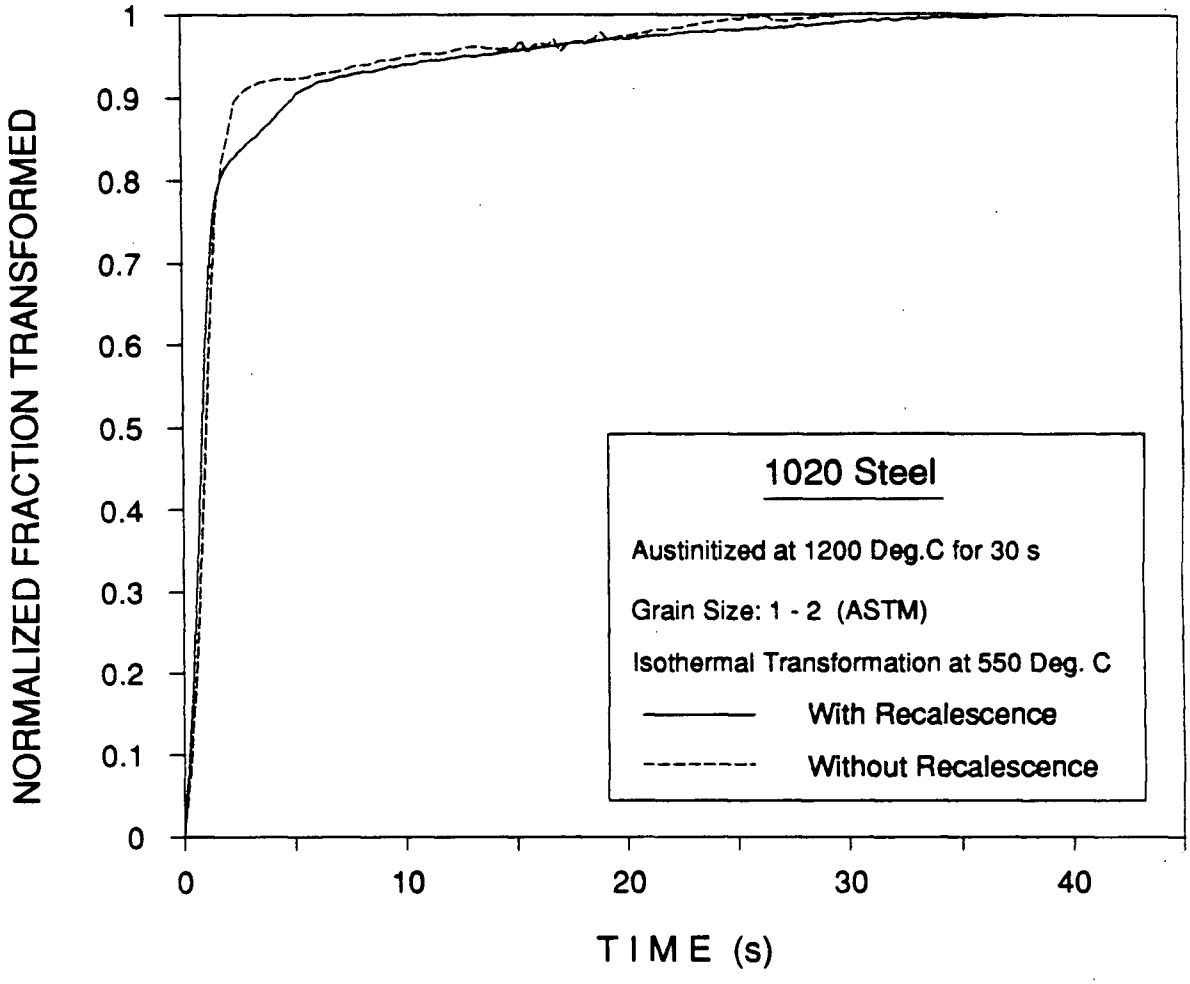

Fig. 7.6 - Comparison of isothermal transformation kinetics of 550°C test with and without recalescence for the 1020 steel.

Fig. 7.7 - Microstructure of 1020 steel transformed completely at 600°*C* and water-quenched, showing the equiaxed new phase (Magnification 440 times).

Fig. 7.8 - Microstructure of 1020 steel transformed completely at 575°*C* and water-quenched, showing the equiaxed new phase (Magnification 440 times).

Fig. 7.9 - Microstructure of 1020 steel transformed completely at 550°*C* and water-quenched, showing the equiaxed new phase and a needle-like phase typical of upper bainite. (Magnification 440 times).

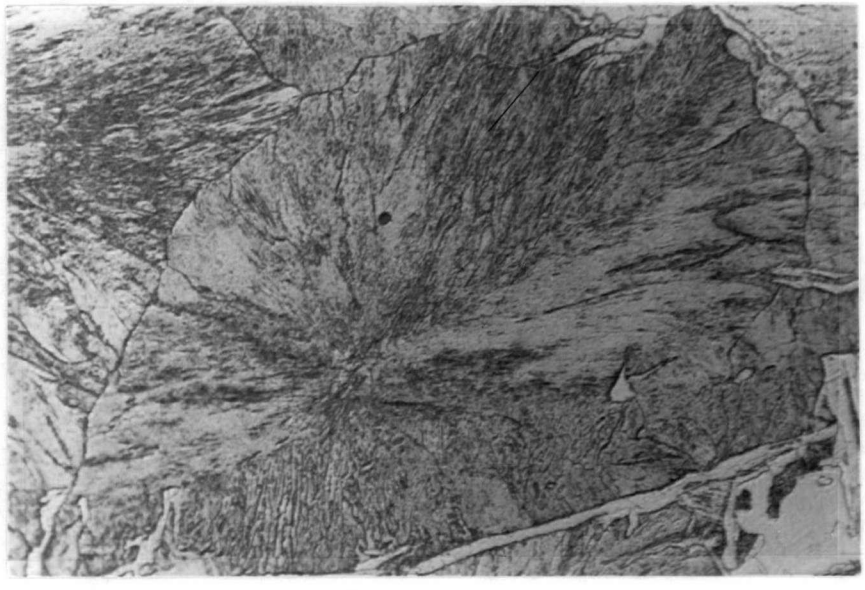

Fig. 7.10 - Microstructure of 1020 steel transformed completely at 575°*C* and water-quenched, showing the radial lines within the unknown equiaxed phase and a needle-like phase typical of upper bainite. (Magnification 440 times).

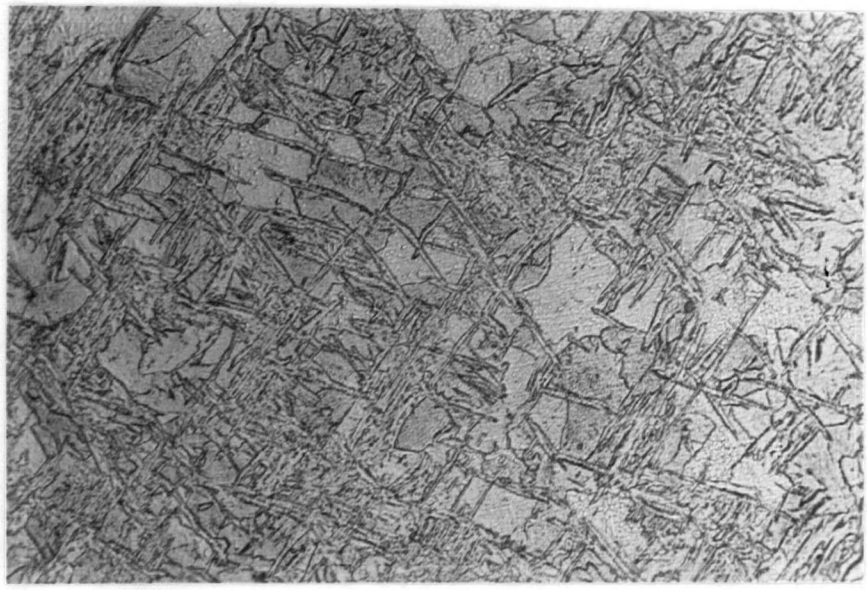

Fig. 7.11 - Microstructure of 1020 steel transformed completely at 525°*C* and water-quenched, showing a mixture of an equiaxed and a needle-like phase, the latter typical of upper bainite. (Magnification 440 times).

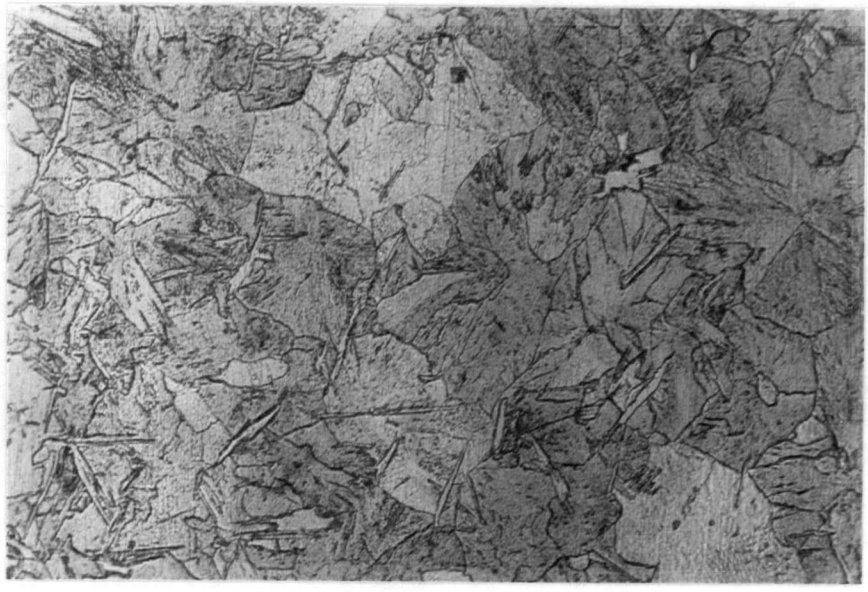

Fig. 7.12 - Microstructure of 1020 steel transformed completely at 550°*C* with recalescence suppressed and water-quenched, showing the equiaxed unknown phase and a needle-like phase, the latter typical of upper bainite. (Magnification 440 times).

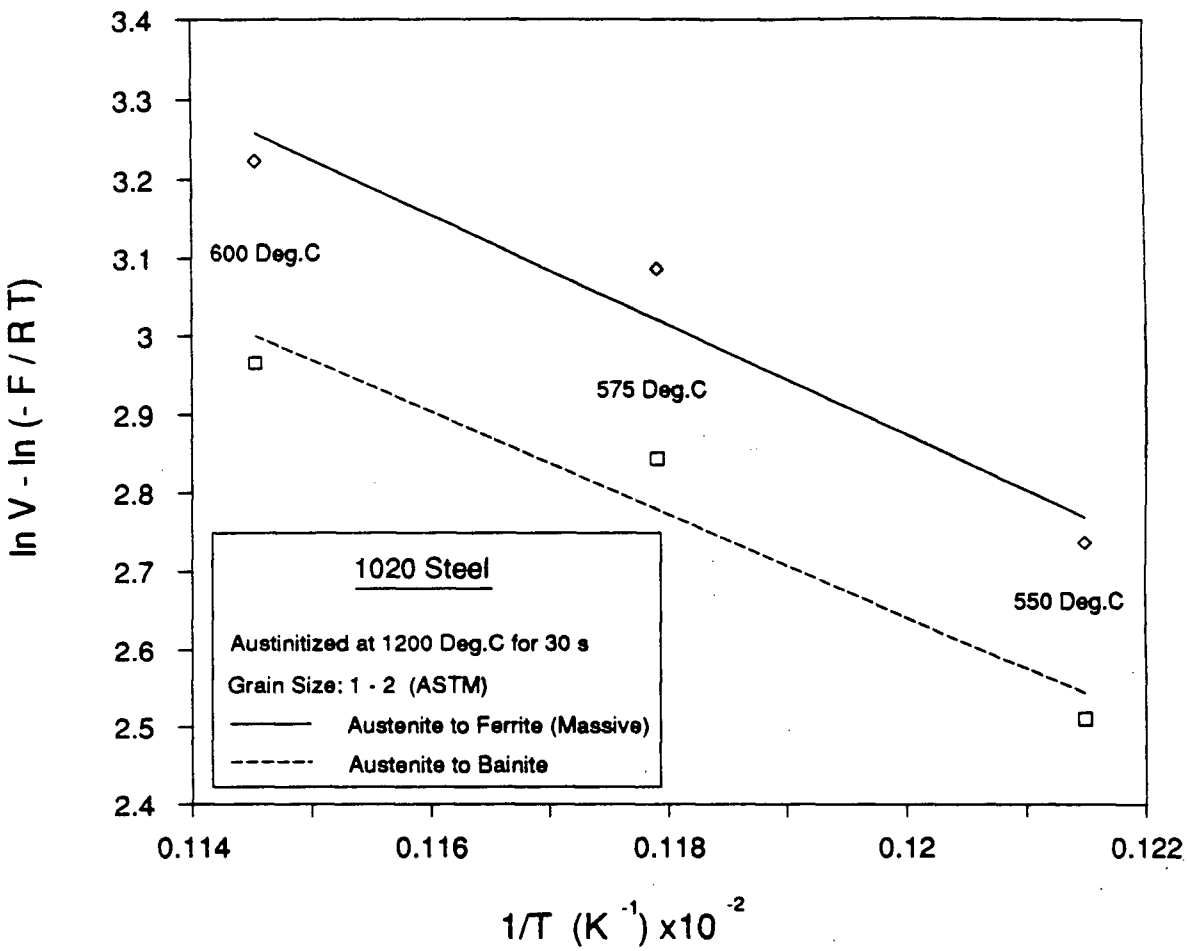

Fig. 7.13 - Growth velocity as a function of transformation temperature for the 1020 steel.

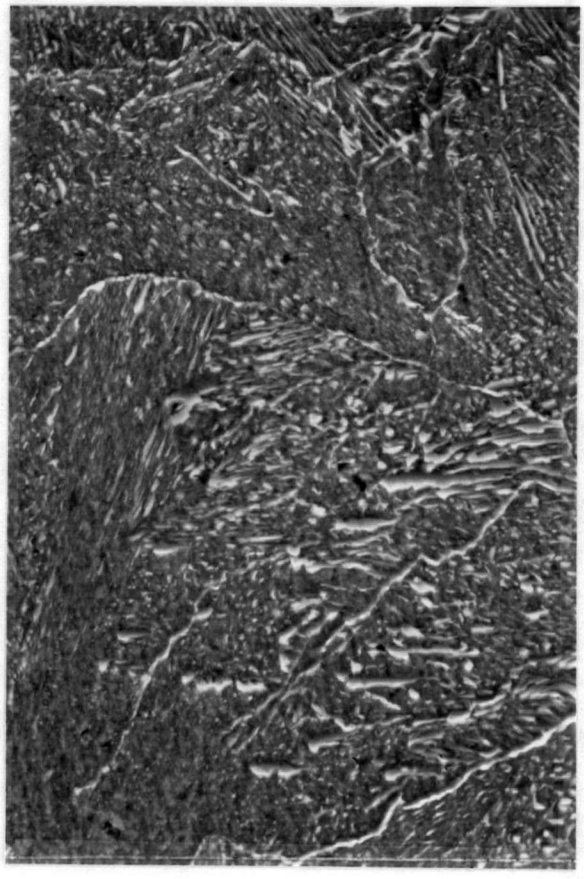

Fig. 7.14 - SEM photomicrograph of the etched microstructure of the 1020 steel transformed completely at 575°*C* and water-quenched, showing the equiaxed boundaries and an acicular product within the boundaries. (Magnification 2000 times).

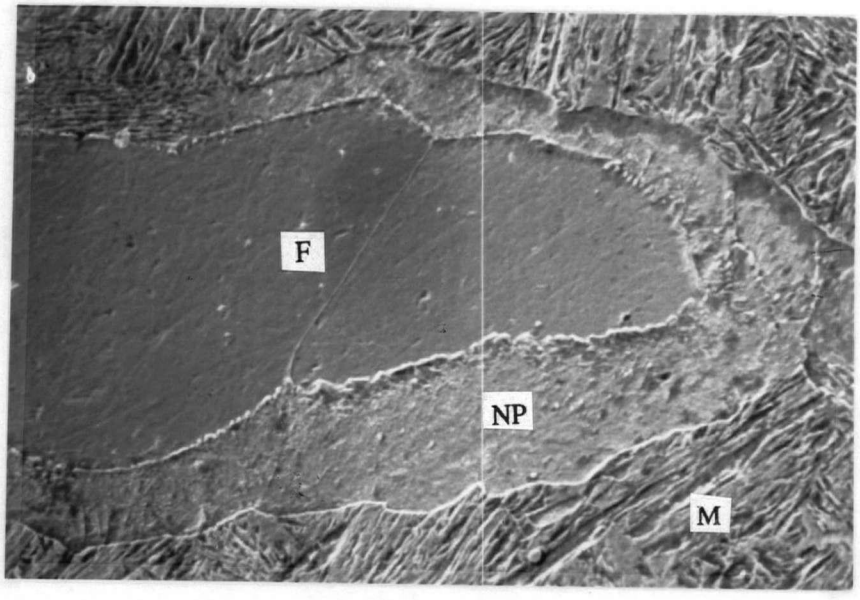

(a)

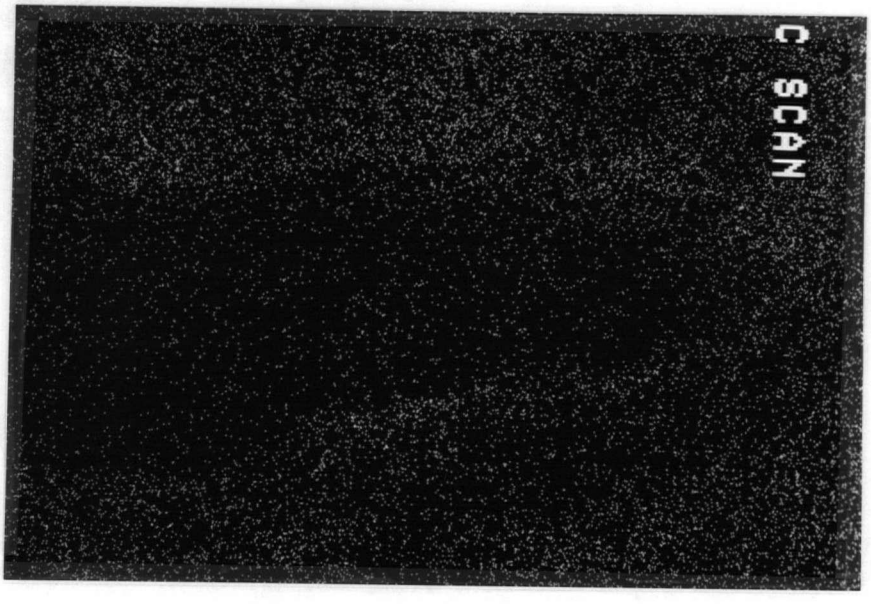

(b)

Fig. 7.15 - (a) SEM photomicrograph of 1020 steel transformed partially at 780°*C* and helium-quenched, showing the equilibrium ferrite (F), the new phase (NP) and the martensite (M) (Magnification 1500 times) and (b) SEM carbon map of the same area (Magnification 1500 times).

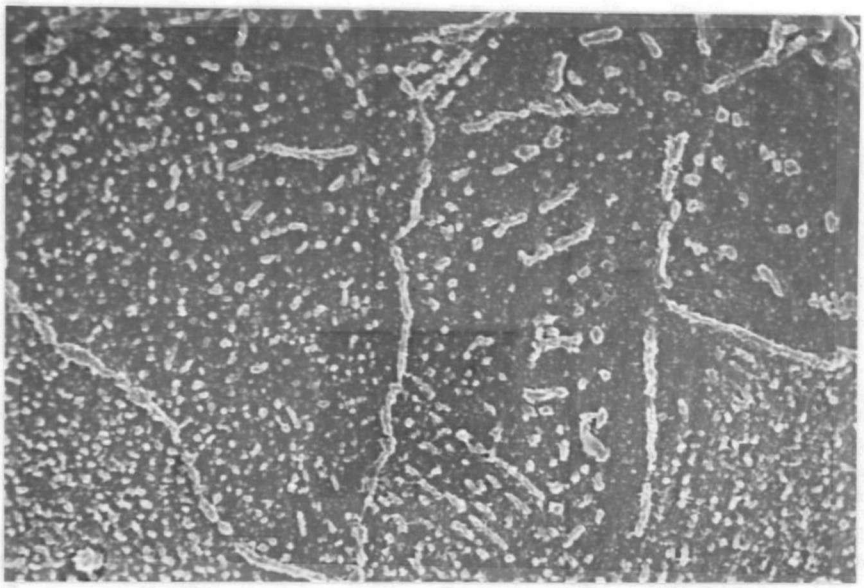

(a)

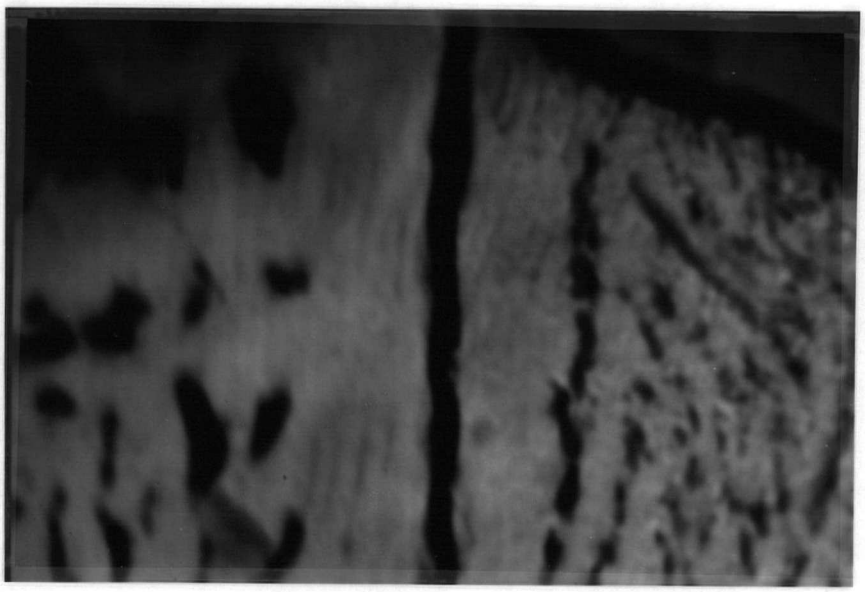

(b)

Fig. 7.16 - STEM photomicrographs of 1020 steel transformed completely at 575°*C* and water-quenched, showing the equiaxed boundaries surrounding internal precipitates in the unknown phase. (a) SEM mode (Magnification 7000 times) and (b) TEM mode (Magnification 25000 times).

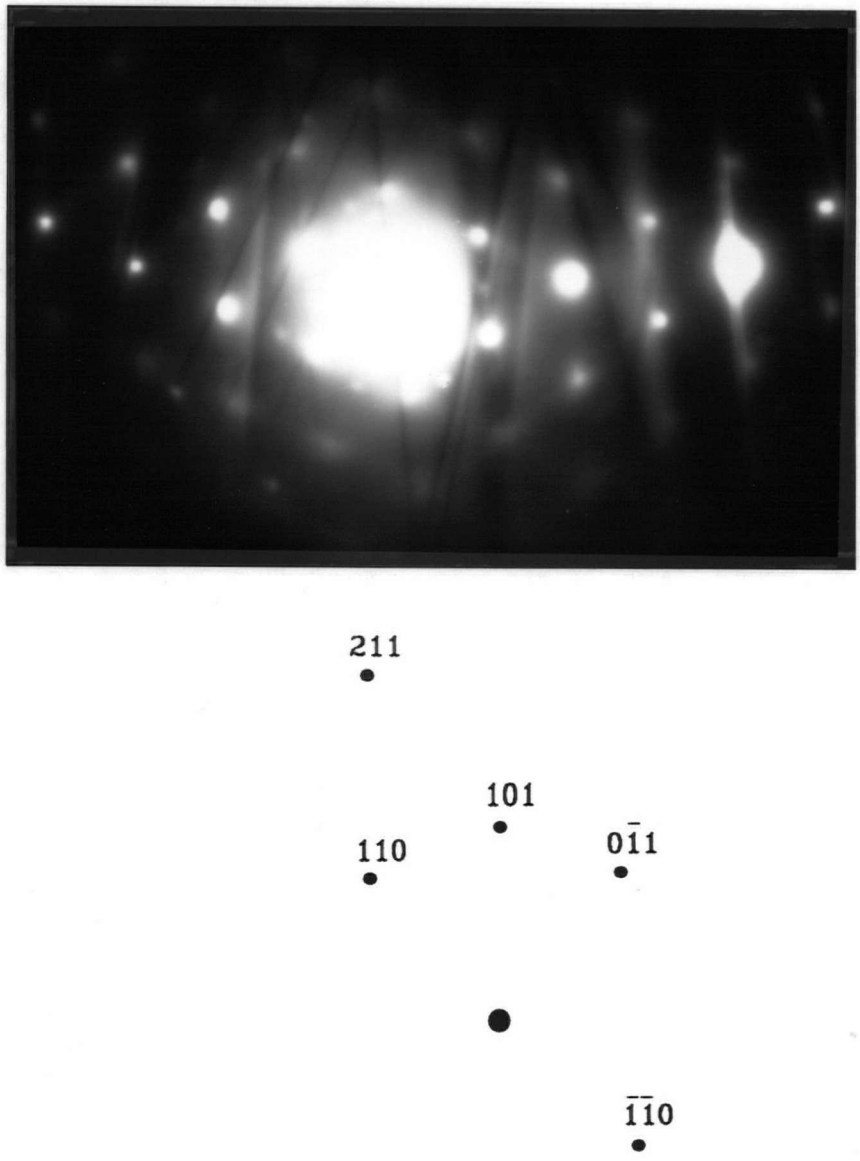

Fig. 7.17 - Selected area electron diffraction pattern and the corresponding indexing of ferrite matrix in the [$1\bar{1}\bar{1}$] zone of the 1020 steel transformed completely at 575°*C* and water-quenched.

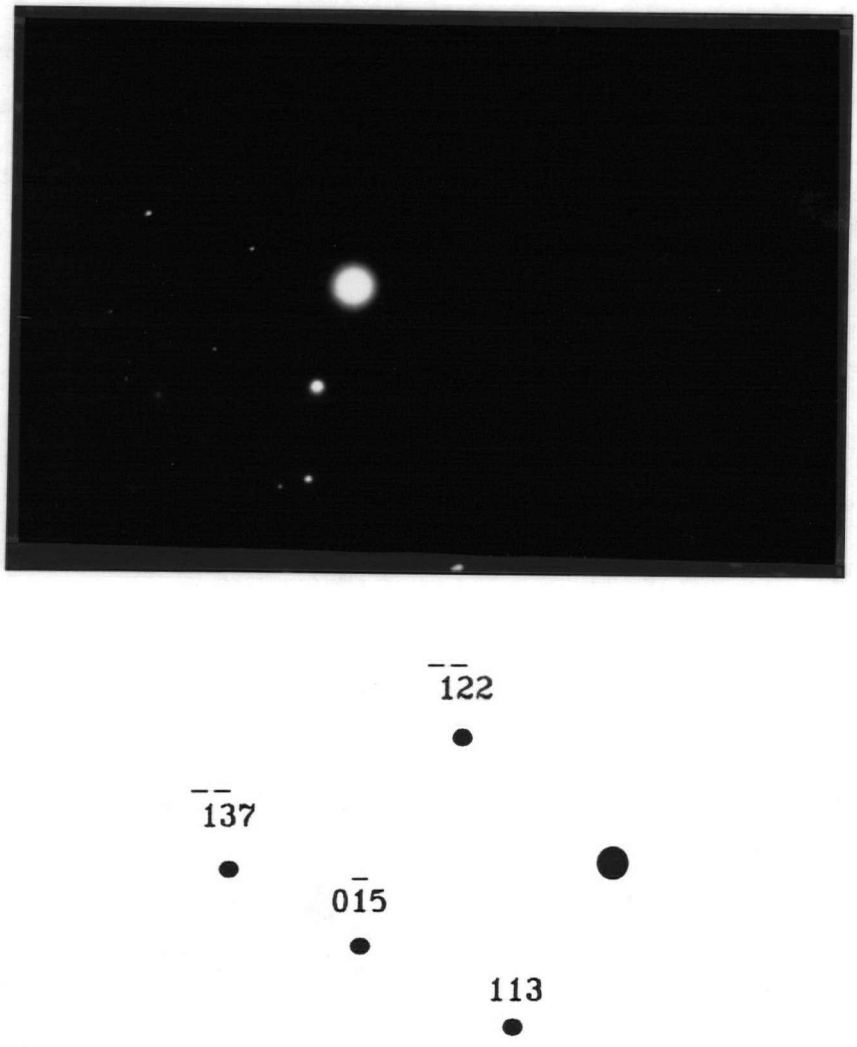

Fig. 7.18 - Selected area electron diffraction pattern and the corresponding indexing of the cementite precipitate in the $[2\bar{5}1]$ zone of the 1020 steel transformed completely at 575°C and water-quenched.

Chapter 8 - SUMMARY AND CONCLUSIONS

8.1 Summary

The applicability of the principle of additivity to the proeutectoid ferrite transformation has been examined. The study was conducted in two parts. The first part of the study involved assessment of the experimental additivity of the austenite-to-ferrite transformation and the second part involved examination of experimental additivity through the development of mathematical models to describe ferrite growth. Three plain-carbon hypo-eutectoid steel grades of known compositions (AISI 1010, 1020 and 1040) were used in the study. Experiments were conducted with the aid of the U.B.C. dilatometer for the 1010 and 1040 steel and a Gleeble 1500 thermomechanical simulator for the 1020 steel. Both pieces of equipment utilize a diametral dilatometer attached to a thin-walled resistively heated tubular test specimen. The $T_{A_{c_1}}$ and the $T_{A_{c_3}}$ temperatures were determined for the three steels. The proeutectoid ferrite transformation kinetics were measured for isothermal, stepped-isothermal and continuous-cooling conditions for the 1010 steel. Isothermal and stepped-isothermal tests were made on the 1020 and 1040 steels. The isothermal transformation kinetics were characterized with the aid of the Avrami equation. The 1010 and 1040 steel specimens exhibited grain boundary allotriomorphs as the predominant ferrite morphology. In the 1020 steel with large prior-austenite grain size, the morphology of the ferrite changed from allotriomorph to predominantly Widmanstätten with decreasing isothermal transformation temperature. Stepped-isothermal tests were carried out with the ferrite morphology changing from allotriomorph to Widmanstätten ferrite. A number of specimens from the three steels were subjected to metallographic examination to obtain prior austenite grain size, volume fraction of ferrite and to assess the ferrite nucleation sites and the morphology.

An unusual bainitic phase, exhibiting some of the characteristics attributed to massive transformation products, was detected in the 1020 steel. A number of tests were performed to measure the isothermal transformation kinetics of this new phase. The new phase was further investigated with the aid of a scanning electron microscope (SEM). Thin foil transmission electron microscopy was also employed and a number of thin foils of isothermally transformed specimens were prepared and examined using TEM and electron diffraction.

The second part of the study involved development of mathematical models which were used to theoretically assess the observed experimental additivity of the proeutectoid ferrite transformation. Only one morphology, namely grain boundary allotriomorph, was considered in developing the models and the model predictions were limited to the 1010 grade. Two models were developed corresponding to two interface geometries, i.e., planar and spherical, representing two limiting cases. A finite-difference technique was used for describing the two-phase, long-range diffusion controlled, austenite-to-ferrite moving-interface problem for a system having finite boundaries. Both models incorporated the changing equilibrium concentration of ferrite and austenite at the phase boundary due to temperature change and the temperature and carbon concentration dependence of the carbon diffusion coefficient in austenite. The models were employed to obtain ferrite growth kinetics at a given temperature and for a given austenite grain size. Tests of the experimental additivity of the austenite-to-proeutectoid ferrite transformation were made by assessing the ferrite growth kinetics under conditions of changing temperature.

8.2 Conclusions

Based on the experimental results obtained and the mathematical model predictions made in the present study, the following conclusions can be drawn:

(1) In the 1010 steel, the proeutectoid ferrite transformation kinetics obtained after rapid change from one temperature to another, attained the isothermal kinetics of the second temperature in a very short time, thereby demonstrating the experimental

additivity of the transformation. The tests were performed under both step-down and step-up quench conditions, and with no change in the grain boundary allotriomorphs morphology of the ferrite. For the step-down quench, the experimental additivity of the proeutectoid ferrite transformation was also established under conditions of significant soft impingement. Early site saturation was observed at all temperatures studied. The stepped-isothermal test results support the previously observed experimental additivity of the ferrite transformation under continuous-cooling conditions.

(2) The Avrami equation used in conjunction with the principle of additivity, under estimated the initial stages of the proeutectoid ferrite transformation obtained under continuous-cooling conditions, although the predicted duration of the transformation compared reasonably well with that experimentally observed in the 1010 steel.

(3) In the 1020 steel, the proeutectoid ferrite changed with decreasing temperature, from predominantly grain boundary allotriomorphs to predominantly a Widmanstätten morphology over the temperature range of 780°*C* to 730°*C*. Early site saturation was observed over this temperature range. The Widmanstätten ferrite plates were observed to originate from the pre-formed grain boundary allotriomorphs.

(4) The stepped-isothermal proeutectoid ferrite transformation tests in which the same Widmanstätten morphology was present at both temperatures were experimentally additive in the 1020 steel.

(5) The stepped-isothermal proeutectoid ferrite transformation tests in which ferrite morphology changed from fully allotriomorphic to predominantly Widmanstätten as a result of the change in transformation temperature showed experimental additivity in the 1020 steel.

(6) The effect of stabilization of the ferrite/austenite interface, obtained by equilibration after formation of the equilibrium amount of ferrite at $780°C$, on the subsequent lower temperature ($730°C$) ferrite transformation kinetics was determined. The ferrite transformation kinetics at the lower temperature were much slower and the amount of Widmanstätten ferrite much less than that obtained in the isothermal case. The stepped-isothermal proeutectoid ferrite transformation after stabilization of ferrite/austenite interfaces showed poorer agreement with the isothermal test results.

(7) In the 1040 steel, the ferrite having a grain boundary allotriomorph morphology, at both stepped-isothermal test temperatures, attained the isothermal kinetics at the second temperature in a very short time interval, thereby demonstrating the experimental additivity of the transformation.

(8) The n and b parameters obtained from the Avrami analysis of the isothermal proeutectoid ferrite transformation kinetics for the three steels showed that the value of n remains almost constant except for the higher transformation temperatures and the b parameter increased with increasing temperature.

(9) In the 1020 steel, a new phase was observed and was shown to be a type of bainite. The new phase exhibited some of the characteristics attributed to massive transformation products.

(10) Predictions of ferrite growth kinetics and associated carbon gradients under the stepped-isothermal conditions were made with the aid of mathematical models having planar and spherical interface geometries. The predictions did show the effect of thermal path on the growth kinetics at the second temperature although the effect was for a short time, consistent with the experimental observations and thereby confirmed the observed experimental additivity of the proeutectoid ferrite transformation in the 1010 steel. Both the models predicted a retrogade motion of

the ferrite/austenite interface for the step-up condition. The spherical model-predicted isothermal ferrite growth compared more favorably with the experimentally measured ferrite transformation kinetics of the 1010 steel.

REFERENCES

1. Atlas of Isothermal Transformation and Cooling Transformation Diagrams, American Society for Metals, Metals Park OH, (1977).

2. Austenite Transformation Kinetics of Ferrous Alloys, Climax Molybdenum Co., Greenwich CT, (1972).

3. Blondeau R., Maynier Ph., Dollet J. and Veillard-Baran B.: Proceedings of the 16th International Heat Treating Conf., Heat Treatment '76, pp. 189-200 (1976).

4. Atkins M.: Atlas of Continuous Cooling Transformation Diagrams for Engineering Steels, American Society for Metals, Metals Park, OH, (1980).

5. Metal Progress Data Book, American Society for Metals, Metals Park OH, (1985).

6. Scheil E.: "Initiation Time for the Austenite Transformation", Arch. Eisenhüttenwesen, vol. 8, pp. 565-567 (1934-1935).

7. Christian J. W.: The Theory of Transformations in Metals and Alloys, 2nd ed., Pergamon Press, Oxford, U.K., pp. 535-543 (1975).

8. Avrami M.: "Kinetics of Phase Change I", J. Chem. Physics, 7, pp. 1103-12 (1939).

9. Avrami M.: "Kinetics of Phase Change II", J. Chem. Physics, 8, pp. 212-24 (1940).

10. Avrami M.: "Kinetics of Phase Change III", J. Chem. Physics, 9, pp. 177-83 (1940).

11. Johnson W. A. and Mehl R. F.: "Reaction Kinetics in Processes of Nucleation and Growth", Trans. AIME, Vol. 135, pp. 416-442 (1939).

12. Cahn J. W.: "The Kinetics of Grain Boundary Nucleated Reactions", Acta Metall., Vol. 6, pp. 449-459 (1956).

13. Cahn J. W.: "Transformation Kinetics During Continuous Cooling", Acta Metall., Vol. 6, pp. 572-575, (1956).

14. Cahn J. W.: "On the Kinetics of Pearlite Reaction", Trans. AIME, Vol. 209, pp. 140-144 Jan. (1957).

15. Kuban M. B., Jayaraman R., Hawbolt E. B. and Brimacombe J. K.: "An Assessment of the Additivity Principle in Predicting Continuous Cooling Austenite-to-Pearlite Transformation Kinetics using Isothermal Data", Metall. Trans. A, Vol. 17A, pp. 1493-1503 (1986).

16. Grange R. A. and Kiefer: "Transformation of Austenite on Continuous Cooling and Its Relation to Transformation at Constant Temperature", Trans. ASM, Vol. 29, pp. 85-116, (1941).

17. Manning G. K. and Lorig C. H.: "The Relationship between Transformation at Constant Temperature and Transformation during Cooling", Metals Technology, Vol. 13, Part 1, Tech Publ. No. 2014 (1946).

18. Moore P. T.: "Anisothermal Decomposition of Austenite in a Medium-Alloy Steel", Journal of Iron Steel Inst., July, pp. 305-311 (1954).

19. Kirkaldy J. S.: "Prediction of Alloy Hardenability from Thermodynamic and Kinetic Data", Metall. Trans., vol. 4, pp. 2327-33, (1973).

20. Kirkaldy J. S., Pazionis G. O. and Feldman S. E.: "An Accurate Prediction for the Jominy Hardenability of Low Alloy Hypoeutectoid Steels", Proceedings of the 16th International Heat Treatment Conf., Heat Treatment '76, pp. 169-175 (1976).

21. Kirkaldy J. S., Thomas B. A. and Baganis E. A.: "Prediction of Multicomponent Equilibrium and Transformation Diagrams for Low Alloy Steels", Symposium Proceedings, Hardenability Concepts with Application to Steel, AIME, pp. 82-125, (1978).

22. Agarwal P. K. and Brimacombe J. K.: "Mathematical Model of Heat Flow and Austenite-Pearlite Transformation in Eutectoid Carbon Steel Rods for Wire", Metall. Trans. B, Vol. 12B, pp. 121-133 (1981).

23. Hawbolt E. B., Chau B. and Brimacombe J. K.: "Kinetics of Austenite-to-Pearlite Transformation in Eutectoid Carbon Steel", Metall. Trans. A, Vol. 14A, pp. 1803-1815 (1983).

24. Iyer J., Brimacombe J. K. and Hawbolt E. B.: "Prediction of the Structure and Mechanical Properties of Control-cooled Eutectoid Steel Rods", Proc. 26th Mechanical Working and Steel Processing Conf., ISS-AIME, Chicago (1984).

25. Hawbolt E. B., Chau B. and Brimacombe J. K.: "Kinetics of Austenite-Ferrite and Austenite-Pearlite Transformations in a 1025 Carbon Steel", Metall. Trans. A, Vol. 16A, pp. 565-578 (1985).

26. Shimizu N. and Tamura I.: "Effect of Discontinuous Change in Cooling Rate during Continuous Cooling on Pearlitic Transformation Behavior of Steel", Trans. ISIJ, Vol. 17, pp. 469-476 (1977).

27. Umemoto M., Komatsubara N. and Tamura I.: "Prediction of Hardenability Effects from Isothermal Transformation Kinetics", J. of Heat Treating, Vol. 1, pp. 57-64 (1980).

28. Umemoto M., Nishioka N. and Tamura I.: "Prediction of Hardenability From Isothermal Transformation Diagrams", J. of Heat Treating, Vol. 2, pp. 130-138 (1981).

29. Umemoto M., Horiuchi K. and Tamura I.: "Transformation Kinetics of Bainite During Isothermal Holding and Continuous Cooling", Trans. ISIJ, Vol. 22, pp. 854-861 (1982).

30. Umemoto M., Horiuchi K. and Tamura I.: "Pearlite Transformation During Continuous Cooling and Its Relation to Isothermal Transformation", Trans ISIJ, Vol. 23, pp. 690-695 (1983).

31. Umemoto M., Nishioka N. and Tamura I.: "Kinetics of Proeutectoid Ferrite Reaction During Isothermal Holding and Continuous Cooling in Plain Carbon Steels", Proceedings of the Int. Conf. on Heat Treatment of Materials, Heat Treatment Shanghai '83, pp. 5.35-5.43 (1983).

32. Hickley C. M. and Woodhead J. H.: "Formation of Ferrite in Hypo-eutectoid Plain Carbon Steels", Journal of Iron Steel Inst., 176, pp. 129-139 (1954).

33. Campbell P. C., Hawbolt E. B. and Brimacombe J. K.: "Application of Microstructural Engineering to the Controlled Cooling of Steel Wire Rod", Proceedings of the International Symposium on Accelerated Cooling of Rolled Steel, Sponsored by The Metallurgical Society of CIM, Winnipeg, Canada, Aug. 24-25, 1987, Ed. by G. E. Ruddle and A. F. Crawley, Vol. 3, Pergamon Press, New York, pp. 309-330 (1987).

34. Campbell P. C.: "Application of Microstructural Engineering to the Controlled Cooling of Steel Wire Rod", Ph. D. Thesis, University of British Columbia (1989).

35. Carpenter H. C. H. and Robertson J. M.: "The Formation of Ferrite from Austenite", Journal of Iron Steel Inst., Vol. No. 1, pp. 345-394 (1931).

36. Aaronson H. I.: "Proeutectoid Ferrite and Proeutectoid Cementite Reactions", in Decomposition of Austenite by Diffusional Processes, V. F. Zackay and H. I. Aaronson eds., Interscience Publishers, New York, N. Y., pp. 387-548 (1962).

37. Reynolds W. T. Jr., Enomoto M. and Aaronson H. I.: "The Proeutectoid Ferrite Reaction", in Phase Transformations in Ferrous Alloys, A. R. Marder and J. I. Goldstein eds., TMS-AIME, Warrendale, PA, pp. 155-200 (1984).

38. Dube C. A., Ph D. Thesis, Carnegie Inst. of Tech. (1948).

39. Mazanec K. and Cadek J., Rev. Met. 212, 501 (1958).

40. Simcoe C. R., Elsea A. R. and Manning G. K.: "Study of the Effect of Boron on the Decomposition of Austenite", Trans. AIME, Vol. 203, pp. 193-200 (1955).

41. Lange W. F. and Aaronson H. I.: "Influence of Undercooling Upon Relative Nucleation Kinetics of Proeutectoid Ferrite at Austenite Grain Faces and Grain Edges", Metall. Trans., Vol. 10A, pp. 1951-1952 (1979).

42. Obara T., Lange W. F., Aaronson H. I. and Dom B. E.: "Prediction of TTT-Curves for Initiation of the Proeutectoid Ferrite Reaction in Fe-C Alloys", Conf. Proceedings, Solid→Solid Phase Transformations, H. I. Aaronson, D. E. Laughlin, R. E. Sekerka and C. M. Wayman eds., TMS-AIME, Warrendale, PA., pp. 1105-1109 (1981).

43. Lange W. F., Enamoto M. and Aaronson H. I.:"The Kinetics of Ferrite Nucleation at Austenite Grain Boundaries in Fe-C Alloys", Metall. Trans., Vol. 19A, pp. 427-440 (1988).

44. Enomoto M., Lange W. F. and Aaronson H. I.: "The Kinetics of Ferrite Nucleation at Austenite Grain Edges in Fe-C and Fe-C-X Alloys", Metall. Trans., Vol. 17A, pp. 1399-1407 (1986).

45. Kinsman K. R. and Aaronson H. I.: "Influence of Molybdenum and Manganese on the Kinetics of the Proeutectoid Ferrite Reaction", in Transformations and Hardenability in Steels, Climax Molybdenum Co., Ann Arbor, Mich., pp. 39-55 (1967).

46. Atkinson C., Aaron H. B., Kinsman K. R. and Aaronson H. I.: "On the Growth Kinetics of Grain Boundary Ferrite Allotriomorphs", Metall. Trans., Vol. 4, pp. 783-792 (1973).

47. Bradley J. R., Rigsbee J. M. and Aaronson H. I.: "Growth Kinetics of Grain Boundary Ferrite Allotriomorphs in Fe-C Alloys", Metall. Trans., Vol. 8A, pp. 323-333 (1977).

48. Simonen E. P., Aaronson H. I. and Trivedi R.: "Lengthening Kinetics of Ferrite and Bainite Sideplates", Metall. Trans., Vol. 4, pp. 1239-1245 (1973).

49. Kinsman K. R., Eichen E. and Aaronson H. I.: "Thickening Kinetics of Proeutectoid Ferrite Plates in Fe-C Alloys", Metall. Trans., Vol. 6A, pp. 303-317 (1975).

50. Bradley J. R. and Aaronson H. I.: "The Stereology of Grain Boundary Allotriomorphs", Metall. Trans., Vol. 8A, pp. 317-322 (1977).

51. Purdy G. R. and Kirkaldy J. S.: "Kinetics of the Proeutectoid Ferrite Reaction at an Incoherent Interface, as Determined by a Diffusion Couple", Trans. TMS-AIME, Vol. 227, pp. 1255-1256 (1963).

52. Kinsman K. R. and Aaronson H. I.: "Influence of Al, Co and Si Upon the Kinetics of the Proeutectoid Ferrite Reaction", Metall. Trans., Vol. 4, pp. 959-967 (1973).

53. Atkinson C.: "A Numerical Method To Describe the Diffusion-Controlled Growth of Particles When the Diffusion Coefficient Is Composition-Dependent", Trans. TMS-AIME, Vol. 245, pp. 801-806 (1969).

54. Murray D. and Landis F.: "Numerical and Machine Solutions of Transient Heat-Conduction Problems Involving Melting or Freezing. Part I-Method of Analysis and Sample Solutions", Trans. ASME, Jour. of Heat Transfer, Vol. 81, May, pp. 106-112 (1959).

55. Wells C., Batz W. and Mehl R. F.: "Diffusion Coefficient of Carbon in Austenite", Trans. AIME, Vol. 188, pp. 553-560 (1950).

56. Christian J. W.: The Theory of Transformations in Metals and Alloys, 2nd ed., Pergamon Press, Oxford, U.K., pp. 482-485 (1975).

57. Vander Voort G. F.: Metallography Principles and Practice, McGraw-Hill, Inc. New York, U. S. A., pp. 435-436 (1984).

58. Krahe P. R., Kinsman K. R. and Aaronson H. I.: "Influence of Austenite Grain Size Upon the Widmanstätten-Start (W_s) Temperature for the Proeutectoid Ferrite Reaction", Acta Metall., Vol. 20, pp. 1109-1121 (1972).

59. Andrews K. W.: "The Calculation of Transformation Temperatures and Austenite-Ferrite Equilibria in Steels", Journal of Iron Steel Inst., Vol. 184, pp. 414-427 (1956).

60. ASTM Standard E112, Part II, ASTM Philadelphia, Pa., 186-219.

61. Townsend R. D. and Kirkaldy J. S.: "Widmanstätten Ferrite Formation in Fe-C Alloys", Trans. ASM, Vol. 61, pp. 605-619 (1968).

62. Fong H. S. and Glover S. G.: "Grain Boundary Widmanstätten Ferrite Spacings in 0.2 Pct C Steel", Metall. Trans., Vol. 15A, pp. 1643-1651 (1984).

63. Shewmon P. G.: "Interfacial Stability in Solid-Solid Transformations", Trans. AIME, Vol. 233, pp. 736-748 (1965).

64. Physical Constants of Some Commercial Steels at Elevated Temperatures, B.I.S.R.A., Butterworths Scientific Publications, London, pp. 15 (1953).

65. Purdy G. R. and Hillert M.: "On the Nature of the Bainite Transformation in Steels", Acta Metall., Vol. 32, pp. 823-828 (1984).

66. Agren J.: "A Revised Expression for the Diffusivity of Carbon in Binary Fe-C Austenite", Scripta Metall., Vol. 20, pp. 1507-1510 (1986).

67. Aaronson H. I., Laird C. and Kinsman K. R.: "Mechanisms of Diffusional Growth of Precipitate Crystals", in Phase Transformations, ASM, Metals Park, Ohio, USA, pp. 313-396 (1970).

68. Plichta M. R. and Aaronson H. I.: "Symposium on the Massive Transformation", Metall. Trans., Vol. 15A, pp. 411-447 (1984).

69. Speich G. R. and Szirmae A.: "Formation of Austenite from Ferrite and Ferrite-Carbide Aggregates", Trans. AIME, Vol. 245, pp. 1063-1074 (1969).

70. Karlyn D. A., Cahn J. W. and Cohen M.: "The Massive Transformation in Copper-Zinc Alloys", Trans. AIME, Vol. 245, pp. 197-207 (1969).

71. Perepezko J. H. and Massalski T. B.: "The β to ζ Massive Transformation in Ag-Al Alloys", Acta Metall., Vol. 23, pp. 621-631 (1975).

72. Plichta M. R., Aaronson H. I. and Perepezko J. H..: "The Thermodynamics and Kinetics of the $\beta \rightarrow \alpha_m$ Transformation in Three Ti-X Systems", Acta Metall., Vol. 26, pp. 1293-1305 (1978).

73. Perepezko J. H.: "Growth Kinetics and Mechanism of the Massive Transformation", Metall. Trans., Vol. 15A, pp. 437-447 (1984).

74. Massalski T. B.: "Massive Transformations", in Phase Transformations, ASM, Metals Park, Ohio, USA, pp. 433-486 (1970).

75. Christian J. W.: The Theory of Transformations in Metals and Alloys, 2nd ed., Pergamon Press, Oxford, U.K., pp. 476-482 (1975).

76. Kaufman L., Radcliffe S. V. and Cohen M.: "Thermodynamics of the Bainite Reaction", in Decomposition of Austenite by Diffusional Processes, V. F. Zackay and H. I. Aaronson eds., Interscience Publishers, New York, N. Y., pp. 313-352 (1962).

77. Christian J. W. and Edmonds D. V.: "The Bainite Transformation", in Phase Transformations in Ferrous Alloys, Proceedings of an International Conference, Sponsored by The Metallurgical Society and ASM, Philadelphia, Penn., USA, Oct. 4-6, 1983, Ed. by A. R. Marder and J. I. Goldstein, pp. 293-325 (1984).

78. Habraken L. J. and Economopoulos M.: "Bainitic Microstructures in Low-Carbon Alloy Steels and Their Mechanical Properties", in Transformations and Hardenability in Steels, Climax Molybdenum Co., Ann Arbor, Mich., pp. 69-132 (1967).

79. Goodhew P. J.: "Electron Diffraction", Engineering Materials Software Series, Dept. of Materials Science and Engineering, Univ. of Surrey, U.K. (1987).

80. Christian J. W.: The Theory of Transformations in Metals and Alloys, 2nd ed., Pergamon Press, Oxford, U.K., pp. 15-20 (1975).

81. Underwood E. E.: Quantitative Stereology, Addison-Wesley Publishing Company, Massachusetts, U. S. A., pp. 23-47 (1970).

Appendix I - Calculation of Activation Energy

The purpose of this appendix is to provide the detailed methodology employed for calculating the activation energy of the bainite-like new transformation product reported in Chapter 7. Since the equiaxed microstructure of the new phase had almost circular grain boundaries, it was assumed that each grain is a sphere and all the grains nucleated at the same instant early, in the transformation. Also, it was assumed that the transformation process is interface controlled. Christian[80] derived the following equation for an interface-controlled transformation in which all nucleation sites are exhausted at an early stage and the transformation product consists of spheres:

$$X = 1 - \exp\left\{ -\frac{4}{3}\pi N (V t)^3 \right\} \qquad (A1.1)$$

where X is the volume fraction transformed in time t, N is the number of nuclei per unit volume and V is the interface growth rate. This equation (Eq. A 1.1) was used to calculate the interface growth rate (V), assuming the volume fraction transformed (X) to be 0.99 and using the metallographically measured number of nuclei per unit volume (N).

The following formula due to Underwood[81] was employed to obtain N.

$$N = \frac{\pi N_A^2}{4 N_L} \qquad (A1.2)$$

where N_A is the number of particles per unit test area and N_L is the number of particles intercepting a unit length of test line. N_A and N_L were obtained using photomicrographs of the specimens transformed at each temperature, and from these results the average number of nuclei per unit volume (N) was calculated using Eq. A 1.2. For each temperature three photomicrographs were employed and for each photomicrograph five readings of N_A and N_L were obtained. The average growth velocity of the spheres at each temperature from 550°C

to 600°C was calculated using Eq. A 1.1 and was found to be 20 mm per s.

The activation energy for growth of the transformation product was calculated using the following Arrhenius-type equation[75],

$$V = C \left(\frac{-\Delta F}{R T}\right) \exp\left(\frac{-Q}{R T}\right) \qquad (A1.3)$$

where ΔF is the free energy difference between the parent and product phases, C is a function of the interface width, the lattice vibration frequency and the fraction of interface sites available, T is the absolute temperature, R the gas constant and Q the activation energy for interface transport. Free energy changes (ΔF) for both the austenite-to-massive ferrite (same composition as austenite) and austenite-to-bainite (ferrite plus cementite) were obtained from the work of Kaufman et al.[76] on the thermodynamics of the bainite reaction. The growth velocity (V) was plotted as a function of the reciprocal absolute temperature (1/T) for austenite-to-massive ferrite and austenite-to-bainite transformation and the slopes of these lines gave the activation energy shown in Fig. 7.13.